Editor's Note

11th International Conference on Circular Dichroism

This special issue of *Chirality* is a snapshot of the exciting presentations and poster contributions made at the 11th International Conference on Circular Dichroism (www.cd2007.fmns.rug.nl) held between the 2nd and the 6th of September 2007 in the University town of Groningen in the North of the Netherlands. As CD spectroscopy is so intimately linked to molecular and supramolecular chirality, *Chirality* is certainly an entirely appropriate venue to give a flavour of CD 2007 in the collected Original Research Papers, Short Communications, or Conference Reports in this special issue.

The conference was an outstanding success with a packed schedule of nine keynote lectures, 28 invited lectures, 26 oral contributions, 78 poster presentations and over 170 participants from 21 countries. The scientific program including contributions in core areas of CD spectroscopy such as absolute configuration determination, chiroptical techniques including vibrational optical activity (vibrational CD,VCD, and Raman optical activity, ROA), circular polarized fluorescence, solid state CD, theory of chiroptical spectroscopy, electronic circular dichroism (ECD), and computational techniques based on Density Functional Theory. CD spectroscopy continues to be an essential method for the study of bio (macro-) molecules as reflected in several outstanding contributions. However a key goal in developing the scientific program for this edition of the series was to expand the scope of the conference beyond the traditional area of CD to cover topics in which CD spectroscopy plays a less apparent, but by no means less important, contribution including nanotechnology, chemical biology, supramolecular chemistry, molecularly modified surfaces and advanced materials. CD studies of molecular nanomachines, self-assembly processes, responsive polymers and chiral surfaces, among others, reflected some of the exciting developments ahead. It is safe to conclude that as a consequence the field of chiroptical spectroscopy is rapidly expanding and new techniques and applications are emerging continuously. The contributions in this special issue with studies ranging from proteins, oligonucleotides and artificial channels to the origin of chirality and single molecule CD are further testimony of the growing importance of this field of science.

The excellent facilities available at the conference venue 'De Oosterpoort' and the venue for the conference dinner 'De Coendersborg' together with the buzzying atmosphere of the city of Groningen ensured that despite the hectic scientific schedule and the sometimes inconvenient weather there was plenty of opportunity to experience all that is best about Dutch hospitality and culture.

The co-chairs, Bert Meijer and Ben Feringa would very much like to express their deepest appreciation for the generosity of our sponsors and the team of organisers, in particular Dr. Wesley Browne, who worked hard to ensure everything ran without a hitch.

The conference on CD will stay in Europe for the next two meetings in the series in Brescia (Italy) in 2009 and in Oxford (UK) in 2011. We hope that we will see you there and share with us many new exciting discoveries in the field of chiroptical spectroscopy.

Professor Ben L. Feringa
Guest Editor
University of Groningen

Professor Nina Berova
Editor
Columbia University

DOI: 10.1002/chir.20643
Published online 20 June 2008 in Wiley InterScience
(www.interscience.wiley.com).

CHIRALITY 20:932–937 (2008)

Detection of the Activity of Ion Channels and Pores by Circular Dichroism Spectroscopy: G-Quartets as Functional CD Probes Within Chirogenic Vesicles

ANDREAS HENNIG AND STEFAN MATILE*
Department of Organic Chemistry, University of Geneva, Geneva, Switzerland

Presented at the 11th International Conference on Circular Dichroism, 2007, Groningen, Netherlands.

ABSTRACT We introduce a method to detect the activity of ion channels and pores with circular dichroism (CD) spectroscopy. G-quartets obtained by potassium templated self-assembly of 5′-guanosine monophosphate (GMP) are used as CD probes, the bee-toxin melittin as representative pore and gramicidin A as representative ion channel. To detect the activity of pores with CD spectroscopy, vesicles were loaded with GMP at concentrations above the dissociation constant (K_D) of G-quartets. GMP efflux through added pores was detectable as CD silencing due to G-quartet disassembly by local dilution. The Hill plot of melittin with Hill coefficient $n = 4$ was faithfully reproduced with CD detection. The same was true for counterion-activated cell-penetrating peptides, confirming their ability to mediate the export of anions such as GMP. The same method is not applicable to the CD detection of the activity of ion channels because GMP efflux does not occur. To do that, the potassium selectivity of G-quartets was used. Namely, vesicles were loaded with GMP at concentrations above the dissociation constant (K_D) of G-quartets stabilized by potassium. External M/K cation exchange resulted in CD silencing by M/K antiport through the added ion channel followed by G-quartet disassembly within the vesicle. Reversal of the direction of M/K antiport was achieved with Cs-loaded vesicles and detected as the appearance of the CD signature of G-quartets in response to K influx. Corroborative examples with gramicidin A include CD detection of the Eisenman I selectivity sequence and the Hill coefficient. *Chirality 20:932–937, 2008.*

KEY WORDS: circular dichroism; G-quartets; ion channels; pores; self-assembly; supramolecular chemistry; vesicles

INTRODUCTION

Circular dichroism (CD) spectroscopy is used routinely in organic chemistry and related fields for structural studies.[1] Common applications include the determination of the absolute configuration and enantiomeric purity of molecules such as natural products or synthetic drugs. Other classical topics that are routinely addressed by CD spectroscopy include conformational changes, self-assembly, and ligand binding of proteins, DNA, RNA, and complex synthetic architectures.[1–3]

In sharp contrast to this popular use to study structures, CD spectroscopy is rarely used to study functions. There are no obvious reasons for this neglect. Advantages known from structural studies, such as sensitivity without interference from achiral components of complex systems, apply also for functional studies. The use of exciton coupled CD (ECCD) spectroscopy appears particularly appealing for functional studies, because the characteristic bisignate ECCD Cotton effect is perfectly suited for the ratiometric detection of changes in CD as response to the activity of interest. Often difficult to obtain with other methods, ratiometric detection is very attractive in functional studies to exclude artifacts with confidence.

One of the rare recent examples for the use of CD spectroscopy for functional studies concerns the introduction of G-quartets as functional CD probes to detect osmotic stress.[4] G-Quartets, which were discovered 1962 in hydrogels formed by 5′-guanosine monophosphate (GMP), are planar supramolecular macrocycles composed of four guanosines (Fig. 1).[5,6] One quartet contains eight intermolecular hydrogen bonds between complementary Watson–Crick and Hoogsteen edges of neighboring guanines. The self-assembly of G-quartets further requires templation by Na^+ or K^+, which coordinate to the four carbonyl oxygens

Contract grant sponsor: Swiss NSF; Contract grant numbers: 200020-109160, 200020-117593.
*Correspondence to: Stefan Matile, Department of Organic Chemistry, University of Geneva, Geneva, CH-1211 Switzerland.
E-mail: stefan.matile@chiorg.unige.ch
Received for publication 3 October 2007; Accepted 26 November 2007
DOI: 10.1002/chir.20526
Published online 1 February 2008 in Wiley InterScience (www.interscience.wiley.com).

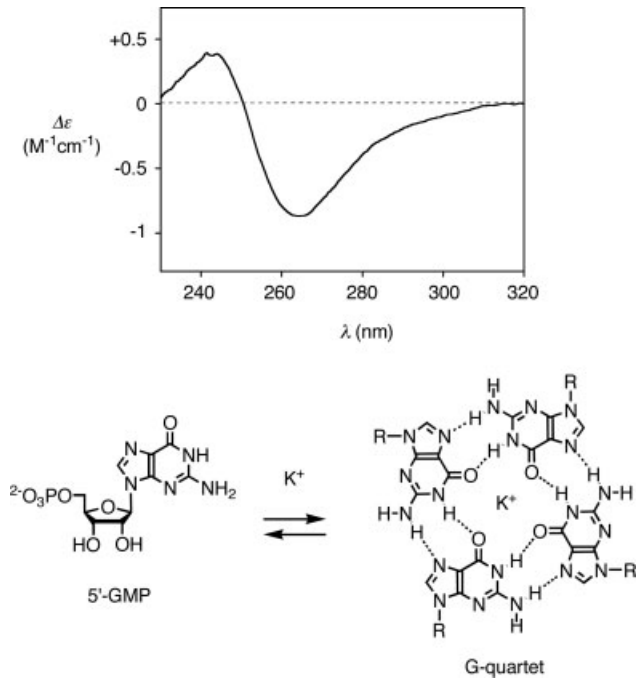

Fig. 1. Potassium-templated self-assembly of the nearly CD-silent GMP into G-quartets with their CD spectrum (continuing assembly into face-to-face π-stacked octamers and higher-order columnar phases is omitted for clarity). A full set of UV-vis and CD spectra of GMP-loaded vesicles with assembled and disassembled G-quartets is shown in Ref. 4.

in the middle of the macrocycle. Coordination to two quartets stabilizes octamers, and face-to-face π–π interactions promote the formation of longer cylindrical π-stacks. G-quartets occur in biology in many variations far beyond telomer DNA and are intensely used in medicinal chemistry (e.g., aptamers), supramolecular chemistry and nanotechnology. Examples include antithrombin G-quartet aptamers[7] or covalent capture of hydrophobic G-quartets as synthetic ion channels.[8]

The CD spectrum of the selected G-quartets of GMP in water is very simple (Fig. 1).[4–6] A negative CD Cotton effect at 262 nm is followed by a positive CD Cotton effect at 241 nm. This bisignate doublet originates from exciton coupling between two stacked G-quartets with an *M*-helical twist. The magnitude of these two signals thus increases and decreases together and can be described as the sum of the two, named CD amplitude. For G-quartets in general, the sign and shape of this couplet can vary, depending on several factors such as the exact structure of the guanylic derivative, the type of facing between quartets, and so on.[9,10]

To detect osmotic stress with CD spectroscopy, vesicles were loaded with GMP-quartets at concentrations around their dissociation constant.[4] Under these conditions, hyperosmotic pressure was reported to increase CD amplitude. This signal transduction occurs because of increasing assembly of intravesicular G-quartets in response to hyperosmotic vesicle shrinking. Hypoosmotic pressure was correspondingly reported as CD silencing caused by G-quartet disassembly in response to vesicle swelling. However, the responsiveness of G-quartets within vesicles to changes in local GMP or cation concentration is naturally not limited to the detection of osmotic stress by CD spectroscopy. Here, we introduce G-quartets within vesicles as functional CD probes to detect the activity of ion channels and pores. Gramicidin A and melittin are used as model ion channels and pores, and nonlinear concentration dependences and ion selectivity sequences are addressed as illustrative examples. Usual methods to detect these activities include conductance measurements in planar bilayer membranes and the use of fluorescence probes in spherical vesicle membranes.[11] Established CD methods to detect the activity of ion channels or pores do not exist.

MATERIALS AND METHODS

Materials

Na_2GMP, melittin, gramicidin A, triton X-100, polyarginine, and all salts and buffers were of the best grade available from Sigma and used as received. 5(6)-carboxyfluorescein (CF) was from Fluka. Egg yolk phosphatidylcholine (EYPC) and a Mini-Extruder used for LUV preparation were from Avanti Polar Lipids. UV-Vis spectra were recorded on a JASCO V-650 spectrophotometer. CD spectra were recorded on a JASCO J-815 spectropolarimeter equipped with a total fluorescence detector. Fluorescence measurements were performed with FluoroMax-2 (Jobin-Yvon Spex). UV-Vis and CD spectra were obtained using quartz glass cells with 1 cm path length; all spectrometers were equipped with a stirrer and a temperature controller (measurements at 25°C).

Preparation of Large Unilamellar Vesicles

A thin film of EYPC (25 mg) was prepared by evaporating a solution in 1 ml MeOH/$CHCl_3$ (1:1) on a rotary evaporator and then in vacuo (>2 h). After hydration (>30 min) with 1.0 ml buffer (100 mM Na_2GMP, 0 (i.e., EYPC-LUVs ⊃ GMP) or 10 mM CF (i.e., EYPC-LUVs ⊃ GMP/CF), 10 mM HEPES, 800 mM MCl, pH 7.4, M = Cs, Rb, K, Na, and Li), the resulting suspension was subjected to >5 freeze-thaw cycles (liquid N_2, warm water bath), and >15 times extruded through a polycarbonate membrane (pore size 100 nm). The extravesicular components were removed by size exclusion chromatography (Sephadex G-50) with 10 mM HEPES, 900 mM MCl (M as in the subsequently used measurement buffer), pH 7.4. The concentration of entrapped GMP in the resulting LUVs dispersion was estimated from the absorption spectrum of coentrapped CF after lysis. Final conditions: 7.5 mM EYPC; inside: 100 mM Na_2GMP, 0 or 10 mM CF, 10 mM HEPES, 800 mM MCl, pH 7.4, outside: 10 mM HEPES, 900 mM MCl, pH 7.4, M = Cs, Rb, K, Na, Li.

Pore Activity by CD

EYPC-LUVs ⊃ GMP or EYPC-LUVs ⊃ GMP/CF (400 μl, M_{inside} = K) were added to gently stirred, thermostated buffer (1600 μl, 10 mM HEPES, 900 mM KCl) in a CD cell. The time courses of $\Delta\varepsilon_t$ at λ_{obs} = 264 nm and of CF emission I at λ_{em} = 517 nm (λ_{ex} = 264 nm) were monitored simultaneously during the addition of melittin (20 μl stock solution, 0–1000 nM final monomer concentra-

tion) at $t = 0$ min, and addition of 80 μl 1.2% (aq.) triton X-100 or melittin at the end of every experiment.

Time courses $\Delta\varepsilon_t$ were normalized to $\Delta\varepsilon$ (per monomeric GMP) using eq. 1 for CD silencing and (2) for chirogenesis (vide infra).

$$\Delta\varepsilon = (\Delta\varepsilon_t - \Delta\varepsilon_\infty)/(\Delta\varepsilon_0 - \Delta\varepsilon_\infty) \quad (1)$$

$$\Delta\varepsilon = (\Delta\varepsilon_t - \Delta\varepsilon_0)/(\Delta\varepsilon_\infty - \Delta\varepsilon_0) \quad (2)$$

where $\Delta\varepsilon_0 = \Delta\varepsilon_t$ at pore addition and $\Delta\varepsilon_\infty = \Delta\varepsilon_t$ at saturation after lysis. The obtained $\Delta\varepsilon$ was further normalized into fractional $\Delta\varepsilon_F$ using eq. 3

$$\Delta\varepsilon_F = \Delta\varepsilon/\Delta\varepsilon_{MAX} \quad (3)$$

where $\Delta\varepsilon_{MAX}$ is the reference value for the varied parameter of interest, e.g., maximal activity just before lysis. Fractional activity Y is introduced to compare fractional $\Delta\varepsilon_F$ at a given time, usually 200 s after the start of the experiment just before lysis.

For Hill analysis, Y was plotted against concentration c_M (monomer of pore forming molecule) and fitted to the Hill eq. 4 to give effective concentration EC_{50} and the Hill coefficient n.

$$Y = Y_\infty + (Y_0 - Y_\infty)/\{1 + c_M/EC_{50})^n\} \quad (4)$$

Y_0 is Y without pore, Y_∞ is Y with excess pore.

Activity of Polyarginine

EYPC-LUVs ⊃ GMP or EYPC-LUVs ⊃ GMP/CF (400 μl, M_{inside} = K) were added to gently stirred, thermostated buffer (1600 μl, 10 mM HEPES, 900 mM KCl) in a CD cell. The time course of $\Delta\varepsilon_t$ was monitored at λ_{obs} = 264 nm during the addition of polyarginine (10 μl, 100 μM in H_2O) and dodecylphosphate (20 μl stock solution in DMSO, 10-1000 μM final concentration) at $t = 0$ min (both sequences of addition), and the addition of triton X-100 at the end of every experiment (80 μl, 1.2% aq). Time courses were analyzed in analogy with eqs. 2–4.

Fluorescence Controls

Fluorescence intensity changes of EYPC-LUVs ⊃ GMP/CF during melittin or polyarginine/dodecylphosphate addition were measured at the emission wavelength λ_{em} = 517 nm on the fluorometer (excitation was at λ_{ex} = 492 nm) and in double-channel experiment on the spectropolarimeter. Time courses were analyzed in analogy with eqs. 2–4.

Ion Channel Activity

EYPC-LUVs ⊃ GMP or EYPC-LUVs ⊃ GMP/CF (400 μl, (M_{inside} = Li, Na, K, Rb, Cs) were added to gently stirred, thermostated buffer (1980 μl, 10 mM HEPES, 100 mM MCl ($M_{outside}$ = Li, Na, K, Rb, Cs, $M_{outside} \neq M_{inside}$) in a CD cell. The time courses of $\Delta\varepsilon_t$ at λ_{obs} = 264 nm and of CF emission I_t at λ_{em} = 517 nm (λ_{ex} = 492 nm) were monitored simultaneously during the addition of gramicidin A (20 μl stock solution, 0–300 nM final monomer concentration) at $t = 0$ min, and triton X-100 at the end of every experiment (80 μl, 1.2% aq). Time courses $\Delta\varepsilon_t$ were normalized as described for pores.

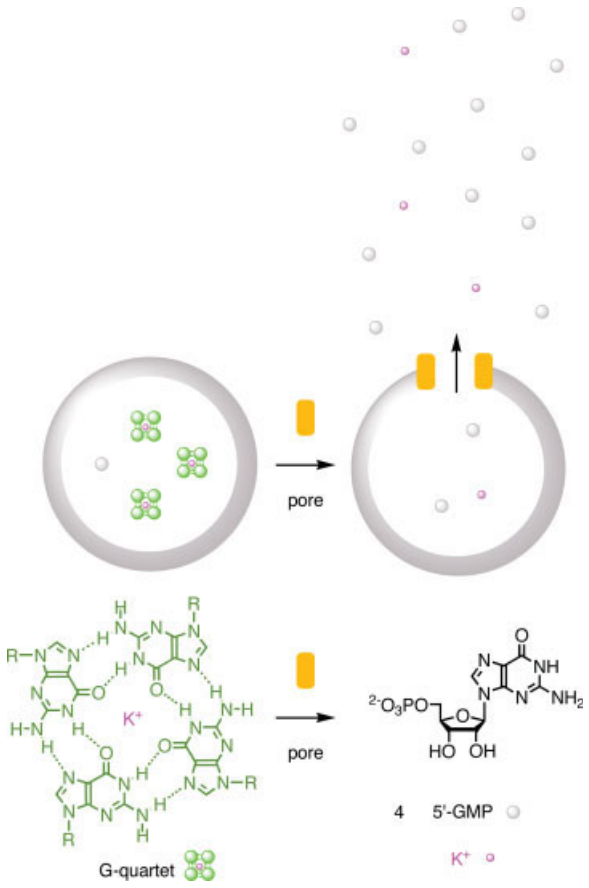

Fig. 2. Detection of the activity of pores by CD spectroscopy. Vesicles are loaded with GMP and potassium at concentrations high enough to give G-quartets with their typical CD signature. The dilution by GMP efflux through added pores causes G-quartet disassembly. [Color figure can be viewed in the online issue, which is available at www.interscience.wiley.com.]

RESULTS AND DISCUSSION

The CD method to detect the activity of pores was designed as follows (Fig. 2). Vesicles were loaded with GMP in potassium-rich buffer at potassium concentrations high enough to template the assembly of G-quartets. The addition of pores to these vesicles would then cause the efflux of GMP. This local GMP dilution would result in the disassembly of the G-quartets, which would then be reported as CD silencing.

Melittin, the pore forming peptide from the bee venom, was selected as model pore to test the validity of this simple concept.[12,13] GMP-loaded large unilamellar EYPC vesicles (EYPC-LUVs ⊃ GMP) were prepared. Their negative $\Delta\varepsilon = -0.8\ M^{-1}\ cm^{-1}$ at 264 nm demonstrated the presence of intravesicular G-quartets (Fig. 1). The addition of melittin to these vesicles caused a rapid decrease in $\Delta\varepsilon$ (Fig. 3A). This change was consistent with G-quartet disassembly due to GMP efflux through the pores formed by melittin.

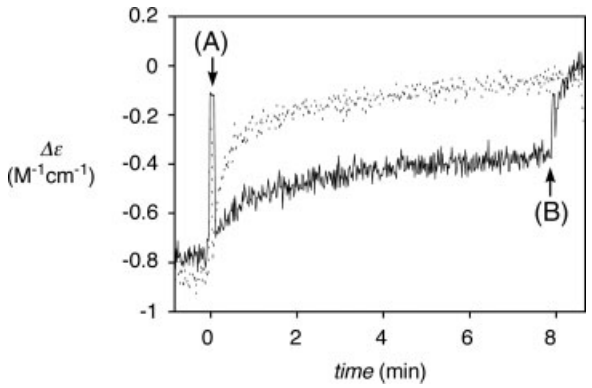

Fig. 3. Change in $\Delta\varepsilon$ (λ_{obs} = 264 nm) during the addition of (**A**) melittin (0.1 (solid) and 0.3 μM (dotted) final concentration) to EYPC-LUVs ⊃ GMP (100 mM Na_2GMP, 10 mM HEPES, 800 mM KCl, pH 7.4) in buffer (10 mM HEPES, 900 mM KCl, pH 7.4), calibrated by (**B**) final addition of excess triton X-100 (80 μl, 1.2% aq).

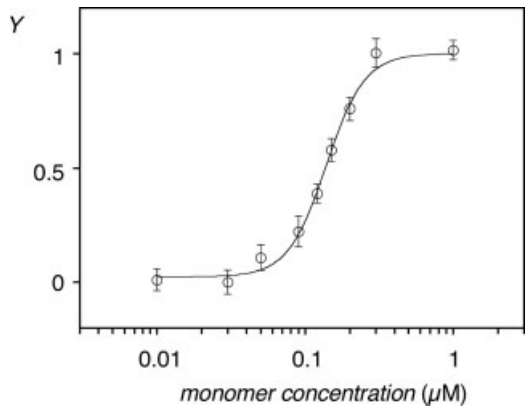

Fig. 4. Hill plot of the activity of melittin determined by CD spectroscopy. The dependence of the fractional activity Y on the concentration c_M of monomeric peptide was determined in EYPC-LUVs ⊃ GMP as specified in Fig. 3.

The final addition of an excess of the detergent triton X-100 caused the nearly complete CD silencing (Fig. 3B). This change was as expected for the full destruction of the vesicles. Independent evidence for the working principle in Figure 2 was obtained by the concomitant increase in fluorescence intensity of EYPC-LUVs ⊃ GMP/CF, in which CF has been coincluded in the vesicles at sufficiently high concentrations to afford self-quenching. Detection of the increase in CF emission in response to pore addition is a classical assay for pore activity.[11,14] Double-channel kinetics with melittin gave identical results for simultaneously detected increase in CF emission and decrease in ECCD of GMP (not shown). This control experiment confirmed that eventual contributions from light scattering or peptide pores to the CD signals in the useful wavelength range from 250 to 290 nm do not interfere with the detection of melittin function by CD. The development of functional CD probes with (a) stronger and (b) red-shifted CD Cotton effects remains nevertheless an attractive objective to minimize noise and maximize sensitivity.

The dependence of the activity of the melittin pore on the peptide concentration was determined next (Fig. 4). The Hill plot obtained with functional CD probes was comparable with the Hill plot of melittin obtained by other methods.[12–14] The good fit found with a Hill coefficient $n = 3.4 \pm 0.5$ was in agreement with the endergonic self-assembly[15] into the tetrameric active suprastructure of melittin.[12,13] The effective monomer concentration found for melittin was $EC_{50} = 139 \pm 6$ nM.

Arginine-rich cell-penetrating peptides (CPPs) represent another class of compounds, which is able to translocate anionic molecules across a lipid bilayer membrane upon activation by amphiphilic counteranions.[16] This activity has, for example, been demonstrated by phosphatidylglycerol-activated export of CF from vesicles in the presence of polyarginine (pR),[16] and was more recently applied to the detection of enzyme inhibitors.[17] It was therefore appealing to investigate, through the novel CD-based assay, whether or not counterion-activated polyarginines also mediate the efflux of GMP.

To do so, dodecylphosphate (DP) and pR were added to a mixture of EYPC-LUVs ⊃ GMP with or without coincluded CF. Increasing CD silencing with increasing DP concentration was found (Fig. 5). This result demonstrated GMP export by synergistic pR-DP transporters with a comparably[17] weak effective concentration $EC_{50} = 93 \pm 7$ μM and a Hill coefficient of $n = 2.4 \pm 0.6$.

The ability of pores and CPPs to translocate molecules as large as GMP made the development of a CD method to detect their activity very easy. The situation with ion channels, limited to the transport of small inorganic ions rather than larger organic molecules, was clearly more challenging, because GMP efflux would not be operational in this case. The addition of an ion channel to vesicles loaded with K^+-stabilized G-quartets will thus not cause any change in CD.

To detect ion channel activity by CD spectroscopy, we thought to exploit the ion selectivity of G-quartets instead (Fig. 6). We first considered vesicles that are loaded with K^+-stabilized G-quartets and permeabilized with the ion channel of interest (Fig. 6A). Exchange of the external K^+

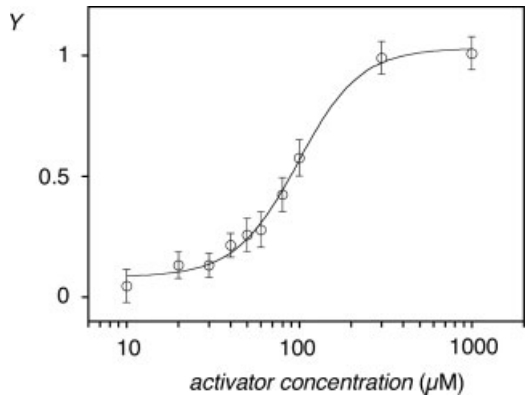

Fig. 5. Hill plot of the activity of polyarginine-dodecylphosphate (pR-DP) transporters determined by CD spectroscopy with respect to the activator DP. The fractional activity Y of pR-DP transporters was determined as CD silencing in response to GMP efflux (cf. Fig. 2). The dependence of Y on the concentration of DP was determined in EYPC-LUVs ⊃ GMP as exemplified in Fig. 3.

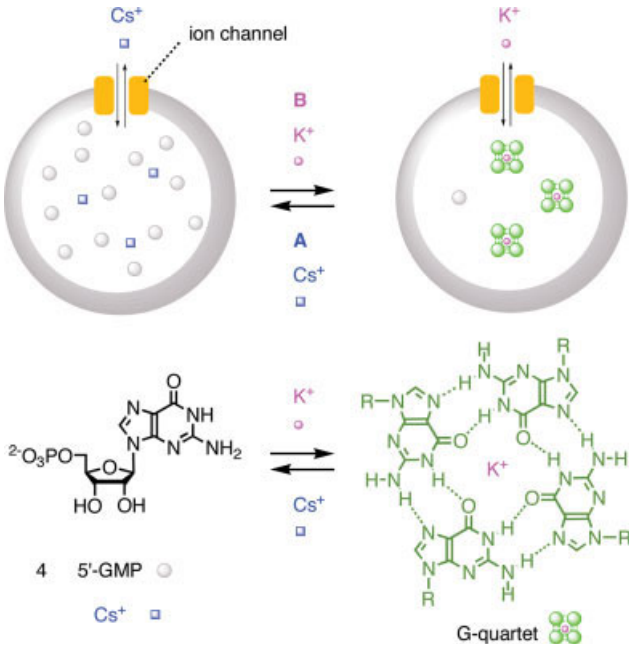

Fig. 6. Detection of the activity of ion channels by CD spectroscopy. (**A**) Vesicles are loaded with GMP and K^+ at concentrations high enough to give G-quartets with their typical CD signature. Channel addition and external K^+/Cs^+ exchange followed by transmembrane Cs^+/K^+ exchange will disassemble the G-quartets within the vesicle. The result is CD silencing. (**B**) The reversed, chirogenic CD detection of ion channel activity starts with vesicles that are loaded with GMP and Cs^+ instead of K^+. Channel addition and external K^+/Cs^+ exchange followed by transmembrane K^+/Cs^+ exchange will in this case cause the assembly of G-quartets within the vesicle. [Color figure can be viewed in the online issue, which is available at www.interscience.wiley.com.]

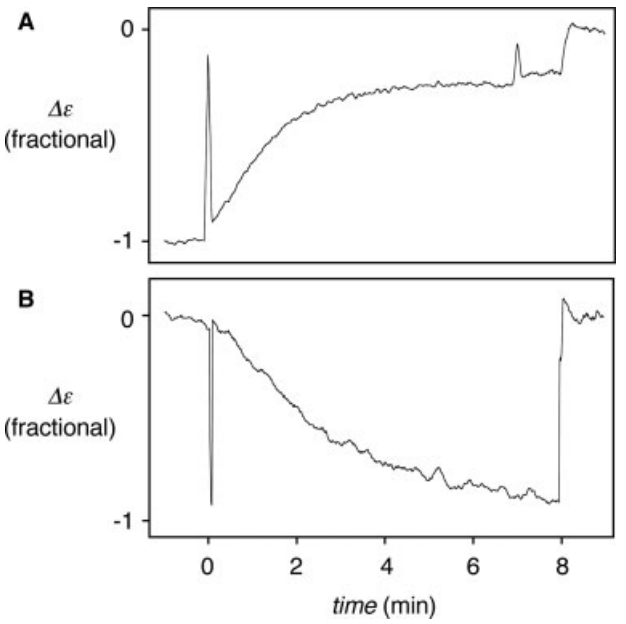

Fig. 7. (**A**) Change in Δε (λ 265 nm) during the addition of gramicidin (0.15 μM final concentration, t = 0 min) to EYPC-LUVs ⊃ GMP (100 mM Na_2GMP, 10 mM HEPES, 800 mM KCl, pH 7.4) in buffer (10 mM HEPES, 900 mM CsCl, pH 7.4), calibrated by final addition of excess triton X-100 (20 μl, 1.2% aq, t = 8 min). (**B**) Same with internal CsCl and external KCl.

with isoosmolar Cs^+ could turn on transmembrane K^+/Cs^+ antiport through the ion channel of interest and fully replace the internal K^+ with Cs^+ because the external volume is much larger than the internal volume. This exchange of the internal K^+ with Cs^+ would cause the disassembly of G-quartets at constant GMP concentration within the vesicle because Cs^+ is too big to act as a template. This intravesicular G-quartet disassembly would be detected as CD silencing. This CD response would directly report on the ability of the ion channel of interest to mediate K^+/Cs^+ antiport. The CD response to exchange of the external K^+ with isoosmolar Rb^+ would then report on K^+/Rb^+ antiport, and so on.

The reversed mode of CD detection was even more appealing because it is chirogenic and can thus demonstrate that ion channels act in intact vesicles (Fig. 6B). For chirogenic detection, we considered vesicles that are loaded with GMP and cesium cations. In the presence of Cs^+, G-quartets will not form and no CD signal will be detected. Exchange of external Cs^+ with isoosmolar K^+ followed by transmembrane Cs^+/K^+ antiport through the ion channel of interest would then initiate the assembly of G-quartets within the vesicle. This intravesicular G-quartet assembly would be detected as appearance of the characteristic bisignate CD doublet.

Gramicidin A was selected as classical model channel to test this new approach to detect ion channel activity with CD spectroscopy.[18,19] Addition of gramicidin to EYPC-LUVs ⊃ GMP with internal K^+ and external K^+ did not cause any changes in CD (not shown). This lack of responsiveness confirmed that gramicidin does not mediate the efflux of GMP. Addition of gramicidin to EYPC-LUVs ⊃ GMP with internal K^+ and external Cs^+, however, caused a rapid decrease in Δε (Fig. 7A). This change was consistent with G-quartet disassembly within the vesicle due to transmembrane Cs^+/K^+ exchange through the gramicidin ion channel. Final lysis with triton X-100 caused the expected complete CD silencing. A constant fluorescence intensity during the addition of gramicidin A to EYPC-LUVs ⊃ GMP/CF further confirmed that the

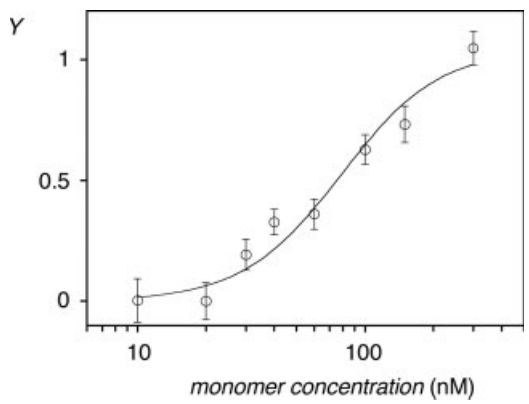

Fig. 8. Hill plot of the activity of the gramicidin ion channel determined by CD spectroscopy. The dependence of the fractional activity Y on the concentration of monomeric peptide was determined in EYPC-LUVs ⊃ GMP with internal RbCl and external KCl as specified in Fig. 6B.

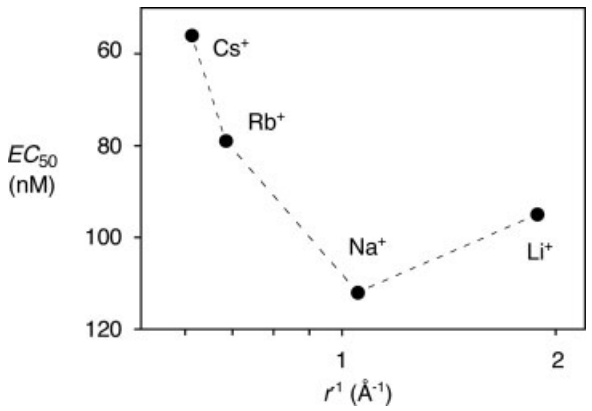

Fig. 9. The Eisenman selectivity topology of gramicidin ion channel determined by CD spectroscopy. The dependence of the EC_{50} as a measure for ion channel activity on the reciprocal cation radius was determined from Hill plots for CD assays with internal MCl and external KCl as specified in Fig. 6.

vesicles were not destroyed and that solely ion transport could be the source of the CD silencing.

The reversed, chirogenic CD detection was tested with EYPC-LUVs ⊃ GMP with internal Cs^+ and external K^+ (Figs. 6B and 7B). Addition of gramicidin caused a rapid appearance of the CD signal characteristic for G-quartet self-assembly (Fig. 7B). This change was as predicted for transmembrane Cs^+/K^+ exchange through the gramicidin ion channel. Final lysis with triton X-100 cleanly removed this CD signal. This complementary CD response to potassium-mediated G-quartet assembly and disassembly corroborated that eventual contributions from light scattering or peptide channels to CD signals at 250–290 nm do not interfere with the detection of gramicidin function by CD. Different to the situation with pores, the development of red-shifted CD probes for the detection of ion channel activity with maximal sensitivity and selectivity will however be more demanding because they have to operate by ion-selective, templated self-assembly.

The CD method to detect the activity of gramicidin as model ion channel was further expanded to a complete series of internal and external Cs^+, Rb^+, Na^+, and Li^+ with K^+ as constant partner. Hill plots were recorded for each situation. The Hill plots with assumed Hill coefficients of $n = 2$ were in excellent agreement with the dimeric active suprastructure of gramicidin (see for example Fig. 8 with internal Rb^+ and external K^+).[18] The effective concentration EC_{50} (i.e., the monomer concentration needed to observe 50% ion channel activity) obtained for Cs/K, Rb/K, Na/K, and Li/K gradients decreased with increasing radius of the variable cation except for a strong Li-anomaly[20] (Fig. 9). The resulting selectivity topology was similar to an Eisenman I selectivity sequence that is exclusively governed by cation dehydration without contributions from cation binding to the channel.[20] This is the selectivity sequence of gramicidin A.[19]

LITERATURE CITED

1. Nakanishi K, Berova N, Woody RW, editors. Circular dichroism—principles and applications. Weinheim: Wiley; 1994.
2. Zhang J, Albelda MT, Liu Y, Canary JW. Chiral nanotechnology. Chirality 2005;17:404–420.
3. Gottarelli G, Lena S, Masiero S, Pieraccini S, Spada GP. The use of circular dichroism spectroscopy for studying the chiral molecular self-assembly: an overview. Chirality (in press) DOI 10.1002/chir.20459.
4. Sakai N, Matile S. G-quartet self-assembly under osmotic pressure: remote control by vesicle shrinking rather than stress. Chirality 2003;15:766–771.
5. Davis JT, Spada GP. Supramolecular architectures generated by self-assembly of guanosine derivatives. Chem Soc Rev 2007;36:296–313.
6. Neidle S, Balasubramanian S. Quadruplex nucleic acids. London: RSC; 2006.
7. Wang KY, McCurdy S, Shea RG, Swaminathan S, Bolton PH. A DNA aptamer which binds to and inhibits thrombin exhibits a new structural motif for DNA. Biochemistry 1993;32:1899–1904.
8. Kaucher MS, Harrell WA Jr, Davis JT. A unimolecular G-quadruplex that functions as a synthetic transmembrane Na^+ transporter. J Am Chem Soc 2006;128:38–39.
9. Gray DM, Wen JD, Gray CW, Repges R, Repges C, Raabe G, Fleischhauer J. Measured and calculated CD spectra of G-quartets stacked with the same or opposite polarities. Chirality (in press) DOI 10.1002/chir.20455.
10. Gottarelli G, Masiero S, Spada GP. The use of CD spectroscopy for the study of the self-assembly of guanine derivatives. Enantiomer 1998;3:429–438.
11. Matile S, Sakai N. The characterization of synthetic ion channels and pores. In: Schalley CA, editor. Analytical methods in supramolecular chemistry. Weinheim: Wiley; 2007. p 391–418.
12. Schwarz G, Beschiaschvili G. Kinetics of melittin self-association in aqueous solution. Biochemistry 1998;20:7826–7831.
13. van Veen M, Georgiou GN, Drake AF, Cherry RJ. Circular-dichroism and fluorescence studies on melittin: effects of C-terminal modifications on tetramer formation and binding to phospholipid vesicles. Biochem J 1995;305:785–790.
14. Matile S, Tanaka H, Litvinchuk S. Analyte sensing across membranes with artificial pores. Top Curr Chem 2007;277:219–250.
15. Bhosale S, Matile S. A simple method to identify supramolecules in action: hill coefficients for exergonic self-assembly. Chirality 2006;18:849–856.
16. Sakai N, Matile S. Anion-mediated transfer of polyarginine across liquid and bilayer membranes. J Am Chem Soc 2003;125:14348–14356.
17. Miyatake T, Nishihara M, Matile S. A cost-effective method for the optical transduction of chemical reactions. Application to hyaluronidase inhibitor screening with polyarginine-counteranion complexes in lipid bilayers. J Am Chem Soc 2006;128:12420–12421.
18. O'Connell AM, Koeppe RE II, Andersen OS. Kinetics of gramicidin channel formation in lipid bilayers: transmembrane monomer association. Science 1990;250:1256–1259.
19. Vescovi A, Knoll A, Koert U. Synthesis and functional studies of THF-gramicidin hybrid ion channels. Org Biomol Chem 2003;1:2983–2997.
20. Eisenman G, Horn R. Ionic selectivity revisited: the role of kinetic and equilibrium processes in ion permeation through channels. J Membrane Biol 1983;76:197–225.

On the Origin of Circular Dichroism in Trigonal Dihedral d^6 Complexes of Bidentate Ligands Containing Only σ-Orbitals. A Qualitative Model Based on a Density Functional Theory Study of Λ-$[Co(en)_3]^{3+}$

JING FAN AND TOM ZIEGLER*

Department of Chemistry, University of Calgary, Calgary, Alberta, Canada

Presented at the 11th International Conference on Circular Dichroism, 2007, Groningen, Netherlands

ABSTRACT Time-dependent density functional theory (TD-DFT) in conjunction with qualitative molecular orbital theory is employed to interpret the circular dichroism (CD) spectrum of Λ-$[Co(en)_3]^{3+}$. The simulated spectrum based on TD-DFT is compared in details with the experimental data. Emphasis is put on a qualitative understanding of the origin of optical activity in σ-bonded trigonal dihedral complexes with bidentate ligands in general. Rotatory strengths associated with the CD bands of both d-d transitions and ligand-to-metal charge transfer (LMCT) are interpreted based on the metal–ligand σ-interactions. These interactions are in turn analyzed in terms of symmetry unique overlaps between metal d- and symmetry ligand-orbitals as well as the dependence of these overlaps on geometrical parameters of the complex. *Chirality 20:938–950, 2008.*

KEY WORDS: optical activity; transition metal complex; time-dependent density functional theory; metal–ligand orbital overlap; geometrical distortion

INTRODUCTION

For a long time, there has been an interest in the circular dichroism (CD)[1] of transition metal complexes, $[M(L\text{-}L)_3]^{n+}$, where the optical activity arises due to the helical arrangement of the chelate rings formed by the bidentate ligand L-L contaning only σ-orbitals. The CD spectrum of $[Co(en)_3]^{3+}$, one of the most familiar and basic of all the tris-bidentate complex ions, exhibits almost all the important features of tris-bidentate complexes. Chiroptical properties of this complex have been extensively studied since the pioneering work of Mathieu[2] and Kobayashi.[3] Moffitt introduced the first quantum-mechanical theory of optical activity in transition metal complexes[4] and the use of sector rules[5] for the correlation of structure with optical activity. Many subsequent theories were developed based upon the Moffitt model. Liehr[6] and Karipides and Piper[7] proposed the first molecular-orbital formulation for optical activity in metal complexes. Although the models do give useful qualitative information about the sensitivity of the rotational strengths of d-d transitions due to distortions within the ML_6 molecular frame, none of them is capable of providing an adequate formulation of the origin of the d-d optical activity in D_3 metal complexes. Other approaches are independent system-perturbation models that include both static[8–11] and dynamic metal ion–ligand polarization interactions.[12,13] These theories, however, are developed in particular to address d-d excitations and cannot describe the nature of the ligand-to-metal charge transfer.

The formulation of CD in terms of time dependent density functional theory (TD-DFT)[14–16] has resulted in a number of TD-DFT applications to moderately sized organic molecules[14,17–20] as well as some transition metal complexes.[21–24] TD-DFT has proved to be an especially attractive approach as it gives reasonable accuracy at a low computational cost. Exploratory studies on the optical activity in tris-bidentate Co (III) and Rh (III)[21–23] complexes as well as other transition metal systems[24] have already appeared.

Tris-diamine complexes $[M(L\text{-}L)_3]^{n+}$ exist in two enantiomeric configurations, Λ or Δ, depending on the helical arrangement of the chelate rings formed by the 1,2-diamine rings around the metal ion, Scheme 1. In addition, the five-membered chelate rings can adopt one of two puckered conformations,[25] λ or δ, depending on whether the N···N direction and the C—C bond form a segment of a left-handed or a right-handed helix, respectively. The $[Co(en)_3]^{3+}$ complex has as already mentioned been studied before based on TD-DFT by our group.[21–23] However, our current objective is to introduce a qualitative framework that can be used to analyze CD spectra of coordination compounds in conjunction with TD-DFT calculations.

Contract grant sponsor: National Science and Engineering Research Council of Canada (NSERC)
*Correspondence to: Tom Ziegler, Department of Chemistry, University of Calgary, 2500 University Drive, Calgary, Alberta, Canada T2N 1N4.
E-mail: ziegler@ucalgary.ca
Received for publication 1 October 2007; Accepted 26 November 2007
DOI: 10.1002/chir.20527
Published online 1 February 2008 in Wiley InterScience (www.interscience.wiley.com).

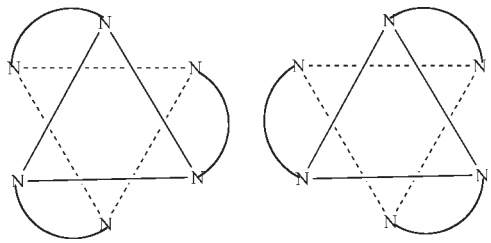

Scheme 1. Enantiomers of $[Co(en)_3]^{3+}$.

The first step towards meeting this objective will be taken in the present study where we shall deal with $[Co(en)_3]^{3+}$ as the prototype for trigonal dihedral d^6 complexes of bidentate ligands containing only σ-orbitals. The scope will later on be extended to ligands with more complex electronic structures or other geometries as well as to metal centers with different d-electron counts. The qualitative analysis is an extension of previous work[18] restricted to d-d transitions only.

MATERIALS AND METHODS

The calculations reported in the present study are carried out with a modified CD version of the Amsterdam density functional (ADF) program.[26–28] The CD version[14–16] contains the methodology for the computation of optical rotations and CD spectra implemented in the previously developed TD-DFT code by Gisbergen et al.[29–31] The 20 lowest spin-allowed excitations have been calculated. On the basis of the computed excitation energies, associated oscillator strengths, and rotatory strengths, spectra have been simulated for a comparison with experimental data. An empirical recipe[32] has been employed to simulate the spectrum in which the band width $\Delta\bar{\nu}$, is given by $\Delta\bar{\nu} = 7.5\sqrt{\bar{\nu}}$, where $\bar{\nu}$ is the absorption frequency in cm^{-1}. Numerical data for the experimental spectra have been extracted using "g3data" software.[33] The frozen core-valence triple-ς polarized "TZP" Slater basis sets of the ADF database have been employed for the calculations. The data presented here are obtained with the dipole-length formula for the rotatory strength. It has been shown[23] for $[Co(en)_3]^{3+}$ that rotatory strengths computed with the this formula are in good agreement with those obtained from dipole-velocity form. The "COnductor-like continuum Solvent MOdel" (COSMO)[34,35] has been applied in the calculations of the CD spectrum to simulate the environment of the +3 ion. Molecular vibrations and other effects on the spectra are neglected in this study.

The Vosko-Wilk-Nusair (VWN)[36] local density approximation (LDA) with the Becke88-Perdew86 (BP86) gradient corrections[37,38] have been used in the CD calculations. The application of other gradient-corrected functionals does not significantly change the simulated spectrum. Except for model molecules, TD-DFT calculations have been carried out based on optimized geometries.

RESULTS AND DISCUSSION

Geometrical Considerations

We start with a hypothetical configuration of tris-ethylenediamine complex in which the molecule contains D_{3h} symmetry. In this configuration the planes of the three diamine rings are situated parallel to the C_3 axis, i.e. *z*-axis in the coordinate system shown in Figure 1a. The three ligands are represented by rectangles for the sake of clarity. The D_{3h} configuration is not chiral due to the reflection planes present in the complex and therefore do not exhibit optical activity.

As illustrated in Figure 1b, a counterclockwise rotation (from the point of view of an observer looking along the axis of rotation towards the metal) of the three diamine rings by ω degrees leads to the Λ-configuration of $[M(en)_3]^{3+}$, which is chiral and thus in principle able to exhibit circular dichroism as its symmetry now is D_3. We note that a rotation by $-\omega$ would have resulted in the Δ-configuration of the complexes. The exact angle of rotation ω observed in $[M(en)_3]^{3+}$ is 34.7° for cobalt, 36.1° for rhodium, and 36.3° for iridium.

The rotation angle can be correlated to the polar ratio[39] (s/h of Fig. 2b), a measure of the polar displacement of the six nitrogens away from the ideal octahedron and the azimuthal angle[39] (φ of Fig. 2c), a parameter for the radial distortion of the six nitrogens away from the ideal octahedron, as:

$$s = \sqrt{3(b^2 + a^2 \sin^2 \omega)}, \quad (1)$$

$$h = 2a \cos \omega, \quad (2)$$

$$\tan(\phi/2) = \frac{a}{b} \sin \omega. \quad (3)$$

Here a is the half distance between two nitrogens on the diamine ligand and b is the distance between the metal and the midpoint of the same two nitrogens. Figure 2a displays the definition of the parameters a and b. We recall that for an ideal octahedron, $s/h = 1.22$ and $\phi = 60°$, which corresponds to $a = b$ and $\omega = 35.3°$.

Simple Orbital Interaction Diagram

To understand the mechanism that makes it possible for $[M(en)_3]^{3+}$ of D_3 symmetry to exhibit CD, we shall now

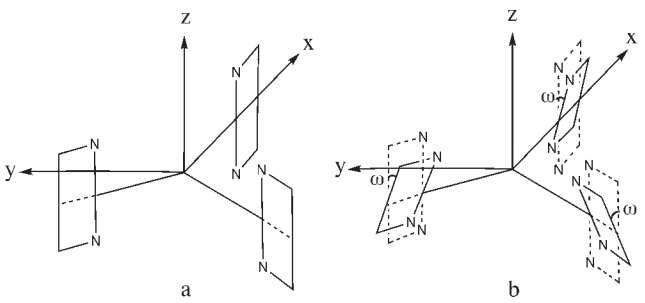

Fig. 1. (**a**) Structure of $[M(en)_3]^{3+}$ D_{3h} symmetry, (**b**) Structure of Λ-$[M(en)_3]^{3+}$ of D_3 symmetry after a rotation of diamine rings by ω degrees.

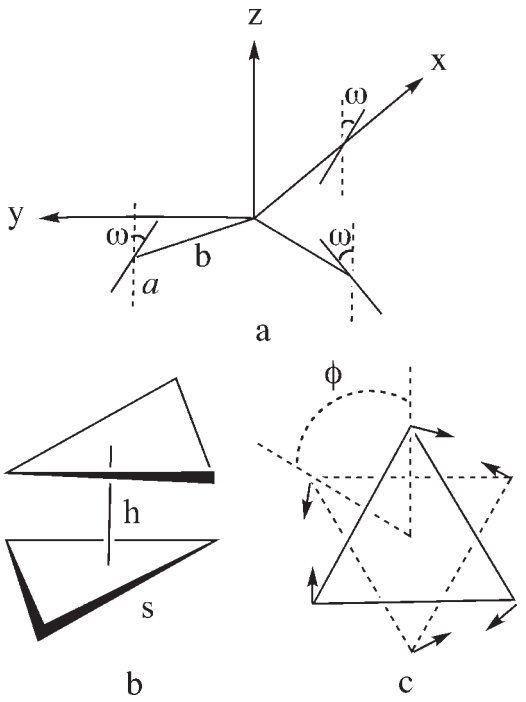

Fig. 2. (**a**) Geometry parameters in $[M(en)_3]^{3+}$, (**b**) polar ration s/h in octahedrons, (**c**) azimuthal angle ϕ in octahedrons.

consider in details the important orbitals that participate in the formation of the $[M(en)_3]^{3+}$ complex, i.e. the nd orbitals on the metal center and the nitrogen based σ-type lone pairs on the diamine ligands.

The nitrogen based lone-pair σ-orbitals on a diamine ring are shown in Figure 3, where they are labeled "a_1" and "b_2" according to C_{2v} symmetry. Linear combinations of the equivalent orbitals on different diamine rings making up the symmetry ligand orbitals in $[M(en)_3]^{3+}$ according to D_{3h} (or D_3) symmetry are listed in Table 1, where the diamine orbitals of a_1 symmetry are expressed as α_i^σ and those of b_2 symmetry as β_i^σ with the subscript indicating the ring they belong to. The same symmetry combinations are displayed in Figure 4 where we also introduce the numbering of the rings and the nitrogen atoms.

Among the nd orbitals of the metal ions are $d\pi_1$, $d\pi_2$, and $d\pi_3$ of t_{2g} symmetry in the O_h parentage. These orbitals transform as a_1 and e in D_3 symmetry, respectively,

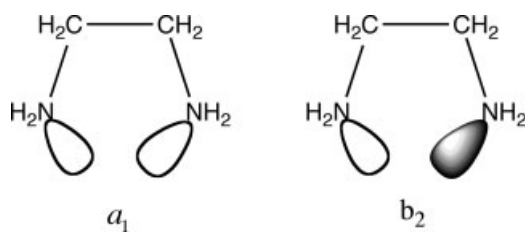

Fig. 3. Nitrogen based σ-orbitals on an ethylenediamine ring.

TABLE 1. Symmetry ligand orbitals in $[M(en)_3]^{3+}$ in terms of diamine orbitals[a,b]

a_1^σ	$1/\sqrt{3}(\alpha_1^\sigma+\alpha_2^\sigma+\alpha_3^\sigma)$
a_2^σ	$1/\sqrt{3}(\beta_1^\sigma+\beta_2^\sigma+\beta_3^\sigma)$
$1e_x^\sigma$	$1/\sqrt{6}(-2\alpha_1^\sigma+\alpha_2^\sigma+\alpha_3^\sigma)$
$1e_y^\sigma$	$1/\sqrt{2}(-\alpha_2^\sigma+\alpha_3^\sigma)$
$2e_x^\sigma$	$1/\sqrt{2}(-\beta_2^\sigma+\beta_3^\sigma)$
$2e_y^\sigma$	$1/\sqrt{6}(2\beta_1^\sigma-\beta_2^\sigma-\beta_3^\sigma)$

[a] α_i^σ is an diamine σ-orbital on ring i (1,3) of a_1 symmetry; β_i^σ is an diamine σ-orbital on ring i (1,3) of b_2 symmetry, see Figure 3.
[b] Numbering of ligands and atoms is shown in Figure 4.

see Figure 5. We have in addition $d\sigma_1$ and $d\sigma_2$ of e_g symmetry in the O_h parentage transforming as e in D_3 symmetry, see Figure 5.

Important information about the bonding in $[M(en)_3]^{3+}$ can be obtained from the overlaps between the metal nd orbitals and the symmetry ligand orbitals. The symmetry unique overlaps between the d-orbitals and the symmetry ligand σ-orbitals are expressed in terms of the geometry parameters of the complexes in Table 2. For the case of $a = b$ and $\omega = 35.3°$, we have the perfect octahedral geometry. The overlaps in the octahedral case are listed in Table 3. It is not surprising that in a perfect octahedral arrangement of the six nitrogens, the ligand σ combinations will only overlap with the dσ orbitals. In the case where the six nitrogens are displaced from the ideal octahedron, the ligand σ combinations overlap with both dσ and dπ orbitals. As an example, the overlaps between the metal d-orbitals and the symmetry ligand σ-orbitals are carried out for $[Co(en)_3]^{3+}$ of D_3 symmetry with a = 1.321 Å, b = 1.445 Å, and $\omega = 33.7°$. We see that with the distorted octahedral geometry, the orbitals $d\pi_1$, $d\pi_2$, and $d\pi_3$ that originally had no overlaps with the σ-orbitals now slightly overlap with these orbitals, see Table 3.

On the basis of the overlap information discussed earlier, a simplified MO interaction diagram can be con-

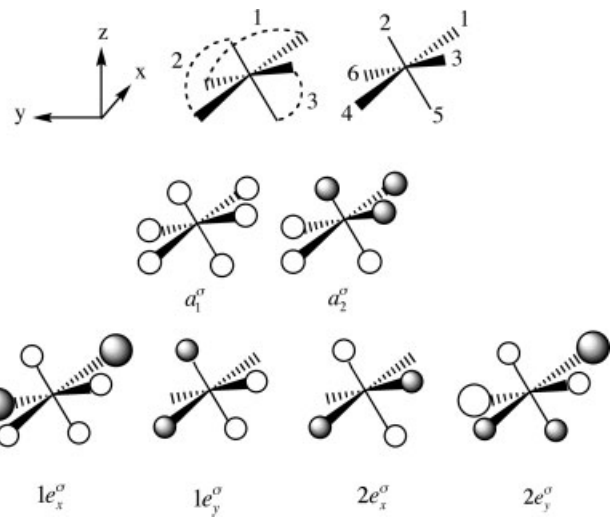

Fig. 4. Symmetry ligand σ-orbitals of $[M(en)_3]^{3+}$ with numbering of the three ligands and six nitrogen atoms.

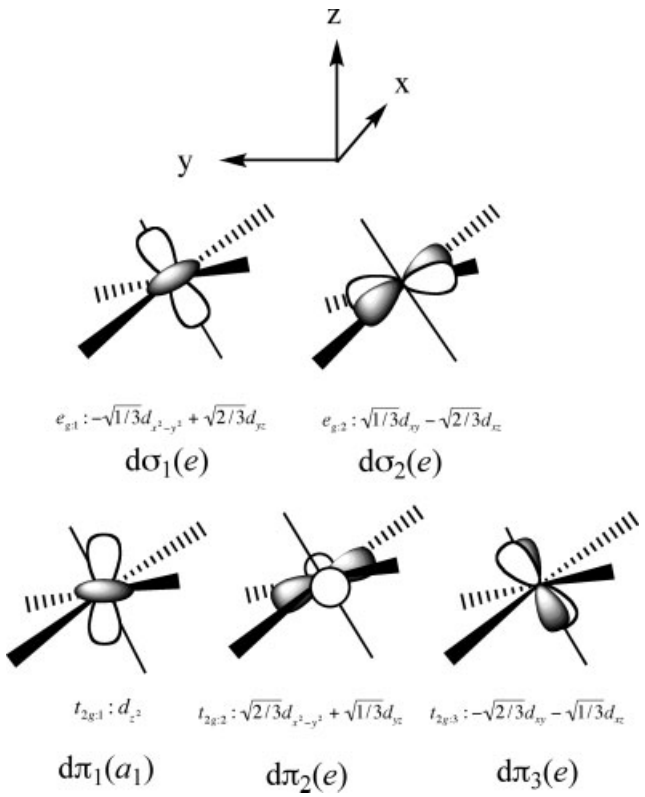

Fig. 5. Metal nd orbitals in O_h and D_3 (in parenthesis) representations.

structed to illustrate the bonding in the $[M(en)_3]^{3+}$ complexes. Figure 6 illustrates the interaction between the metal dσ orbitals of Figure 5 and the symmetry ligand σ-orbitals of Table 1. It follows from Table 3 that the dσ orbitals transforming as e in D_3 symmetry overlap both with the $1e^\sigma$ combination (Table 1) made up of the a_1 nitrogen lone-pair ring orbitals (see Fig. 4) and with the $2e^\sigma$ combination constructed from similar nitrogen lone-pair orbitals of b_2 (C_{2v}) symmetry, see Figure 4. We can by denoting the two group overlaps $S(d\sigma_1,1e_x^\sigma)$ and $S(d\sigma_1,2e_x^\sigma)$ of Table 2 as $S_1(\sigma)$ and $S_2(\sigma)$, respectively, construct two symmetry σ-ligand combinations

$$1\hat{e}_x^\sigma = \frac{1}{\sqrt{S_1^2(\sigma) + S_2^2(\sigma)}}[S_1(\sigma)2e_x^\sigma - S_2(\sigma)1e_x^\sigma] \qquad (4)$$

and

$$2\hat{e}_x^\sigma = \frac{1}{\sqrt{S_1^2(\sigma) + S_2^2(\sigma)}}[S_1(\sigma)1e_x^\sigma - S_2(\sigma)2e_x^\sigma]. \qquad (5)$$

Similar expressions can be obtained for $1\hat{e}_y^\sigma$ and $2\hat{e}_y^\sigma$ from combing overlaps $\boldsymbol{S}(d\sigma_2,1e_y)$ and $\boldsymbol{S}(d\sigma_2,2e_y)$. As a result, the $1\hat{e}^\sigma$ combination has zero overlap with dσ whereas $2\hat{e}^\sigma$ has a full overlap of $1S_\sigma$ with dσ. Figure 6 depicts the level diagram from the metal–ligand σ-interactions. The orbital of lowest energy is $1e$ made up mostly of $2\hat{e}^\sigma$ stabilized by bonding interactions with dσ. This over-

TABLE 2. Unique overlaps between the metal nd orbitals[a] and the symmetry ligand orbitals[b] in Λ-$[M(en)_3]^{3+}$

Overlaps	Expressions[c,d]
$S(d\sigma_1,1e_x^\sigma)$; $S(d\sigma_2,1e_y^\sigma)$	$\frac{b}{2a}\left[\frac{1}{\sqrt{2}}\left(\frac{b^2-a^2\sin^2\omega}{b^2}\right) + \left(\frac{a^2\sin 2\omega}{b^2}\right)\right]S_{xz}^0$
$S(d\sigma_1,2e_x^\sigma)$; $S(d\sigma_2,2e_y^\sigma)$	$(\frac{1}{\sqrt{2}}\sin\omega + \cos\omega)S_{xz}^0$
$S(d\pi_1,a_1^\sigma)$	$-\frac{3\sqrt{3}}{2}\left(\frac{a^2\cos^2\omega}{a^2+b^2} - \frac{1}{3}\right)S_\sigma$
$S(d\pi_2,1e_x^\sigma)$; $S(d\pi_3,1e_y^\sigma)$	$-\frac{b}{2a}\left[\left(\frac{b^2-a^2\sin^2\omega}{b^2}\right) - \frac{1}{\sqrt{2}}\left(\frac{a^2\sin 2\omega}{b^2}\right)\right]S_{xz}^0$
$S(d\pi_2,2e_x^\sigma)$; $S(d\pi_3,2e_y^\sigma)$	$-(\sin\omega - \frac{1}{\sqrt{2}}\cos\omega)S_{xz}^0$

[a]See Figure 5.
[b]See Table 1.
[c]$S_{xz}^0 = \frac{\sqrt{3}ab}{a^2+b^2}S_\sigma$.
[d]S_σ is the overlap between a d_{z^2} orbital on the metal and a σ-ligand orbital pointing along the z-axis towards the metal.

TABLE 3. Calculated unique overlaps between the metal nd orbitals and the symmetry ligand σ-orbitals[a] in Λ-$[Co(en)_3]^{3+}$

Overlaps	Case I[b]	Case II[c]
$S(d\sigma_1,1e_x^\sigma)$; $S(d\sigma_2,1e_y^\sigma)$	0.612 S_σ	0.611 S_σ
$S(d\sigma_1,2e_x^\sigma)$; $S(d\sigma_2,2e_y^\sigma)$	1.061 S_σ	1.056 S_σ
$S(d\pi_1,a_1^\sigma)$	0	0.047 S_σ
$S(d\pi_2,1e_x^\sigma)$; $S(d\pi_3,1e_y^\sigma)$	0	−0.094 S_σ
$S(d\pi_2,2e_x^\sigma)$; $S(d\pi_3,2e_y^\sigma)$	0	0.030 S_σ

[a]See Table 2 for the definition of overlaps.
[b]Octahedron case with $a = b$, $\omega = 35.3^\circ$.
[c]Real geometry of Λ-$[Co(en)_3]^{3+}$, a = 1.321 Å, b = 1.445 Å, and ω = 33.7°.

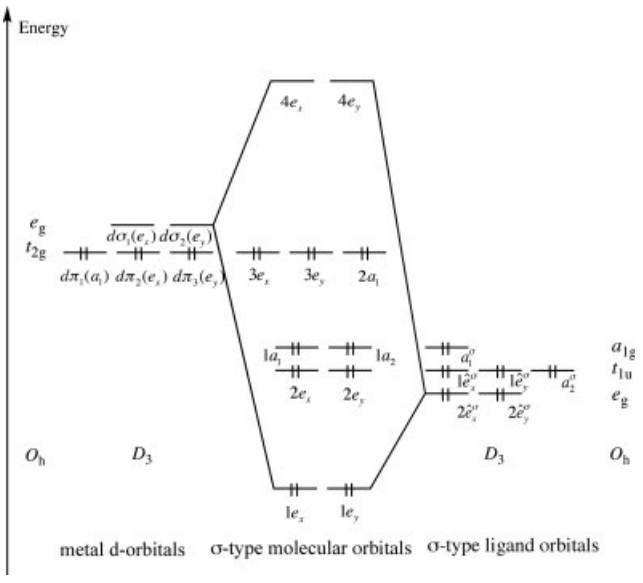

Fig. 6. Schematic orbital interaction diagram for complexes $[M(en)_3]^{3+}$. The metal d-orbitals are given in Figure 5. The symmetry ligand orbitals are shown in Figure 4 and Table 1.

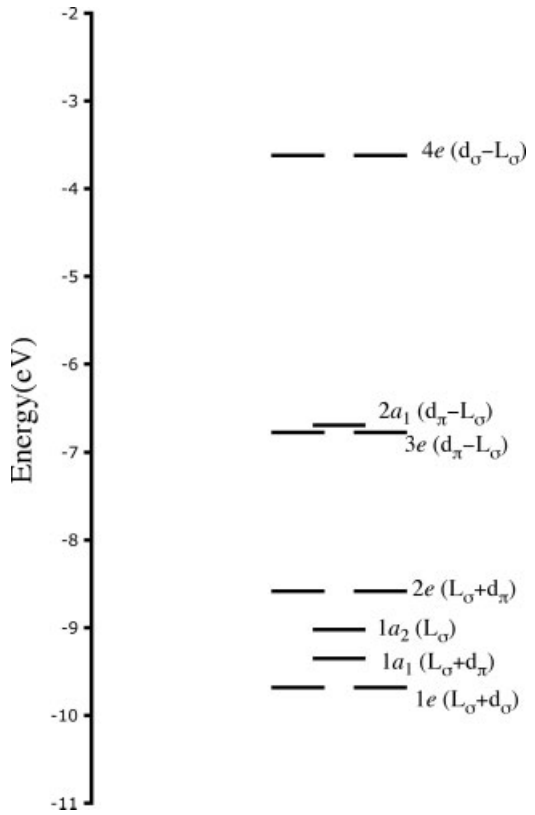

Fig. 7. Molecular orbital diagram of $[Co(en)_3]^{3+}$ from DFT calculations.

lap corresponds to the e_g component of the bonding σ-type orbitals in O_h symmetry. Next in Figure 6 are the nonbonding ligand σ combinations $2e$ made up of $1\hat{e}^{\sigma}$, and $1a_1$, $1a_2$ made up of $1\alpha_1^{\sigma}$ and $1\alpha_2^{\sigma}$, respectively. These orbital levels correspond to the $t_{1u}(2e, 1a_2)$ and $a_{1g}(a_1)$ σ-ligand levels in O_h symmetry. We have finally, the nonbonding dπ orbitals labeled $2a_1(d\pi_1)$ and $3e(d\pi_2, d\pi_3)$ respectively, as well as the dσ orbitals destabilized by $2\hat{e}^{\sigma}$ ligand combinations and labeled $4e$. We note that $2a_1(d\pi_1)$ and $3e(d\pi_2,d\pi_3)$ are the t_{2g} d-set in octahedral complexes whereas $4e(d\sigma_1, d\sigma_2)$ is the corresponding e_g-set. It is also noted that overlaps between the dπ orbitals and the ligand σ-combinations become different from zero when the conformation of the six nitrogen atoms differ from O_h symmetry as in Case II of Table 3. The new overlaps will not change the position of the energy levels significantly. They will however change the composition of the molecular orbitals enough to introduce CD, as we shall see shortly.

Analysis of CD Spectra for Λ-[Co(en)$_3$]$^{3+}$

The qualitative bonding analysis we have introduced so far and the qualitative spectral analysis we are about to introduce should apply to most trigonal dihedral complexes $[M(L\text{-}L)_3]^{n+}$ of bidentate ligands containing only σ-orbitals. However, we shall introduce our analysis scheme in combination with quantitative TD-DFT calculations on $[Co(en)_3]^{3+}$. This species was chosen as it has a rich experimental CD spectrum and an extensive theoretical literature discussion on the spectrum. The actual calculated orbital diagram is displayed in Figure 7 where the orbital splitting and composition (in parentheses) are indicated for comparison to the qualitative interaction diagram in Figure 6. Figure 8 displays the simulated CD spectrum of Λ-$[Co(en)_3]^{3+}$. The corresponding experimental spectrum is displayed in Figure 9. Important one-electron excitations contributing to the bands as numbered in the simulated spectrum are listed in Table 4.

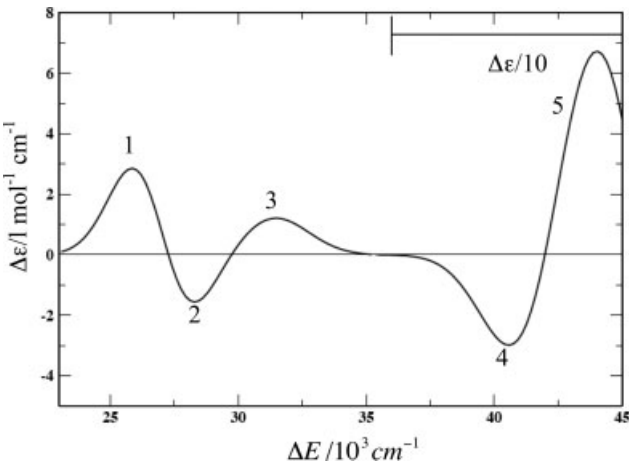

Fig. 8. Simulated CD spectrum of Λ-$[Co(en)_3]^{3+}$.

Recorded and simulated CD spectrum for Λ-[Co(en)$_3$]$^{3+}$ in the d-d transition region. In the low energy absorption region, the two CD bands (25,000–30,000 cm^{-1}) with rotatory strength of opposite signs (1 and 2) are due to d-d transitions from the metal based HOMOs of t_{2g} parentage in O_h symmetry to the metal-based LUMOs of e_g parentage in O_h symmetry, i.e., $A_{1g}^1 \rightarrow T_{1g}^1$ of Scheme 2. The two bands correspond to the E and A_2 components of O_h parentage in the D_3 point group, see Scheme 2, with contributions from $2a_1 \rightarrow 4e$

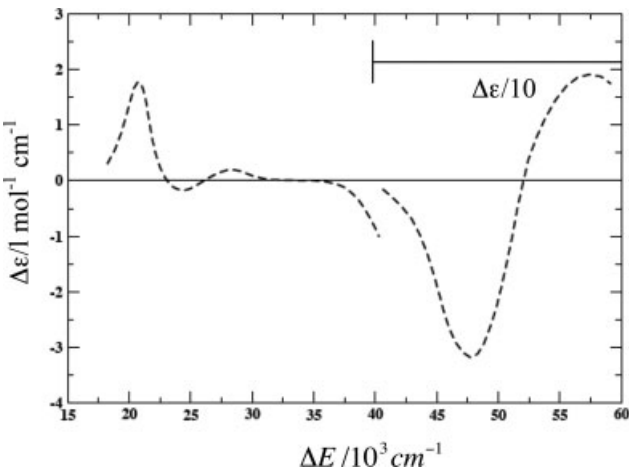

Fig. 9. Experimental CD spectrum of Λ-$[Co(en)_3]^{3+}$.

TABLE 4. Calculated and experimental excitation energies and rotatory strengths for Λ-[Co(en)3]$^{3+}$

	R^a (10^{-40} cgs)		ΔE^b (10^3 cm^{-1})				One-electron transition[e]	
Band	Calc.	Obs.	Calc.	Obs.	Symmetry[c]	Excitation[d]	MO → MO	%
1	+33.08	+4.8[f]	26.7	20.3[f]	E (T_{1g})	$1A_1^1 \rightarrow 1E^1$	$2a_1 \rightarrow 4e$	57
		+59.9[g]		20.76[g]			$3e \rightarrow 4e$	43
2	−30.00	−0.4[f]	27.1	23.7[f]	A_2 (T_{1g})	$\rightarrow 1A_2^1$	$3e \rightarrow 4e$	100
		−55.7[g]		20.99[g]				
3	+2.98	+0.7[f]	31.4	28.5[f]	E (T_{2g})	$\rightarrow 2E^1$	$3e \rightarrow 4e$	57
							$2a_1 \rightarrow 4e$	43
4	−91.99	−67[f]	41.3	47.2[f]	E (T_{1u})	$\rightarrow 3E^1$	$2e \rightarrow 4e$	77
							$1a_2 \rightarrow 4e$	22
5	+162.87	–	43.9	–	A_2 (T_{1u})	$\rightarrow 2A_2^1$	$2e \rightarrow 4e$	81

[a]Rotatory strength.
[b]Excitation energy.
[c]Symmetry of excited states with O_h parentage.
[d]State-to-state transition involved.
[e]Major contributions from one electron transitions to each state-to-state excitation.
[f]Values for an aqueous solution of the complex ion, Ref. 1.
[g]Values for single-crystal, Ref. 40.

and $3e \rightarrow 4e$ one electron excitation, Table 4. From our calculations the positive band at lower energy is of E-symmetry, in agreement with experiments.[13] The A_2-band is only barely noticeable in the experimental spectrum, due to an extensive cancellation of the rotatory strengths of the two components, E and A_2, since the trigonal splitting, i.e., splitting of T_1^1 (O_h) into E^1 and A_2^1 (D_3), is small. The rotatory strengths are calculated to be +33.08 and −30.00 × 10^{-40} cgs at 26,700 and 27,100 cm^{-1} for the E- and A_2-band respectively, when compared with +4.8 and −0.4 × 10^{-40} cgs at 20,300 and 23,700 cm^{-1} from the measurements in solution.[1] On the other hand, the calculated rotatory strengths are in good agreement with the value from the crystal CD spectrum,[40] which is an order of magnitude larger than that recorded in solution. In addition, both experiment and theory reveal a positive weak band (3) at ~31,000 cm^{-1}. The calculated rotatory strength, +2.98 at 31,400 cm^{-1}, is again compared to the observation, +0.7 at 28,500 cm^{-1}. The band has a low intensity since it corresponds to the d-d transition $A_1^1 \rightarrow 2E^1$ where E^1 is of T_{2g}^1 O_h parentage with the $A_{1g}^1 \rightarrow T_{2g}^1$ transition being both electrically and magnetically forbidden, see Scheme 2. As indicated in Table 4, the computed excitation energies of the d-d transitions are systematically overestimated by ~4000 cm^{-1}.

The wave functions of the states involved in the d-d transitions are expressed in determinantal form in Table 5. The one electron excitations involved are $2a_1 \rightarrow 4e$ and $3e \rightarrow 4e$ for the $A_1^1 \rightarrow 1E^1$ and $A_1^1 \rightarrow 2E^1$ excitations and $3e \rightarrow 4e$ for the $A_1^1 \rightarrow A_2^1$ transition. We can view the $1E^1$ and $2E^1$ excited states as due to interactions between the $2a_1 \rightarrow 4e$ and $3e \rightarrow 4e$ one-electron transitions. In O_h symmetry, the mix would be equal with $c_1 = \pm c_2$, see Table 5. Further, the combination of higher energy gives rises to T_{2g}^1, see Scheme 2. In D_3 symmetry the $1E^1(T_{1g}^1)$ state of lower energy has a larger contribution from $2a_1 \rightarrow 4e$ than from $3e \rightarrow 4e$ whereas the opposite is the case for $2E^1(T_{2g}^1)$. This is consistent with the fact that the $2a_1 \sim 4e$ energy gap is smaller than the $3e \sim 4e$ gap, Figure 7.

Recorded and simulated CD spectrum for Λ-[Co(en)$_3$]$^{3+}$ in the LMCT region. CD bands in the higher energy region are ascribed to LMCT caused by excitations from the ligand-based orbitals of t_{1u} parentage in O_h symmetry to the metal-based LUMOs of e_g parentage in O_h symmetry, i.e., $A_{1g}^1 \rightarrow T_{1u}^1$, Scheme 2. In D_3 symmetry the ligand orbitals are $1a_2$ and $2e$, and the metal orbital $4e$, Figure 7. The corresponding transitions are termed $A_1^1 \rightarrow 3E^1$ and $A_1^1 \rightarrow 2A_2^1$, Scheme 2. The $3E^1$-component

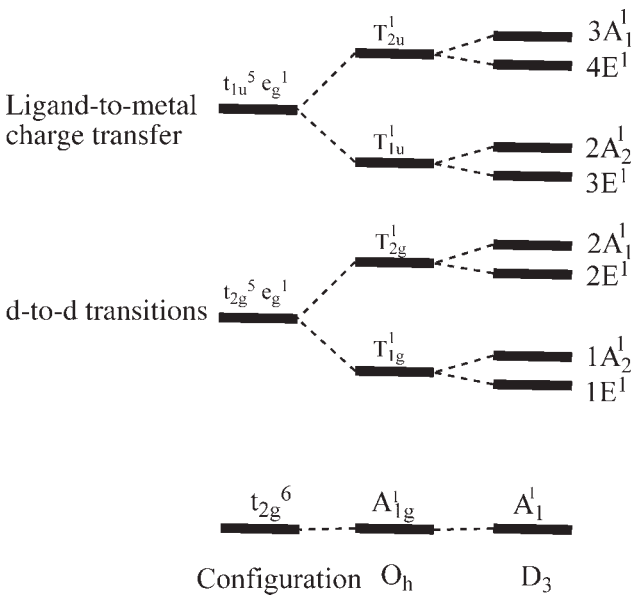

Scheme 2. Lowest singlet excited states for an octahedral complex with a d^6 ground state configuration and their splitting in D_3 point group symmetry.

TABLE 5. Many-electron determinantal wave functions for the states involved in the d-d and ligand-to-metal charge transfer transitions for the $[Co(en)_3]^{3+}$ complexes

State		Wave function[a,b]
A_1^1 (GS)		$\lvert 2a_1 2\bar{a}_1 3e_x 3\bar{e}_x 3e_y 3\bar{e}_y \rvert$
T_{1g}	$1A_2^1$	$\frac{1}{2}\{\lvert 3e_y 4\bar{e}_x\rvert - \lvert 3\bar{e}_y 4e_x\rvert - \lvert 3e_x 4\bar{e}_y\rvert + \lvert 3\bar{e}_x 4e_y\rvert\}$
	$1E_x^1$	$\frac{1}{2}c_1\{\lvert 3e_x 4\bar{e}_x\rvert - \lvert 3\bar{e}_x 4e_x\rvert - \lvert 3e_y 4\bar{e}_y\rvert + \lvert 3\bar{e}_y 4e_y\rvert\} + \frac{1}{\sqrt{2}}c_2\{\lvert 2a_1 4\bar{e}_x\rvert - \lvert 2\bar{a}_1 4e_x\rvert\}$
	$1E_y^1$	$\frac{1}{2}c_1\{\lvert 3e_y 4\bar{e}_x\rvert - \lvert 3\bar{e}_y 4e_x\rvert + \lvert 3e_x 4\bar{e}_y\rvert - \lvert 3\bar{e}_x 4e_y\rvert\} + \frac{1}{\sqrt{2}}c_2\{\lvert 2a_1 4\bar{e}_y\rvert - \lvert 2\bar{a}_1 4e_y\rvert\}$
T_{2g}	$2E_x^1$	$\frac{1}{2}c_2\{\lvert 3e_x 4\bar{e}_x\rvert - \lvert 3\bar{e}_x 4e_x\rvert - \lvert 3e_y 4\bar{e}_y\rvert + \lvert 3\bar{e}_y 4e_y\rvert\} - \frac{1}{\sqrt{2}}c_1\{\lvert 2a_1 4\bar{e}_x\rvert - \lvert 2\bar{a}_1 4e_x\rvert\}$
	$2E_y^1$	$\frac{1}{2}c_2\{\lvert 3e_y 4\bar{e}_x\rvert - \lvert 3\bar{e}_y 4e_x\rvert + \lvert 3e_x 4\bar{e}_y\rvert - \lvert 3\bar{e}_x 4e_y\rvert\} - \frac{1}{\sqrt{2}}c_1\{\lvert 2a_1 4\bar{e}_y\rvert - \lvert 2\bar{a}_1 4e_y\rvert\}$
T_{1u}	$2A_2^1$	$\frac{1}{2}\{\lvert 2e_y 4\bar{e}_x\rvert - \lvert 2\bar{e}_y 4e_x\rvert - \lvert 2e_x 4\bar{e}_y\rvert + \lvert 2\bar{e}_x 4e_y\rvert\}$
	$3E_x^1$	$\frac{1}{2}c_3\{\lvert 2e_x 4\bar{e}_x\rvert - \lvert 2\bar{e}_x 4e_x\rvert - \lvert 2e_y 4\bar{e}_y\rvert + \lvert 2\bar{e}_y 4e_y\rvert\} + \frac{1}{\sqrt{2}}c_4\{\lvert 1a_2 4\bar{e}_x\rvert - \lvert 1\bar{a}_2 4e_x\rvert\}$
	$3E_y^1$	$\frac{1}{2}c_3\{\lvert 2e_y 4\bar{e}_x\rvert - \lvert 2\bar{e}_y 4e_x\rvert + \lvert 2e_x 4\bar{e}_y\rvert - \lvert 2\bar{e}_x 4e_y\rvert\} + \frac{1}{\sqrt{2}}c_4\{\lvert 1a_2 4\bar{e}_y\rvert - \lvert 1\bar{a}_2 4e_y\rvert\}$

[a]Refer to Figure 7 for one-electron molecular orbitals.
[b]Please note that a one-electron transition $\psi_i\alpha \rightarrow \psi_j\alpha$ is represented by the Slater determinant $\lvert\bar{\psi}_i\psi_j\rvert$ where all the other occupied ground state orbitals are omitted. In the same way $\psi_i\beta \rightarrow \psi_j\beta$ is represented by $\lvert\psi_i\bar{\psi}_j\rvert$.

(band 4) corresponding to the $A_1^1 \rightarrow 3E^1$ transition is of lower energy with a negative sign for $R(3E^1)$ and the $2A_2^1$-component (band 5) corresponding to the $A_1^1 \rightarrow 2A_2^1$ transition is of higher energy with a positive sign for $R(2A_2^1)$. The band intensity in this region is much higher than that of the d-d transitions as the excitations are electrically allowed, see later. Besides the fact that the calculated rotatory strength agrees well with the experiment for the E component, the excitation energies in this region are underestimated by $\sim$6000 cm^{-1}, Table 4.

Molecular orbitals of Λ-$[Co(en)_3]^{3+}$ in terms of metal and ligand symmetry orbitals. It follows from Figure 6 that $[M(en)_3]^{3+}$ is formed from the interaction of the five d-orbitals with the ligand combinations $1\hat{e}^\sigma$, $2\hat{e}^\sigma$ of eqs. 4 and 5 and α_1^σ and α_2^σ of Table 1. We display in Table 6 the ligand–metal overlaps for the octahedral Case I as well as the actual geometry, Case II. In Case I, we have only one ligand–metal overlap involving dσ and $2\hat{e}^\sigma$ and it is positive. In Case II we see the emergence of another two positive overlaps involving $S(d\pi_1,a_1^\sigma)$ and $S(d\pi_2,1\hat{e}_x^\sigma)$, $S(d\pi_3,1\hat{e}_y^\sigma)$. We shall shortly demonstrate that the latter two symmetry equivalent overlaps are essential for the appearance of CD in $[M(en)_3]^{3+}$. We note that $1\hat{e}^\sigma$ in Case I can be written as $1\hat{e}^\sigma = (-\sqrt{3}/2)1e^\sigma + (1/2)2e^\sigma$ whereas $2\hat{e}^\sigma = (1/2)1e^\sigma + (\sqrt{3}/2)2e^\sigma$. The two orbitals are displayed in Figure 10. It follows from Figure 10 that $1\hat{e}^\sigma$ has the appearance of a t_{1u} ligand σ-orbital in O_h symmetry whereas $2\hat{e}^\sigma$ corresponds to the t_{2g} σ-orbital. The compositions of $1\hat{e}^\sigma$ and $2\hat{e}^\sigma$ are only slightly changed in going to Case II. Table 7 displays the composition of the molecular orbitals in terms of d and ligand combinations. We find in line with the qualitative discussion that ψ_{1e} is a bonding orbital between dσ and $2\hat{e}^\sigma$, where dσ and $2\hat{e}^\sigma$ add in-phase to ψ_{1e} as $S(d\sigma,2\hat{e}^\sigma)$ is positive. The ψ_{2e} orbital is predominantly $1\hat{e}^\sigma$ with an in-phase contribution from dπ as $S(d\pi,2\hat{e}^\sigma)$ is positive. ψ_{3e} is the corresponding anti-bonding orbital where $1\hat{e}^\sigma$ adds out-of-phase to the predominant dπ component. Also ψ_{4e} is the anti-bonding out-of-phase combination between dσ and $2\hat{e}^\sigma$. We finally have that ψ_{1a_1} is ligand-based (a_1^σ) whereas ψ_{2a_1} is represented by dπ and ψ_{1a_2} by a_2^σ.

It is clear from the discussion earlier that we can write in general the molecular orbitals in $[M(en)_3]^{3+}$ as linear combinations of symmetry ligand and/or metal orbitals. Thus,

TABLE 6. Calculated unique overlaps between the metal nd orbitals and the transformed symmetry ligand σ-orbitals[a] in Λ-$[Co(en)_3]^{3+}$

Overlaps[b]	Case I[c]	Case II[d]	Case III[e]
$S(d\sigma_1,2\hat{e}_x^\sigma)$; $S(d\sigma_2,2\hat{e}_y^\sigma)$	1.225 S_σ	1.220 S_σ	1.193 S_σ
$S(d\sigma_1,1\hat{e}_x^\sigma)$; $S(d\sigma_2,1\hat{e}_y^\sigma)$	0	−0.001 S_σ	0.013 S_σ
$S(d\pi_1,a_1^\sigma)$	0	0.047 S_σ	0.287 S_σ
$S(d\pi_2,1\hat{e}_x^\sigma)$; $S(d\pi_3,1\hat{e}_y^\sigma)$	0	0.096 S_σ	−0.102 S_σ
$S(d\pi_2,2\hat{e}_x^\sigma)$; $S(d\pi_3,2\hat{e}_y^\sigma)$	0	−0.021 S_σ	−0.160 S_σ

[a]See text for the relation between e^σ and $\hat{e}^\sigma$.
[b]See Figure 6 for the orbital symmetry.
[c]Octahedron case with $a = b$, $\omega = 35.3°$.
[d]Real geometry of Λ-$[Co(en)_3]^{3+}$, a = 1.321 Å, b = 1.445 Å, and ω = 33.7°. (ϕ = 53.7°, s/h = 1.28).
[e]Model geometry of Λ-$[Co(en)_3]^{3+}$, a = 1.321 Å, b = 1.445 Å, and ω = 45.6° (ϕ = 66.3°, s/h = 1.61).

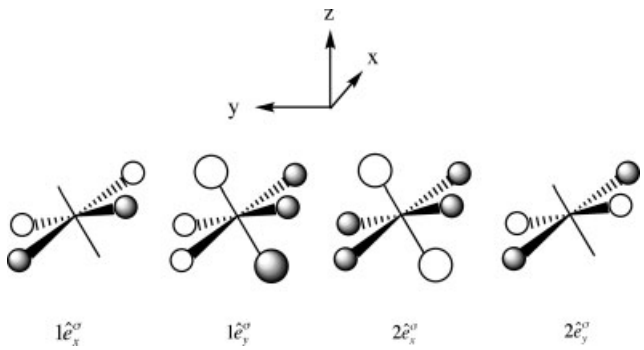

Fig. 10. Representation of $1\hat{e}^\sigma$ and $2\hat{e}^\sigma$.

TABLE 7. Combination coefficients for molecular orbitals of Λ-[Co(en)$_3$]$^{3+}$ in terms of the symmetry ligand and/or metal orbitals

ψ_{1a_1} [a]	$c(1a_1,1) = 0.5610$, $c(1a_1,2) = 0.0019$
ψ_{2a_1}	$c(2a_1,1) = 0.0119$, $c(2a_1,2) = 0.9833$
ψ_{1a_2} [b]	$C(1a_2) = 0.8633$
ψ_{1e} [c]	$C(1e,1) = 0.0718$, $C(1e,2) = 0.5828$, $C(1e,3) = 0.4497$, $C(1e,4) = 0.0085$
ψ_{2e}	$C(2e,1) = 0.8866$, $C(2e,2) = -0.1145$, $C(2e,3) = -0.0564$, $C(2e,4) = 0.1176$
ψ_{3e}	$C(3e,1) = -0.0979$, $C(3e,2) = 0.0077$, $C(3e,3) = 0.0042$, $C(3e,4) = 0.9725$
ψ_{4e}	$C(4e,1) = 0.0048$, $C(4e,2) = -0.7788$, $C(4e,3) = 0.8582$, $C(4e,4) = 0.0033$

[a]For ψ_{na_1}: 1 = a_1^σ; 2 = $d\pi_1$, see Table 1.
[b]For ψ_{na_2}: 1=a_2^σ, see Table 1.
[c]For ψ_{ne}: 1=1$\hat{e}^\sigma$; 2 = 2$\hat{e}^\sigma$; 3 = $d\sigma$; 4 = $d\pi$, see Table 1.

$$\psi_{na_1} = \sum_i^2 c(na_1, i)\chi_i, \tag{6}$$

where $\chi_1 = a_1^\sigma$ and $\chi_2 = d\pi_1$, and

$$\psi_{ne_{xy}} = \sum_i^4 c(ne_{xy}, i)\chi_i, \tag{7}$$

with $\chi_1 = 1\hat{e}^\sigma$, $\chi_2 = 2\hat{e}^\sigma$, $\chi_3 = d\sigma$ and $\chi_4 = d\pi$, whereas

$$\psi_{na_2} = c(na_2)a_2^\sigma. \tag{8}$$

We indicate in eq. 8 that a_2 is a pure ligand orbital as symmetry prevents any overlaps with the d-orbitals.

Analysis of the Origin of the Rotatory Strengths in Λ-[Co(en)$_3$]$^{3+}$

The rotatory strength of a transition from the ground state (o) to the excited state (i) is in general given as the scalar product of the electric transition dipole moment and the magnetic transition dipole moments as

$$R_{oi} = \mathrm{Im}[\langle o|\hat{\boldsymbol{\mu}}|i\rangle \cdot \langle i|\hat{\boldsymbol{m}}|o\rangle] \tag{9}$$

where $\hat{\boldsymbol{\mu}}$ and $\hat{\boldsymbol{m}}$ are the electronic and magnetic dipole moment operators.

Analysis of the rotatory strengths in the d-d transition region. For the d-d transition $A_1^1 \rightarrow 1A_2^1$, the rotatory strength is given as

$$R(1A_2^1) = \mathrm{Im}[\langle A_1^1|\hat{\boldsymbol{\mu}}|1A_2^1\rangle \cdot \langle 1A_2^1|\hat{\boldsymbol{m}}|A_1^1\rangle]. \tag{10}$$

Since the transition in this case is caused by one-electron excitations from the molecular orbital 3e to 4e, by substituting the wave functions of Table 5 into eq. 10, we are able to express $R(1A_2^1)$ in terms of molecular orbitals as

$$\begin{aligned} R(1A_2^1) &= 4[\langle 3e_x|\hat{\boldsymbol{\mu}}|4e_y\rangle \cdot \langle 4e_y|\hat{\boldsymbol{m}}|3e_x\rangle] \\ &= 4\sum_{i=1}^4\sum_{j=1}^4 c(3e_x, i)c(4e_y, j)\langle\chi_i|\hat{\boldsymbol{\mu}}|\chi_j\rangle \\ &\quad \times \sum_{k=1}^4\sum_{l=1}^4 c(4e_y, k)c(4e_x, l)\langle\chi_k|\hat{\boldsymbol{m}}|\chi_l\rangle \end{aligned} \tag{11}$$

where we on the right hand side of eq. 11 have expanded the molecular orbitals in terms of symmetry orbitals according to eqs. 6–8.

For the transition $A_1^1 \rightarrow A_2^1$ to be allowed, it is required that the electric transition moment integral $\langle A_1^1|\hat{\boldsymbol{\mu}}|1A_2^1\rangle \neq 0$. This integral over all space is non-zero only when the integrand is totally symmetric, which in group theory leads to the conclusion that the components of the electric transition dipole moment operator $\hat{\mu}$, transforming as x, y, or z, should belong to the same irreducible representation as the direct product $A_1 \times A_2 = A_2$. We notice that in our case where Λ-[Co(en)$_3$]$^{3+}$ has D_3 symmetry, only the z component transforms as A_2. It therefore follows that the $A_1^1 \rightarrow 1A_2^1$ transition should be polarized in the z direction with respect to the coordinate system in Figure 1. We are thus able to see from inspection of eq. 11 which type of integrals $\langle\chi_i|\hat{\boldsymbol{\mu}}|\chi_j\rangle$ and $\langle\chi_i|\hat{\boldsymbol{m}}|\chi_j\rangle$ will contribute to $R(1A_2^1 \rightarrow$ in eq. 10. Let us first look at the electric component containing the dipole integral $\langle\chi_i|\hat{\boldsymbol{\mu}}|\chi_j\rangle$. When both χ_i and χ_j in $\langle\chi_i|\hat{\boldsymbol{\mu}}|\chi_j\rangle$ are pure metal d-orbitals, the integrand can be considered as having (at least) O_h symmetry. It is further seen that the integral is zero as the direct product of two gerade d-orbitals is gerade while the dipole operator is ungerade. We are now left with contributions $\langle\chi_l|\hat{\boldsymbol{\mu}}|\chi_k\rangle$ where χ_l is a d-orbital whereas χ_k is a ligand combination, or where both χ_l and χ_k are ligand combinations. It turns out from the numerical calculations that the major contribution comes from $\langle 1\hat{e}_x^\sigma|z|2\hat{e}_y^\sigma\rangle$ through the contribution $c(3e_x,1)$ from $1\hat{e}_x^\sigma$ to ψ_{3e_x} and $c(4e_y,2)$ from $2\hat{e}_y^\sigma$ to ψ_{4e_y}, Table 7. That $\langle 1\hat{e}_x^\sigma|z|2\hat{e}_y^\sigma\rangle$ is non-zero is not surprising as $1\hat{e}_x^\sigma$ is ungerade whereas $2\hat{e}_y^\sigma$ is gerade, Figure 10.

It is readily seen that the metal d-orbitals will have a major contribution to the magnetic part of the expression in eq. 11 through the contribution $c(4e_y,3)$ from $d\sigma_2$ to ψ_{4e_y} and $c(3e_x,4)$ from $d\pi_2$ to ψ_{3e_x} in the form of $c(4e_y,3)c(3e_x,4)c(4e_y,3)c(3e_x,4) \cdot \langle d\sigma_2|\hat{\boldsymbol{m}}|d\pi_2\rangle$. By definition, a non-zero rotatory strengh should intrinsically require a component of magnetic transition moments pointing, in the case of the A_2 transitions, along the z-axis, i.e. $\langle d\sigma_2|m_z|d\pi_2\rangle$. With $\hat{\boldsymbol{m}} = \frac{eh}{2mc}\hat{\boldsymbol{l}}$, where $\hat{\boldsymbol{l}}$ is the orbital angular momentum operator, the action of the magnetic operator m_z on an orbital is simply to rotate the orbital around z-axis by 90°. It is readily seen that $\langle d\sigma_2|\hat{m}_z|d\pi_2\rangle = \sqrt{2}/3(\langle d_{xy}|\hat{m}_z|d_{x^2-y^2}\rangle - \langle d_{xz}|\hat{m}_z|d_{yz}\rangle)$. The effect of the orbital angular momentum operators on d atomic orbitals is tabulated in the literature.[41]

On the basis of the arguments made earlier, the expression in eq. 11 becomes

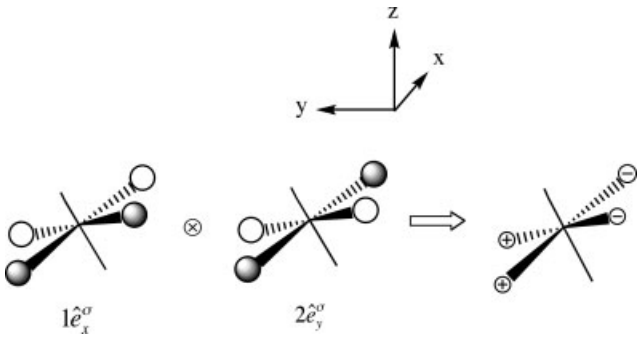

Fig. 11. Product of two symmetry ligand σ-orbitals with respect to the coordinate system.

$$R(1A_2^1) = \frac{4\sqrt{2}}{3}[c(3e_x,1)c(4e_y,2)\langle 1\hat{e}_x^\sigma|z|2e_y^\sigma\rangle] \times [c(4e_y,3)c(3e_x,4)\cdot(\langle d_{xy}|m_z|d_{x^2-y^2}\rangle - \langle d_{xz}|m_z|d_{yz}\rangle)]. \quad (12)$$

We note that in a basis of real orbitals, $\langle i|\hat{\boldsymbol{\mu}}|j\rangle = \langle j|\hat{\boldsymbol{\mu}}|i\rangle$, $\langle i|\hat{\boldsymbol{m}}|j\rangle = -\langle j|\hat{\boldsymbol{m}}|i\rangle$, and $\langle 1\hat{e}_x^\sigma|z|2\hat{e}_y^\sigma\rangle = -\langle 2\hat{e}_x^\sigma|z|1\hat{e}_y^\sigma\rangle$.

It is possible from eq. 12 to determine the sign of $R(1A_2^1)$. For the transition dipole part we have that $c(3e_x,1)\cdot c(4e_y,2)$ is positive, Table 7, as $c(3e_x,1)$ and $c(4e_y,2)$ both are negative according to our bonding analysis. For $\langle 1\hat{e}_x^\sigma|z|2\hat{e}_y^\sigma\rangle$, we plot the integrant $1\hat{e}_x^\sigma \cdot 2\hat{e}_y^\sigma$ in Figure 11. It follows from this plot that $1\hat{e}_x^\sigma \cdot 2\hat{e}_y^\sigma$ is negative for positive *z*- values and positive for negative *z*-values. The integral $\langle 1\hat{e}_x^\sigma|z|2\hat{e}_y^\sigma\rangle$ is as a consequence negative as is the total electric transition dipole moment $c(3e_x,1)c(4e_y,2)\langle 1\hat{e}_x^\sigma|z|2\hat{e}_y^\sigma\rangle$. Turning next to the magnetic transition dipole moment, we have that $c(4e_y,3)$, $c(3e_x,4)$, and $c(4e_y,3)\cdot c(3e_x,4)$ all are positive according to Table 7 and our qualitative bonding analysis. On the other hand, tabulations[41] clearly show that $\langle d_{xz}|m_z|d_{x^2-y^2}\rangle - \langle d_{xy}|m_z|d_{yz}\rangle$ is positive so that the total magnetic transition dipole moment is positive. Finally, with the electric and magnetic transition dipole moments being of different signs, we must have that $R(1A_2^1)$ is negative, in agreement with experiment and our quantitative DFT calculations.

We can within the same framework analyze the *E* component of the d-d transition $A_1^1 \rightarrow 1E^1$. The rotatory strength here can be written as

$$R(1E^1) = \mathrm{Im}[\langle A_1^1|\hat{\boldsymbol{\mu}}|1E^1\rangle \cdot \langle 1E^1|\hat{\boldsymbol{m}}|A_1^1\rangle] \quad (13)$$

Using symmetry arguments introduced earlier for the A_2 component, the $A_1^1 \rightarrow 1E^1$ transition will be polarized in the *xy* plane shown in Figure 1 since $A_1 \times E = E$ and *x*, *y* together transform as *E* in the D_3 point group. By making use of Table 5, we are able to write the following expressions for $R(1E_x)$ in terms of molecular orbitals

$$R(1E_x) = 4c_1^2\langle 3e_x|\hat{\boldsymbol{\mu}}|4e_x\rangle \cdot \langle 4e_x|\hat{\boldsymbol{m}}|3e_x\rangle + 2\sqrt{2}c_1c_2\langle 3e_x|\hat{\boldsymbol{\mu}}|4e_x\rangle \cdot \langle 4e_x|\hat{\boldsymbol{m}}|a_1\rangle + 2\sqrt{2}c_1c_2\langle 2a_1|\hat{\boldsymbol{\mu}}|4e_x\rangle \times \langle 4e_x|\hat{\boldsymbol{m}}|3e_x\rangle + 2c_2^2\langle 2a_1|\hat{\boldsymbol{\mu}}|4e_x\rangle \cdot \langle 4e_x|\hat{\boldsymbol{m}}|2a_1\rangle \quad (14)$$

with a similar expression for $R(1E_y)$ by applying the $1E_y^1$ wave function in Table 5. Here c_1 and c_2 of Table 5 would be $c_1 = c_2 = 1/\sqrt{2}$ in octahedral symmetry. In the actual system, c_1 is slightly smaller than c_2, see Table 4. By making use of arguments similar to those applied for analyzing contributions to $R(A_2^1)$ we find that the important contributions to the electric transition dipole moment of $R(E^1)$ now come from $\langle 1\hat{e}^\sigma|x,y|2\hat{e}^\sigma\rangle$. The $A_1^1 \rightarrow 1E^1$ transition is made up of $2a_1 \rightarrow 4e$ and $3e \rightarrow 4e$ one-electron excitations and the d components in both excitations contribute to the magnetic transition dipole moment in $R(1E^1)$, see eq. 14.

The third band at 31,400 cm^{-1}, see Table 4, is as mentioned already due to the transition $A_1^1 \rightarrow 2E^1$ where $2E^1$ is the higher energy component of the coupling between the one electron transitions $2a_1 \rightarrow 4e$ and $3e \rightarrow 4e$, Table 5. The $A_1^1 \rightarrow 2E^1$ transition is polarized in the *x,y* direction. We get by using Table 5 $R(2E_x^1)$ in terms of molecular orbitals as

$$R(2E_x^1) = 4c_2^2\langle 3e_x|\hat{\boldsymbol{\mu}}|4e_x\rangle \cdot \langle 4e_x|\hat{\boldsymbol{m}}|3e_x\rangle - 2\sqrt{2}c_1c_2\langle 3e_x|\hat{\boldsymbol{\mu}}|4e_x\rangle \times \langle 4e_x|\hat{\boldsymbol{m}}|2a_1\rangle - 2\sqrt{2}c_1c_2\langle 2a_1|\hat{\boldsymbol{\mu}}|4e_x\rangle \cdot \langle 4e_x|\hat{\boldsymbol{m}}|3e_x\rangle + 2c_1^2\langle 2a_1|\hat{\boldsymbol{\mu}}|4e_x\rangle \cdot \langle 4e_x|\hat{\boldsymbol{m}}|2a_1\rangle \quad (15)$$

A similar expression is obtained for $R(2E_y^1)$ by using the $2E_y^1$ wave function. We get again that the transition becomes dipole allowed due to contributions from $\langle 1\hat{e}^\sigma|x,y|2\hat{e}^\sigma\rangle$. For this transition $c_1 = c_2 = 1/\sqrt{2}$ in octahedral symmetry.

As indicated from both the calculations and experiment, the rotatory strengths of the two *E* component, $1E^1$ and $2E^1$, are of a different order of magnitude. The contributions of the transition moments from different molecular orbitals are shown in eqs. 14 and 15, in which the corresponding matrix elements in the four terms are identical, while the coefficients of the second and third terms change sign in going from $R(1E^1)$ to $R(2E^1)$. The values of the transition moments calculated are given in Table 8. It is no surprise that the electric transition moments associated are of one or two order of magnitude smaller than the corresponding magnetic transition moments since d-d transition is formally forbidden. With all the positive-valued transition moments and c_1 and c_2 ($c_1 = 0.929/\sqrt{2}, c_2 = 1.064/\sqrt{2}$ from the computations), it is readily seen from eqs. 14 and 15 that while the relevant one-electron transitions $2a_1 \rightarrow 4e$ and $3e \rightarrow 4e$ add up in the $A_{1g}^1 \rightarrow T_{1g}^1$ transition they tend to cancel out in the $A_{1g}^1 \rightarrow T_{2g}^1$ case.

Analysis of the rotatory strengths in the LMCT region. The CD bands (4 and 5) in the UV region are

TABLE 8. Some of the relevant integrals[a] used to calculate the rotatory strength of the $1E^1$ and $2E^1$ bands

$\langle 3e_x\|\hat{\boldsymbol{\mu}}\|4e_x\rangle$	$\langle 2a_1\|\hat{\boldsymbol{\mu}}\|4e_x\rangle$	$\langle 4e_x\|\hat{\boldsymbol{l}}\|3e_x\rangle$	$\langle 4e_x\|\hat{\boldsymbol{l}}\|2a_1\rangle$
0.06911	0.005643	0.5372	0.7678

[a]Integrals expressed in atomic units.

ascribed to the LMCT with the E component corresponding to $A_1^1 \rightarrow 3E^1$ and the A_2 component to $A_1^1 \rightarrow 2A_2^1$. We can write the rotatory strengths as

$$R(2A_2^1) = \mathrm{Im}[\langle A_1^1|\hat{\boldsymbol{\mu}}|2A_2^1\rangle \cdot \langle 2A_2^1|\hat{\boldsymbol{m}}|A_1^1\rangle] \quad (16a)$$

$$R(3E^1) = \mathrm{Im}[\langle A_1^1|\hat{\boldsymbol{\mu}}|2E^1\rangle \cdot \langle 2E^1|\hat{\boldsymbol{m}}|A_1^1\rangle]. \quad (16b)$$

or in terms of one-electron excitations from the ligand-based orbital $2e$ to the metal-based LUMO $4e$.

$$R(2A_2^1) = 4[\langle 2e_x|\hat{\boldsymbol{\mu}}|4e_y\rangle \cdot \langle 4e_y|\hat{\boldsymbol{m}}|2e_x\rangle] = 4\sum_{i=1}^{4}\sum_{j=1}^{4} c(2e_x,i)c(4e_y,j)\langle\chi_i|\hat{\boldsymbol{\mu}}|\chi_j\rangle \times \sum_{k=1}^{4}\sum_{l=1}^{4} c(4e_y,k)c(2e_x,l)\langle\chi_k|\hat{\boldsymbol{m}}|\chi_l\rangle \quad (17a)$$

$$R(3E^1) = 4[\langle 2e_x|\hat{\boldsymbol{\mu}}|4e_x\rangle \cdot \langle 4e_x|\hat{\boldsymbol{m}}|2e_x\rangle] = 4\sum_{i=1}^{4}\sum_{j=1}^{4} c(2e_x,i)c(4e_y,j)\langle\chi_i|\hat{\boldsymbol{\mu}}|\chi_j\rangle \times \sum_{k=1}^{4}\sum_{l=1}^{4} c(4e_x,k)c(2e_x,l)\langle\chi_k|\hat{\boldsymbol{m}}|\chi_l\rangle \quad (17b)$$

where we have omitted the minor contribution to $3E^1$ from the $1a_1 \rightarrow 4e$ transition represented by c_4 of Table 5 and retained the major contribution from $3e \rightarrow 4e$ given by c_3 as $c_3 = 1$. In our calculation, $1a_2 \rightarrow 4e$ contributes only 22%, see Table 4. Thus neglecting c_4 is justified in a qualitative discussion. The actual quantitative $R(3E^1)$ value of Table 4 contains contributions from both c_3 and c_4.

The rotatory strength for the charge transfer transition $A_1^1 \rightarrow 2A_2^1$ shown in eqs. 16a and 17a has its polarization in the z direction. It has substantial contributions to the electric transition dipole moment from $\langle 1\hat{e}^\sigma|z|2\hat{e}^\sigma\rangle$ as $2e$ is primarily a ligand based orbital made up of $1\hat{e}^\sigma$ whereas the d-based $4e$ has a contribution from $2\hat{e}^\sigma$, Table 7. We note that these contributions are much larger than for $R(1A_2^1)$, Table 7. On the other hand, the contribution to the magnetic transition dipole moment of $R(2A_2^1)$ comes from the large $d\sigma_2$ component in $4e_y$ and the small but crucial $d\pi_2$ component in $2e_x$, Table 7, through $c(4e_y, 3)c(2e_x, 4) \cdot \langle d\sigma_2|m_z|d\pi_2\rangle$. We can thus write $R(2A_2^1)$ in the form given in eq. 18.

$$R(2A_2^1) = \frac{4\sqrt{2}}{3}[c(2e_x,1)c(4e_y,2)\langle 1\hat{e}_x^\sigma|z|2\hat{e}_y^\sigma\rangle] \times [c(4e_y,3)c(2e_x,4) \cdot (\langle d_{xy}|m_z|d_{x^2-y^2}\rangle - \langle d_{xz}|m_z|d_{yz}\rangle)]. \quad (18)$$

We note that the approximate expressions for $R(1A_2^1)$ in eq. 12 and $R(2A_2^1)$ are related as

$$R(2A_2^1) = R(1A_2^1) \cdot \frac{c(2e_x,1)c(2e_x,4)}{c(3e_x,1)c(3e_x,4)} \quad (19)$$

Now in $\psi_{2e_x} = c(2e_x,1)1e_x^\sigma + c(2e_x,4)d\pi_2$, the coefficients $c(2e_x,1)$ and $c(2e_x,4)$ are of the same sign as ψ_{3e} is bonding, Table 7. On the other hand in $\psi_{3e_x} = c(3e_x,1)1e_x^\sigma + c(3e_x,4)d\pi_2$, the coefficients are of opposite signs as ψ_{3e} is anti-bonding. We predict thus in agreement with experiment $R(1A_2^1)$ and $R(2A_2^1)$ to be of opposite signs. The same can be shown for $R(1E^1)$ and $R(3E^1)$.

For the $A_1^1 \rightarrow 3E^1$ transition with x, y polarization we get again large contributions to the electric transition dipole moment, now from $\langle 1\hat{e}^\sigma|x,y|2\hat{e}^\sigma\rangle$, and modest contributions to the magnetic transition dipole moment from $d\sigma$ of $4e$ and $d\pi$ of $2e$.

The dependence of the rotatory strength on the molecular parameters a, b, and ω. Relationships between the geometry of a tris-bidentate complex and its optical activity were first suggested by Stiefel and Brown[36] as well as Judkins and Royer as an experimental observation without any theoretical justification.[42] Polar distortion, s/h of Figure 2b, and azimuthal distortion, ϕ of Figure 2c, were related to the splitting and signs of the two CD bands in the d-d transition region. It was found that, to first order, the polar distortion, s/h, gives rise to the A_2-E energy separation but makes no contribution to the rotatory strength while the azimuthal distortion, ϕ, is responsible for the rotatory strength but makes no contribution to the A_2-E splitting.[42]

We shall in the following show, how the rotatory strength of $[Co(en)_3]^{3+}$ is influenced by the geometrical parameters a, b, and ω introduced in Figure 2a. We compare to this end in Table 6 under Case III the calculated ligand–metal overlaps for a model geometry that has an azimuthal expansion of $\Delta\phi = +6.3^\circ$ corresponding to $\omega = 45.6^\circ$ with overlaps for Case II, corresponding to the real geometry of Λ-$[Co(en)_3]^{3+}$ where $\Delta\phi = -6.3^\circ$ and $\omega = 33.7^\circ$. Here $\Delta\phi$ is the deviation from the octahedral value for ϕ of $\phi = 60^\circ$. We see from $S(d\sigma_2,2\hat{e}_y^\sigma)$ and $S(d\pi_2,1\hat{e}_x^\sigma)$, the overlaps of the most importance to the rotatory strengths according to our qualitative analysis made above, that the latter changed in sign from positive for Case II with $\Delta\phi = -6.3^\circ$ to negative for $\Delta\phi = -6.3^\circ$ of Case III. On the basis of the same molecular orbital arguments made earlier, the coefficient $c(3e,1)$ in Table 7 and eq. 12 should be positive in Case III in order to add $1\hat{e}^\sigma$ out-of-phase to the $d\pi$ component of ψ_{3e}, as the overlap $S(d\pi_2,1\hat{e}_x^\sigma)$ is now negative. With the sign, not necessarily the magnitude, of the other contributions in eq. 12 remaining the same, the sign of $R(1A_2^1)$ should change when the direction of the azimuthal distortion changes, in agreement with the experimental observations and computations.[6,7,9,43] We plot in Figure 12 the calculated rotatory strengths for the three bands in the d-d region of Figure 8 as a function of ω. The corresponding overlaps $S(d\pi_2,1\hat{e}_x^\sigma)$ in different geometries are also plotted against ω in the same figure. It is noted that all the model molecules with different ω are obtained by rotating three ligands (see Fig. 1b) in the real molecule of Λ-$[Co(en)_3]^{3+}$ based on geometry optimizations. Obviously, as shown in Figure 12, the rotatory strengths as well as the overlap tend to change sign at an angle around 40°. Note that with the same a and

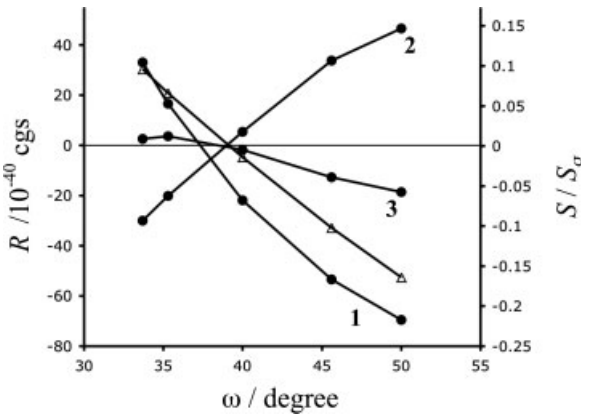

Fig. 12. Plots of rotatory strengths (R) and overlaps (S) between $d\pi_2$ and $1\hat{e}_x^{\sigma}$ at different ω. The labels correspond to the numbers in Table 4.

b, i.e., $a = 1.321$ Å, $b = 1.445$ Å, a geometry that has $\Delta\phi = 0^{\circ}$ corresponds to $\omega = 39.2^{\circ}$.

The sign change of the overlap is depicted in Scheme 3 and shown numerically in Figure 12. In Scheme 3, the three ligands are rotated from the D_{3h} geometry ($\omega = 0^{\circ}$) over the azimuthal contraction ($\omega = 33.7^{\circ}$), and the approximate octahedral orientation ($\omega = 35.3^{\circ}$) to the azimuthal expansion ($\omega = 45.6^{\circ}$). It can be seen that while the two shaded negative lobes of the ligand orbitals have dominant overlaps with the negative lobes of the d-orbitals in the contraction geometry ($\omega = 33.7^{\circ}$), they ($\omega = 45.6^{\circ}$) overlap more with the positive lobes of the d-orbitals in the expansion geometry. It is also obvious that in the ideal octahedral case where $\omega = 35.3^{\circ}$ and $a = b$, $S(d\pi_2, 1\hat{e}_x^{\sigma})$ goes to zero, since the four lobes of the ligand orbitals are now situated in the nodal planes of the d-orbital. On the other hand, $2\hat{e}_y^{\sigma}$ will maintain a positive overlap with $d\sigma_2$ during the rotation depicted in Scheme 3. We refer to the relevant orbitals displayed in Figures 5 and 10.

CONCLUSION

We have presented a qualitative analysis of the CD spectrum of Λ-$[Co(en)_3]^{3+}$, where the complex was chosen as a prototype for d^6 complexes of bidentate ligands containing only σ-orbitals. The analysis was based on TD-DFT and qualitative molecular orbital theory. The CD spectrum consists of two groups. In the first group we find three d-d bands of moderate intensity in the visible and near-ultraviolet region. Here $A_{1g}^1 \rightarrow 1E^1$ and $A_{1g}^1 \rightarrow 1A_2^1$ are ascribed to the magnetically allowed $A_{1g}^1 \rightarrow T_{1g}^1$ transition of O_h parentage whereas $A_{1g}^1 \rightarrow 1E^1$ corresponds to the both electrically and magnetically forbidden $A_{1g}^1 \rightarrow T_{2g}^1$ transition in octahedral symmetry, Scheme 2. In the second group, we find the allowed ligand-to-metal charge transfer transitions $A_{1g}^1 \rightarrow 3E^1$ and $A_{1g}^1 \rightarrow 2A_2^1$ of $A_{1g}^1 \rightarrow T_{1u}^1$ parentage, Scheme 2. The rotatory strengths associated with these bands are interpreted based on the metal–ligand orbital interactions. In $[M(L\text{-}L)_3]^{3+}$, where L-L denotes a diamine ligand containing only σ-orbitals, the ligand σ combinations on the nitrogen atoms will overlap only with the dσ orbitals on the metal center in a perfect octahedral arrangement of the six nitrogens. In the case where the six nitrogens are displaced from the ideal octahedron, the originally nonbonding dπ orbitals can slightly overlap with the ligand σ-orbitals. The small portion of the ligand σ-orbitals participating in the HOMO metal-based dπ orbitals will contribute to the d-d electric transition moment through $\langle 1\hat{e}^{\sigma}|\hat{\boldsymbol{\mu}}|2\hat{e}^{\sigma}\rangle$. Likewise, the metal d-orbitals mixed into the ligand-based orbitals will have a contribution to the magnetic transition moments of the CT through $\langle d\pi|\hat{\boldsymbol{m}}|d\sigma\rangle$. These contributions are responsible for the CD in trigonal dihedral d^6 complexes of bidentate ligands containing only σ-orbitals.

Within the simple model outline here, the rotatory strength of the A_2 component of the d-d transitions is written as shown in eq. 12 in terms of the contribution to the electric part exclusively from $\langle 1\hat{e}_x^{\sigma}|z|2\hat{e}_y^{\sigma}\rangle$ and the magnetic part from $\langle d_{xz}|m_z|d_{yz}\rangle$ and $\langle d_{xy}|m_z|d_{x^2-y^2}\rangle$ only. On the basis of the simplified expression for $R(1A_2^1)$ in eq. 12, we are able to predict the sign of $R(1A_2^1)$ to be negative in agreement with experiment. We are able, on the other hand, to predict that $R(2A_2^1)$ in agreement with experiment is positive. The change in sign comes from the fact that ψ_{2e} involved in the $1A_1^1 \rightarrow 2A_2^1$ transition and ψ_{3e} involved in the $1A_1^1 \rightarrow 1A_2^1$ transition are respectively bonding and antibonding with respect to the same metal and ligand components. The fact that the ψ_{2e} is the bonding com-

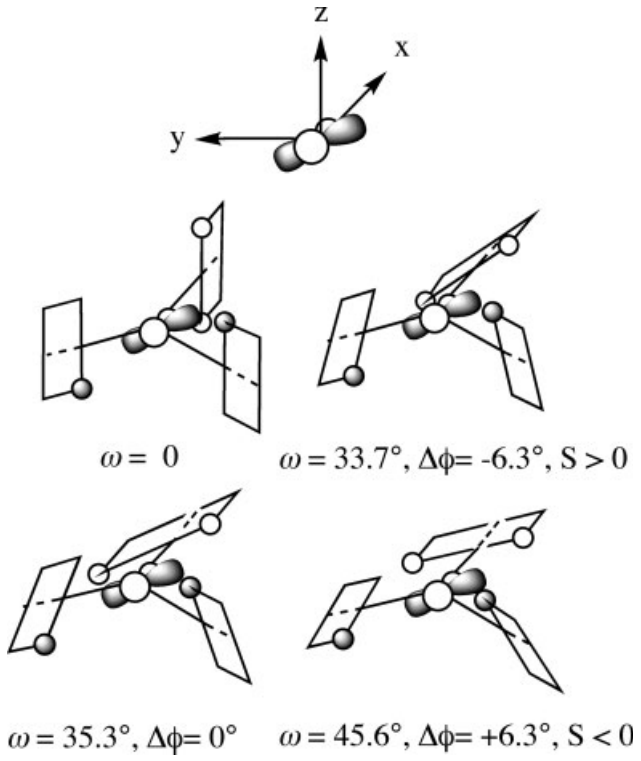

Scheme 3. Dependence of overlap $S(d\pi_2, 1e_x^{\sigma})$ on geometric parameter ω.

ponent can further be used to explain why $|R(1A_2^1)| < |R(2A_2^1)|$. Similar arguments apply to the relative signs and magnitudes of $R(1E^1)$ and $R(3E^1)$.

It follows from both calculations and experiment that the rotatory strengths of the two E component, $1E^1$ and $2E^1$ of the $A_{1g}^1 \rightarrow T_{1g}^1$ and $A_{1g}^1 \rightarrow T_{2g}^1$ transitions, respectively, are of different order of magnitude. This is due to the fact that while the relevant one-electron transitions $2a_1 \rightarrow 4e$ and $3e \rightarrow 4e$ add up in the contribution to $R(1E^1)$, they subtract in the contribution to $R(2E^1)$.

We have finally shown how the rotatory strength can change sign as a function of the molecular parameters a, b, and ω.

ACKNOWLEDGMENTS

J.F. would like to acknowledge the financial support of Alberta Ingenuity Fund (AIF). T.Z. would like to thank the Canadian Government for a Canada Research Chair.

LITERATURE CITED

1. Kuroda R, Saito Y. Circular dichroism of inorganic complexes: interpretation and applications. In: Nakanishi K, Berova N, Woody RW, editors. Circular dichroism: principle and applications. New York: VCH; 1994. p 217–258.
2. Mathieu JP. Circular dichroism, valence bonds, and secondary asymmetric synthesis. Ann Phys 1944;19:335–354.
3. Kobayashi M. Optical rotatory power and circular dichroism. III. Rotatory dispersion of D-$[Coen_3]Br_3$. J Chem Soc Jpn 1943;64:648–653.
4. Moffitt W. Optical rotatory dispersion of transition-metal complexes. J Chem Phys 1956;25:1189–1198.
5. Moffitt W, Woodward RB, Moscowitz A, Klyne W, Djerassi C. Structure and the optical rotatory dispersion of saturated ketones. J Am Chem Soc 1961;83:4013–4018.
6. Liehr AD. Interaction of electromagnetic radiation with matter. I. Theory of optical rotatory power: topic A. Trigonal dihedral compounds. J Phys Chem 1964;68:665–722.
7. Karipides A, Piper TS. Optical activity of coordination compounds. II. A molecular orbital model and an analysis of experimental data for complexes of trigonal symmetry. J Chem Phys 1964;40:674–682.
8. Richardson FS. Optical activity of trigonally distorted cubic systems. J Phys Chem 1971;75:692–712.
9. Richardson FS. Sector rules and the circular dichroism of ligand field bands in transition metal complexes. Inorg Chem 1971;10:2121–2130.
10. Richardson FS. Optical activity of transition metal compounds. I. Sector rules for metal complexes of the pseudotetragonal class. J Chem Phys 1971;54:2453–2468.
11. Richardson FS. Theory of natural optical activity in crystalline $NiSO_4 \cdot 6H_2O$. J Chem Phys 1972;57:589–604.
12. Richardson FS. Optical activity of dissymmetric six-coordinate cobalt(III) complexes. Inorg Chem 1972;11:2366–2378.
13. Mason SF, Seal RH. The optical activity of cobalt(III) chelate diamine complexes: a dynamic-coupling ligand-polarization model. Mol Phys 1976;31:755–775.
14. Autschbach J, Ziegler T, van Gisbergen SJA, Baerends EJ. Chioptical properties from time-dependent density functional theory. I. Circular dichroism spectra of organic molecules. J Chem Phys 2002;116:6930–6940.
15. Autschbach J, Ziegler T. Calculating molecular electric and magnetic properties from time-dependent density functional response theory. J Chem Phys 2002;116:891–896.
16. Autschbach J, Ziegler T, Patchkovskii S, van Gisbergen SJA, Baerends EJ. Chiroptical properties from time-dependent density functional theory. II. Optical rotations of small to medium sized organic molecules. J Chem Phys 2002;117:581–592.
17. Fukuyama T, Matsuo K, Gekko K. Vacuum-ultraviolet electronic circular dichroism of L-alanine in aqueous solution investigated by time-dependent density functional theory. J Phys Chem A 2005;109:6928–6933.
18. Mori T, Inoue Y, Grimme S. Quantum chemical study on the circular dichroism spectra and specific rotation of donor-acceptor cyclophanes. J Phys Chem 2007;111:7995–8006.
19. Mori T, Grimme S, Inoue Y. A combined experimental and theoretical study on the conformation of multiarmed chiral aryl ethers. J Org Chem 2007;72:6998–7010.
20. Furche F, Ahlrichs R, Wachsmann C, Weber E, Sobanski A, Vogtle F, Grimme S. Circular dichroism of helicenes investigated by time-dependent density functional theory. J Am Chem Soc 2000;122:1717–1724.
21. Jorge FE, Autschbach J, Ziegler T. On the oringin of optical activity in tris-diamine complexes of Co(III) and Rh(III): a simple model based on time-dependent density function theory. J Am Chem Soc 2005; 127:975–985.
22. Jorge FE, Autschbach J, Ziegler T. On the origin of the optical activity in the d-d transition region of tris-bidentate Co(III) and Rh(III) complexes. Inorg Chem 2003;42:8902–8910.
23. Autschbach J, Jorge FE, Ziegler T. Density functional calculations on electronic circular dichroism spectra of chiral transition metal complexes. Inorg Chem 2003;42:2867–2877.
24. Guennic BL, Hieringer W, Görling A, Autschbach J. Density functional calculation of the electronic circular dichroism spectra of the transition metal complexes $[M(phen)_3]^{2+}$ (M = Fe, Ru, Os). J Phys Chem A 2005;109:4836–4846.
25. Corey EJ, Bailar JC. The stereochemistry of complex inorganic compounds. XXII. Stereospecific effects in complex ions. J Am Chem Soc 1959;81:2620–2629.
26. Fonseca Guerra C, Visser O, Snijders JG, te Velde G, Baerends EJ. Parallelisation of the Amsterdam density functional program. In: Clementi E, Corongiu C, editors. Methods and techniques for computational chemistry. Cagliari: STEF; 1995. p 303–395.
27. te Velde G, Bickelhaupt FM, Baerends EJ, van Gisbergen SJA, Fonseca Guerra C, Snijders JG, Ziegler T. Chemistry with ADF. J Comput Chem 2001;22:931–967.
28. Amsterdam Density Functional program. Theoretical chemistry. Amsterdam: Vrije Universiteit. Available at: http://www.scm.com.
29. van Gisbergen SJA, Snijders JG, Baerends EJ. A density functional theory study of frequency-dependent polarizabilities and Van der Waals dispersion coefficients for polyatomic molecules. J Chem Phys 1995;103:9347–9354.
30. van Gisbergen SJA, Snijders JG, Baerends EJ. Implementation of time-dependent density functional response equations. Comput Phys Commun 1999;118:119–138.
31. van Gisbergen SJA, Fonseca Guerra C, Baerends EJ. Towards excitation energies and (hyper)polarizability calculations of large molecules. Application of parallelization and linear scaling techniques to time-dependent density functional response theory. J Comput Chem 2000;21:1511–1523.
32. Brown A, Kemp CM, Mason SF. Electronic absorption, polarised excitation, and circular dichroism spectra of [5]-helicene (dibenzo[*c*,*g*]phenanthrene). J Chem Soc A 1971;751–755.
33. Frantz J. "g3data", 2002; Available at: http://beam.helsinki.fi/frantz/software/g3data.php.
34. Klamt A, Schüürmann G. COSMO: a new approach to dielectric screening in solvents with explicit expressions for the screening energy and its gradient. J Chem Soc Perkin Trans 1993;2:799–805.
35. Pye CC, Ziegler T. An implementation of the conductor-like screening model of solvation within the Amsterdam density functional package. Theor Chem Acc 1999;101:396–408.
36. Vosko SH, Wilk L, Nusair M. Accurate spin-dependent electron liquid correlation energies for local spin density calculations: a critical analysis. Can J Phys 1980;58:1200–1211.
37. Becke AD. Density-functional exchange-energy approximation with correct asymptotic behavior. Phys Rev A 1988;38:3098–3100.

38. Perdew JP. Density-functional approximation for the correlation energy of the inhomogeneous electron gas. Phys Rev B 1986;33:8822–8824.
39. Stiefel EI, Brown GF. On the detailed nature of the six-coordinate polyhedra in tris(bidentate ligand) complexes. Inorg Chem 1972;11:434–436.
40. Kuroda R, Saito Y. Solid-state circular dichroism spectra of tris(diamine)cobalt(III) complexes: decomposition into E and A_2 components. Bull Chem Soc Jpn 1976;49:433–436.
41. McGlynn SP, Vanquickenborne LG, Kinoshita M, Carroll DG. Appendix H. In: McGlynn SP, Vanquickenborne LG, Kinoshita M, Carroll DG, editors. Introduction to applied quantum chemistry. New York: Holt, Rinehart and Winston; 1972. p 442–444.
42. Judkins RR, Royer DJ. Optical rotatory strength of tris-bidentate cobalt (III) complexes. Inorg Chem 1974;13:945–950.
43. Piper TS, Karipides A. Optical activity of trigonal coordination compounds. Mol Phys 1962;5:475–483.

CHIRALITY 20:951–960 (2008)

Circular Dichroism of Polynucleotides: Interactions of $NiCl_2$ with Poly(dA-dT)·Poly(dA-dT) and Poly(dG-dC)·Poly(dG-dC) in a Water-in-Oil Microemulsion

MARTA AIROLDI,[1] GIUSEPPE GENNARO,[1] MARCELLO GIOMINI,[2,3] ANNA MARIA GIULIANI,[1]* AND MAURO GIUSTINI[2,3]

[1]*Dipartimento di Chimica Inorganica e Analitica "Stanislao Cannizzaro," Università di Palermo, 90128 Palermo, Italy*

[2]*Dipartimento di Chimica, Università "La Sapienza," 00185 Roma, Italy*

[3]*Consorzio per lo Sviluppo di Sistemi a Grande Interfase (CSGI), U.O.: Università del Molise, 86100 Campobasso, Italy*

Presented at the 11th International Conference on Circular Dichroism, 2007, Groningen, Netherlands

ABSTRACT The thermal behavior of the synthetic, high molecular weight, double stranded polynucleotides poly(dA-dT)·poly(dA-dT) [polyAT] and poly(dG-dC)·poly(dG-dC) [polyGC] solubilized in the aqueous core of the quaternary water-in-oil cationic microemulsion CTAB|*n*-pentanol|*n*-hexane|water in the presence of increasing amounts of $NiCl_2$ at several constant ionic strength values (NaCl) has been studied by means of circular dichroism and electronic absorption spectroscopies. In the microemulsive medium, both polynucleotides show temperature-induced modifications that markedly vary with both Ni(II) concentration and ionic strength. An increase of temperature causes denaturation of the polyAT duplex at low nickel concentrations, while more complex CD spectral modifications are observed at higher nickel concentrations and ionic strengths. By contrast, thermal denaturation is never observed for polyGC. At low Ni(II) concentrations, the increase of temperature induces conformational transitions from B-DNA to Z-DNA form, or, more precisely, to left-handed helical structures. In some cases, at higher nickel concentrations, the CD spectra suggest the presence of Z′-type forms of the polynucleotide. *Chirality 20:951–960, 2008.*

KEY WORDS: model polynucleotides; thermal denaturation; water-in-oil microemulsions; nickel (II) ions; CD and UV spectroscopies

INTRODUCTION

The polymorphic behavior and the flexibility of both natural DNA's and synthetic model polynucleotides is well known: they depend not only on the type and the sequence of nucleotides in each strand but also on even local modifications of the medium.[1–3] The factors that mainly influence the conformational polymorphism of DNA are the pH of the medium, the hydration of the polymer, and the nature and concentration of added electrolytes.[3–11]

The so called hard metals (alkaline and alkaline earth cations) interact with DNA primarily at the level of phosphate groups and stabilize the double helix reducing the electrostatic repulsion between adjacent negatively charged groups; the soft metals (transition metal cations), on the other hand, interact preferentially with the nucleic bases breaking the base pairs and destabilizing the structure of the polymer. The separation between the two classes, however, is not clear-cut and the existence of borderline ions, for which the binding affinities for the two types of sites can be modulated by the experimental conditions, has been evidenced.[12–18]

DNA molecule, in-vivo, exhibits an extreme degree of compactness that cannot be simply explained by the double helix model of its secondary structure. It is well known, for example, that the double helix of DNA in its extended form has dimensions that far exceed those of the biological structures where it is found, and that, in the cells, the nucleic acids are present in extremely compacted or condensed forms as in chromatin or in the bacteriophage head.[11,19,20] The structure and reactivity of polynucleotides confined in such restricted volumes could be different from those observed in solution. Since, in-vivo, the nucleic acids are often associated with bilayer-type structures, such as those of membranes, one might reasonably wonder if the presence of an interface can contribute to the phenomena of their superpackaging.[21]

For the study of the phenomena connected with these characteristics of the polynucleotydes, the huge complexity of the living systems suggests to resort to appropriate model systems. Therefore, the use of synthetic polynucleotides of known base sequence confined in the aqueous domain of the simplified model of the endocellular

*Correspondence to: Prof. Anna Maria Giuliani, Dipartimento di Chimica Inorganica e Analitica "Stanislao Cannizzaro," Università di Palermo, Viale delle Scienze—Pad. 17, 90128 Palermo, Italy. E-mail: denebdue@unipa.it

Received for publication 30 October 2007; Accepted 29 November 2007
DOI: 10.1002/chir.20531
Published online 1 February 2008 in Wiley InterScience (www.interscience.wiley.com).

microenvironment known as "water-in-oil microemulsions" (w/o μE), or reverse micelles, is strongly recommended.[22–24] The term microemulsion indicates the homogeneous, optically transparent, and isotropic dispersion of two immiscible liquids (an organic solvent -the oil- and water, for example) mediated by the presence of a surfactant, which is necessary for significant lowering of the oil–water interfacial tension. When moderate quantities of water are added to the organic solvent, the w/o μE are obtained: they are characterized by the presence of discrete aggregates of water microdrops dispersed in the hydrophobic continuum. The average size of such droplets falls in the range 5–100 nm: they are polydisperse in nature and the polydispersity decreases with decreasing particle size. In a great number of cases, the stabilization of the water–oil interface requires the presence of a fourth component, the cosurfactant (as a rule, an alkanol with five or six carbon atoms) which aids the surfactant in lowering the interfacial tension between the two immiscible liquids.[25,26]

To define from a physico-chemical point of view the quaternary microemulsions (surfactant|cosurfactant|oil|water) it is necessary to know the value of three parameters: the surfactant concentration, the amount of solubilized water (W_0 = [water]/[surfactant]) on which the dimensions of the droplets depend[27] and the amount of cosurfactant (P_0 = [cosurfactant]/[surfactant]), which modifies the spontaneous curvature of the interface and the viscosity of the medium.[28] Our research group, in several previous studies, has utilized the quaternary w/o μE CTAB|*n*-pentanol|*n*-hexane|water (CTAB = hexadecyltrimethylammonium bromide) of the following characteristics: [CTAB] = 0.10 M; W_0 = 15; P_0 = 8.5. This system can easily dissolve in its aqueous microdomain the synthetic model duplex polynucleotides poly(dA-dT)·poly(dA-dT) and poly(dG-dC)·poly(dG-dC), from now on indicated, respectively, as polyAT and polyGC. The solubilization in w/o μE does not alter the fundamental characteristics of the polynucleotides, such as the well known hyperchromic effect that accompanies the denaturation of the double helix or the possibility of their reversible chemical (acid and basic) denaturation.[29–32]

Nevertheless, the presence of the cationic interface exerts a remarkable stabilizing effects on the double helix, since, indeed, the thermal denaturation of polyAT is prevented. Furthermore, in the presence of electrolytes at moderately high concentration (e.g., [NaCl] $\geq$ 300 mM) the confinement in the aqueous compartment of the μE favors the formation of condensed structures of the DNA model molecules similar to those obtained, for the natural polynucleotide, in the presence of high molecular weight polymers (Ψ forms).[33,34] Recently, we have examined the thermal behavior of polyAT in aqueous solution in the presence of $NiCl_2$. The melting temperature of the double helix to random coil transition increases with ionic strength at constant $NiCl_2$ concentration and decreases with Ni(II) concentration at constant ionic strength.[35] PolyGC, instead, exhibits a B- to Z- conformational transition induced by $NiCl_2$, requiring increasing nickel concentrations at increasing ionic strength.[36] The model, high molecular weight polynucleotide duplexes polyAT and polyGC were solubilized in the quaternary cationic w/o microemulsion CTAB|*n*-hexane|*n*-pentanol|water in the presence of increasing amounts of $NiCl_2$ and at several ionic strength values and their thermal behavior was studied by means of circular dichroism and electronic absorption spectroscopies. The results are collected and discussed in the present article.

MATERIALS AND METHODS

Chemicals

Hexadecyltrimethylammonium bromide (CTAB, Fluka) was purified and stored as described elsewhere.[37]

PolyAT (sodium salt, MW = 900 ÷ 1900 kDa) was purchased from Sigma in vials of 50 U (1 U is the amount of polynucleotide giving an absorbance of 1.0 at 260 nm, when dissolved in 1 ml of water in a 1.0-cm optical pathlength cuvette). PolyGC (sodium salt, MW = 490 ÷ 520 kDa) was also a Sigma product and arrived in vials of 25 U. Lyophilized polyAT and polyGC samples were prepared in Eppendorf vials and stored over silica gel as previously described.[34]

NaCl (Merck Suprapur) was dried at 383 K for 5 h in an oven and then stored over silica gel under vacuum.

$NiCl_2.6H_2O$ (Aldrich, 99.9999%) was used as received. Concentrated stock solution of $NiCl_2$ titrated with EDTA (Fluka) using Red Eriochrome B as indicator,[38] was diluted as required for each experiment.

UV-spectroscopy grade *n*-pentanol (Fluka), used as cosurfactant, and *n*-hexane (Fluka) were used without purification.

Tris, 2-amino-2(hydroxymethyl)-1,3-propanediol, was a Sigma product and was used as received.

Twice distilled water was always employed.

Instrumentation

The CD spectra were acquired with a Jasco J715 spectropolarimeter under nitrogen flux. The temperature was controlled to ±1 K by means of a Julabo F10 thermostat. The variable temperature UV spectra were obtained from the data collected with the J715 instrument, by processing them with the appropriate algorithm implemented in the Jasco program.

The initial, room temperature, UV spectra, used to obtain the actual concentration of polynucleotide (in monomer units) of each sample, were recorded with a double beam Varian Cary 100 spectrometer.

The concentration was calculated by means of the Beer–Lambert equation using the absorbance value at 262 nm, A_{262}, for polyAT, and at 255 nm, A_{255}, for polyGC (both corrected for A_{350}) and the ε_{262} value of 6650 mol^{-1} l cm^{-1},[39] and the ε_{255} value of 8400 mol^{-1} l cm^{-1},[18] respectively.

The contents of Eppendorf vials obtained by lyophilizing equal aliquots of the stock solutions of polyAT, or polyGC, did not differ from one another by more than 10%.

Hellma Quartz Suprasil cuvettes of 1.0 cm optical pathlength were always used. The spectral region explored

was 230–350 nm; the high absorption of the medium bars the region of $\lambda < 230$ nm.

The temperature was varied between 293 and 336K; the high limit being set by the boiling temperature of the *n*-hexane. At least 10 min were allowed for thermal equilibration at each temperature.

The reported CD spectra are all baseline corrected by subtraction of the appropriate blank spectra. The blanks were microemulsions identical to the measurement samples but "empty," i.e. without the polynucleotide.

Microemulsions Preparation

All microemulsions, either "empty" or "filled" (with polynucleotide), had the following characteristics: [CTAB] = 0.10 M, P_0 (i.e.[*n*-pentanol]/[CTAB]) = 8.5 and W_0 (i.e.[H_2O]/[CTAB]) = 15.

The $NiCl_2$-NaCl solutions required for the preparation of the microemulsions were obtained at the selected metal ion concentration and (nominal) ionic strength, *I*, by weighing in a volumetric flask the necessary amount of NaCl, adding with a microsyringe the appropriate volume of the metal ion stock solution and taking to volume with 1.0 mM Tris buffer solution (pH = 7.8 ± 0.2). The *I* value was calculated neglecting the contribution of the buffer and of the polynucleotide.

To obtain the microemulsive samples for the measurements, an empty microemulsion was first prepared by weighing in a volumetric flask the appropriate amounts of CTAB and *n*-pentanol, adding the volume of the selected NaCl-$NiCl_2$ solution necessary to reach $W_0 = 5$ and then *n*-hexane to volume: the system was vortex stirred until a clear isotropic solution was obtained. Separately the lyophilized polyAT (or polyGC) content of an Eppendorf vial was dissolved in the volume of the selected NaCl-$NiCl_2$ solution required to have a W_0 value of 15 in the final sample; the appropriate volume of the matched empty microemulsion at $W_0 = 5$ was added and the system was vortex stirred until a clear solution was obtained.

The blanks were prepared by the same procedure, without the polynucleotide.

All microemulsions were prepared immediately before starting the measurements.

EXPERIMENTAL RESULTS

Variable temperature UV and CD spectra of polyAT solubilized in the aqueous core of CTAB|*n*-hexane|*n*-pentanol|water reverse micelles, in the presence of increasing concentrations of $NiCl_2$ were recorded between 293 and 336 K. The measurements were performed at different *I* values ranging from 0.003 to 0.21.

For polyGC solubilized in the reverse micelles, CD and UV variable temperature (293 ÷ 336 K) spectra were collected at fixed *I* (0.21; NaCl) and variable $NiCl_2$ concentration (1.0 ÷ 70.0 mM), and at fixed $NiCl_2$ concentration (1.0 mM) and variable *I* (0.003 ÷ 0.21; NaCl).

Effects of $NiCl_2$ on PolyAT

The CD spectrum of polyAT at 293 K, for all the samples considered, corresponds to that of a canonical B, or more often of the B-family, double helix.[40–43] The corresponding electronic absorption spectra showed the characteristic band centered at 262.2 ± 0.2 nm.

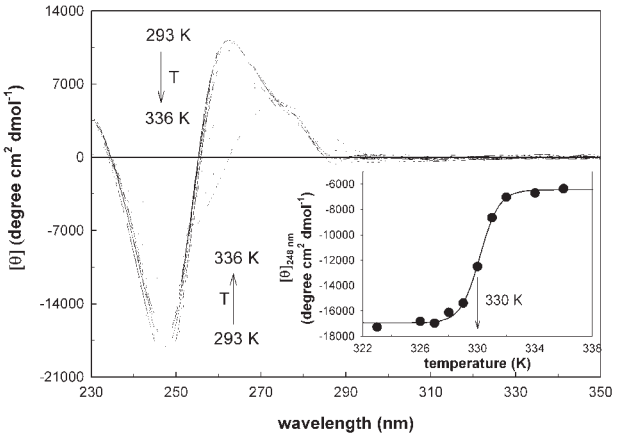

Fig. 1. Thermal behavior of polyAT in the quaternary w/o microemulsion. [polyAT] = 8.60×10^{-5} M in monomer units; [$NiCl_2$] = 10 mM; I = 0.12. Inset. Molar ellipticity evolution as a function of the temperature (number refers to the inflection point of the sigmoid as derived by the best fit procedure described in the text).

On increasing the temperature, the CD spectra exhibited a marked dependence both on the *I* value and on the nickel concentration. At 1.0 mM $NiCl_2$, for all values of *I*, only small spectral variations were observed, resembling those indicated as "pre-melting" changes in solution,[39,44] but no thermal melting occurred.

At 5.0 mM $NiCl_2$, for all I values, in addition to the "pre-melting" changes, the beginning of thermal denaturation was observed at temperatures close to the upper limit of the available range ($T \leq 336$ K). The melting was indicated by hyperchromism in the UV band, and decreased amplitude and red-shift of the CD spectra, consequent to the loss of base-stacking and ordered double helical structure. Since complete melting could not be observed, the hyperchromic effect measured (5–10%) was much smaller than that observed for thermal denaturation in solution[34] or chemical denaturation in microemulsion,[45] that can be larger than 50%.

When the $NiCl_2$ concentration was increased to 10.0 mM, complete thermal denaturation could be observed at certain I values, entailing a 32–34% hyperchromic effect and a small blue shift of the maximum in the electronic absorption spectra. The corresponding CD spectra exhibited a marked decrease of the amplitude and a red-shift of the bands (see Fig. 1). In these cases it was possible to obtain a melting curve by plotting the absorbance or the molar ellipticity value at a fixed wavelength as a function of temperature. From these sigmoidal curves, which indicate that melting is a cooperative process, the melting temperature, T_m, i.e. the temperature value at the inflection point, was obtained by a fitting procedure with a four-parameters sigmoid (Sigmaplot software). A typical experimental melting curve, together with the one calculated by means of the fitting procedure, is shown in the inset of Figure 1. Curves of absorbance or CD at a fixed wavelength vs. temperature were constructed also for samples

TABLE I. Transition temperatures, T_t ($K \pm$ half dispersion), of polyAT in the w/o microemulsion CTAB|*n*-hexane|*n*-pentanol|water in the presence of $NiCl_2$ at several values of I [a]

$[NiCl_2]$/mM	$I = 0.003$	$I = 0.03$	$I = 0.06$	$I = 0.12$	$I = 0.21$
0.0[b]		325.8	(331.1)	(336.3)	(340.6)
1.0	[c]	[c]	[c]	[c]	[c]
5.0		[c]	330.8 ± 0.4	>333	>336
			(334.4 ± 0.2)	(336.4 ± 0.2)	(340.2 ± 0.1)
10.0		327.4 ± 0.3	329.1 ± 0.1	330.0 ± 0.1	325.1 ± 0.1
		(328.6 ± 0.6)	(332.9 ± 0.1)	(335.7 ± 0.2)	(339.5 ± 0.2)
20.0			320.1 ± 0.1	319.6 ± 0.2	309.8 ± 2.1
			(325.9 ± 0.1)	(330.9 ± 0.5)	318.0
					(335.6 ± 0.2)
30.0				313.2 ± 0.4	310.5
				(327.6 ± 0.8)	326.2
					(333.0 ± 0.5)
50.0					309.5 ± 0.1
					315.4
					(326.1 ± 0.3)
70.0					311.9 ± 0.6
					(322.5 ± 0.3)

[a]In parentheses are the melting temperatures of the matched aqueous solutions (from Ref. 35).
[b]From Ref. 34.
[c]Only premelting modifications.

with $NiCl_2$ 1.0 mM, but these were not complete and could be fitted only when defined up to beyond the inflection point. Regular melting curves were recorded for $NiCl_2$ 10.0 mM at the I values 0.03, 0.06, and 0.12; for $NiCl_2$ 20.0 mM at I equal to 0.06 and 0.12 and for $NiCl_2$ 30.0 mM at I equal to 0.12. At the other $NiCl_2$ concentrations at the different ionic strengths, cooperative transitions, that were not melting, were observed upon increasing the temperature. Fitting of the sigmoidal $A_{(\lambda)}$ or $CD_{(\lambda)}$ vs. T curves yielded transition temperatures, that are collected together with the regular melting temperatures in Table 1, and all are named T_t.

A comparison of the CD spectra of the thermally modified polyAT in the presence of 10.0 mM $NiCl_2$ at I equal to 0.12 and 0.21 (Fig. 2), immediately showed that the two high temperature conformations were different. In addition, the lower hyperchromicity recorded at $I = 0.21$ was in bearing with a nonmelting transition under these conditions (Fig. 2, inset).

The thermal behavior of polyAT at $I = 0.21$ in the presence of progressively higher concentrations of $NiCl_2$ became less easy to interpret.

For $NiCl_2$ concentrations 20.0 and 30.0 mM, the increase of the temperature lead initially to the appearance of a very intense maximum in the CD spectra (Fig. 3, Panel A), while an absorbance decrease of the order of 10–15% was observed in the UV band centered at about 260 nm.

A further increase of temperature seemed to induce denaturation of such high chirality form, as suggested by the lowering of the molar ellipticity and the marked hyperchromic effect (45–50%) (Fig. 3, Panel B).

The high temperature CD spectra exhibited the same features observed for polyAT thermally denatured in the presence of $NiCl_2$ (see Fig. 1).

At higher $NiCl_2$ concentrations (50.0 and 70.0 mM), when the temperature was raised above 293 K, an absorbance increase of 30–35% was observed for the UV electronic absorption band, while the CD spectrum changed from a noncanonical B pattern, to one with the minimum (247 nm) and the maximum (262 nm) of lower amplitude and the small minimum at about 288 nm of increased amplitude and red shifted.

A further increase of temperature caused an abrupt decrease of intensity of the CD spectrum, that became nearly conservative with a minimum at 251 nm and a maximum at 276 nm: apparently the spectrum of the denatured nickelated polyAT as observed for $NiCl_2$ 10.0 mM at $I = 0.12$ (compare Fig. 1).

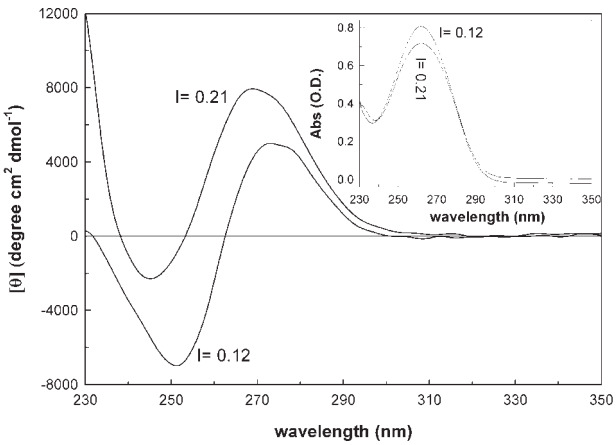

Fig. 2. CD spectra of the thermally modified polyAT in the quaternary w/o microemulsion at two different values (0.12 and 0.21) of the ionic strength. [polyAT] = 8.60×10^{-5} M in monomer units; $[NiCl_2]$ = 10 mM; $T = 336$ K. Inset. UV spectra of the same systems.

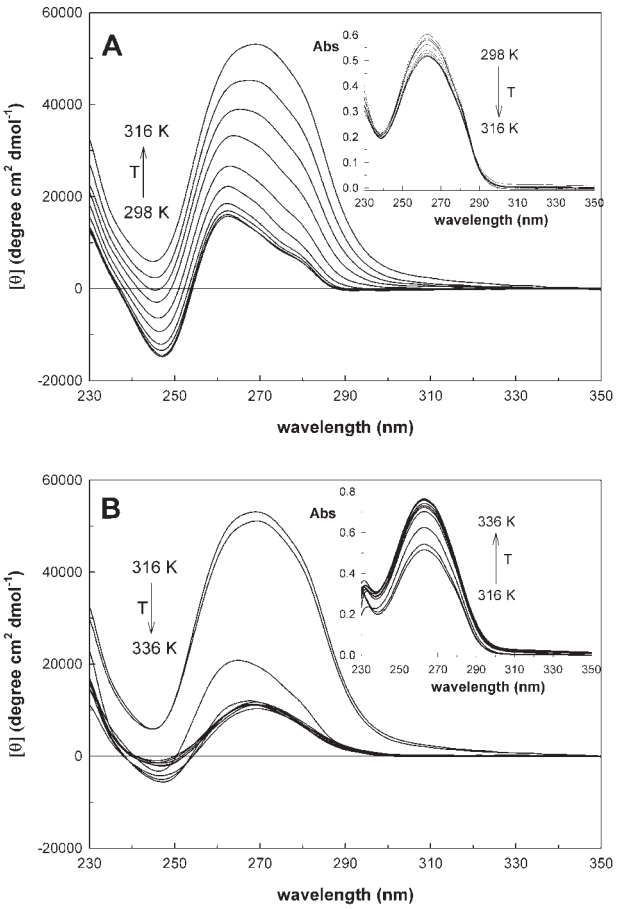

Fig. 3. Thermal behavior of polyAT in the quaternary w/o microemulsion. [polyAT] = 9.23×10^{-5} M in monomer units; [$NiCl_2$] = 20 mM; I = 0.21. (See text for details). Insets. UV spectra of the same system.

However, while in the latter case, denaturation was reversible, i.e. lowering of the temperature restored the initial UV and CD spectra, this did not occur in the former case. For such samples, on cooling below the melting temperature, a different form of polyAT was observed, characterized by high intensity CD spectra and UV spectra exhibiting the same hyperchromism of the denatured polynucleotide.

Effects of $NiCl_2$ on PolyGC

The CD spectrum at 293 K of polyGC in the CTAB|*n*-hexane|*n*-pentanol|water microemulsion in the presence of $NiCl_2$ 1.0 mM (no NaCl) exhibited the characteristic pattern of the canonical B form (minimum at 252.2 ± 0.4 nm; less intense maximum at 273 ± 1 nm with a shoulder at ca. 291 nm). When the I value of the aqueous core of the microemulsion was raised, and adjusted to the selected values by addition of NaCl, the CD spectra suggested conformational deviations from the B double helix. At all I values, the electronic absorption spectrum presented the expected band centered at 257 nm; its absorbance decreased ~7–10% upon increasing the temperature while a shoulder developed at longer wavelengths (285–290 nm). Temperature effects, dependent on I value, were observed at constant 1.0 mM $NiCl_2$ in the CD spectra.

In the absence of added NaCl, a thermal transition starts around 325 K leading to the Z form of polyGC, as indicated by the characteristic minimum developing at 294.2 ± 0.4 nm and a more pronounced maximum at 269 ± 1 nm (Fig. 4). The existence of a well defined isoelliptic point at 281.0 ± 0.4 nm implies an equilibrium between the two forms.

At increasing I, the thermal evolution of both CD an UV spectra pointed to a conformational transition to the Z form, starting at a temperature that increased with the I value and was in any case close to the upper limit of the explorable temperature range. Consequently, the complete transition could never be recorded, at variance with the observation in the absence of NaCl.

However, since the B- to Z-transition is known to be slow,[7,46,47] the time evolution of the high temperature spectra was followed for some samples.

Indeed, the amount of Z-form does increase with time, to eventually become the only one present in some cases, as shown in Figure 5 for I = 0.12.

The dependence of the thermal stability on the $NiCl_2$ concentration, at constant I, was also investigated. The I value of 0.21 was chosen to allow for a larger range of nickel concentrations. At 293 K, the CD spectra suggested a B-DNA (see Fig. 6) or, possibly, partially C-DNA,[48–52] type of conformation for the polynucleotide when the $NiCl_2$ concentration was 1.0 or 2.0 mM, while at metal concentrations 3.0 and 5.0 mM the spectral pattern hinted to the simultaneous presence of B- and Z-forms.

Indeed, the spectra exhibited a minimum at about 252 nm, a maximum centered at 272 nm and a second minimum at 293 nm, characteristic of the Z-form[36,52–54] and closely resembled those calculated as the sum of B- and Z-polyGC spectra, mixed in different proportions.[53] For $NiCl_2$ concentrations in the range 10.0–70.0 mM, the CD spectra (Fig. 6), with two minima centered at 256 and 291 nm, suggested the simultaneous presence of the polynucleotide in the C-form and in one of the Z-family exhibiting a single minimum at about 293 nm.[53] At all nickel concen-

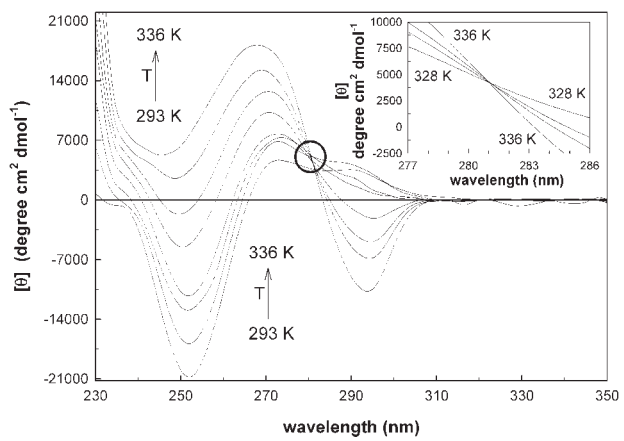

Fig. 4. Thermal behavior of polyGC in the quaternary w/o microemulsion. [polyGC] = 1.06×10^{-4} M in monomer units; [$NiCl_2$] = 1.0 mM; I = 0.003. Inset. The isoelliptic point at 281.0 nm.

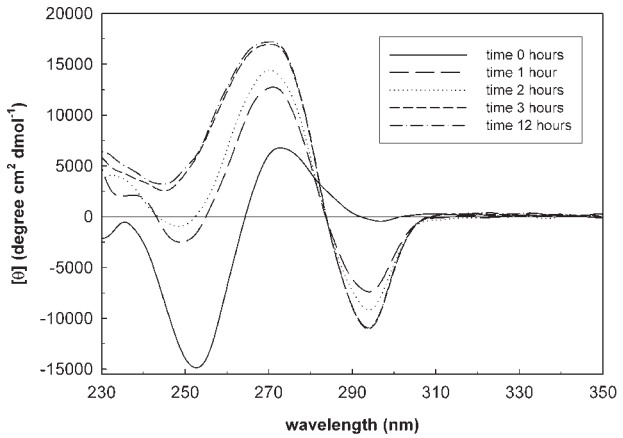

Fig. 5. Time evolution of the high temperature spectra of polyGC in the quaternary w/o microemulsion. [polyGC] = 1.01×10^{-4} M; [$NiCl_2$] = 1.0 mM; $I = 0.12$.

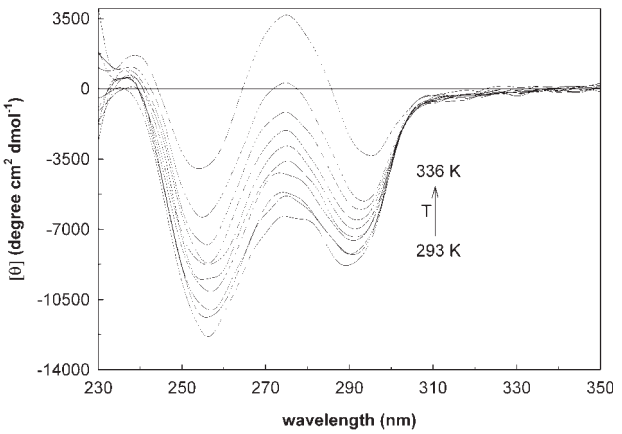

Fig. 7. Thermal behavior of polyGC in the quaternary w/o microemulsion. [polyGC] = 1.03×10^{-4} M in monomer units; [$NiCl_2$] = 70.0 mM; $I = 0.21$.

trations, both the CD and the electronic absorption spectra underwent marked changes, upon increasing the temperature, and the high temperature spectra evolved with time.

At 1.0 and 2.0 mM $NiCl_2$ concentrations the temperature-induced changes were a hypochromic effect in the UV spectrum (7.0 and 16.5%, respectively) and a change of the CD spectrum towards that of the Z-DNA form. The time evolution of the high temperature (336 K) spectra suggested an increase of the Z conformer, but no isoelliptic point was detectable.

At higher $NiCl_2$ concentrations, 10.0–70.0 mM, the temperature-induced changes were even less easily rationalized. In the Figures 7 and 8 the temperature and, respectively, the time CD spectral evolution are shown for a $NiCl_2$ concentration 70.0 mM, as an example.

The changes of the electronic absorption spectra, on the other hand, were not very conspicuous: the main feature was the increase of the ratio of absorbances at 290 nm (where an evident shoulder developed) and at 257 nm (where an hypochromic effect of ~8%, becoming 14% with time).[55] Scattering at $\lambda > 300$ nm, ascribable to sedimentation of aggregates[14,15,35,56,57] was never observed.

DISCUSSION AND CONCLUSIONS

Effects of $NiCl_2$ on PolyAT

The effects of $NiCl_2$ on the thermal stability of polyAT in aqueous solution[35] are consistent with the borderline nature of the metal, i.e. a stabilization is observed at low concentrations due to preferential binding of the metal cations to the phosphate groups, while destabilization and formation of aggregates occurs at high concentrations. This is reflected in the values of T_m, when, at a given ionic strength, $NiCl_2$ replaces NaCl (Table 1).

At variance, in microemulsion, even low concentrations of $NiCl_2$ destabilize the double helix and, in many cases, lead to melting at temperatures lower than in the matched aqueous solutions (Table 1).

Such destabilizing effect is even more surprising when one considers that thermal melting of polyAT in micro-

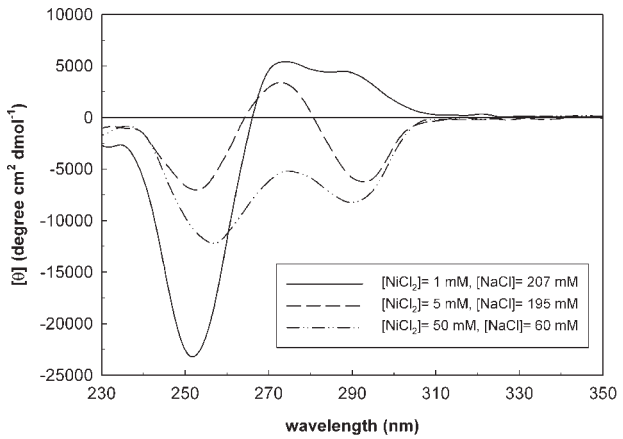

Fig. 6. Dependence of the conformation of polyGC in the quaternary w/o microemulsion on the $NiCl_2$ concentration at constant ionic strength ($I = 0.21$). [polyGC] = 1.03×10^{-4} M in monomer units; $T = 293$ K.

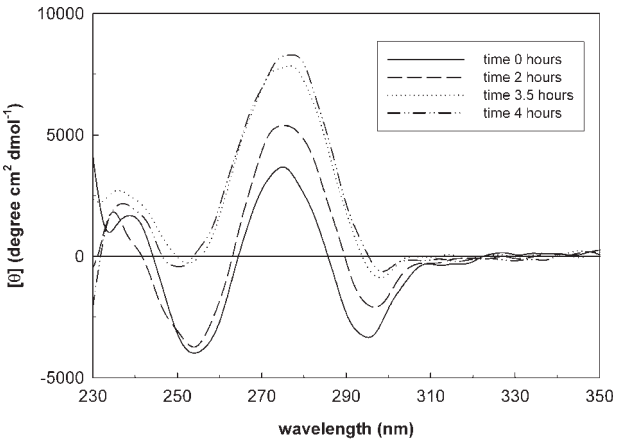

Fig. 8. Time evolution of the high temperature spectra ($T = 336$ K) of polyGC in the quaternary w/o microemulsion. [polyGC] = 1.03×10^{-4} M in monomer units; [$NiCl_2$] = 70 mM; $I = 0.21$.

emulsion, in the absence of nickel, cannot be observed even at NaCl concentrations as low as 10.0 mM, where in aqueous solution melting occurs at 317.5 K.[34]

However, even in microemulsion, when the observed temperature-induced transition is really melting, an increase of the nickel concentration leads to lower values of T_m, in agreement with the literature reports on the effects of multivalent cations on polynucleotides in aqueous solution.[15,58]

Consistent with the known behavior in aqueous solution is also the T_m increase observed at increasing I, when the $NiCl_2$ concentration is kept constant (Table 1). However, this is true at low values of I and $NiCl_2$ concentration, while the experimental thermal behavior of polyAT is not so easily interpretable when I and the nickel concentrations are increased. The anomalies begin at $I = 0.12$ and become more marked at $I = 0.21$. Thus, the melting temperature of polyAT for a 20.0 mM $NiCl_2$ concentration at $I = 0.12$, is lower than at $I = 0.06$: this can be accounted for only considering the behavior at higher ionic strength (vide infra). When at the same I value, the nickel concentration was raised at 30.0 mM, after the melting transition a decrease of both the absorbance at the maximum and of the CD spectra was recorded. Such spectral changes can be ascribed to the formation of a small amount of sediment, probably comprised of condensed structures. It is indeed well documented the aggregation of the thermally denatured DNA in the presence of divalent cations, not only soft or borderline, but even hard, by formation of interstrand bonds.[14,15,59,60] The aggregates, once formed, would leak from the reverse micelles due to their dimensions.

At ionic strength 0.21, the variable temperature behavior is consistent with the findings obtained at lower I values only for low $NiCl_2$ concentrations (1.0 and 5.0 mM), while, as already mentioned, the thermal transition observed at 10.0 mM nickel concentration is not the double helix-to-coil melting. Some clues to infer the nature of the transition can be gained from the findings obtained at higher nickel concentrations.

The prominent CD maximum recorded for 20.0 mM nickel concentration at temperatures intermediate between room and melting, suggests the formation of either an A-form of polyAT or Ψ(+) aggregates,[61–67] both exhibiting a strong CD maximum, at 260 nm for the canonical A-form of polyAT[65] and at about 280 nm for the Ψ(+) form obtained in the ethanol (33.6%)-$NaClO_4$ (0.61 M) solvent at 267 K.[63] However it is well known that the A-form of polyAT can be obtained only at low temperatures[61] and that the B-to-A transition is inhibited by even very low concentrations of nickel.[63] A typical feature of the A-form, in addition, is a strong CD minimum in the region 210–220 nm.[63] In microemulsion, the region below 230 nm cannot be explored, but the appearance of our spectra would suggest, instead, the growth of a strong positive band in that spectral region, in analogy with what has been reported for the Ψ(+) aggregates.[63,67] It is, therefore, reasonable to assign the first temperature-induced conformational change to the transition from a B-family double helix to a Ψ(+) compact form of polyAT, while the second thermal process can be identified as the melting of the Ψ(+) aggregates to yield the denatured polynucleotide.

A similar sequence of temperature-induced changes was observed at 30.0 mM nickel concentration, but the transition to the Ψ(+) form was not yet completed when the abrupt melting occurred.

It is worth noting (Table 1) that the conformational transition occurs at the same temperature for $NiCl_2$ concentrations 20.0 and 30.0 mM, while the melting temperature is higher when the metal concentration is higher. Since the Ψ(+) aggregates are favored and stabilized by interhelix bonds, made possible by the presence of divalent cations, it is reasonable to assume that the number of such bridges would increase with the metal concentration and thus lead to a higher T_m value.

When the nickel concentration increases (50.0 and 70.0 mM), the B-family to Ψ(+) transition temperature, that seems to be independent on the metal concentration, and T_m of polyAT duplex, that decreases with $NiCl_2$ concentration, approach one another and the two transitions become competitive. Thus, while at 50.0 mM nickel the beginning of the B-to-Ψ(+) transition was observed, at 70.0 mM nickel only the double helix-to-coil melting was recorded at a temperature consistent with the destabilizing effect of high nickel concentrations.[15,58]

Effects of $NiCl_2$ on PolyGC

It is well known that polynucleotides containing GC sequences tend to assume the Z-DNA conformation.[11] Z-type structures are favored by low water activity and by divalent cations; in particular, Ni^{+2} ions are well known inducers of the B–Z transition.[18,36,40,46,56,68,69] The aqueous microdomain of w/o microemulsions should be a very favorable medium for the formation of Z-structures, since the endomicellar water has activity and dielectric constant much lower than bulk water.[70–73] Indeed, in w/o microemulsion, in the absence of added NaCl, 10.0 mM $NiCl_2$ induces the B-to-Z transition of polyGC, when the temperature is increased (see Fig. 4), even though the Z-form of nickelated polyGC has CD spectral features appreciably different from the Z-form in the absence of the metal (see Fig. 9). At higher I values, and $NiCl_2$ 10.0 mM, the room temperature CD spectra would suggest a shift of the B-form towards a C-DNA form.[49]

The C-DNA, found in fibers at low relative humidity, is generally considered a right-handed overwound helix[48]; yet, some authors have suggested for C-DNA a left-handed helix conformation.[50,51] Such, possibly partially C, form undergoes a thermal transition towards the Z-DNA form, but more slowly and at higher temperature than in the absence of NaCl. The time evolution of the high temperature Z-form leads to a CD spectrum where the maximum has a higher amplitude than the minimum (see Fig. 5), at variance with the Z-form. The thermal and time evolution of the CD spectra at higher $NiCl_2$ concentration ($I = 0.21$) might suggest a rationale for such behavior. The CD spectra, that at room temperature seem to arise from a mixture of B (or partially C) and Z-form of polyGC, evolve with temperature to spectral patterns reminiscent of Z′ polyGC.[46,53,63] Such conformation has been reported for

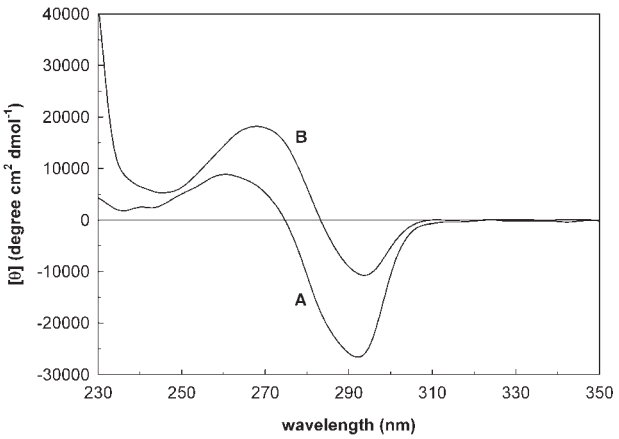

Fig. 9. Z-form of polyGC in the quaternary w/o microemulsion in the absence (**A**) and in the presence (**B**) of 1.0 mM $NiCl_2$.

polyGC solutions at high ethanol (85%) or methanol (88%) content[53] or for 85% ethanol solutions in the presence of multivalent cations. Isomerization to Z′ form of polyAT and of poly(dA-dC)·poly(dG-dT) has been induced in aqueous solution of ethanol (15 and 28%, respectively)-$NaClO_4$ (4.3 and 3 M, respectively) by addition of submillimolar concentrations of $NiCl_2$.[63] Thus, Z′ structures of polynucleotides have been observed in media of low water activity and dielectric constant largely smaller than that of bulk water. Such medium characteristics are well matched by endomicellar water, especially at fairly high I values. Thus, we confidently attribute the CD spectra, $I = 0.21$ and high nickel concentrations to Z′ forms of polyGC. One point worth of notice of such $NiCl_2$ -induced conformational transitions is that they occur at temperatures near 273 K in solution, while in microemulsions they are prompted by a temperature increase.

CONCLUSIONS

The above discussed results evidence once more the basic difference between solution and microemulsion behavior of polynucleotides. The most interesting feature is the variety of conformations elicited by $NiCl_2$ in microemulsion, both for polyAT and polyGC that are not found in solutions of matched composition. Some of such conformations appear to exist in a very limited range of medium composition, as, for instance, the Ψ(+) form of polyAT, observed only at $I = 0.21$, nickel concentration in the range 20.0–50.0 mM and temperatures between room and about 313 K. Such finding, however, is not anomalous since the Ψ(+) form in solution has been observed only in special conditions, namely temperatures near 273 K and perchlorate-ethanol solutions[63] or in the presence of trivalent cations.[66] Moreover, in solution, the Ψ(+) form is very unstable and can easily be transformed in the Ψ(−) aggregates by increasing the temperature from 267 to 284 K (in perchlorate-ethanol solutions)[63] or by mere mechanical stirring.[66]

In microemulsion the Ψ(+) form of polyAT, while observed only in a very limited range of conditions, is stable and does not convert to Ψ(−) aggregates or other condensed form that would give scattering or sedimentation. Even for polyGC, the Z′ form has been observed only in ethanol[53,74] or methanol[53] rich solutions, the several forms of the Z-family in trifluoroethanol rich (66–78%) water solutions[52] and the C-form in 3.8 M LiCl solution.[49]

It is worth of comment that Z and Z′ forms could be induced in microemulsion for polyGC but not for polyAT. It is well known that in solution transitions to left-handed forms can be observed for polyGC under a large range of experimental conditions,[6,7,18,36,46,47,53–55,65,68,74–77] whereas such transitions have been reported for polyAT only in a limited number of cases. Thus, the Z′-DNA form of polyAT has been observed only in ethanol(15%)-$NaClO_4$ (4.3 M) solutions in the presence of $\geq$0.87 mM $NiCl_2$ at 271 K.[63] The Z-DNA form, on the other hand has been identified either in films,[78,79] typically at low water content (RH 76%), high polynucleotide concentration, and in the presence of two Ni^{2+} per nucleotide,[78] or in solution at 5 M NaCl/95 mM $NiCl_2$ with polyAT concentration of 1 OD/μl.[80] The B-to-Z transition of polyAT in solution requires the combined effect of high sodium chloride and $NiCl_2$ in a very narrow range of concentrations (85–95 mM).[80–82] It is possible that stringent conditions of similar type are required also in microemulsion for the Z-DNA form of polyAT to occur, and were not met in any of the systems investigated.

Therefore the most interesting aspect of the rich nickel-induced variety of polymorphs in microemulsion is that they all occur in the same aqueous medium and at not very high salt concentrations. Certainly the peculiar characteristics of the aqueous compartment of the w/o microemulsions[70–73] resemble those of aqueous solutions rich in alcohol or with high salt concentrations, but they are also similar to those of the water near biological membranes.

The results presented here, therefore, might be relevant to tackle the problem of the reactivity of DNA packed in the eukaryotic cell nuclei or superpackaged in the chromatin of cells in metaphase.

Another point which is worth of comment is the temperature range where some conformations have been observed, in particular the Ψ(+) compact form of polyAT. In solution, Ψ(+) has only been observed at temperatures near 273 K, while in microemulsion the B-to- Ψ(+) transition occurs around the physiological temperature of 310 K, and denaturation at $T > 313$ K.

Therefore, even the Ψ(+) conformation could be biologically significant.

The results presented here suggest once more that the use of w/o microemulsions as models of the endocellular compartment would be appropriate when studying the reactivity and the conformational stability of DNA.

LITERATURE CITED

1. Jovin TM, Soumpasis DM, Mc Intosh LP. The transition between B-DNA and Z-DNA. Annu Rev Phys Chem 1987;38:521–560 and references therein.
2. Ivanov VI, Krylov DY. A-DNA in solution studied by diverse approaches. In: Lilley DMJ, Dahlberg JE, editors. Methods in enzymology, Vol. 211. San Diego, CA: Academic Press; 1992. p 111–126.

3. Jovin TM, Rippe K, Ramsing NB, Klement R, Elhorst W, Voijiliskova M. Parallel stranded DNA. In: Sarma RH, Sarma MH, editors. Structure and methods, Vol. 3. Guilderland, NY: Adenine Press; 1991. p 155–174.
4. Robinson H, van der Marel GA, van Boom JH, Wang AHJ. Unusual DNA conformation at low pH revealed by NMR: parallel-stranded DNA duplex with homo base pairs. Biochemistry 1992;31:1051–1057.
5. Suresh Kumar G, Maiti M. DNA polymorphism under the influence of low pH and low temperature. J Biomol Struct Dyn 1994;12:183–201.
6. Segers-Nolten GMJ, Sijtsema NM, Otto C. Evidence for Hoogsteen GC base pairs in the proton-induced transition from right-handed to left-handed poly(dG-dC)·poly(dG-dC). Biochemistry 1997;36:13241–13247 and references therein.
7. Gonzales VM, Fuertes MA, Perez JM, Alonso C. Kinetics of the salt-induced B- to Z-DNA transition. Eur Biophys J 1998;27:417–423.
8. Denisov VP, Carlström G, Venu K, Halle B. Kinetics of DNA hydration. J Mol Biol 1997;268:118–136 and references therein.
9. Berman HM. Hydration of DNA. Curr Opin Struct Biol 1994;4:345–350.
10. Kochoyan M, Leroy JL. Hydration and solution structure of nucleic acids. Curr Opin Struct Biol 1995;5:329–333.
11. Bloomfield VA, Crothers DM, Tinoco I Jr. Nucleic acid: Structures, properties, and functions. Sausalito, CA: University Science Book; 2000.
12. Spiro TG. Metal ions in biology, Vol. 1. New York, NY: Wiley; 1980.
13. Eichhorn GL. Inorganic biochemistry, Vol. 2. Amsterdam, NL: Elsevier; 1973. Chapter 34.
14. Duguid J, Bloomfield VA, Benevides J, Thomas GJ Jr. Raman spectroscopy of DNA-metal complexes. Interactions and conformational effects of the divalent cations Mg, Ca, Sr, Ba, Mn, Co, Ni, Cu, Pd, and Cd. Biophys J 1993:65;1916–1928.
15. Duguid J, Bloomfield VA. Aggregation of melted DNA by divalent metal ion-mediated cross linking. Biophys J 1995;69:2642–2648.
16. Sigel A, Sigel H, editors. Metal ions in biological systems, Vol. 32. New York: Marcel Dekker; 1996.
17. Sigel A, Sigel H, editors. Metal ions in biological systems, Vol. 33. New York: Marcel Dekker; 1996.
18. Rossetto FE, Nieboer E. The interactions of metal ions with synthetic DNA: induction of conformational and structural transitions. J Inorg Biochem 1994;54:167–186.
19. Fasman GD. Histone-DNA interactions: circular dichroism studies. In: Li HJ, Ekhard RA, editors. Chromatin and chromosomes structure. New York: Academic Press; 1977. p 71–142.
20. Lerman LS. Polymer and salt-induced condensation of DNA. In: Duchesne J, editor. Physical chemical properties of nucleic acids. London, UK: Academic Press; 1973. p 59–76.
21. Podestà A, Indrieri M, Bragioli D, Manning GS, Milani P, Guerra R, Finzi L, Dunlap D. Positively charged surfaces increase the flexibility of DNA. Biophys J 2005;89:2558–2563.
22. Luisi PL, Giomini M, Pileni MP, Robinson BH. Reverse micelles as hosts for proteins and small molecules. Biochim Biophys Acta 1988;947:209–246.
23. Walde P, Giuliani AM, Boicelli CA, Luisi PL. Phospholipid-based reverse micelles. Chem Phys Lipids 1990;53:265–288.
24. Fendler JH. Membrane mimetic chemistry. New York: Wiley; 1982.
25. Moulik SP, Paul BK. Structure, dynamics and transport properties of microemulsions. Adv Colloid Interface Sci 1998;78:99–195.
26. Evans DP, Wennerström H. The colloidal domain, 2nd ed. New York: Wiley-VCH; 1999.
27. Luisi PL, Walde P, Oberholzer T. Enzymatic RNA synthesis in self-reproducing vesicles: an approach to the construction of a minimal synthetic cell. Ber Bunsen Ges Phys Chem 1994;98:1160–1165.
28. Palazzo G, Lopez F, Giustini M, Colafemmina G, Ceglie A. Role of the co-surfactant in the CTAB/n-pentanol/n-hexane/water water-in-oil microemulsion. 1. Pentanol effect on the microstructure. J Phys Chem B 2003;107:1924–1931.
29. Balestrieri E, Giomini M, Giustini M, Giuliani AM, Ceglie A. Spectroscopic study of polynucleotides in cationic w/o microemulsions. Progr Colloid Polym Sci 1999;112:89–92.
30. Airoldi M, Gennaro G, Giomini M, Giuliani AM, Giustini M. Alkaline titrations of poly(dG-dC)·poly(dG-dC): microemulsion versus solution behavior. J Biomol Struct Dyn 2007;24:561–569.
31. Airoldi M, Boicelli CA, Gennaro G, Giomini M, Giuliani AM, Giustini M. Acid titrations of poly(dG-dC)·poly(dG-dC) in aqueous solution and in w/o microemulsion. J Biomol Struct Dyn 2006;23:465–477.
32. Airoldi M, Boicelli CA, Cadoni F, Gennaro G, Giomini M, Giuliani AM, Giustini M. Titration of poly(dA-dT)·poly(dA-dT) in solution at variable NaCl concentration. Biopolymers 2004;75:118–127.
33. Airoldi M, Boicelli CA, Gennaro G, Giomini M, Giuliani AM, Giustini M, Scibetta L. Different factors affecting polyAT conformation in microemulsions: effects of variable P_0 and KCl concentration. Phys Chem Chem Phys 2002;4:3859–3864.
34. Airoldi M, Boicelli CA, Gennaro G, Giomini M, Giuliani AM, Giustini M. A spectroscopic study of poly(dA-dT)·poly(dA-dT) in microemulsions. Phys Chem Chem Phys 2000;2:4636–4641.
35. Airoldi M, Gennaro G, Giomini M, Giuliani AM, Giustini M. Interaction of the alternating double stranded copolymer poly(dA-dT)·poly(dA-dT) with $NiCl_2$ and $CdCl_2$: solution behavior. J Biomol Struct Dyn 2007;25:77–84.
36. Schoenknecht T, Diebler H. Spectrophotometric and kinetic studies of the binding of Ni^{2+}, Co^{2+}, and Mg^{2+} to poly(dG-dC)·poly(dG-dC). Determination of the stoichiometry of the Ni^{2+} induced B→Z transition. J Inorg Biochem 1993;50:283–298.
37. Giustini M, Palazzo G, Colafemmina G, Della Monica G, Giomini M, Ceglie A. Microstructure and dynamics of the water-in-oil CTAB/*n*-pentanol/*n*-hexane/water microemulsion: a spectroscopic and conductivity study. J Phys Chem 1996;100:3190–3198.
38. Vogel AI. Quantitative inorganic analysis, 3rd ed. London, UK: Longmans; 1961.
39. Gennis RB, Cantor CR. Optical studies of a conformational change in DNA before melting. J Mol Biol 1972;65:381–399.
40. Kankia BI. Hydration effects of Ni^{2+} binding to synthetic polynucleotides with regularly alternating purine-pyrimidine sequences. Nucl Acids Res 2000;28:911–916 and references therein.
41. Vorlíčková M, Kypr J. Conformational variability of poly(dA-dT)·poly(dA-dT) and some other deoxyribonucleic acids includes a novel type of double helix. J Biomol Struct Dyn 1985;3:67–83.
42. Jia X, Marzilli LG. Zinc ion-DNA polymer interactions. Biopolymers 1991;3:23–44.
43. Ivanov VI, Minchenkova LE, Schyolkina AK, Poletayev AI. Different conformations of double-stranded nucleic acid in solution as revealed by circular dichroism. Biopolymers 1973;12:89–110.
44. Chan SS, Breslauer KJ, Hogan ME, Kessler DJ, Austin RH, Ojemann J, Passner JM, Wiles NC. Physical studies of DNA premelting equilibria in duplexes with and without homo dA·dT tracts: correlations with DNA bending. Biochemistry 1990;29:6161–6171.
45. Airoldi M, Boicelli CA, Cadoni F, Gennaro G, Giomini M, Giuliani AM, Giustini M. PolyAT chemical denaturation in w/o microemulsion. Phys Chem Chem Phys 2004;6:1453–1457.
46. Harder ME, Curtis Johnson W Jr. Stabilization of the Z′ form of poly(dGdC)·poly(dGdC) in solution by multivalent ions relates to the Z form in crystals. Nucl Acids Res 1990;18:2141–2148.
47. Fuertes MA, Pérez JM, Gonzales VM, Alonso C. Kinetics of the salt-induced B- to Z-DNA transition. J Biol Inorg Chem 2001;6:675–682.
48. Neidle S. DNA structure and recognition. Oxford UK: Oxford University Press; 1994.
49. Sage E, Leng M. Conformational changes of poly(dG-dC)·poly(dG-dC) modified by the carcinogen N-acetoxy-N-acetyl-2-aminofluorene. Nucl Acids Res 1981;9:1241–1250.
50. Premilat S, Albiser G. Conformations of C-DNA in agreement with fiber X-ray and infrared dichroism. J Biomol Struct Dyn 1984;2:607–613.
51. Premilat S, Albiser G. DNA models for A, B, C and D conformations related to fiber X-ray, infrared and NMR measurements. J Biomol Struct Dyn 1986;3:1033–1043.

52. Ivanov VI, Minyat EE. The transition between left- and right-handed forms of poly(dG-dC)·poly(dG-dC). Nucl Acids Res 1981;9:4783–4798.
53. Hall KB, Maestre MF. Temperature dependent reversible transition of poly(dG-dC)·poly(dG-dC) in ethanolic and methanolic solutions. Biopolymers 1984;23:2127–2139.
54. Chen F-M. Base protonation facilitates B-Z interconversion of poly(dG-dC)·poly(dG-dC). Biochemistry 1984;23:6159–6165.
55. Pohl FM, Jovin TM. Salt-induced co-operative conformational change of a synthetic DNA: equilibrium and kinetic studies with poly(dG-dC)·poly(dG-dC). J Mol Biol 1972;67:375–396.
56. Sitko JC, Mateescu EM, Hausma HG. Sequence-dependent DNA condensation and the electrostatic zipper. Biophys J 2003;84:419–431.
57. Wells RD, Larson JE, Grant RC, Shortle BE, Cantor CR. Physicochemical studies on polydeoxyribonucleotides containing defined repeating nucleotide sequences. J Mol Biol 1970;54:465–497.
58. Eichhorn LG, Shin YA. Interaction of metal ions with polynucleotides and related compounds. XII. The relative effect of various metal ions on DNA helicity. J Am Chem Soc 1968;90:7323–7328.
59. Kejnovsky E, Kypr J. Millimolar concentration of zinc and other metal cations causes sedimentation of DNA. Nucl Acids Res 1998;26:5295–5299.
60. Knoll DA, Fried MG, Bloomfield VA. Heat-induced DNA aggregation in the presence of divalent metal salts. In: Sarma RH, Sarma MH, editors. Structure and expression, Vol. 2. Guilderland, NY: Adenine Press; 1988. p 123–145.
61. Kypr J, Sági J, Szakonyi E, Ebinger K, Peňázová H, Chládková J, Vorlíčková M. Thymine methyl groups stabilize the putative A-form of the synthetic DNA poly(amino2dA-dT). Biochemistry 1994;33:3801–3806 and references therein.
62. Malenkov G, Minchenkova L, Minyat E, Schyolkina A, Ivanov V. The nature of the B–A transition of DNA in solution. FEBS Lett 1975;51:38–42.
63. Vorlíčková M. Conformational transitions of alternating purine-pyrimidine DNAs in perchlorate ethanol solutions. Biophys J 1995;69:2033–2043.
64. Gray DM, Edmondson SP, Lang D, Vaughan M, Nave C. The circular dichroism and X-ray diffraction of DNA condensed from ethanolic solutions. Nucl Acids Res 1979;6:2089–2107.
65. Vorlíčková M, Subirana JA, Chládková J, Tejralová I, Huynh-Dinh T, Arnold L, Kypr J. Comparison of the solution and crystal conformation of (G+C)-rich fragments of DNA. Biophys J 1996;71:1530–1538.
66. Shin YA, Feroli SL, Eichhorn GL. Psi compaction of poly(dA-dT) poly(dA-dT). Biopolymers 1986;25:2133–2148.
67. Vorlíčková M, Sági M, Szabolcs A, Szemzö A, Ötvös L, Kypr J. Conformation of the synthetic DNA poly(amino2dA-dT) duplex in high-salt and aqueous alcohol solutions. Nucl Acids Res 1998;16:279–289.
68. Kypr J, Stěpán J, Chládková J, Vorlíčková M. Circular dichroism spectroscopy analysis of conformational transitions of a 54 base pair DNA duplex composed of alternating CGCGCG and TATATA blocks. Biospectroscopy 1999;5:253–262.
69. Vorlíčková M, Sági J. Transitions of poly(dI-dC), poly(dI-methyl5dC) and poly(dI-bromo5dC) among and within the B-, Z-, A- and X-DNA families of conformations. Nucl Acids Res 1991;19:2343–2347.
70. El Seoud OA. Acidities and basicities in reversed micellar systems. In: Luisi PL, Straub BE, editors. Reverse micelles. New York, NY: Plenum Press; 1984. p 81–93.
71. Gierasch LM, Thompson KF, Lacy JE, Rockwell AL. Exploring peptide interactions with interfacial water using reverse micelles. In: Luisi PL, Straub BE, editors. Reverse micelles. New York, NY: Plenum Press; 1984. p 265–277.
72. Wong M, Thomas JR, Novak T. Structure and state of water in reversed micelles. J Am Chem Soc 1977;99:4730–4736.
73. Wells MA. Nature of water inside phosphatidylcholine micelles in diethyl ether. Biochemistry 1974;13:4937–4942.
74. Pohl FM. Polymorphism of a synthetic DNA in solution. Nature 1976;26:365–366.
75. Rich A, Nordheim A, Wang AH-J. The chemistry and biology of left-handed Z-DNA. Annu Rev Biochem 1984;53:791–846.
76. Taboury JA, Bourtayre P, Liquier J, Taillandier E. Interactionn of Z form of poly(dG-dC)·poly(dG-dC) with divalent metal ions: localization of the binding sites by IR spectroscopy. Nucl Acids Res 1984;12:4247–4258.
77. Zacharias W, Martin JC, Wells RD. Condensed form of $(dG\text{-}dC)_n$.$(dG\text{-}dC)_n$ as an intermediate between the B- and Z-type conformation induced by sodium acetate. Biochemistry 1983;22:2398–2405.
78. Adam S, Liquier J, Taboury JA, Taillandier E. Right- and left-handed helixes of poly[d(A-T)].poly[d(A-T)] investigated by infrared spectroscopy. Biochemistry 1986;25:3220–3225.
79. Adam S, Bourtayre P, Liquier J, Taillandier E. Interaction of transition metal ions with Z form of polyd(A-C)·poly d(G-T) and poly d(A-T) studied by IR spectroscopy. Nucl Acids Res 1986;14:3501–3513.
80. Bourtayre P, Liquier J, Pizzorni L, Taillandier E. Z Form of poly d(A-T) poly d(A-T) in solution studied by CD and UV spectroscopies. J Biomol Struct Dyn 1987;5:97–104.
81. Ridoux JP, Liquier J, Taillandier E. Raman spectroscopy of Z-form poly [d(A-T)] poly[d(A-T)]. Biochemistry 1988;27:3874–3878.
82. Miskovsky P, Chinsky L, Laigle A, Turpin PY. The Z-conformation of poly d(A-T) poly d(A-T) in solution as studied by ultraviolet resonance Raman spectroscopy. J Biomol Struct Dyn 1989;7:623–637.

CHIRALITY 20:961–968 (2008)

Photoelectron Circular Dichroism: Chiral Asymmetry in the Angular Distribution of Electrons Emitted by (+)-*S*-Carvone

IVAN POWIS*

School of Chemistry, The University of Nottingham, University Park, Nottingham, United Kingdom

Presented at the 11th International Conference on Circular Dichroism, 2007, Groningen, Netherlands.

ABSTRACT The technique of photoelectron circular dichroism (PECD) is introduced and illustrated by the presentation of results obtained for the C 1*s* core ionization of (+)-*S*-carvone enantiomers. Using circularly polarized ionizing radiation, large chiral effects in the angular distribution of photoelectrons emitted from a dilute, randomly oriented gas phase sample can be detected. This effect is predicted in the pure electric dipole approximation and is expected to be quite general. The forward–backward asymmetry regularly exceeds 10%, as demonstrated here for the carbonyl C 1*s* photoemission of carvone. Calculations are presented that reveal a pronounced dependence of this effect on molecular conformation. In the case of carvone the PECD associated with the C 1*s* electron localized at the carbonyl group varies with orientation of the isopropenyl tail group at the opposite end of the molecule. Comparisons of calculations with experiment confirm the molecular configuration and permit inferences to be drawn concerning the relative conformer populations in the experimental sample. *Chirality 20:961–968, 2008.*

KEY WORDS: photoionization; photoelectron spectroscopy; synchrotron radiation; molecular conformation; core electrons; photoemission

INTRODUCTION

Photoelectron circular dichroism (PECD) is a relatively new technique that is based upon the measurement of chiral asymmetries in the angular distribution of photoelectrons emitted following ionization by a beam of circularly polarized radiation. Perhaps the most remarkable feature of this photoemission asymmetry is that it is already present in the lowest order, pure electric dipole approximation; no recourse to higher order interactions in the photon-molecule interaction (i.e., neither electric quadrupole, nor magnetic dipole terms) is required to explain the phenomenon. Consequently, since the effect was first predicted[1] it was always anticipated that it would be large. The first fully realistic calculations suggested that asymmetry factors of the order of a few 10% should be expected, a prediction which has subsequently been borne out by experiment in a number of different molecules.[2–11]

As a form of photoelectron spectroscopy, PECD is naturally performed under vacuum conditions using vapour phase samples of randomly oriented molecules; either at low pressure ($\leq 5 \times 10^{-5}$ mbar) in a gas cell or effusive jet, or in a supersonic molecular beam in the spectrometer interaction region. In either case the sample molecules are effectively isolated, noninteracting and nonsolvated. The absence of solvent permits the possibility to examine the intrinsic molecular conformation and removes solvent interference effects. An enormous range of photon energies, from near the photoionization threshold (typically ~8 eV) through to the soft X-ray region (500 eV or more) can therefore be used, with a correspondingly rich variety of behavior observed. The combination of energy and angular measurement of the photoelectrons provides for PECD phenomena to be resolved into contributions made by individual initial orbitals.[8,9,11]

The exceptional size of PECD asymmetry factors, several orders of magnitude greater than typically encountered in normal CD measurements made with isolated molecules (i.e., in the absence of cooperative condensed phase enhancement mechanisms) suggests that high sensitivities are potentially achievable. However, it should be stressed that this arises from the ability of the technique to provide angular resolution of the final state wave function. Once integration over all possible photoemission directions takes place, as in a total cross-section measurement, the enhanced PECD asymmetry is lost. Conventional circular dichroism may persist in the angle-integrated photoionization cross-section, just as in bound-bound photoabsorption measurement, but with the anticipated strength reduced by orders of magnitude.

*Correspondence to: I. Powis, School of Chemistry, The University of Nottingham, University Park, Nottingham NG7 2RD, UK.
E-mail: ivan.powis@nottingham.ac.uk
Received for publication 8 November 2007; Accepted 6 December 2007
DOI: 10.1002/chir.20537
Published online 19 February 2008 in Wiley InterScience (www.interscience.wiley.com).

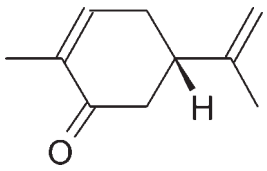

Scheme 1. *S*-carvone.

There are clear indications that PECD measurements, particularly when spanning a range of energies and/or different orbital ionizations, may be strongly sensitive to molecular geometry, and thus able to differentiate between alternative molecular conformations.[7,11–13] At the same time the successful application of theoretical models to treat the experimental data provides clear evidence that not just molecular conformation, but also absolute configuration could be assigned with such experimental data.

In the following the author outlines the basis for the phenomenon and its theoretical treatment and then provides an example to demonstrate principal features of the technique that draws upon a fresh analysis of results obtained for the C 1*s* ionization of *S*-carvone ($C_{10}H_{14}O$-Scheme 1). It might be thought that measurements made with core electrons were unpromising territory for the study of molecular chirality; an initial 1*s* orbital is spherical (achiral) and localized. As such it must be very largely uninfluenced by the handedness of the molecular framework within which it is located, especially so when, as in carvone, it is localized at some distance from the asymmetric carbon centre. Nevertheless, core level PECD[4,7] has been found to be at least comparable in magnitude to typical valence shell results.[8,9,11]

PECD

The quite general expression, in the electric dipole approximation, for the normalized angular distribution of photoelectron flux in a single photon ionization takes the phenomenological form:

$$I_p(\theta) = 1 + b_1^p P_1(\cos\theta) + b_2^p P_2(\cos\theta) \quad (1)$$

where P_n is the nth order Legendre polynomial and the coefficients b_n^p depend on the photoionization dynamics as well as on the polarization (or photon helicity), p. For linear polarization ($p = 0$) the laboratory frame direction, θ, is understood to be measured from the electric vector axis, while for circularly polarized light (CPL), or for an unpolarized beam of light, it is appropriate to measure θ from the light beam propagation direction.

Theoretical analysis[1,14] of the electric dipole photon-molecule interaction indicates that the coefficients b depend on summations over complex expressions involving various angular momentum coupling terms and the radial electric dipole matrix elements. The former dictates various symmetry properties for the b coefficients.

Of principal interest here is that the b_1^p coefficient must vanish for all but CPL, but will be then antisymmetric (change sign) with respect to a switch between positive and negative helicity radiation i.e., from left ($p = +1$) to right ($p = -1$) handed CPL. This is not, however, sufficient as the photoionization matrix elements that have opposite projections of angular momentum must be inequivalent, otherwise there will be a self-cancellation over the full summation. In other words, only for chiral molecules ionized with CPL does the additional 1st Legendre polynomial term (simply a cosine function) appear in the angular distribution. But when it does it, the odd inversion character of the cos θ term implies a forward–backward asymmetry in the angular distribution relative to the direction of the photon beam. In addition, from angular momentum considerations[1,14] it may be shown that $b_1^{\{+1\}} = -b_1^{\{-1\}}$ for a given molecular enantiomer and that b_1^p will also swap sign with exchange of enantiomer. Thus the dissymmetry in the angular distribution should reverse on swapping the handedness of either the light or the molecule.

These properties of the angular distribution mean that there exists a circular dichroism in the angle resolved photoemission. A PECD asymmetry factor, Γ, can hence be defined using eq. 1 for a given enantiomer as:

$$\Gamma(\theta) = I_L(\theta) - I_R(\theta) = 2b_1^{\{+1\}}\cos\theta \quad (2)$$

Here I_L and I_R refer respectively to distributions obtained with left- and right-handed CPL. As a special case the PECD in the forward direction, $\theta = 0^\circ$, is then just:

$$\Gamma_0 = (I_L(0) - I_R(0)) = -(I_L(180) - I_R(180)) = 2b_1^{\{+1\}} \quad (3)$$

Alternatively, a quantitative measure of the photoelectron angular asymmetry for a given enantiomer and light helicity, p, can be defined from eq. 1 as the difference in the electron fluxes through equal area elements on the unit sphere in the 0° and 180° directions normalized to the mean flux through an area element (average over the whole sphere) as

$$G_{AD} = |I_p(0)\sin\theta\ d\theta\ d\varphi - I_p(180)\sin\theta\ d\theta\ d\varphi/\sin\theta\ d\theta\ d\varphi| = |2b_1^p|. \quad (4)$$

The PECD and angular asymmetry factors are thus seen to be essentially equivalent, but provide alternative approaches to measure the chiral b_1^p parameters. In principle, G_{AD} can be determined with a single light polarization and measurements taken at two or more angles. Nevertheless, it is usually convenient to measure the dichroism at one or more detection angles using alternate left- and right CPL, as this approach can be used to achieve cancellation of instrumentally induced asymmetry (for example any angular variation in electron detection sensitivity).

Equation 1 will undoubtedly be more familiar without the middle P_1 term, given the far more common circumstances where linearly polarized radiation and/or achiral molecules are investigated. In such cases $b_1^0 = 0$ and the 2nd Legendre polynomial coefficient can be readily identified with the familiar β anisotropy parameter; more completely the relationships are: $\beta = b_2^0 = -2b_2^{\{\pm1\}} = -2b_2^{unpol}$.

EXPERIMENTAL DETAILS

The experiments were made at the UE56/2 beamline at the BESSY II synchrotron radiation facility (Berlin). This beamline has twin undulators that may be set to produce CPL of opposite handededness.[15] A mechanical chopper arrangement is then used to provide 0.1 Hz switching between alternate polarizations at the experimental station. In this experimental chamber the photon beam passes through a heated gas cell (80°C) containing a vapour of (+)-*S*-carvone (Aldrich 96%) from which electrons are extracted into an electron analyser. Background pressures in the system are $\leq 10^{-6}$ mbar. The hemispherical electron analyser system accepts electrons at 54.7° to the photon beam propagation direction. A potential experimental difficulty lies in the need to normalize the experimental counts rather than work directly with eq. 2. For example:

$$\Gamma(\theta) = (N_{+1}I_{+1}(\theta) - N_{-1}I_{-1}(\theta)) \\ /((N_{+1}I_{+1}(\theta) + N_{-1}I_{-1}(\theta))/2) \quad (5)$$

Assuming that the sampling conditions are set or compensated so that the angle integrated counts are comparable, i.e., $N_{+1} = N_{-1}$, the expected form of the angular distribution, Eq. 1, implies that the denominator will still depend on the (probably unknown) $b_2^{\{\pm 1\}}$ coefficients, impeding the extraction of the chiral $b_1^{\{\pm 1\}}$ parameters from the measured $\Gamma(\theta)$. However, the particular choice of $\theta = 54.7°$, the so-called magic angle at which $P_2(\cos\theta) = 0$, means that the measured data will be independent of $b_2^{\{\pm 1\}}$, and consequently $b_1^{\{\pm 1\}}$ can be independently determined at this measurement angle.

Full experimental details and an explanation of the data analysis needed are given in a previous paper.[7]

COMPUTATIONAL DETAILS

The evaluation of the angular distribution parameters, b_J^p, requires the calculation of the electric dipole matrix elements for the ionization process.[14] A feasible approach for doing this, applicable to molecules of the size of typical chiral species, is the continuum multiple scattering model, using the Xα local-exchange potential (CMS-Xα).[16,17] This computational method for obtaining photoionization matrix elements has been described in the context of molecule-frame photoelectron angular distributions for polyatomic systems[18,19] and was subsequently extended to treat arbitrary light polarization states and, specifically, the estimation of PECD parameters.[14,20]

In the present work we update previous calculations made for the carvone molecule.[7,12] CMS-Xα calculations are made using model potentials that subdivide the molecule into overlapping spherical regions centred at each atomic site, the positions of these atomic centres being obtained from MP2/6-31G(p,d) optimized geometries. For the new work the atomic sphere radii have been taken from the optimized values suggested by Takai and Johnson,[21] however, the H atom radius suggested by this source leads to excessive overlap of the central carbon atom in tetrahedral geometries, and experience with CMS-Xα PECD calculations suggests that consequently overemphasised spatial averaging in the C atom vicinity can excessively smear the potential. Instead, an alternative, smaller choice for the H atom radius is preferred.[22] This hybrid set of atomic sphere radii has recently been established to work well in rather large molecules such as fenchone.[10]

The CMS_Xα calculations work with a set of angular basis functions located on each atomic site, while the radial functions are obtained directly by numerical integration. The angular basis requires truncation at some appropriate values of the angular momentum, l_{max}. An earlier study of carvone demonstrated how, exceptionally for the calculation of PECD effects, the l_{max} limit in the asymptotic region had to be set as large as 18. Following this finding the truncation limits for the calculation of the continuum functions are set here at 18,10,5 in (respectively) the outer-, the first row atom-, and the H-atom spherical regions. The truncation limits for the initial state calculation are also increased from the earlier papers[7,12] to [6,3,1] (with the same ordering) as recent experience has indicated the importance of using more than the minimal $l = 0$ basis on H atoms, even when the initial orbital considered contains negligible H atom contributions.

RESULTS AND DISCUSSION

In the carbon *K*-edge region the carvone X-ray photoelectron spectrum (XPS) possesses three distinct peaks that are assigned to the carbonyl **C**=O, the isopropenyl **C**H_2=, and the remaining **C**H C 1*s* photoemissions. An example spectrum, recorded at a photon energy of 300 eV, is shown in Figure 1, with these assignments indicated. Figure 1 in fact includes two *S*-enantiomer spectra, S_L and S_R recorded with left- and right-handed CPL. These recordings are made in such a way that exact comparability is ensured, compensating for variations in vapour pressure, light intensity, etc.[7] It can then be seen that there is a perceptible intensity difference for the **C**=O $1s^{-1}$ peaks

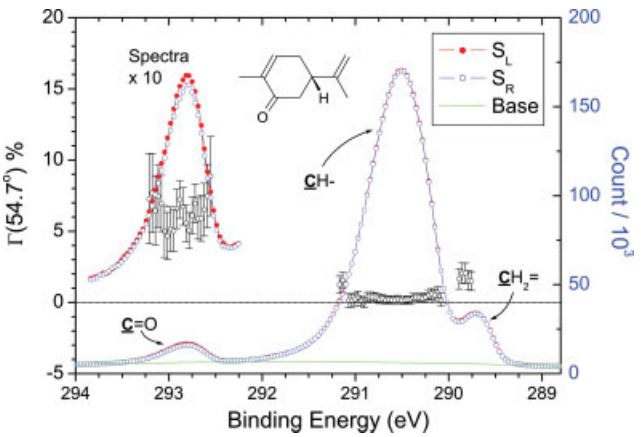

Fig. 1. C 1*s* region XPS ($h\nu$ = 300 eV) recorded with (+)-*S*-carvone enantiomer. S_L and S_R are recordings made with, respectively, left and right circular polarization. Normalized asymmetry is shown with error bars (left axis scale). [Color figure can be viewed in the online issue, which is available at www.interscience.wiley.com.]

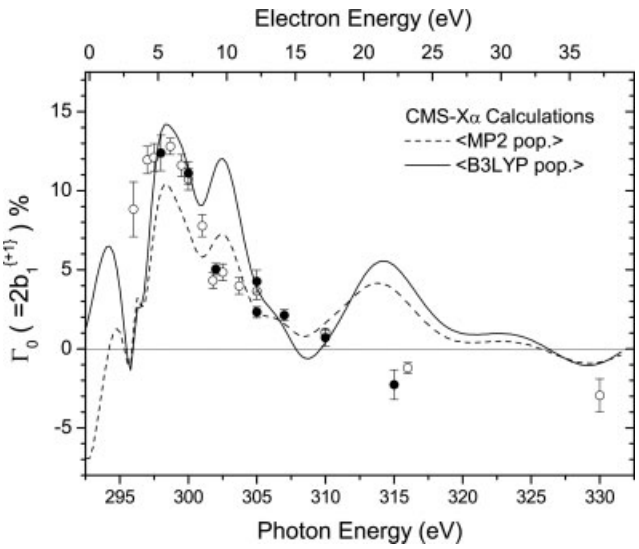

Fig. 2. PECD of the (+)-*S*-carvone **C**=O 1*s* photoemission. Open and filled plotting symbols distinguish measurements made on separate occasions. The curves show two CMS-Xα calculations assuming alternative conformer populations, discussed in the text.

in the two spectra as a result of the dichroism. Also included in the figure are the asymmetry factors, $\Gamma(54.7^\circ)$, obtained from the difference spectrum, S_L-S_R, as given in eq. 5. These are presented point by point in those regions where they are statistically significant.

In the carbonyl peak region the *S*-enantiomer asymmetry $\Gamma(54.7^\circ) \approx 6\%$. This corresponds to a forward-backward angular asymmetry, G_{AD}, of over 10% (eqs. 2–4). It is also clear from Figure 1 that the PECD asymmetry in the XPS at this single photon energy varies with the peak, or the identity of the ionized orbital. The isopropenyl **C**H_2= peak displays a smaller Γ of a few percentage, while for the principal **C**H peak it barely exceeds zero. It should be noted however, that this latter peak is a composite of many superimposed orbital contributions. As such the individual orbitals may contribute a non-negligible PECD asymmetry, but because some may be positive, some negative, their average will always tend to move towards zero. This expectation has been quantitatively demonstrated in the case of a similar composite peak in camphor.[4] The asymmetries recorded also show a dependence upon the photon energy (equivalently the electron kinetic energy upon ejection from a given orbital).

Figure 2 presents the mean asymmetries for the *S*-enantiomer sample, averaged over the FWHM of the carbonyl **C**=O 1*s* peak, as a function of photon energy. The experimental asymmetries $\Gamma(54.7^\circ)$ have been trivially converted by factoring out the $\cos(54.7^\circ)$ so as to plot $\Gamma_0(\equiv 2b_1^{\{+1\}})$ for this enantiomer, facilitating comparison with theoretical predictions of the $b_1^{\{\pm1\}}$ coefficient. The experimental data analysis undertaken to produce Figure 2 incorporates an improved spectrum baseline correction treatment. Although any background is automatically cancelled in forming the difference spectrum, it can still influence the outcome if it is retained in the denominator in eq. 5 when normalizing. An incomplete baseline subtraction in the denominator will therefore introduce magnitude errors to the deduced asymmetry factors. Application of the improved baseline correction has now reduced the scatter in previously published carvone PECD results[7] and additional *S*-enantiomer data points have also been added in. The *S*-enantiomer data displayed in Figure 2 were obtained over two separate beamtime allocations at BESSY. Where they overlap it can be seen that the reproducibility is good.

A carvone enantiomer has six possible conformations, corresponding to equatorial and axial positions for the isopropenyl tail group, with three rotational conformers in each case.[12,23,24] These are illustrated for the *S*-enantiomer in Figure 3, but otherwise employ the same labelling as in

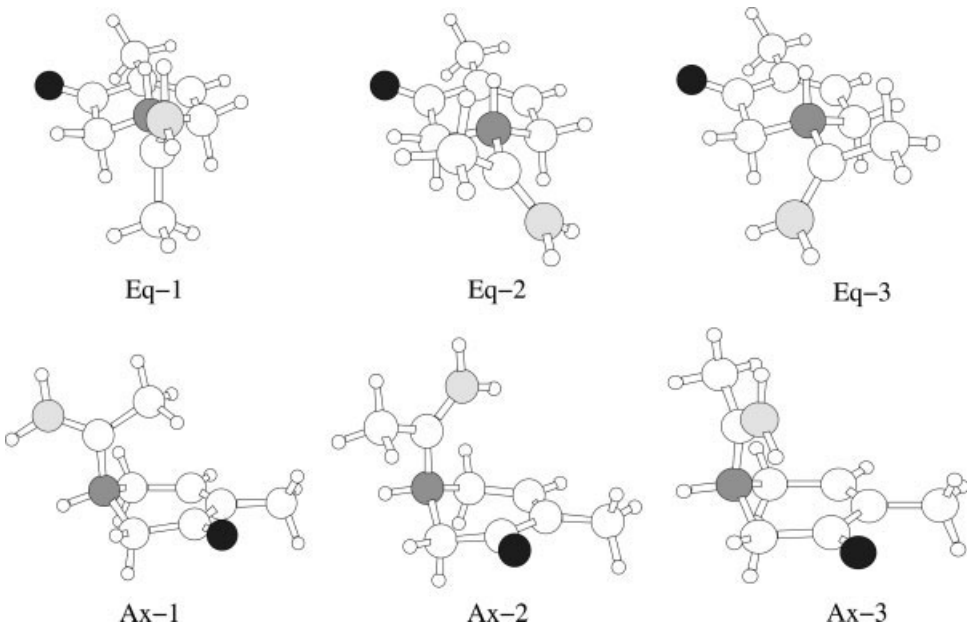

Fig. 3. *S*-carvone conformations. Oxygen atom is drawn in black, asymmetric carbon is shaded dark gray.

TABLE 1. Absolute energies, *E*, free energies, *G*, and estimated relative populations at 350 K for carvone conformers

Conformer	Eq-1	Eq-2	Eq-3	Ax-1	Ax-2	Ax-3
B3LYP/6-31G**						
E (a.u.)	−464.7154211	−464.7149355	−464.7150088	−464.7120498	−464.7121499	−464.7125433
Δ*E* (eV)[a]	0.000	0.013	0.011	0.092	0.089	0.078
Δ*E* (cm^{-1})[a]	0.00	106.58	90.48	739.93	717.95	631.62
Population (350 K)	0.41	0.26	0.28	0.02	0.02	0.03
G (a.u.)	−464.536555	−464.535844	−464.535869	−464.532509	−464.532872	−464.53309
Δ*G* (eV)[a]	0.000	0.019	0.019	0.110	0.100	0.094
Δ*G* (cm^{-1})[a]	0.00	156.05	150.56	888.00	808.33	760.49
Population (350 K)	0.47	0.24	0.25	0.01	0.01	0.02
MP2/6-31G**						
E (a.u.)	−463.3014004	−463.3004316	−463.3007744	−463.299837	−463.3001968	−463.3008793
Δ*E* (eV)[a]	0.000	0.026	0.017	0.043	0.033	0.014
Δ*E* (cm^{-1})[a]	0.00	212.62	137.39	343.13	264.15	114.36
Population (350 K)	0.32	0.13	0.18	0.07	0.10	0.20
G (a.u.)	−463.116939	−463.116534	−463.116441	−463.114544	−463.115133	−463.115270
Δ*G* (eV)[a]	0.000	0.011	0.014	0.052	0.036	0.032
Δ*G* (cm^{-1})[a]	0.00	88.89	109.30	416.35	287.08	257.01
Population (350 K)	0.32	0.22	0.20	0.05	0.09	0.11

[a]Differences relative to the Eq-1 conformer.

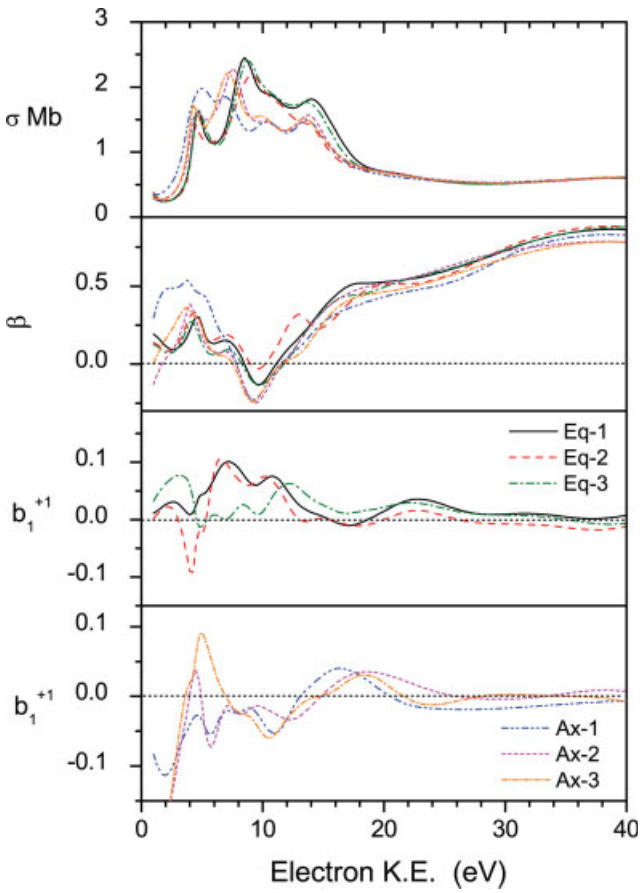

Fig. 4. CMS-Xα calculations for the six *S*-carvone conformers. From the top: cross-sections (σ); β-parameters; $b_1^{\{+1\}}$ coefficients for the equatorial conformers; $b_1^{\{+1\}}$ coefficients for the axial conformers. The same keys apply to all panels. [Color figure can be viewed in the online issue, which is available at www.interscience.wiley.com.]

previous computational studies made for the *R*-enantiomer.[12,23] Table 1 lists the results of two sets of calculations for these conformers, made using the Gaussian-03 programme[25] with either a B3LYP functional or an MP2 post Hartree–Fock method and, in either case a 6-31G(p,d) basis. In addition to the absolute energy for each conformer, free energy differences are estimated using calculated vibrational frequencies, and estimated populations at the experimental temperature of 350 K estimated from these. It is seen that the equatorial conformations are the most stable and that only a relatively small thermal population of the axial conformations is expected. Nevertheless, the exact population ratios are quite model dependent owing to the small energy differences (<250 cm^{-1} or, equivalently, <1 kcal mol^{-1}) between the three rotamers in each group.

Figure 4 compares the newly extended CMS-Xα calculations for the photoionization of the C=O 1*s* orbital of each of these *S*-(+) conformers. The cross-section results for the three equatorial conformers are quite similar to one other, and the conformers Ax-2 and Ax-3 are also very similar to the other. But these two groups differ somewhat, both from each other and also from the Ax-1 conformer. The amount of variation is a little unexpected, and this is underlined by the core binding energies (CEBEs) for the carbonyl C 1*s* orbital, calculated Chong's ΔE_{KS}(PW86−PW91) method[26–28] with relativistic corrections,[29] and shown in Table 2. As can be seen these show negligible differences, suggesting that any changes in electron density at the carbonyl group as a result of the changed conformation are negligible with consequently no variation in the binding energy shift.

The calculated β anisotropy parameters (equivalently $b_2^{\{p\}}$ coefficients) are similar for all conformers, only the Ax-1 and Eq-2 showing much deviation from the mean,

TABLE 2. C−O 1*s* core binding energies calculated by the ΔE_{KS}(PW86 − PW91) + C_{rel} method

Conformer	CEBE (eV)
Eq-1	292.43
Eq-2	292.53
Eq-3	292.55
Ax-1	292.42
Ax-2	292.49
Ax-3	292.52

and even then only over limited energy ranges. However, the $b_1^{\{+1\}}$ coefficients (lower panels of Figure 4) show big differences, most notably between the axial and equatorial conformations, but also within these groups. In other words the *chiral* part of the angular distribution is much more sensitive to molecular conformation than the regular β parameter. This is now expected behavior from other studies[11,13,20] and arises because of the different way in which the chiral $b_1^{\{\pm1\}}$ coefficient is sensitive to phase shifts induced as the electron scatters from the ion core, even when the relative phase differences are quite small.[12]

We can anticipate that the dominant contribution to the experimental PECD comes from the equatorial conformers, based upon the much larger predicted populations of this group (Table 1). Focussing on this set of curves in Figure 4, it can be seen that significantly, in the region broadly centred around 10 eV above the threshold where the experimental data are concentrated, the eq-3 conformer predictions are for a much smaller $b_1^{\{+1\}}$ coefficient than for either the eq-1 or eq-2 structures. In this same region, the axial conformers all have predicted $b_1^{\{+1\}}$ values that are negative. The net sign and amplitude of the experimental asymmetry in this region should thus be sensitive to the relative contributions made by the (eq. 1, eq. 2) pair, the eq-3 conformer, and the axial conformers.

Figure 2 includes results from the CMS-Xα calculations in a form allowing direct comparison with experiment. The relative conformer populations suggested by the MP2 and B3LYP free energy calculations in Table 1 are used to generate two curves as appropriately weighted averages of the individual conformer $b_1^{\{+1\}}$ curves that are displayed in Figure 4. Strictly, an additional weighting factor at each energy should be obtained from the relative conformer ionization cross-sections as well as populations, but this is thought unlikely to significantly change the present findings. In plotting these curves on Figure 2 an energy scale offset of −1.25 eV has been introduced to allow the predicted and experimental maxima to coincide. This is because the Xα potential is overall insufficiently attractive, so that continuum features appear shifted up in energy. While this could be overcome by tuning the Xα parameterizations the ad hoc plotting offset is usually sufficient to permit useful comparisons.

From Figure 2 it may be seen that the calculations provide at least semiquantitative agreement with experiment; significantly the sign and approximate magnitude of the peak asymmetry are convincingly reproduced. Looking more closely at the averaging, it can be seen in Table 1 that the MP2 and B3LYP calculations differ principally in the predicted 350 K populations of the axial conformers. These are essentially negligible in the latter calculation, only slightly less so in the former. Within the group of equatorial conformations the calculations agree on nearly equal population for eq-2 and eq-3, but differ in the predicted eq-1 population relative to these. As noted above mixing in more contribution from the eq-3 conformer will have the effect of reducing the magnitude of the peak asymmetry; mixing in more eq-1 contribution will increase this magnitude. The MP2 weighted $b_1^{\{+1\}}$ curve, with a smaller (eq-1 + eq-2): eq-3 ratio has a correspondingly smaller peak amplitude than the alternative B3LYP weighted curve. However, it is clearly possible to infer from the theory-experiment comparison that a conformer other than eq-1 and/or eq-2 is populated in the experiment, for either of these alone predicts the peak asymmetry $\Gamma_0(\equiv 2b_1^{\{+1\}})$ to be ∼20%, which is clearly greater than that which is observed in the experiment. Given the expectations about the reduced stability of the axial conformers it seems improbable that they would be present in significant amount, so that a clear deduction can be made that there is around 25% population of the eq-3 conformer present in our thermal sample.

Previous gas phase electron diffraction experiments[23] while concurring about the dominant presence of equatorial conformers, were unable to distinguish the relative contributions made by eq-2 and eq-3. A laser spectroscopy investigation of carvone, performed in a seeded supersonic molecular beam,[30] found features which could be attributed to each of the three equatorial conformers, with eq-1 making the major contribution. The present finding is complementary to these, clearly indicating the presence of significant eq-3 populations.

Compared to an earlier investigation of PECD for this molecule,[12] the improvements that have now been implemented in both the experimental data analysis and the theoretical modeling allow the present work to arrive at a much more definitive conclusion than was previously obtained. Discrepancies between theory and experiment remain, however, most notably the predicted secondary peak in the $b_1^{\{+1\}}$ curve at ∼10 eV kinetic energy. It can be seen from Figure 4 that this peak in the PECD curves correlates with structure predicted in the cross-section and, most significantly, a pronounced dip in the β-parameter curves. Such characteristics are frequently used to infer the presence of a shape resonance in the ionization continuum, and it is postulated that this is the case here also. Shape resonances provide a well-documented difficulty for current computational approaches, which typically over-estimate the magnitude of the behavior they induce. In the present case it can be seen that while there is indeed a suggestion of a shoulder in the experimental PECD data at 10 eV, this falls short of the distinct peak predicted—all of which is consistent with a resonance that currently impedes a fully quantitative comparison in this region.

CONCLUSIONS

The C 1*s* core ionization of (+)-*S*-carvone enantiomers by circularly polarized soft X-ray radiation displays many of the more general features now being encountered in PECD investigations. The chiral asymmetries in angle-resolved photoemission can be large—at least 12% here—even though for a 1*s* ionization the initial orbital is achiral and so oblivious to the molecular handedness. The photoelectron must therefore "sense" the chirality only after its ejection, as it is scattered by the molecular ion core. There is then paradoxical evidence that the PECD does strongly depend upon which orbital is being ionized. In the case of these supposedly achiral 1*s* orbitals this must be attributable to their localization at different sites within the molecule where they can provide different point emission sources for a kind of in situ low energy electron scattering.

A dramatic feature of this chiral electron scattering is the marked dependence upon molecular conformation. Although this has been noted in different circumstances, it is perhaps most surprising here, in carvone. The carbonyl C $1s^{-1}$ photoelectron angular asymmetry is strong yet at some energies can seemingly be "quenched" or even reversed by changes in the orientation of the isopropenyl tail located at some distance from the initial emission site. The comparisons with theory that are provided here allow a fairly strong inference that there is a significant population of the eq-3 conformer together with the eq-1 and/or eq-2 conformers. Because of the small energy differences between the conformers, predicted population distributions are quite model sensitive, but on balance an eq-1:eq-2:eq-3 ratio of 2:1:1 looks to be plausible.

Whatever ambiguities may persist in the theory to experiment comparisons, and so may serve to limit full quantitative agreement—due perhaps to theoretical limitations, experimental limitations, population uncertainties, shape resonances—it is abundantly clear that the present level of calculation can accurately predict the sign of the key features in the photon energy dependent PECD spectra. There is thus a capability to use such experiments and accompanying modeling to assign absolute configuration where this is not already known.

ACKNOWLEDGMENTS

The author wishes to acknowledge the role played by U. Hergenhahn, S. Barth, S. Joshi, V. Ulrich, and E. Mikajlo in the original carvone C $1s^{-1}$ experiments, and especially C. Harding for his contribution to both experiment and the analysis. Computational resources were provided, in part, by the EPSRC National Service for Computational Chemistry Software.

LITERATURE CITED

1. Ritchie B. Theory of the angular distribution of photoelectrons ejected from optically active molecules and molecular negative ions. Phys Rev A 1976;13:1411–1415.
2. Böwering N, Lischke T, Schmidtke B, Müller N, Khalil T, Heinzmann U. Asymmetry in photoelectron emission from chiral molecules induced by circularly polarized light. Phys Rev Lett 2001;86:1187–1190.
3. Garcia GA, Nahon L, Lebech M, Houver JC, Dowek D, Powis I. Circular dichroism in the photoelectron angular distribution from randomly oriented enantiomers of camphor. J Chem Phys 2003;119:8781–8784.
4. Hergenhahn U, Rennie EE, Kugeler O, Marburger S, Lischke T, Powis I, Garcia G. Photoelectron circular dichroism in core level ionization of randomly oriented pure enantiomers of the chiral molecule camphor. J Chem Phys 2004;120:4553–4556.
5. Lischke T, Böwering N, Schmidtke B, Muller N, Khalil T, Heinzmann U. Circular dichroism in valence photoelectron spectroscopy of free unoriented chiral molecules: camphor and bromocamphor. Phys Rev A 2004;70:art. no.022507.
6. Turchini S, Zema N, Contini G, Alberti G, Alagia M, Stranges S, Fronzoni G, Stener M, Decleva P, Prosperi T. Circular dichroism in photoelectron spectroscopy of free chiral molecules: experiment and theory on methyl-oxirane. Phys Rev A 2004;70:art. no. 014502.
7. Harding CJ, Mikajlo EA, Powis I, Barth S, Joshi S, Ulrich V, Hergenhahn U. Circular dichroism in the angle-resolved C 1s photoemission spectroscopy of gas-phase carvone enantiomers. J Chem Phys 2005;123:234–310.
8. Stranges S, Turchini S, Alagia M, Alberti G, Contini G, Decleva P, Fronzoni G, Stener M, Zema N, Prosperi T. Valence photoionization dynamics in circular dichroism of chiral free molecules: the methyl-oxirane. J Chem Phys 2005;122:244–303.
9. Nahon L, Garcia GA, Harding CJ, Mikajlo EA, Powis I. Determination of chiral asymmetries in the valence photoionization of camphor enantiomers by photoelectron imaging using tunable circularly polarized light. J Chem Phys 2006;125:114–309.
10. Ulrich V, Barth S, Joshi S, Hergenhahn U, Mikajlo EA, Harding CJ, Powis I. Giant chiral asymmetry in the C 1s core level photoemission from randomly oriented fenchone enantiomers. J Phys Chem A 2008; DOI: 10.1021/jp709761a.
11. Garcia GA, Nahon L, Harding CJ, Powis I. Chiral signatures in angle resolved valence photoelectron spectroscopy of pure glycidol enantiomers. Phys Chem Chem Phys 2008; DOI: 10.1039/b714095a.
12. Harding CJ, Powis I. Sensitivity of photoelectron circular dichroism to structure and electron dynamics in the photoionization of carvone and related chiral monocyclic terpenone enantiomers. J Chem Phys 2006; 125:234–306.
13. Di Tommaso D, Stener M, Fronzoni G, Decleva P. Conformational effects on circular dichroism in the photoelectron angular distribution. Chem Phys Chem 2006;7:924–934.
14. Powis I. Photoelectron circular dichroism of the randomly oriented chiral molecules glyceraldehyde and lactic acid. J Chem Phys 2000; 112:301–310.
15. Weiss MR, Follath R, Sawhney KJS, Senf F, Bahrdt J, Frentrup W, Gaupp A, Sasaki S, Scheer M, Mertins HC, Abramsohn D, Schäfers F, Kuch W, Mahler W. The elliptically polarized undulator beamlines at BESSY II. Nucl Instrum Methods Phys Res Sect A: Accel Spectrometers Detectors Associated Equip 2001; 467:449–452.
16. Dill D, Dehmer JL. Electron-molecule scattering and molecular photoionization using the multiple scattering method. J Chem Phys 1974; 61:692–699.
17. Davenport JW. Theory of photoemission from molecules in the gas phase and on solid surfaces. Ph.D. thesis, University of Pennsylvania, PA; 1976.
18. Downie P, Powis I. The $5a_1^{-1}$ photoionization of oriented CF_3I molecules: angular distributions of the ka_1 and ke photoelectron continua. J Chem Phys 1999;111:4535–4547.
19. Hikosaka Y, Eland JHD, Watson TM, Powis I. Molecule frame photoelectron angular distributions from oriented methyl chloride and methyl fluoride molecules. J Chem Phys 2001;115:4593–4603.
20. Powis I. Photoelectron spectroscopy and circular dichroism in chiral biomolecules: L-alanine. J Phys Chem A 2000;104:878–882.
21. Takai Y, Johnson KH. SCF-Xa-SW calculations for small molecules using the optimization technique of atomic-sphere radii. Chem Phys Lett 1992;189:518–523.
22. Takai Y, Donovan MM, Johnson KH, Kalonji G. Optimization of atomic sphere radii in the scattered-wave Xα method: a second look at the water molecule. Chem Phys Lett 1989;159:376–382.

23. Egawa T, Kachi Y, Takeshima T, Takeuchi H, Konaka S. Structural determination of carvone, a component of spearmint, by means of gas electron diffraction augmented by theoretical calculations. J Mol Struct 2003;658:241–251.
24. Hoffmann GG. Infrared, Raman and VCD spectra of (*S*)-(+)-carvone-comparison of experimental and ab initio theoretical results. J Mol Struct 2003;661:525–539.
25. Frisch MJ, Trucks GW, Schlegel HB, Scuseria GE, Robb MA, Cheeseman JR, Montgomery JA, Vreven T, Kudin KN, Burant JC, et al. Gaussian 03 Revision C.01. Wallingford, CT: Gaussian Inc.; 2004.
26. Takahata Y, Chong DP. DFT calculation of core-electron binding energies. J Electron Spectrosc Relat Phenom 2003;133:69–76.
27. Chong DP, Aplincourt P, Bureau C. DFT calculations of core-electron binding energies of the peptide bond. J Phys Chem A 2002;106:356–362.
28. Cavigliasso G, Chong DP. Accurate density-functional calculation of core-electron binding energies by a total-energy difference approach. J Chem Phys 1999;111:9485–9492.
29. Chong DP. Density-functional calculation of core-electron binding-energies of C, N, O, and F. J Chem Phys 1995;103:1842–1845.
30. Mineyama M, Egawa T. Conformational property of carvone as studied by laser-jet spectroscopy and theoretical calculations. J Mol Struct 2005;734:61–65.

CHIRALITY 20:969–972 (2008)

Spectroscopic Studies of Oligomers Containing 2,5-*trans* Furanoid Sugar Amino Acids

ALISON A. EDWARDS,[1]* BRUCE D. ALEXANDER,[2] GEORGE W. J. FLEET,[3] AND GEORGE E. TRANTER[4]

[1]*Medway School of Pharmacy, Universities of Kent and Greenwich at Medway, Kent, United Kingdom*
[2]*School of Science, University of Greenwich, Kent, United Kingdom*
[3]*Department of Organic Chemistry, Chemistry Research Laboratory, University of Oxford, Oxford, United Kingdom*
[4]*Chiralabs Limited, Begbroke Centre for Innovation and Enterprise, Oxford University Begbroke Science Park, Oxfordshire, United Kingdom*

Presented at the 11th International Conference on Circular Dichroism, 2007, Groningen, Netherlands

ABSTRACT Sugar amino acids and their oligomers, known as carbopeptoids, are commonly studied as foldamers. However, study of their conformational preference is often challenging when the adopted conformations are extended and/or disordered. This study is the first to explore the disordered nature of such carbopeptoids by utilizing a family of 2,5-*trans* carbopeptoids. An array of spectroscopic techniques has been used to investigate the conformational preference of these carbopeptoids. However, using this data alone it has not been possible to assign conformational preference as an ordered extended conformation or as a disordered family of closely related conformations. Computational methods need to be employed to achieve reliable interpretation of the spectroscopic data. *Chirality 20:969–972, 2008.*

KEY WORDS: circular dichroism; sugar amino acids; conformation; extended; ordered; disordered; dipeptide isosteres; peptidomimetics

INTRODUCTION

Sugar amino acids (SAAs) are a structurally diverse class of compounds which are commonly used as dipeptide isosteres in the field of peptidomimetics.[1–4] As such, the understanding of the conformational preference of the corresponding oligomers, known as carbopeptoids, is vital to successfully utilize SAAs to create biologically active analogues.[5] The strategy for interpretation of carbopeptoid conformational preference has been previously discussed in detail and relies on the combination of an array of spectroscopic techniques to gain a deeper understanding of the conformational preference of these systems.[6] A combination of ^{1}H NMR, infrared (IR), and circular dichroism (CD) data will be discussed here to illustrate the issues of conformational assignment of extended and disordered systems. The conformational assignment of disordered systems is still an ongoing issue, even for the most well-defined foldamer systems such as α-peptides and proteins. Disordered conformations have been identified as important for biological function[7] and thus the identification and understanding of such systems is vital to the further understanding of structure–function relationships in biological systems. For clarity, the phrases used to describe secondary structure are defined as follows: ordered, where a single conformation (regular or irregular) is adopted; disordered, when dynamic switching occurs between ordered structures or when the backbone is flexible and can adopt a continuum of conformations; irregular, when a single conformation is adopted, which has no regularity, e.g., a static loop; regular, a single conformation with a regular repeating unit, e.g., an α-helix; extended, a conformation where no close contacts occur, e.g., the polyproline type II helix.

The carbopeptoids discussed herein refer to a family of δ-amino acids derived from SAAs of basic structure **1**. The presence of a 2,5-*cis* relationship has been identified as the important structural feature of **1** which led to the adoption of repeating β-turn-type conformations (a regular, ordered hydrogen-bonded conformation) in tetramers and longer oligomers. This work has recently been extended to the gas phase and similar results are observed as for the solution phase.[8] In contrast, only one of the 2,5-*trans* carbopeptoid series shown in Figure 1 has been found to adopt a regular, ordered hydrogen-bonded conformation. The 3,4-*O*-acetonide protected D-*talo* octamer (**2**) adopted a left-handed helix (akin to that of a π-helix).[9] By the use of CD, in combination with NMR and IR, it was possible to establish that the shorter tetrameric carbopeptoid adopted an extended conformation closely related to that of the octamer. One other 2,5-*trans* carbopeptoid series, of D-*manno* stereochemistry, has been studied for conformational preference as unprotected (**3**: tetramer, hexamer, and octamer)[10] and acetyl-protected (**4**: tetramer) oligomers.[11,12] None of these D-*manno* oligomers were found to adopt ordered, regular hydrogen-bonded conformations.

*Correspondence to: Alison Anne Edwards, Medway School of Pharmacy, Universities of Kent and Greenwich at Medway, Central Avenue, Chatham Maritime, Kent ME4 4TB, UK. E-mail: a.a.edwards@kent.ac.uk
Received for publication 2 November 2007; Accepted 21 December 2007
DOI: 10.1002/chir.20538
Published online 29 February 2008 in Wiley InterScience (www.interscience.wiley.com).

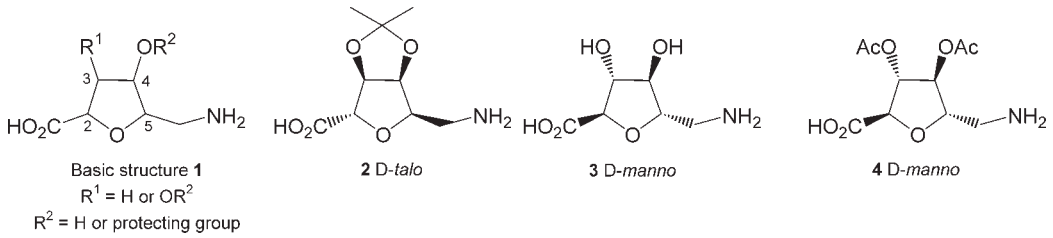

Fig. 1. Previous 2,5-*trans* related carbopeptoids studied for conformational preference.

To gain further insight into which structural features gave rise to the observed helical conformation for octamer **2**, simplified versions of the 2,5-*trans* SAA were prepared and studied, where R^1 = H for the basic structure **1**. To obtain maximum information from this 3-deoxy SAA, two stereochemistries at C-4 were studied and the hydroxyl group derivatized to ascertain the effect of modification at C-4 upon the conformational preference of the peptidomimetic backbone (see Fig. 2a).

MATERIALS AND METHODS

The unprotected (R^3 = H) carbopeptoids were prepared from the corresponding SAAs[13] in good yields using standard methodology in solution phase; this involved selective deprotection and subsequent iterative coupling using peptide-coupling reagents.[14] The triethylsilyl ether (TES) and acetyl ester protected carbopeptoids were prepared from the corresponding unprotected carbopeptoids. There was only one exception to this: the unprotected L-*arabino* octamer **12** was isolated as the free acid after deprotection of the TES-protected carbopeptoid **14**. The CD, solution IR, and NMR spectroscopic data were acquired in a similar manner to that reported previously.[9]

RESULTS AND DISCUSSION

Data Acquisition for the Unprotected Carbopeptoids

The presence of only one hydroxyl on each SAA monomer facilitates the analysis of the unprotected oligomers, even octamers, in a range of solvents including water. This is in contrast to previous carbopeptoid studies where two hydroxyls were present in the monomer unit. Unfortunately, the presence of unprotected hydroxyls complicates the NH region of the solution IR spectrum and renders the oligomers (longer than dimers) insoluble in $CDCl_3$. Despite this, NMR studies were conducted for the tetramers in pyridine-d_5. The advantage of unprotected carbopeptoids is the ability to study the conformational preference in an aqueous environment. Exchange of amide protons with deuterium in H_2O/D_2O meant that the full assignment of ^{1}H NMR spectra in aqueous media was not attempted. Because of these issues, CD has become the preferred technique for the study of the unprotected oligomers in a range of solvents including water. However, it should be borne in mind that the interpretation of the CD spectra using the basis spectra for α-peptides is not reliable because of the difference in the environment between the amide chromophores.

Data Acquisition for the Protected Carbopeptoids

As in earlier spectroscopic studies, NMR spectra recorded in $CDCl_3$ can give a wealth of secondary structure information when sufficient signal dispersion is achieved in the ^{1}H NMR spectrum.[9] This is usually the case for regular hydrogen-bonded conformations where the NH protons are dispersed and are shifted above 7.2 ppm. In contrast, when the NH signals are not disperse, and typically also with δ_{NH} around 7.2 ppm, then there is a greater degree of signal overlap which restricts the conformational information that can be obtained. In general, it is assumed that in such circumstances there are little long-range nOes evident in the spectrum, for

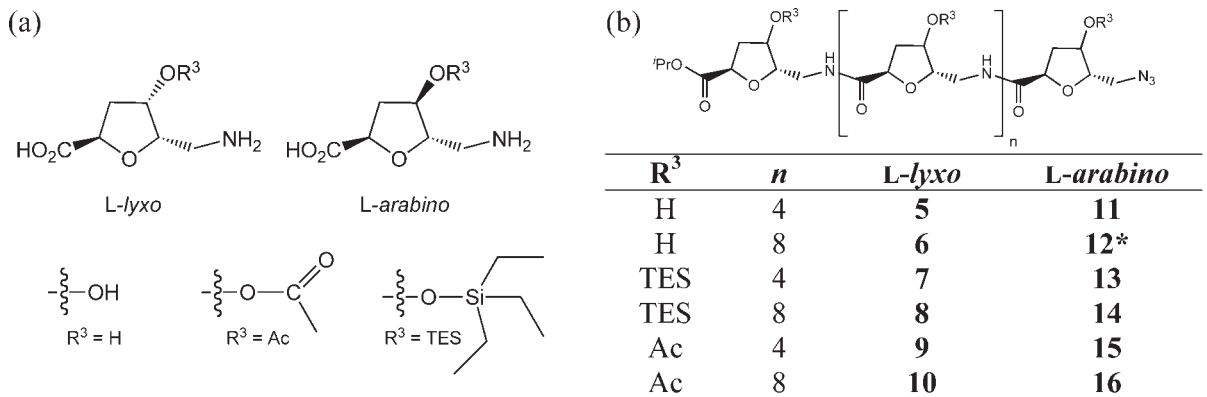

R^3	*n*	L-*lyxo*	L-*arabino*
H	4	**5**	**11**
H	8	**6**	**12***
TES	4	**7**	**13**
TES	8	**8**	**14**
Ac	4	**9**	**15**
Ac	8	**10**	**16**

*Free acid not isopropyl ester

Fig. 2. The 3-deoxy carbopeptoid series of δ-amino acids. (**a**) The structural diversity and (**b**) carbopeptoids studied.

TABLE 1. Spectroscopic data acquired for the tetrameric and octameric carbopeptoids

R^3	NMR $CDCl_3$	NMR Pyridine-d_5	Solution IR $CHCl_3$	CD TFE	CD H_2O
H	✗[a]	✓	✗[a]	✓	✓
TES	✓[b]	–	✓	✓	✗[a]
Ac	✓[b]	–	✓	✗[c]	✗[c]

TFE, 2,2,2,-trifluoroethanol. NMR data were obtained at 400 or 500 MHz, IR data were collected in the NH stretch region, and CD spectra were acquired in the far UV region.
[a]Not obtained due to solubility.
[b]Some ^1H and ^{13}C NMR spectra were assigned in benzene-d_6 because of decreased signal overlap relative to $CDCl_3$.
[c]Not obtained due to signal overlap.

example, due to the presence of ordered extended conformations or an increase in disorder which results in conformational averaging, or a combination of these. Under such circumstances, NMR does not provide detailed conformational information. Study of the NH region by IR, even when there is poor signal dispersion by ^1H NMR, can reveal useful information on the environment(s) of the NH protons and similarly their population(s). The IR data reported here relates to the NH stretch region only, as the data observed from the amide I and amide II bands, to date, has proved inconclusive in terms of secondary structural features for this family of compounds. Employing solvents such as 2,2,2-trifluoroethanol (TFE), it is possible to obtain CD spectra of both the protected and unprotected carbopeptoids in the same solvent, thus obtaining structural information which can be directly compared to ascertain if there is any conformational effect attributable to modification of the hydroxyl moiety. Unfortunately, the presence of carbonyl group in the acetyl-protected carbopeptoids complicates the far UV region of the CD spectrum and has meant that only the unprotected and triethylsilyl-protected oligomers could be studied.

By using a combination of techniques it is possible to asses the effect of both the stereochemistry and derivatization of the hydroxyl groups on the conformational preference of the carbopeptoid backbone (see Table 1).

The ^1H NMR data obtained for all the triethylsilyl- and acetyl-protected carbopeptoids (in $CDCl_3$) and the unprotected tetramers (in pyridine-d_5) showed poor signal dispersion and the δ_{NH} were consistent with nonhydrogen-bonded environments. The solution IR spectra of the NH region for the oligomers were largely consistent with these observations, but the combination of increased chain length, L-*lyxo* stereochemistry, and acetyl derivatization led to a significant increase of a second amide environment (occurring in the region 3320–3380 cm^{-1}) in relation to the nonhydrogen-bonded amide environment observed at ca. 3422 cm^{-1} (see Fig. 3). This would indicate that hydrogen-bonded environments can be adopted by the amide protons of this family of protected carbopeptoids and that the population of this second environment is enhanced by the 4,5-*cis* relationship when a small protecting group capable of hydrogen bonding is present at C-4. Further information is required to deduce the specific hydrogen-bonding interactions responsible for the second amide environment observed. Because of the signal overlap by ^1H NMR and the noncrystalline nature of the protected oligomers, only computational methods would be able to provide additional insight into the conformational preference.[15]

CD spectra can give direct information on the similarity of conformational preference of the peptidomimetic backbone of different carbopeptoids because of the phenomenon of exciton coupling, as evidenced for α-peptides and proteins. The CD spectra discussed here are displayed according to the concentration of amide linkages (200 μM) in each carbopeptoid to enable a direct comparison of the amide bond environment to be visualized independent of chain length. Each octamer exhibited a similar spectrum to the corresponding tetramer, whether unprotected or TES-protected, indicating that the conformational preference is not significantly altered by increased chain length (data not shown). Both the L-*lyxo* and L-*arabino* TES-protected oligomers (**8** and **14**) in TFE display similar spectral features although the position of the positive maxima and the intercept of the wavelength-axis differ by ca. 5 nm (see Fig. 4a). Similarly, the unprotected octamers (**6** and **12**) in TFE exhibit negative maxima ca. 5 nm apart, but the L-*lyxo* octamer **6** displays a second positive maxima at 210 nm (nearly meeting the wavelength-axis) which is in contrast to the L-*arabino* octamer **12** that does not display such a positive maxima. By comparison of the TES-pro-

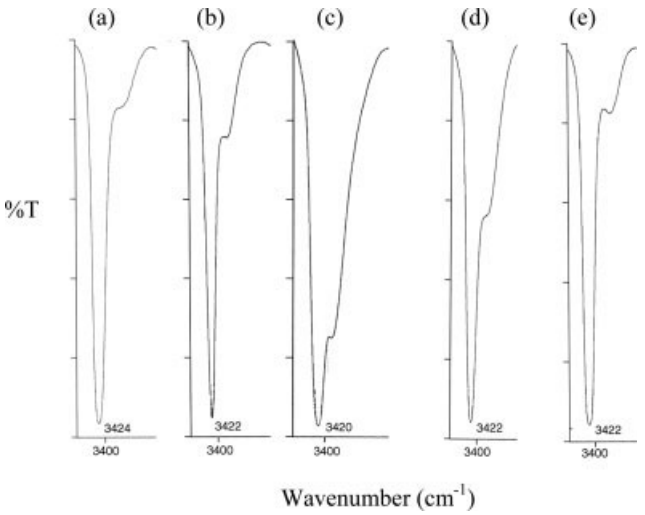

Fig. 3. Solution IR spectra of amide N–H stretch region at 2 mM in $CHCl_3$ at room temperature. (**a**) TES protected L-*lyxo* octamer **8**; (**b**) Ac protected L-*lyxo* tetramer **9**; (**c**) Ac protected L-*lyxo* octamer **10**; (**d**) Ac protected L-*arabino* octamer **16**; (**e**) TES protected L-*arabino* octamer **14**.

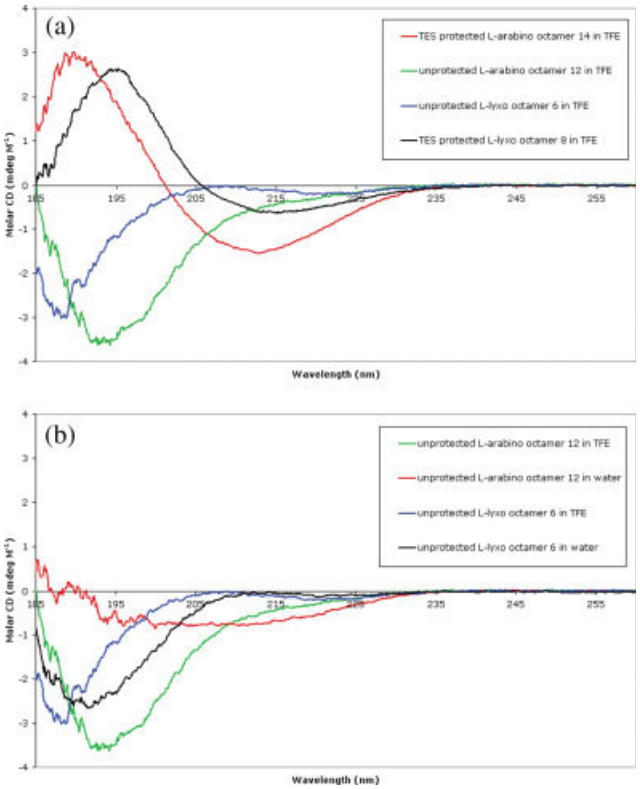

Fig. 4. Circular dichroism spectra of the octameric carbopeptoids (recorded on a Jasco J600 at 298 K). (**a**) The triethylsilyl-protected and unprotected L-*lyxo* and L-*arabino* octamers in TFE and (**b**) The unprotected L-*lyxo* and L-*arabino* octamers in TFE and water. [Color figure can be viewed in the online issue, which is available at www.interscience.wiley.com.]

tected and unprotected octamers in TFE, it is clear that there is a significant conformational effect introduced by protection of the hydroxyl groups with triethylsilyl; this is unsurprising given the steric hindrance introduced by this bulky protecting group. It is apparent that the inversion of stereochemistry at C-4 does have an effect upon the conformational preference.

The CD spectrum of the unprotected L-*lyxo* octamer **6** does not differ dramatically on change of solvent from TFE to water (see Fig. 4b). However, for the unprotected L-*arabino* octamer **12,** the change in the CD spectrum on going from TFE to water is much more pronounced because of changes in the spectral features; the negative maxima at ca. 195 nm in TFE virtually disappears and is replaced by a broad negative maxima at ca. 220 nm in water. This would indicate that water has the ability to alter the conformational preference of octamer **12**. Insufficient spectroscopic evidence is present to enable the determination of whether this is due to disruption of hydrogen-bonded conformations present in the octamer **12** in TFE or by the formation of hydrogen bonds to the solvent water, or a combination of both.

CONCLUSION

In summary, much spectroscopic evidence has been obtained for this family of carbopeptoids, but it has still not been possible to unambiguously interpret this evidence to assign conformational preference. To facilitate the correct interpretation of the spectroscopic data, computational studies will need to be undertaken. Early results by computational methods indicate that further detailed interpretation will be possible. The spectroscopic evidence indicates that these oligomers prefer to adopt more than one conformation and that, by CD, increased chain length does not alter this preference for the unprotected and TES-protected carbopeptoids. However, by CD and IR, variation in conformational preference was observed when inversion of stereochemistry or derivatization of the hydroxyl group occurred. Perhaps what is most surprising is the effect induced by inversion of the hydroxyl remote to the backbone. The aim of this work is to establish an approach for identification of disordered foldamer systems; with further computational studies, this will be achieved.

LITERATURE CITED

1. Risseeuw MDP, Overhand M, Fleet GWJ, Simone MI. A compendium of sugar amino acids (SAA): scaffolds, peptide- and glyco-mimetics. Tetrahedron: Asymmetry 2007;18:2001–2010.
2. Schweizer F. Glycosamino acids: building blocks for combinatorial synthesis—implications for drug discovery. Angew Chem Int Ed 2002;41:231–253.
3. Gruner SAW, Locardi E, Lohof E, Kessler H. Carbohydrate-based mimetics in drug design: sugar amino acids and carbohydrate scaffolds. Chem Rev 2002;102:491–514.
4. Trabocchi A, Guarna F, Guarna A. γ- and δ-Amino acids: synthetic strategies and relevant applications. Curr Org Chem 2005;9:1127–1153.
5. Chakraborty TK, Ghosh S, Jayaprakash S, Sharma JARP, Ravikanth V, Diwan PV, Nagaraj R, Kunwar AC. Synthesis and conformational studies of peptidomimetics containing furanoid sugar amino acids and a sugar diacid. J Org Chem 2000;65:6441–6457.
6. Edwards AA, Fleet GWJ, Tranter GE. Classification of conformation for sugar amino acid systems using chiroptical spectroscopy. Chirality 2006;18:265–272.
7. Vucetic S, Obradovic Z, Vacic V, Radivojac P, Peng K, Iakoucheva LM, Cortese MS, Lawson JD, Brown CJ, Sikes JG, et al. DisProt: a database of protein disorder. Bioinformatics 2005;21:137–140.
8. Jockusch RA, Talbot FO, Rogers PS, Simone MI, Fleet GWJ, Simons JP. Carbohydrate amino acids: the intrinsic conformational preference for a β-turn-type structure in a carbopeptoid building block. J Am Chem Soc 2006;128:16771–16777.
9. Claridge TDW, Long DD, Baker CM, Odell B, Grant GH, Edwards AA, Tranter GE, Fleet GWJ, Smith MD. Helix-forming carbohydrate amino acids. J Org Chem 2005;70:2082–2090.
10. Chakraborty TK, Jayaprakash S, Srinivasu P, Chary MG, Diwan PV, Nagaraj R, Sankar AR, Kunwar AC. Synthesis and structural studies of oligomers of 6-amino-2,5-anhydro-6-deoxy-D-mannonic acid. Tetrahedron Lett 2000;41:8167–8171.
11. Smith MD, Fleet GWJ. Designing secondary structures: 5-azidomethyl tetrahydrofuran-2-carboxylates as carbohydrate-derived dipeptide isosteres. J Peptide Sci 1999;5:425–441.
12. Smith MD, Long DD, Martin A, Marquess DG, Claridge TDW, Fleet GWJ. Absence of secondary structure in a carbopeptoid tetramer of a *trans*-5-aminomethyl-tetrahydrofuran-2-carboxylate. Tetrahedron Lett 1999;40:2191–2194.
13. Watterson MP, Edwards AA, Leach JA, Smith MD, Ichihara O, Fleet GWJ. Synthesis of all diastereomeric methyl 2,5-anhydro-3-deoxy-hexonates: precursors to C-2-deoxynucleosides and THF-templated γ- and δ-amino acids. Tetrahedron Lett 2003;44:5853–5857.
14. Edwards AA, Sanjayan GJ, Hachisu S, Tranter GE, Fleet GWJ. A novel series of oligomers from 4-aminomethyl-tetrahydrofuran-2-carboxylates with 2,4-*cis* and 2,4-*trans* stereochemistry. Tetrahedron 2006;62:7718–7725.
15. Baron R, Bakowies D, van Gunsteren WF. Carbopeptoid folding: effects of stereochemistry, chain length, and solvent. Angew Chem Int Ed 2004;43:4055–4059.

CHIRALITY 20:973–977 (2008)

Dendritic Crystal Growth, Differential Circular Scattering, and the Origin of Biomolecular Homochirality

BART KAHR* AND JOHN H. FREUDENTHAL
Department of Chemistry, University of Washington, Seattle, Washington

Presented at the 11th International Conference on Circular Dichroism, 2007, Groningen, Netherlands

ABSTRACT Phthalic acid rapidly crystallizing in thin aqueous films is deposited radially and rhythmically as dendritic banded spherulites that have heterochiral mesotextures in hemi-circles. The chiral fields differentially scatter left and right circularly polarized light. A scenario for chiral amplification and the origin of biomolecular homochirality is thus proposed that combines the influences of crystals and light. *Chirality 20:973–977, 2008.*

KEY WORDS: biomolecular homochirality; dendritic crystals; circularly polarized light; light scattering; phthalic acid

BIOMOLECULAR HOMOCHIRALITY

Speculation about the origin of biomolecular homochirality continues apace.[1–6] Proposals run from deterministic chemical expressions of the dissymmetry of nuclei[7–10] to stochastic fluctuations of an optically inactive medium[11] followed by asymmetric autocatalysis.[12–15] But, fluctuations need not be stochastic. Local fluctuations might have been encouraged by enantioselective adsorption to chiral crystals[16,17] or by asymmetric photochemistry[18–20] induced by a circularly polarized light (CPL) source.

Chiral crystals have their advocates while others consider asymmetric photochemistry decisive. Crystals or light? While two credible hypotheses may compete for favor, Nature need not be parsimonious and may honor both. Herein, on the basis of our observations of the dendritic growth of phthalic acid (PA) and the light scattering properties of ensembles of these crystallites, we propose a scenario for chiral amplification that employs asymmetric adsorption to crystals and asymmetric photochemistry in concert. Perhaps the combined action of two or more small influences was manifest.

CRYSTALS

Chiral discrimination of organic compounds by minerals has been a rich subject for speculation since the early suggestions by Goldschmidt[21] and Bernal[22] that quartz[23] or chiral clays,[24–26] respectively, may have been responsible for the origin of biomolecular homochirality. Scientists have subsequently worked out many mechanisms of chiral discrimination of molecules by crystal surfaces.[27–35] Others have taken advantage of the chirality of crystal surfaces to achieve practical aims such as heterogeneous asymmetric catalysis.[36] The use of high index metal surfaces in this regard has become an explosive theme.[37]

α-Quartz, the most widely distributed mineral in the earth's crust, has pride of place among studies of the enantioselective adsorption of racemates to minerals.[38] Many researchers have claimed to have partially resolved racemic mixtures with D or L-quartz powders[39–48] but their reports were called into question by Amariglio et al., whose careful reinvestigation of small residual optical activities following presumed enantioselective adsorption were determined to be experimentally insignificant.[49,50] Bonner and Kavasmaneck ultimately collected reliable data on asymmetric adsorption to quartz.[51–53] Most recently, Soai et al. demonstrated the enantioselective reduction of aldehydes in the presence of quartz.[54] However, in the aggregate, research on enantioselective adsorption of chiral compounds to quartz has been protracted and characterized by weak selectivities. Downs and Hazen showed that the facets of quartz are barely chiral according to a reasonable "chirality function" of their invention.[55] We showed computationally that their insights were well founded.[56]

Dextrorotatory and levorotatory quartz appear to be equally distributed on earth.[57] Therefore, a chiral crystal can only be responsible for biomlecular homochirality if we invoke the amplification of the influence of just one such crystal. Given the necessity of this singular "immaculate adsorption," it is evident that enantiomorphous crystals are by no means a requirement in a crystal based mechanism of the origin of biomolecular homochirality. As emphasized by Hazen and coworkers, one of a pair of enantiomorphous faces of achiral crystals may well have produced a local enantiomeric excess.[16,17] Likewise, enantiomorphous vicinal faces of hillocks on achiral faces

Contract grant sponsor: US-National Science Foundation.
*Correspondence to: Bart Kahr, Department of Chemistry, Box 351700, University of Washington, Seattle, WA 98195-1700. E-mail: kahr@chem.washington.edu
Received for publication 2 November 2007; Accepted 21 December 2007
DOI: 10.1002/chir.20539
Published online 29 February 2008 in Wiley InterScience (www.interscience.wiley.com).

might have been sufficient to produce a local chiral bias. De Yoreo et al. showed that racemic aspartic acid was enantioselectively adsorbed to the spiral hillocks on the {104} faces of calcite.[58] Further reduction requires the consideration of enantiomorphous kinks on achiral steps.[59,60]

LIGHT

Feringa and van Delden[4] distinguish three classes asymmetric photochemical processes: preferential photodestruction of one enantiomer, photoresolution of a racemic mixture, and enantioselective photochemical transformation. They trace considerations of enantiodifferentiating photoreactions to the stereochemistry pioneers, Van't Hoff, Le Bel, and Cotton. Kuhn and coworkers first successfully observed such a process.[61,62] However, asymmetric light-induced transformations typically yield small enantiomeric excesses (ees) by virtue of the fact that differences in extinction coefficients for left and right CPL tend to be small. Bonner, by irradiating racemic leucine at 212.8 nm (180 J), achieved only 2% ee.[63,64]

CPL was proposed as a biomolecular homochirality inducing agent in 1977.[65,66] However, photochemical etiologies for the origin of biomolecular homochirality require sources of CPL. Interstellar sources of CPL were first detected by Bailey.[67] He later considered the role of this CPL in the origin of life on earth,[68] albeit while displacing the problem of symmetry breaking to outer space.[69]

Living creatures can be excellent sources of CPL. Some beetles effectively produce CPL by differential reflection, a mechanism akin to that giving rise to the reflection band in cholesteric liquid crystals.[70] However, the authors are unaware of any prebiotic substances with such characteristics. The differential specular reflection of left and right CPL from ordinary crystal surfaces is a weak effect.[71–73]

PHTHALIC ACID SPHERULITES

We previously described PA precipitated rapidly by evaporation of single drops of 20% ethanol/water solutions on glass slides.[74] Concentric polycrystalline (established as the $C2/c$ structure[75] by powder XRD) rings separated by about 30 μm were observed spreading over several square millimeters. Viewed between crossed polarizers, these rings showed "Maltese cross" extinction characteristic of organized radial bodies.

Analysis of the PA aggregates by atomic force microscopy (AFM) revealed that PA is a type-2 spherulite[76] in which the nucleus is a needle rather than a point source. The ends of the needle branch dendritically, covering a plane as they fold around the nucleus to approximate a circular shape.

When rhythmic PA precipitates were imaged at low magnification[74] with a previously described circular extinction imaging microscope[77,78] at 550 nm, they showed division into two large heterochiral fields one of which passes right-handed light more effectively than left-handed light, and vice versa. The general phenomenon described here is known as circular intensity differential scattering (CIDS).[79,80] The average difference in circular transmission $(I_R - I_L)/(I_R + I_L)$ for 0.1 mm^2 sections was ±4(1)%. PA has a mirror plane perpendicular to the [010] axis, and a twofold axis parallel to [010]. In accordance with the Neumann–Curie principle, the division of spherulites into homochiral fields is consistent with a vertical (010) mirror. Any such crystal lying with its *b*-axis on a substrate would have C_s symmetry when the crystal is considered in relation to the surface. Birefringence imaging indicated that the slow axis was always oriented in the radial direction for banded PA spherulites.[81] The largest refractive index of PA is along [010] (n = 1.756).[82] Thus, on average the radii of the branching dendrites are parallel to [010], the slow axis of the crystal.

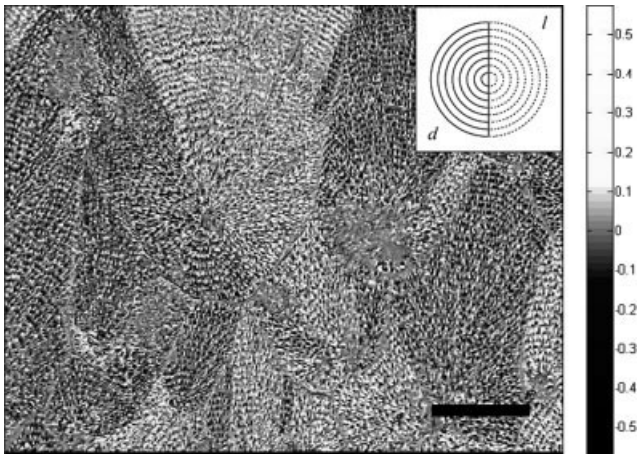

Fig. 1. Phthalic acid spherulites. Micrograph made with a Stokes–Mueller imaging polarimeter. Scale at right is $(I_R - I_L)/(I_R + I_L)$. Scale bar is 0.3 mm. Inset shows schematically the dextrorotatory and levoroatory halves of the spherulites. For a comparable image in color, see Ref. 74.

To verify the nature of the image in Ref. 74, we reproduced it using a wholly different instrument, a homemade Stokes–Mueller imaging polarimeter.[83] A monochromatic light source of 532 nm (diode or Nd:YAG) was passed through a 532 nm interference filter (ThorLabs), linear polarizer (TECHSPEC), and rotatable quarter wave plate (Thorlabs 532 nm Zero Order Waveplate). The sample was placed on the stage of a Amscope microscope whose base was removed. Images were recorded with a 4× objective and a Canon RebelXT digital camera. The quantity $(I_R - I_L)/(I_R + I_L)$ was computed for each green pixel to produce the image in Figure 1. In this way, we obtained large heterochiral fields of 0.1–0.2 mm^2 that preferentially reflect one sense of circular polarization to the extent of about 3–4% when averaged over large portions of like handed halves. The circularly polarized input was analyzed after removing the sample with a Stokes analyzer (rotating quarter waveplate and linear polarizer). The Stokes vectors for the right circular input were [0.98, −0.04, 0.02, 0.95], and for the left circular input were [0.99, 0.03, −0.04, −0.95].

A COMBINED PROPOSAL

It is conceivable that heterochiral mesostructures as observed in PA can be formed by many type-2 spherulitic substances. We can therefore imagine the following sce-

nario for the origin of biomolecular homochirality that takes advantage asymmetric adsorption to crystals and asymmetric photochemistry.

- A common, prebiotic mineral forms macroscopic heterochiral fields of dendritic crystals.
- Enhanced surface areas of dendritic formations, relative to single crystals, favor the adsorption of small organic compounds (PA, for instance, has been shown to orient and overgrow a large number of dyes.[84–89]) enantioselectively, in the respective spherulite hemi-circles.
- One part of the spherulite is in shade while the other part is illuminated.
- The illuminated part scatters light with one circular polarization.
- The other circular polarization acts on organic adsorbates resulting in asymmetric photochemistry, thus producing and concentrating chiral organic compounds with nonenantiomorphous configurations.

In this scenario, we can imagine weak enantioselective adsorption augmented by enantioselective photochemistry. We are not advocating this mechanism. However, the existence of optical micrographs such as those shown in Figure 1, elevate this mechanism to the realm of possibility and it should be considered among any others.

Which likely prebiotic minerals can we identify? Hazen and coworkers have pointed out that the evaporative minerals gypsum (hydrous calcium sulfate), barite (barium sulfate), and apatite (calcium phosphate) display enantiomorphous faces.[16,17] Fibrous,[90] morphologically complex[91] crystals of $BaSO_4$ have been described. Apatite grows spherulitically.[92] These minerals could well be amenable to the mechanism that we propose above on the basis of the optical characterization of rhythmic precipitates of PA.

ACKNOWLEDGMENTS

We thank E. Gunn for her assistance. We are also grateful to the many scholars who have contributed to the accumulated literature on the origins of biomolecular homochirality. We tried to give representative citations but have made no attempt to be exhaustive in this brief report. Our apologies to those whose relevant contributions were omitted.

LITERATURE CITED

1. Mason SF. Molecular handedness and the origins of chiral discrimination. Int Rev Phys Chem 1983;3:217–241.
2. Bonner WA. Origins of chiral homogeneity in Nature. Top Stereochem 1988;18:1–96.
3. Janoschek R. Theories of the origin of biomolecular handedness. In: Janoschek R, editors. Chirality-from weak bosons to the α-helix. Heidelberg: Springer; 1991. p 18–33.
4. Feringa BL, van Delden RA. Absolute asymmetric synthesis: the origin, control, and amplification of chirality. Angew Chem Int Ed Engl 1999;38:3418–3438.
5. Podlech J. Origin of organic molecules and biomolecular homochirality. Cell Mol Life Sci 2001;58:44–60.
6. Weissbuch I, Leiserowitz L, Lahav M. Stochastic "mirror symmetry breaking" via self-assembly, reactivity and amplification of chirality: relevance to abiotic conditions. Top Curr Chem 2005;259:123–165.
7. Bonner WA. Parity violation and the evolution of biomolecular homochirality. Chirality 2000;12:114–126.
8. MacDermott AJ. The ascent of parity-violation: exochirality in the solar system and beyond. Enantiomer 2000;5:153–168.
9. Quack M, Stohner J. Parity violation in chiral molecules. Chimia 2005;59:530–538.
10. Lente G. Stochastic analysis of the parity-violating energy difference between enantiomers and its implications for the origin of biological chirality. J Phys Chem A 2006;110:12711–12713.
11. Siegel JS. Homochiral imperative of molecular evolution. Chirality 1998;10:24–27.
12. Bonner WA. The origin and amplification of biomolecular chirality. Orig Life Evol Biosph 1991;21:59–111.
13. Avalos M, Babiano R, Cintas P, Jiménez JL, Palacios JC. Chiral autocatalysis: where stereochemistry meets the origin of life. Chem Commun 2000:887–892.
14. Soai K, Sato I. Asymmetric autocatalysis and homochirality of biomolecules. Viva Origino 2002;30:186–198.
15. Plasson R, Kondepudi DK, Bersini H, Commeyras A, Asakura K. Emergence of homochirality in far-from-equilibrium systems: mechanisms and role in prebiotic chemistry. Chirality 2007;19:589–600.
16. Hazen RM, Sholl DS. Chiral selection on inorganic crystalline surfaces. Nat Mater 2003;2:367–374.
17. Asthagiri A, Hazen RM. An ab initio study of adsorption of alanine on the chiral calcite (2131) surface. Mol Simul 2007;33:343–351.
18. Jorissen A, Cerf C. Asymmetric photoreactions as the origin of biomolecular homochirality: a critical review. Orig Life Evol Biosph 2002;32:129–142.
19. Meierhenrich UJ, Thiemann WHP. Photochemical concepts on the origin of biomolecular asymmetry. Orig Life Evol Biosph 2004;34: 111–121.
20. Lucas PW, Hough JH, Bailey J, Chrysostomou A, Gledhill TM, McCall A. UV circular polarisation in star formation regions: the origin of homochirality? Orig Life Evol Biosph 2005;35:29–60.
21. Goldschmidt VM. Geochemical aspects of the origin of complex organic molecules on the earth, as precursors to organic life. New Biol 1952;12:97–105.
22. Bernal JD. The physical basis of life. London: Routledge and Paul; 1951.
23. Klabunovskii EI. Can enantiomorphic crystals like quartz play a role in the origin of homochirality on earth? Astrobiology 2001;1:127–131.
24. Bondy SC, Harrington ME. L-amino acids and D-glucose bind stereospecifically to a colloidal clay. Science 1979;23:1243–1244.
25. Friebele E, Shimoyama A, Ponnamperuma C. Possible selective adsorption of enantiomers by sodium montmorillonite. Orig Life 1981;11:173–182.
26. Julg A. Stabilité relative des deux formes inverses optiques de la kaolinite. Application à l'homochiralité L des acides aminés des protéins. C R Acad Sci Ser 2 1988;306:1153–1156.
27. Cody AM, Cody RD. Chiral habit modification of gypsum from expitaxial-like adsorption of stereospecific growth inhibitors. J Cryst Growth 1991;113:508–519.
28. Addadi L, Berkovitch-Yellin Z, Weissbuch I, Lahav M, Leiserowitz L. A link between macroscopic phenomena and molecular chirality: crystals as probes for the direct assignment of absolute-configuration of chiral molecules. In: Eliel EL, Willen SH, Allinger NL, editors. Topics in stereochemistry. New York: Wiley; 1986. p 1–85.
29. Weissbuch I, Popovitz-Biro R, Lahav M, Leiserowitz L. Understanding and control of nucleation, growth, habit, dissolution and structure of 2-dimensional and 3-dimensional crystals using tailor-made auxiliaries. Acta Crystallogr Sect B 1995;51:115–148.
30. Addadi L, Geva M. Molecular recognition at the interface between crystals and biology: generation, manifestation and detection of chirality at crystal surface. Cryst Eng Comm 2003;5:140–146.
31. Kahr B, Gurney RW. Dyeing crystals. Chem Rev 2001;101:893–951.
32. Kahr B, Lovell S, Subramony JA. The progress of logwood extract. Chirality 1998;10:66–77.

33. Gurney RW, Mitchell C, Bastin L, Ham S, Kahr B. Salting benzenes. J Phys Chem B 2000;104:878–892.
34. Kaminsky W, Geday M, Herreros-Cedrés J, Kahr B. Optical rotatory and circular dichroic scattering. J Phys Chem A 2003;107:2800–2807.
35. Kaminsky W, Herreros-Cedrés J, Geday M, Kahr B. Dispersion of optical rotatory and circular dichroic signals in dyed K_2SO_4 crystals. Chirality 2004;16:S55–S61.
36. Sato I, Kadowaki K, Ohgo Y, Soai K. Highly enantioselective asymmetric autocatalysis induced by chiral ionic crystals of sodium chlorate and sodium bromate. J Mol Catal A: Chem 2004;216:209–214.
37. Horvath JD, Gellman AJ. Naturally chiral surfaces. Top Catal 2003;25:9–15.
38. Bonner WA. Origins of molecular chirality. In: Ponnamperuma CP, editor. Exobiology. New York: North Holland Publishing; 1972. p 170–234.
39. Tsuchida R, Kobayashi M, Nakamura A. Asymmetric adsorption of complex salts on quartz. J Chem Soc Jpn 1935;56:1339–1345.
40. Tsuchida R, Kobayashi M, Nakamura A. The configuration of chlorobis-dimethylglyoximoamine cobalt. Bull Chem Soc Jpn 1936;11: 38–40.
41. Bailar JC Jr, Peppard DF. Stereochemistry of complex inorganic compounds. VI. Study of the stereoisomers of dichloro-diamino-ethylenediamine cobaltic ion. J Am Chem Soc 1940;62:105–109.
42. Kuebler JR Jr, Bailar JC Jr. The stereoisomerism of complex inorganic compounds. XIV. Studies upon the stereochemistry of saturated tetravalent nitrogen compounds. J Am Chem Soc 1952;74:3535–3528.
43. Busch DH, Bailar JC Jr. The stereochemistry of complex inorganic compounds. XVII. The stereochemistry of hexadentate ethylenediaminetetraacetic acid complexes. J Am Chem Soc 1953;75:4574–4575.
44. DasSarma B, Bailar JC Jr. The stereochemistry of metal chelates with polydentate ligands. I. J Am Chem Soc 1955;77;5476–5480.
45. Karagounis G, Coumoulos G. A new method for resolving a racemic compound. Nature 1938;142;162–163.
46. Nakahara A, Tsuchida R. Synthesis of the tris-(dimethylglyoximo)-cobaltate III. J Am Chem Soc 1954;76:3103.
47. Klabunovskii EI, Patrikeev VV. Mechanism of the asymmetrizing effect of metal catalysts deposited on right and left quartz. Dokl Akad Nauk SSSR 1951;78:485–487.
48. Terent'ev AP, Klabunovskii EI, Patrikeev VV. Asymmetric synthesis with the aid of catalysts deposited on right and left quartz. Dokl Akad Nauk SSSR 1950;74:947–950.
49. Amariglio A, Amariglio H, Duval X. Asymmetric reactions on optically active quartz. Helv Chim Acta 1968;51:2110–2132.
50. Amariglio A, Amariglio H, Duval X. La synthése asymétrique. Ann Chim 1968;3:5–25.
51. Bonner WA, Kavasmaneck PR, Martin FS, Flores JJ. Asymmetric adsorption by quartz – model for prebiotic origin of optical-activity. Orig Life Evol Biosph 1975;6:367–376.
52. Kavasmaneck PR, Bonner WA. Adsorption of amino acid derivatives by D-and L-quartz. J Am Chem Soc 1977;99:44–50.
53. Bonner WA, Kavasmaneck PR. Asymmetric adsorption of DL-alanine hydrochloride by quartz. J Org Chem 1976;41:2225–2226.
54. Soai K, Osanai S, Kadowaki K, Yonekubo S, Shibata T, Sato I. D- and L-quartz promoted highly enantioselective synthesis of a chiral organic compound. J Am Chem Soc 1999;121:11235–11236.
55. Downs RT, Hazen RM. Chiral indices of crystalline surfaces as a measure of enantioselective potential. J Mol Cat A Chem 2004;216:273–285.
56. Kahr B, Chittenden B, Rohl A. Robert Boyle's chiral crystal chemistry: computational re-evaluation of enantioselective adsorption on quartz. Chirality 2005;18:127–133.
57. Klabunovskii E, Thiemann W. The role of quartz in the origin of optical activity on earth. Orig Life Evol Biosph 2000;30:431–434.
58. Orme CA, Noy A, Wierzbicki A, McBride MT, Grantham M, Teng HH, Dove PM, DeYoreo JJ. Formation of chiral morphologies through selective binding of amino acids to calcite surface steps. Nature 2001;411:775–779.
59. Attard GA, Harris C, Herrero E, Feliu J. Influence of anions and kink structure on the enantioselective electro-oxidation of glucose. Faraday Discuss 2002;121:253–266.
60. Yagi I, Chiba M, Uosaki K. Optical recognition of surface chirality at Au(hkl) single crystalline surfaces by second harmonic generation rotational anisotropy. J Am Chem Soc 2005;127:12743–12746.
61. Kuhn W, Braun E. Photochemische erzeugung optisch aktiver stoffe. Die Naturwissenschaften 1929;17:727–728.
62. Kuhn W, Knopf EP. Darstellung optisch aktiver Stoffe mit Hilfe von Licht. Z phys Chem 1930;B7:292.
63. Flores JJ, Bonner WA, Massey GA. Asymmetric photolysis of (RS)-leucine with circularly polarized UV light. J Am Chem Soc 1977;99:3622–3625.
64. Pagni RM, Compton RN. Is circularly polarized light an effective reagent for asymmetric synthesis? Mini Rev Org Chem 2005;2:203–209.
65. Izumi Y, Tai A. Stereo-differentiating reactions, the nature of asymmetric reactions. New York: Academic Press; 1977.
66. B.Nordén . Was photoresolution of amino acids the origin of optical activity in life? Nature 1977;206:567–568.
67. Bailey J, Chrysostomou A, Hough JH, Gledhill TM, McCall A, Clark S, Ménard F, Tamura M. Circular polarization in star-formation regions: implications for biomolecular homochirality. Science 1998; 281:672–674.
68. Bailey J. Astronomical sources of circularly polarized light and the origin of homochirality. Orig Life Evol Biosph 2001;31:167–183.
69. Caglioti L, Holczknecht O, Fujii N, Zucchi C, Palyi G. Astrobiology and biological chirality. Orig Life Evol Biosp 2006;36:459–466.
70. Srinivasarao M. Nano-optics in the biological world: beetles, butterflies, birds, and moths. Chem Rev 1999;99:1935–1962.
71. Silverman MP, Badoz J. Light-reflection from a naturally optically-active birefringent medium. J Opt Soc Am A 1990;7:1163–1173.
72. Silverman MP, Badoz J, Briat B. Chiral reflection from a naturally optically-active medium. Opt Lett 1992;17:886–888.
73. Silverman MP, Badoz J. Ellipsometric study of specular reflection from a naturally optically-active medium. Thin Solid Films 1993;234:491–495.
74. Gunn E, Sours R, Kaminsky W, Kahr B. Mesoscale chiroptics of rhythmic precipitates. J Am Chem Soc 2006;128:14234–14235.
75. Ermer O. Unusual structural feature of crystalline phthalic-acid. Helv Chim Acta 1981;64:1902–1909.
76. Gránásy L, Pusztai T, Tegze G, Warren J, Douglas J. Growth and form of spherulites. Phys Rev E 2005;72:011605.
77. Claborn K, Puklin-Faucher E, Kurimoto M, Kaminsky W, Kahr B. Circular dichroism imaging microscopy: application to enantiomorphous twinning in 1,8-dihydroxyanthrquinone. J Am Chem Soc 2003;125: 14825–14831.
78. Kaminsky W, Claborn K, Kahr B. Polarimetric imaging of crystals. Chem Soc Rev 2004;33:514–525.
79. Bustamante C, Maestre MF, Tinoco I. Circular intensity differential scattering of light by helical structures. II. Applications. J Chem Phys 1980;73:6046–6055.
80. Bustamante C, Maestre MF, Tinoco I. Circular intensity differential scattering of light by helical structures. I. Theory. J Chem Phys 1980;73:4273–4281.
81. Glazer AM, Lewis JG, Kaminsky W. An automated optical imaging system for birefringent media. Proc R Soc London A 1996;452:2751–2765.
82. Winchell AN. Optical properties of organic compounds. Chicago IL: McCrone Research Institute; 1987. p 122.
83. Goldstein D. Polarized light, 2nd ed. New York: Marcel Dekker; 2003.
84. Mitchell C, Lovell S, Thomas K, Savickas P, Kahr B. Charge transfer interactions in dyed aromatic acid crystals and their relevance to MALDI mass spectrometry. Angew Chem Int Ed Engl 1996;35:1021–1023.
85. Chmielewski J, Lewis J, Lovell S, Zutshi R, Savickas P, Mitchell C, Subramony JA, Kahr B. Single crystal matrix isolation of biopolymers. J Am Chem Soc 1997;119:10565–10566.
86. Lovell S, Marquardt BB, Kahr B. Crystal violet's shoulder. J Chem Soc Perkin2 1999:2241–2248.

87. Kurimoto M, Bastin LD, Fredrickson D, Gustafson PN, Jang S-H, Kaminsky W, Lovell S, Mitchell CA, Chmielewski J, Kahr B. Intrasectoral zoning of proteins and nucleotides in simple crystalline hosts. In: De Yoreo JJ, Casey WH, Malkin AJ, Vlieg E, Ward MD, editors. Morphology and dynamics of crystal surfaces in complex molecular systems. Pittsburgh: Mater Res Soc 2001;620:M981–M9810.
88. Gurney RW, Kurimoto M, Subramony JA, Bastin L, Kahr B. Optical probes of crystal growth mechanisms: intrasectoral zoning, anisotropic organic materials—approaches to polar order. In: Glaser R, Kaszynski P, editors. ACS symposium series, Vol 798. Washington, DC: American Chemical Society; 2001. p 143–156.
89. Benedict JB, Cohen D, Lovell S, Rohl A, Kahr B. What is syncrystallization? States of pH indicator methyl red in single phthalic acid crystals. J Am Chem Soc 2006;128:5548–5559.
90. Limin Q, Cölfen H, Antonietti M, Li M, Hopwood JD, Ashley AJ, Mann S. Formation of $BaSO_4$ fibres with morphological complexity in aqueous polymer solutions. Chem Eur J 2001;7:3526–3532.
91. Shikazono N. Precipitation mechanisms of barite in sulfate-sulfide deposits in back-arc basins. Geochim Cosmochim Acta 1994;58:2203–2213.
92. Shyu JJ, Wu JM. Growth-kinetics of spherulitic apatite in some MgO-CaO-SiO_2-P_2O_5 glasses. J Mater Sci 1994;29:3167–3171.

6-Thioguanine in DNA as CD-Spectroscopic Probe to Study Local Structural Changes upon Protein Binding

RUDOLF REPGES, CHRISTINE BEUCK,† ELMAR WEINHOLD,* GERHARD RAABE,* AND JORG FLEISCHHAUER*
Institute of Organic Chemistry, RWTH Aachen University, Landoltweg 1, D-52074 Aachen, Germany

Presented at the 11th International Conference on Circular Dichroism, 2007, Groningen, Netherlands

ABSTRACT A combination of experimental and theoretical circular dichroism (CD) spectroscopy was used to study local deformations of DNA caused by binding of the base flipping DNA methyltransferase M.TaqI. To selectively study the structural changes within the DNA, we replaced single guanine residues at six different positions in duplex DNA with 6-thioguanine (s^6G), which absorbs at 342 nm where unmodified DNA and the enzyme are transparent. The shape and the transition wavelength of a CD signal around 340 nm in the spectra of the free DNA and the M.TaqI-bound DNA were found to depend on the position of the s^6G probe. Theoretical rotational strengths were calculated employing the matrix method which is frequently used to model the CD of large biomolecules. The only chromophores in these calculations were the nucleic acid bases. Comparison of the measured and the calculated CD spectra showed that the applied computational method qualitatively reproduces the dominant band observed around 340 nm in all cases. From our results we conclude that the spectral changes observed upon binding of the enzyme to the DNA are indeed predominantly due to structural changes within the DNA and not to other effects caused by the presence of the enzyme. *Chirality 20:978–984, 2008.*

KEY WORDS: circular dichroism; matrix method calculations; protein binding; structural changes; DNA; M.TaqI; 6-thioguanine

INTRODUCTION

Circular dichroism (CD) spectroscopy is a useful tool to study global conformational changes of the DNA double helix. Thus, for example, the A, B, and Z form of DNA[1] give different characteristic CD spectra. Enzymes which modify the nucleobases in DNA often gain access to their targets by flipping the corresponding base out of the inner part of the DNA helix (see Fig. 1). Such a base flipping can cause in principle significant structural changes both within the DNA and the enzyme, and thus a strong influence on the CD of both components is expected. However, since the absorption bands of the DNA bases strongly overlap with those of the proteinogenic aromatic amino acid side chains, it is extremely difficult to correlate the observed changes of the total CD with certain structural changes in either the DNA or the enzyme part of the complex. Thus, for the selective observation of local structural changes within the DNA, we incorporated[3] a CD spectroscopic probe into the nucleic acid which absorbs in a range where there is no overlap with the UV absorptions of the unmodified part of the DNA or of the enzyme.

A similar approach was previously pursued by Johnson and von Hippel using 2-aminopurine (2-AP),[4–6] a structural isomer of adenine, and pyrrolo-cytosine (PC),[7] a bicyclic cytosine derivative, both absorbing above 300 nm where nucleic acids and proteins are transparent. Replacement of adenine residues with 2-AP or cytosine residues with PC produced strong CD signals depending on their nearest neighbors and was utilized to monitor local structural changes in DNA and RNA. However, these structural modifications—moving the exocyclic amino function of adenine or fusing another ring to cytosine—could interfere significantly with binding of proteins that specifically recognize nucleobases, especially when the two base analogues are placed within the recognition sequence. To avoid such problems we replaced single guanine residues within a DNA duplex containing 14 base pairs (14 mer) by 6-thioguanine (s^6G) as a CD-spectroscopic probe to study local structural changes upon protein binding.[3] 6-Thioguanine which can be incorporated into DNA by solid-phase DNA synthesis,[8] is an analogue of guanine where only the

This work was performed by R. R. and C. B. in partial fulfilment of the requirements for the Ph.D. degree at the Institute of Organic Chemistry, RWTH Aachen University.

†Present address: The Scripps Research Institute, Department of Molecular Biology, MB-33, 10550 North Torrey Pines Road, La Jolla, CA 92037, USA.

Contract grant sponsor: Studienstiftung des deutschen Volkes.

*Correspondence to: Jörg Fleischhauer or Elmar Weinhold or Gerhard Raabe, Institute of Organic Chemistry, RWTH Aachen University, Landoltweg 1, D-52074 Aachen, Germany.
E-mail: joerg.fleischhauer@thc.rwth-aachen.de or elmar.weinhold@oc.rwth-aachen.de or gerd.raabe@thc.rwth-aachen.de

Received for publication 31 October 2007; Accepted 21 December 2007
DOI: 10.1002/chir.20540
Published online 21 February 2008 in Wiley InterScience (www.interscience.wiley.com).

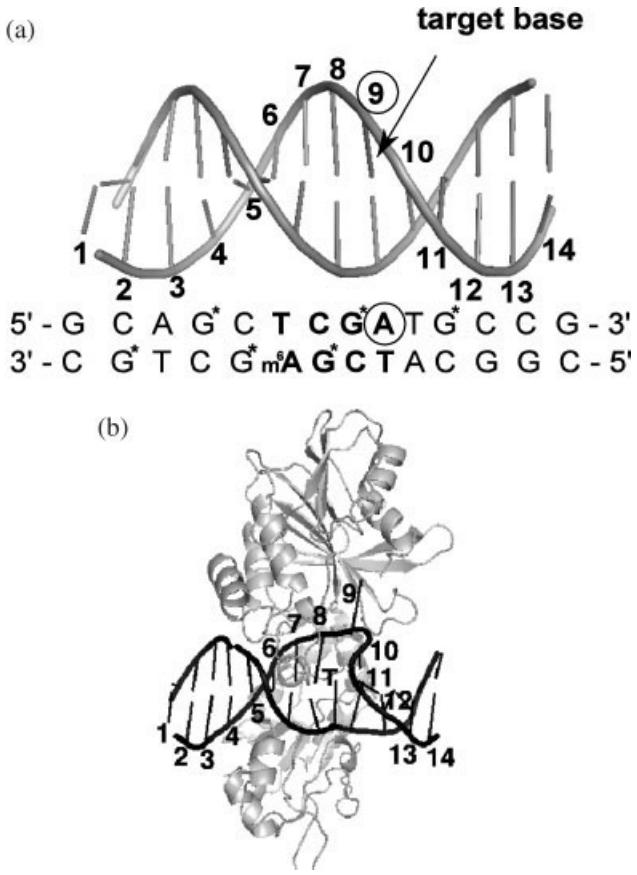

Fig. 1. (**a**) Structure of the free DNA (14 mer) generated with the 3DNA software.[2] The target base modified by M.TaqI is the adenine residue at base pair position 9. The target adenine of the complementary strand was methylated at the N6 position (m^6A = N6-methyladenine) to direct binding of M.TaqI in a single orientation. Guanine residues which were individually replaced by 6-thioguanine are starred and the recognition sequence of M.TaqI is in bold type. (**b**) Structure of the DNA (14 mer) in complex with M.TaqI generated from the coordinates of the DNA (10 mer) bound to M.TaqI (Protein Data Bank entry number 1G38). The figure shows the flipped-out target adenine at base pair position 9 and the opposing thymine (labeled T) partly inserted into the opened space left behind.

carbonyl oxygen atom is replaced by sulphur and exhibits a UV maximum at 342 nm.[9,10] When this probe is incorporated into DNA, the resulting CD-spectrum above 300 nm should predominantly depend on the local environment of the thiobase, especially on its orientation relative to the neighboring stacked nucleobases.

To support the assumption that the observed changes of the CD spectra above 300 nm which are caused by addition of M.TaqI are indeed predominantly due to structural changes in the DNA and not to other effects caused by the presence of the enzyme, we performed calculations on the CD spectra of both the free DNA and the DNA in complex with the enzyme. The matrix method of Bayley et al.[11] in its dipole–dipole approximation has recently been used successfully to understand at least qualitatively the differences between the CD spectra of three different G-quadruplexes, while matrix method calculations using INDO/S monopoles gave less satisfying results.[12] Encouraged by the good performance of the dipole–dipole approximation we decided to apply the same method to the current problem.

MATERIALS AND METHODS

Modified DNA, Enzyme, and Measurement of CD spectra

s^6G-substituted DNA was produced by solid-phase DNA synthesis employing the 5′-dimethoxytrityl-N2-trifluoroacetyl-2′-deoxy-6-(2-cyanoethyl)thioguanosine,3′-[(2-cyanoethyl)-(*N*,*N*-diisopropyl)]-phosphoramidite (Glen Research, Sterling, VA) and used to detect local deformations caused by protein binding. For this purpose we used the structurally well characterized N6-adenine-DNA-methyltransferase from *Thermus aquaticus* (M.TaqI) which binds as a monomer to the double-stranded 5′-TCGA-3′ recognition sequence and flips the target adenine out of the helix while inserting the partner thymine into the space left behind (Fig. 1b).[13] To direct binding of M.TaqI on the palindromic recognition sequence in one orientation, the target adenine of the lower complementary strand was methylated. At six different positions of a DNA duplex with fourteen base pairs (14 mer, Fig. 1a) single guanine residues were replaced by 6-thioguanine and the CD spectra of the six free DNA duplexes (25 μM) and of the six DNA duplexes (25 μM) with M.TaqI (31 μM) were measured in solution. The CD spectra were recorded at room temperature in a buffered aqueous solution (20 mM Tris/HOAc, 10 mM $Mg(OAc)_2$, 50 mM KOAc, 1 mM DTT, 0.01% Triton X-100 reduced form, pH 7.9) on an AVIV (Lakewood, NJ) 62DS spectrometer. The path length of the optical cell was 10 mm and the spectral bandwidths were 2 nm at $\lambda \leq 250$ nm and 1 nm at $\lambda > 250$ nm.

Computational Methods

The matrix method calculations were performed using a modified version[14] of the program MATMAC.[15] The model structures of the free modified DNA duplexes containing 14 base pairs (14 mer) were generated using the 3DNA software package.[2] The structures of the DNA duplexes bound to M.TaqI were generated starting from the solid state structure of a 10 mer DNA duplex in complex with M.TaqI[13] which was completed to 14 mers using the same software as for the free DNA. As a result the structures of the DNA in complex with the enzyme and the free DNA are identical at base pair positions 1 and 2 as well as 13 and 14.

This process is described in detail in Ref. 3. The nucleic acid bases were the only chromophoric groups used in the calculations on both the free DNA and the DNA in complex with the enzyme. The influence of the sugar backbone was neglected since the corresponding electronic transitions occur at wavelengths shorter than those of the measured CD spectra. Moreover, the influence of the chromophores of the enzyme was also neglected because of their large distance from the thiobase. As in Ref. 12 the centre of the positive charge of the heavy atoms of each base was chosen as the origin of the corresponding dipole moment. Calculated transition energies and electric transition moments were used throughout this study. The geometries of the nucleic acid base molecules were optimized under constraint of C_s symmetry at the B3LYP/DGDZVP[16–19] level of density functional theory as implemented in the

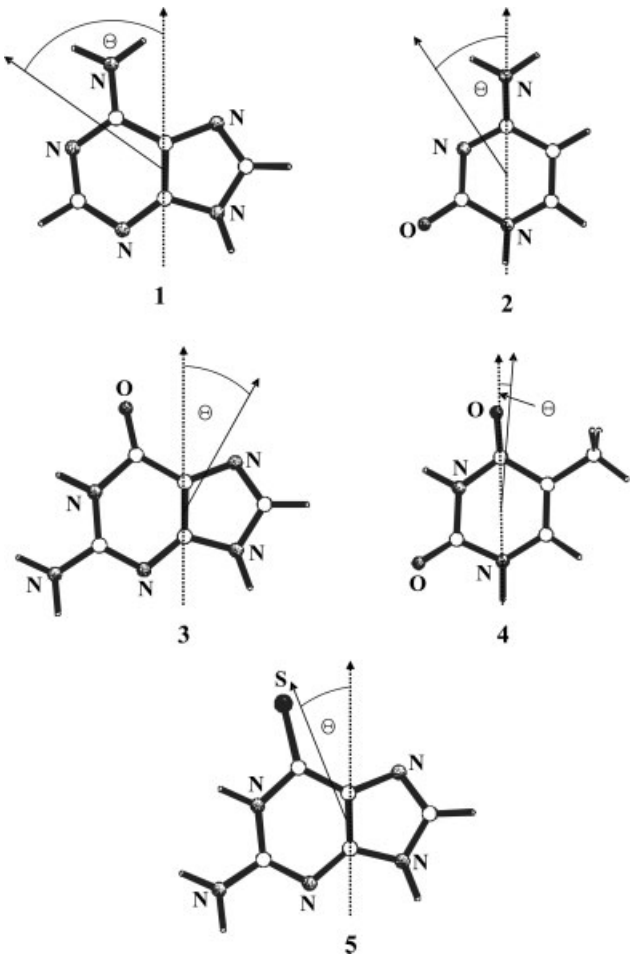

Fig. 2. Structures of adenine (1), cytosine (2), guanine (3), thymine (4), and 6-thioguanine (5) optimized at the B3LYP/DGDZVP level of density functional theory showing schematically the definition of the orientation of the lowest electronic $\pi \rightarrow \pi^*$ transition dipole moment relative to the heavy atom skeletons of the molecules. The actual numerical values for Θ are given in Tables 1–5. Molecular structures were plotted using the program SCHAKAL.[24]

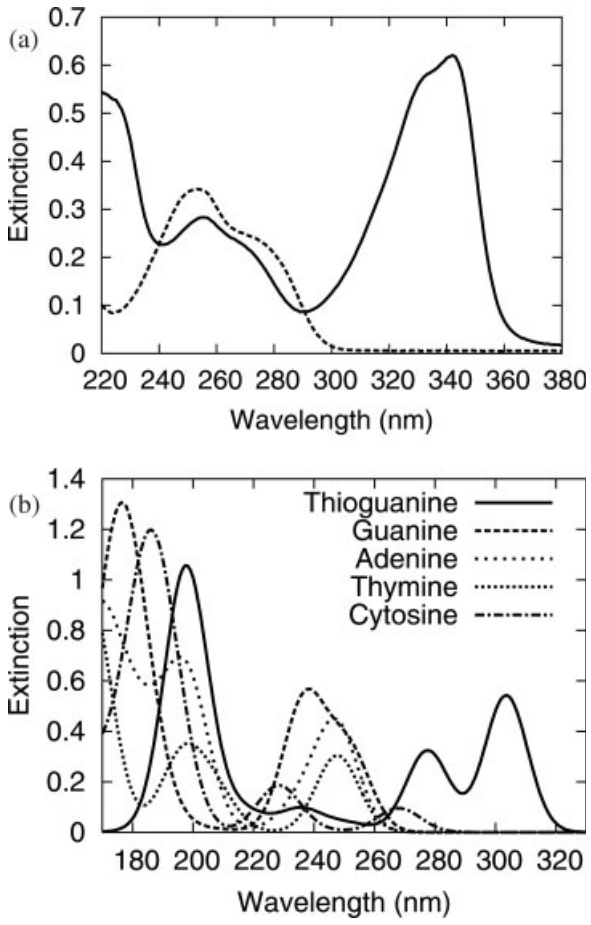

Fig. 3. (**a**) The experimental absorption spectra of 6-thio-2′-desoxyguanosine (solid line) and 2′-desoxyguanosine (dashed line). (**b**) The absorption spectra of adenine (1), cytosine (2), guanine (3), thymine (4), and 6-thioguanine (5) calculated with the time dependent density functional theory using the B3LYP functional, the TZVP basis set, and the B3LYP/DGDZVP-optimized molecular structures. Note that 6-thioguanine causes a relatively strong absorption in a region where the other bases are transparent.

GAUSSIAN03 suite of quantum-chemical routines.[20] Using the resulting geometries the excitation energies and transition moments were calculated at the time-dependent level of density functional theory (TDDFT)[21] using the program TURBOMOLE,[22] the same functional and the TZVP[23] basis set. The TDDFT calculations of the free nucleic acid bases have been performed considering the 15 lowest transitions. The two lowest $\pi \rightarrow \pi^*$ transitions emerging from these calculations have then been used in the calculation of the CD spectra with the matrix method shown in Figure 4. The calculated CD curves were obtained as a sum of Gaussians. Each of the Gaussians was centred at the corresponding transition wavelength (λ_{max}) and was multiplied with the rotational strength belonging to this transition. The Gaussians were generated using a half bandwidth of $\Gamma = 10$ nm at $\Delta\varepsilon_{max}/e$. As mentioned in the introduction the matrix calculations were performed using the dipole–dipole approximation. In the case of the isolated nucleobases adenine, cytosine, guanine, and thymine only the two energetically lowest $\pi \rightarrow \pi^*$ transitions were included while only the low-

TABLE 1. Transition wavelengths (λ, nm), oscillator strengths (*f*), absolute values of the electric transition moments (|μ|, Debye), and transition moment directions (Θ, degrees) for the two energetically lowest electronic π→π* transitions of guanine calculated at the TDDFT/B3LYP/DGDZVP//B3LYP/TZVP level

	TDDFT	Exp.
λ	250	278
f	0.13	0.16
|μ|	2.63	3.07
Θ	−34	−4(3)
λ	236	254
f	0.24	0.25
|μ|	3.47	3.67
Θ	+76	+105(3)

The experimental data given for reasons of comparison are for 9-ethylguanine from Ref. 25. Compilations of experimental and theoretical values for the excitation energies, transition moment directions, and oscillator strengths from different sources for adenine and guanine, cytosine, and thymine as well as for some of their derivatives are given in Refs. 26, 27, and 28.

TABLE 2. Transition wavelengths (λ, nm), oscillator strengths (*f*), absolute values of the electric transition moment (|μ|, Debye), and transition moment directions (Θ, degrees) for the energetically lowest electronic π→π* and *n*→π* transitions of 6-thioguanine calculated at the TDDFT/B3LYP/DGDZVP//B3LYP/TZVP level. The experimental data given for reasons of comparison are for the N9H tautomer of 6-thioguanine from Refs. 9 and 10

	TDDFT	Exp
π→π*		
λ	301	342
f	0.26	0.47
|μ|	4.08	5.84
Θ	+18	–
n→π*		
λ	396	
f	0.00	
|μ|	0.00	
Θ	–[a]	

[a]The transition moment direction of the *n*→π* transition is perpendicular to the plane of the molecule.

est π → π* transition was used for 6-thioguanine. Addition of the very weak calculated *n* → π* transition at 396 nm (see Table 2) in the matrix calculations caused only negligible changes of all of the calculated spectra. Moreover, increasing the number of π → π* transitions to 10 did not change the spectra significantly. Like in Ref. 12 magnetic transition moments were omitted in these calculations, and in addition, the transition moments between the excited states as well as the three permanent electric moments (i.e., those of the ground state and the two excited states) were neglected. This procedure was successfully used in our study of G-quartets to understand at least qualitatively their CD spectra.[12] We call this approximation Method 1.

In another set of calculations (Method 2) calculated quadrupole transition moments were included where the origins of the moments were chosen as in the case of the dipole moments.

TABLE 3. Transition wavelengths (λ, nm), oscillator strengths (*f*), absolute values of the electric transition moments (|μ|, Debye), and transition moment directions (Θ, degrees) for the two energetically lowest electronic π→π* transitions of adenine calculated at the TDDFT/B3LYP/DGDZVP//B3LYP/TZVP level

	TDDFT	Exp
λ	246	275
F	0.18	0.10
|μ|	3.07	2.42
Θ	+58	+83(8)
λ	234	255
f	0.06	0.20
|μ|	1.68	3.39
Θ	+31	+25(5)

The experimental data given for reasons of comparison are from Ref. 29. See footnote Table 1.

TABLE 4. Transition wavelengths (λ, nm), oscillator strengths (*f*), absolute values of the electric transition moments (|μ|, Debye), and transition moment directions (Θ, degrees) for the two energetically lowest electronic π→π* transitions of cytosine calculated at the TDDFT/B3LYP/DGDZVP//B3LYP/TZVP level

	TDDFT	Exp.
λ	266	268
f	0.04	0.06
|μ|	1.50	1.85
Θ	+39	+6(2)
λ	227	241
f	0.09	0.07
|μ|	2.09	1.89
Θ	0	−35(30)[a]

The experimental data given for reasons of comparison are for cytosine monohydrate from Ref. 30. See footnote Table 1.
[a]Value uncertain.

To further test for the influence of magnetic moments we included them in a third series of calculations (Method 3).

RESULTS AND DISCUSSION

DFT and TDDFT Calculations on the Five Nucleic Acid Bases

The optimized structures of the five nucleic acid bases and the definition of the directions of the transition moments of the lowest excitations relative to the heavy atom skeletons of the molecules as defined by the angle Θ are shown in Figure 2b, and the calculated absorption spectra are given in Figure 3. Numerical values for λ_{max}, the oscillator strengths, and the angles Θ for each of the five bases are given in Tables 1–5. Compared with the experimental data the TDDFT results for the first and second π → π* transitions of the bases are shifted to the blue. T1-T5

Experimental and Calculated CD Spectra

The experimental[3] and the CD spectra calculated with Method 1[14] are shown in Figure 4, columns one and two,

TABLE 5. Transition wavelengths (λ, nm), oscillator strengths (*f*), absolute values of the electric transition moments (|μ|, Debye), and transition moment directions (Θ, degrees) for the two energetically lowest electronic π→π* transitions of thymine calculated at the TDDFT/B3LYP/DGDZVP//B3LYP/TZVP level

	TDDFT	Exp.
λ	246	275
F	0.14	–
|μ|	2.70	–
Θ	−5	−12
λ	206	213
F	0.07	–
|μ|	1.75	–
Θ	−34	(−31 or +91)[a]

The experimental data given for reasons of comparison are from Ref. 31. See footnote Table 1.
[a]Value uncertain.

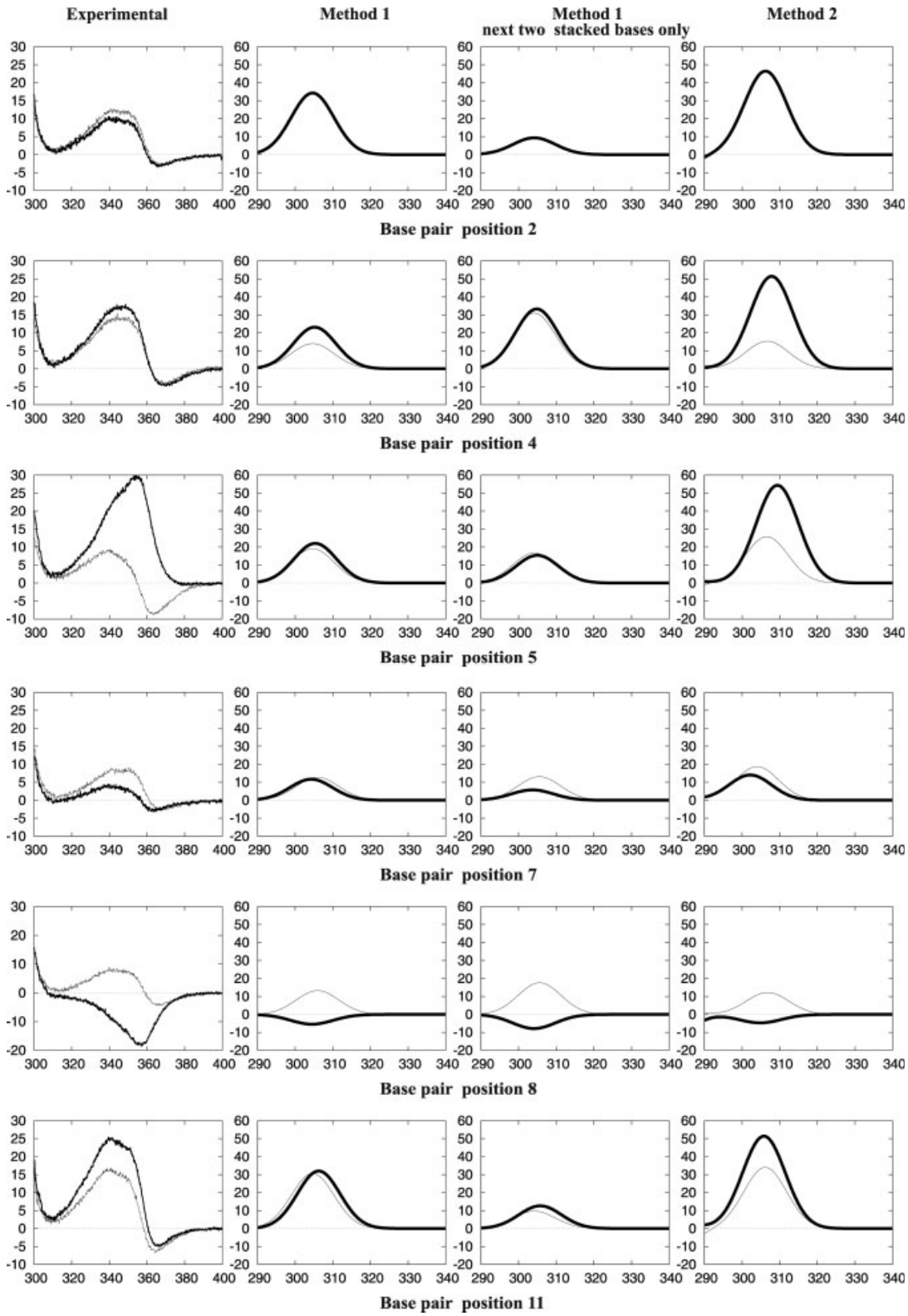

Fig. 4. Experimental (first column) and calculated (columns 2–4) CD spectra of pure DNA (gray, light-faced) and theDNA/MTaqI complexes (black, bold) with 6-thioguanine at 6 different positions. The CD is in $\Delta\varepsilon$ (1000 cm^2/mol), the wavelengths are in nm. The spectra shown in column two are those calculated with Method 1. Those in column 3 were also calculated with Method 1, however, only the two nearest stacked neighbors of the thiobase were included. Finally the spectra shown in column four were obtained with Method 2. Note that compared with the experimental spectra the calculated CD curves are somewhat shifted to the blue resulting in different wavelength scales for the observed and the theoretical spectra.

respectively, where the gray curves are the CD spectra of the free and the black ones those of the DNA in complex with the enzyme. The CD peak observed near 340 nm showed changes upon M.TaqI binding which were found to depend on the position of the thiobase. These changes were most significant for base pair positions 8 and 5 (Figs. 1 and 4). Because the structures of the DNA in complex with the enzyme and the free DNA are identical at base pair positions 1 and 2 the environment of the 6-thioguanine in position 2 is very similar in both structures and their calculated CD curves essentially coincide. With one exception the experimental CD spectra have dominant positive Cotton effects around 340 nm. The exception is the DNA/enzyme complex with s^6G at base pair position 8 (see Figs. 1 and 4) which is the position in immediate vicinity of the flipped adenine and the interstrand stacked partner thymine (inserted into the opened space after base flipping). This structure gives a negative CD curve between 310 and 400 nm. Compared with the experimental spectra the calculated bands are shifted about 30 nm to the blue. A similar blue shift of 18–36 nm was observed in our previous study of G-quartets[12] when experimental excitation energies and transition dipole moments were replaced by values obtained at the TDDFT level using the same functional and basis set as in this study. In spite of the blue shift the calculated spectra qualitatively reproduce the shape of their experimental counterparts around 340 nm. This is also true for the structure that causes a negative CD curve between 310 and 400 nm (base pair position 8) where s^6G is expected to be stacked between its 5′ neighbor and the interstrand stacked partner of the target adenine. However, a small negative Cotton effect observed for all but one* structure around 365 nm is missing in the calculated spectra. This band is probably due to coupling of the energetically lowest $n \rightarrow \pi^*$ transition with the $\pi \rightarrow \pi^*$ transitions of s^6G in the static field of the DNA which was omitted in our calculations. Yet the good qualitative reproduction of the experimental spectra around 340 nm supports the assumption that the changes of the CD spectra above 300 nm observed upon addition of M.TaqI to single-atom-edited DNA are largely due to structural changes of the DNA caused by the enzyme.

We also performed calculations on the free DNA and on the DNA/enzyme complex where only the two nearest stacked neighbours of s^6G were considered. The results are shown in column three of Figure 4. With the exception of the CD spectrum calculated for s^6G in base pair position 5, where compared with the experimental result the curves for the free nucleic acid and the DNA/M.TaqI complex are interchanged, these calculated spectra also qualitatively reproduce the general shapes of their experimental counterparts around 340 nm. Therefore, we conclude that the bands observed around 340 nm are predominantly due to coupling of the energetically lowest $\pi \rightarrow \pi^*$ transition of the thiobase with the lowest $\pi \rightarrow \pi^*$ transitions of its stacked nucleobase neighbors.

Using quadrupole moments in addition to the dipole moments (Method 2) gave the CD spectra shown in column four of Figure 4. As far as the relative intensities of the CD curves calculated for the free DNA and the DNA in complex with the enzyme are concerned, the agreement between the calculated and the measured CD spectra is improved for substitution at base pair positions 5 and 11, while it got worse for substitution at base pair position 4.

Inclusion of magnetic moments (Model 3) does not change the calculated CD spectra significantly. The resulting CD curves are, therefore, not shown.

*The exception is the structure where s^6G is in base pair position 5 of the DNA/M.TaqI complex.

CONCLUSIONS

The matrix method in the dipole–dipole approximation using transition energies and transition moments calculated with the time-dependent density functional theory was successfully used to reproduce qualitatively the general features of the experimental CD spectra of single-atom-edited DNA (replacement of oxygen in single G residues by sulfur) in its free form and in complex with M.TaqI above 300 nm. The only structural changes caused by the addition of the complex considered in our calculations were those of the DNA. Compared with the experimental data the calculated bands are shifted about 30 nm to the blue. However, the generally good qualitative agreement between theoretical and measured CD spectra led us to the conclusion that the spectral changes observed around 340 nm upon the addition of the enzyme are mainly due to local structural changes in the DNA caused by binding of the enzyme and are not merely because of the presence of the enzyme. Thus, s^6G in duplex DNA can serve as a good CD-spectroscopic tool to study local DNA deformations induced by protein binding.

A detailed description of all experimental aspects of this study is currently being prepared and will be published separately.

LITERATURE CITED

1. Saenger W. Principles of nucleic acid structure. New York: Springer-Verlag; 1984. p 253.
2. Lu X-J, Olson WK. 3DNA: a software package for the analysis, rebuilding and visualization of three-dimensional nucleic acid structures. Nucleic Acids Res 2003;31:5108–5121.
3. Beuck C. DNA mit Thiobasen und polycyclischen aromatischen Basensurrogaten zur Untersuchung des Base Flippings am Beispiel der DNA-Methyltransferase M.TaqI. Doctoral thesis, Aachen 2004. Aachener Beiträge zur Chemie, Vol. 59. Druck und Verlagshaus Mainz GmbH, Aachen.
4. Johnson NP, Baase WA, von Hippel PH. Low-energy circular dichroism of 2-aminopurine dinucleotide as a probe of local conformation of DNA and RNA. Proc Natl Acad Sci USA 2004;101:3426–3431.
5. Johnson NP, Baase WA, von Hippel PH. Low energy CD of RNA hairpin unveils a loop conformation required for λN antitermination activity. J Biol Chem 2005;280:32177–32183, 41123–41124.
6. Datta K, Johnson NP, von Hippel PH. Mapping the conformation of the nucleic acid framework of the T7 RNA polymerase elongation complex in solution using low-energy CD and fluorecence spectroscopy. J Mol Biol 2006;360:800–813.
7. Johnson NP, Baase WA, von Hippel PH. Investigating local conformations of double-stranded DNA by low-energy circular dichroism of pyrrolo-cytosine. Proc Natl Acad Sci USA 2005;102:7169–7173.
8. Christopherson MS, Broom AD. Synthesis of oligonucleotides containing 2′-deoxy-6-thioguanosine at a predetermined site. Nucleic Acids Res 1991;19:5719–5724.

9. Rubin YuV, Blagoy YuP, Bokovoy VA, Leontiev VS, Lee RG. The investigation of structural transitions and energy transfer in DNA solution in range 4.2–273K using 6-thioguanine. Int J Quantum Chem: Quantum Biol Symp 1994;21:187–194.
10. Rubin YuV, Blagoi YuP, Bokovoy VA. 6-Thioguanine luminescence probe to study DNA and low-molecular-weight systems. J Fluorescence 1995;5:263–272.
11. Bayley PM, Nielsen EB, Schellman JA. The rotatory properties of molecules containing two peptide groups: theory. J Phys Chem 1969; 73:228–243.
12. Gray DM, Wen J-D, Gray CW, Repges R, Repges Ch, Raabe G, Fleischhauer J. Measured and calculated CD spectra of G-quartets stacked with the same or opposite polarities. Chirality 2008;20:431–440.
13. Goedecke K, Pignot M, Goody RS, Scheidig AJ, Weinhold E. Structure of the N6-adenine DNA methyltransferase M.TaqI in complex with DNA and a cofactor analog. Nat Struct Biol 2001;8:121–125.
14. Repges R. Berechnung des Circulardichroismus von β-Oligopeptiden und Oligonucleotiden mit dem klassischen, Dipole Interaction Model' und der quantenmechanischen Matrixmethode. Doctoral thesis, Aachen, Germany, 2006.
15. Fleischhauer J, Kramer B, Zobel E, Koslowski A. The program MATMAC allows calculation of the rotational strengths of biopolymers using Tinoco's method and the matrix method. Aachen, Germany, 1991. (A copy of the program code is available from J.Fleischhauer or G.Raabe).
16. Becke AD. A new mixing of Hartree–Fock and local density functional theories. J Chem Phys 1993;98:1372–1377.
17. Becke AD. Density-functional thermochemistry. III. The role of exact exchange. J Chem Phys 1993;98:5648–5652.
18. Stephens PJ, Devlin FJ, Chabalowski CF, Frisch MJ. Ab initio calculation of vibrational absorption and circular dichroism spectra using density functional force fields. J Phys Chem 1994;98:11623–11627.
19. Godbout N, Salahub DR, Andzelm J, Wimmer E. Optimization of gaussian-type basis sets for local spin density functional calculations. I. Boron through neon, optimization technique and validation. Can J Chem 1992;70:560–571.
20. Frisch MJ, Trucks GW, Schlegel HB, Scuseria GE, Robb MA, Cheeseman JR, Montgomery JA Jr, Vreven T, Kudin KN, Burant JC, Millam JM, Iyengar SS, Tomasi J, Barone V, Mennucci B, Cossi M, Scalmani G, Rega N, Petersson GA, Nakatsuji H, Hada M, Ehara M, Toyota K, Fukuda R, Hasegawa J, Ishida M, Nakajima T, Honda Y, Kitao O, Nakai H, Klene M, Li X, Knox JE, Hratchian HP, Cross JB, Adamo C, Jaramillo J, Gomperts R, Stratmann RE, Yazyev O, Austin AJ, Cammi R, Pomelli C, Ochterski J W, Ayala PY, Morokuma K, Voth GA, Salvador P, Dannenberg JJ, Zakrzewski VG, Dapprich S, Daniels AD, Strain MC, Farkas O, Malick DK, Rabuck AD, Raghavachari K, Foresman JB, Ortiz JV, Cui Q, Baboul AG, Clifford S, Cioslowski J, Stefanov BB, Liu G, Liashenko A, Piskorz P, Komaromi I, Martin RL, Fox DJ, Keith T, Al-Laham MA, Peng CY, Nanayakkara A, Challacombe M, Gill PMW, Johnson B, Chen W, Wong MW, Gonzalez C, Pople JA. GAUSSIAN03, Revision C.02. Wallingford CT: Gaussian, Inc.; 2004.
21. Bauernschmitt R, Ahlrichs R. Treatment of electronic excitations within the adiabatic approximation of time dependent density functional theory. Chem Phys Lett 1996;256:454–464.
22. Ahlrichs R, Bär M, Baron H-P, Bauernschmitt R, Böcker S, Ehrig M, Eichkorn K, Elliott S, Furche F, Haase F, Häser M, Horn H, Huber C, Huniar U, Kattannek M, Kölmel C, Kollwitz M, May K, Ochsenfeld C, Öhm H, Schäfer A, Schneider U, Treutler O, von Arnim ,M, Weigend F, Weis P, Weiss H. TURBOMOLE Version 5. Lehrstuhl für Theoretische Chemie: Universität Karlsruhe; 1998.
23. Schäfer A, Huber C, Ahlrichs R. Fully optimized contracted Gaussian basis sets of triple zeta valence quality for atoms Li to Kr. J Chem Phys 1994;100:5829–5835.
24. Keller E. SCHAKAL. A FORTRAN program for the graphical representation of molecular and solid-state structure models. Albert-Ludwigs-Universität Freiburg: Kristallographisches Institut. (See also: Keller E. Neues von SCHAKAL. Chem u Z 1986;20:178–181).
25. Clark LB. Electronic spectra of crystalline 9-ethylguanine and guanine hydrochloride. J Am Chem Soc 1977;99:3934–3938.
26. Fülscher MP, Serrano-Andrés L, Roos BO. A theoretical study of the electronic spectra of adenine and guanine. J Am Chem Soc 1997;119: 6168–6176.
27. Fülscher MP, Roos BO. Theoretical study of the electronic spectrum of cytosine. J Am Chem Soc 1995;117:2089–2095.
28. Lorentzon J, Fülscher MP, Roos BO. Theoretical study of the electronic spectra of uracil and thymine. J Am Chem Soc 1995;117:9265–9273.
29. Clark LB. Electronic spectrum of the adenine chromophore. J Phys Chem 1990;94:2873–2879.
30. Žaloudek F, Novros JS, Clark LB. The electronic spectrum of cytosine. J Am Chem Soc 1985;107:7344–7351.
31. Novros JS, Clark LB. On the electronic spectrum of 1-methyluracil. J Phys Chem 1986;90:5666–5668.
32. Anex BG, Fucaloro AF, Dutta-Ahmed A. Single-crystal quartz-ultraviolet spectra of thymine anhydrate. Further evidence for the degeneracy of the 260-μm band of the uracils. J Phys Chem 1975;79:2636–2639.

CHIRALITY 20:985–994 (2008)

Review Article

Investigating by CD the Molecular Mechanism of Elasticity of Elastomeric Proteins

BRIGIDA BOCHICCHIO, ANTONIETTA PEPE, AND ANTONIO M. TAMBURRO*
Department of Chemistry, University of Basilicata, 85100 Potenza, Italy

Presented at the 11th International Conference on Circular Dichroism, 2007, Groningen, Netherlands

ABSTRACT Elastomeric proteins are widespread in the animal kingdom, and their main function is to confer elasticity and resilience to organs and tissues. Besides common functional properties, elastomeric proteins share a common sequence design. They are usually constituted by repetitive sequences with a high content of glycine residues. From a conformational point of view, all the elastomeric proteins since now analyzed show a dynamic equilibria between folded (mainly β-turns) and extended (poly-proline II and β-strands) conformations that could be at the origin of the high entropy of the relaxed state. As a matter of fact, elastin, lamprin, abductin, as well as the PEVK domain of titin share the same conformational ensemble, thus pointing to a common molecular mechanism as the origin of elasticity. CD spectroscopy represents the proper spectroscopic technique to be used overall because of its particular sensitivity to the presence of PPII structure. Its use in the molecular studies of elastin, abductin, and lamprin as well as the recently analyzed protein resilin will be presented. *Chirality 20:985–994, 2008.*

KEY WORDS: elastin; abductin; resilin; sliding β-turns; poly-proline II

INTRODUCTION

Elastomeric proteins are present in a wide range of living organisms spanning from plants to humans. They are contained in vertebrates (elastin,[1,2] titin,[3] lamprin[4]), plants (gluten[5]), insects (resilin,[6–8] flagelliform silk[9,10]), bivalve molluscs (abductin[11]), and mussels (byssus threads[12]). The main function of elastomeric proteins is to confer rubber-like elasticity to organs and tissues thus enabling them to undergo high deformation without rupture and to return to their original state on removal of the stress.[13] Accordingly, the energy stored during the deformation process is entirely conserved and returned. The second stage of this process is passive and does not require an input of energy. This mechanism is of entropic origin and it well adapts to materials able to last a long time. For example, in the case of elastin the aortic elastin undergoes millions of stress–strain cycles in a human life span, and in mussels where byssus threads binding to rocks resist wave actions. Furthermore, the elastomeric polypeptide sequences are characterized by the presence of constraints that render them resistant to rupture, localized into nonelastic domains, and called cross-links. The elasticity will depend on the length of elastic sequences and on the extent of the cross-link domains. As a matter of fact, the presence of a network of crosslinks (covalent or noncovalent) should be one of the common features to most of those proteins together with that of elastic repeated sequences with highly flexible monomeric chains and with high content of glycyl residues (Table 1).

These observations lead us to investigate, on the basis of structural studies, the possibility of a common molecular mechanism of elasticity for the elastomeric proteins. Within this framework, CD studies were fundamental in order to work out a structure–function relationship for elastin.[14–16] On this basis, in this article our aim is to report on the extension of CD studies to other elastomeric proteins of extracellular matrix, different from elastin such as, for example, resilin and abductin. While elastin is the well-known and widely investigated elastomeric protein of vertebrates, structural studies regarding resilin, present in insects such as locusts, cicades, dragonflies, and fruit flies, and abductin, present in mollusc bivalves, such as scallops, are very few, if any. A further element of interest rose from the knowledge that elastin and resilin express their resilience after removal of the extension force, whereas abductin responds to a compressive force.

Contract grant sponsor: The European Union; Contract grant number: 018960
*Correspondence to: Antonio M. Tamburro, Department of Chemistry, University of Basilicata, Via N. Sauro 85, 85100 Potenza, Italy.
E-mail: antonio.tamburro@unibas.it
Received for publication 31 October 2007; Accepted 21 December 2007
DOI: 10.1002/chir.20541
Published online 21 February 2008 in Wiley InterScience (www.interscience.wiley.com).

TABLE 1. Repetitive sequences and cross-link nature of some elastomeric proteins

Elastomeric protein	Elastomeric repeat motifs	Crosslinks
*Elastin	VGVAPG, VGVPG, VPGG V*GGLG*, L*GGLG*	Desmosines; isodesmosines; Lysinonorleucines; (dehydro)lysinonorleucines
Lamprin	V*GGLG*, Y*GGLG*	Pyridinolines
*Abductin	F*GGM*G*GG*NA*G*, G*GF*G*GM*GGG*X	Disulphide bridges
*Resilin	P*GGG*N*GG*RPSDTY*G*A (N-terminal repeat) P*GG*QDL*GG*YS*GG*R (C-terminal repeat)	Dityrosines, trityrosines
Gluten	P*G*Q*G*QQ, *G*YYPTSPQQ	Disulphide bridge
Flagelliform silk	*GPGG*SGP*GG*Y	Non covalent bonds (hydrogen and hydrophobic bonds)
Byssus	GPGGG	DOPA-lysines

The stars indicate the proteins discussed in the present review.

The first conformational studies on elastomeric sequences were performed on some repetitive sequences of elastin, such as (LGGVG)n,[17–19] (VPGVG)n[20–22] and independent domains containing quasi-repetitive sequences.[14–16]

The last approach has been used, and validated, particularly for elastin even if it is currently applied also to other elastomeric proteins.

In the following we will give some general information on those proteins, before trying to review our most important results on the molecular mechanism(s) of elasticity.

Elastin

Human Tropoelastin is constituted by 760 aminoacides encoded by 34 exons.[23,24] The abundance of glycine residues is high, followed by alanine, valine, and proline residues. Although, in minor amount also lysine residues are present. They play an important functional role because are responsible of the cross-links formation that enable the protein to undergo relatively high deformation without rupture. The sequences responsible for cross-linking are of two different types, the KP- and KA-rich polypeptides, that is those containing lysines and prolines, and those containing short polyalanine stretches with lysine residues, respectively. In elastin, the lysine residues are responsible for the formation of cross-links. The cross-links are originated by the enzymic oxidation of some lysine ε-amino groups which form α-aminoadipic acid δ-semialdehyde (allysine).[25] Then, through either aldol condensation or Schiff reactions (dehydro)lysinonorleucine, desmosine, and isodesmosine cross-links are chemically synthesized.[26–29] There are also a small number of additional cross-links present in insoluble elastin, including lysinonorleucine (formed by the condensation of allysine and lysine side chains), and allysine aldol (formed by the condensation of two allysine side chains), (Table 1).

The gene of human tropoelastin has a "cassette-like" structure where the exons encoding for hydrophobic, putatively responsible for the elastic properties of the protein, and cross-linking sequences regularly alternate giving rise to polypeptide sequences with autonomous and independent conformations and functions[24] (Fig. 1). The study of the individual exons encoding an independent and self-contained structure has been called the "reductionist approach" and has been shown to work in a series of papers.[14-16,30-34] Obviously, this approach will not apply to globular proteins where the concept of autonomous domains is usually not applicable. However, even in the case of elastin some scepticism could be present. It is the opinion of the present authors that this originates essentially from the reluctance of some researchers to realize the profound differences indeed existing between globular and elastomeric proteins. As a matter of fact, the last ones are characterized by many repetitive sequences which, of course, adopt the same conformations. Let us use elastin as a classical example. Previous studies,[14] mainly carried out by CD on polymerized repetitive sequences, demonstrated essentially unstructured conformations in aqueous solution, whereas β-turns confined to PG, GG, and XG (X = V, L, A) were dominant in TFE solutions.

Based on those archaic investigations, two different mechanisms of elasticity were put forward.

The first one has become very popular in the past decades, Urry and coworkers[35,36] proposed a structure called β-spiral and constituted by consecutive β-turns of type II which is the dominant conformation in solvents of low polarity. In particular, on the basis of extensive studies on

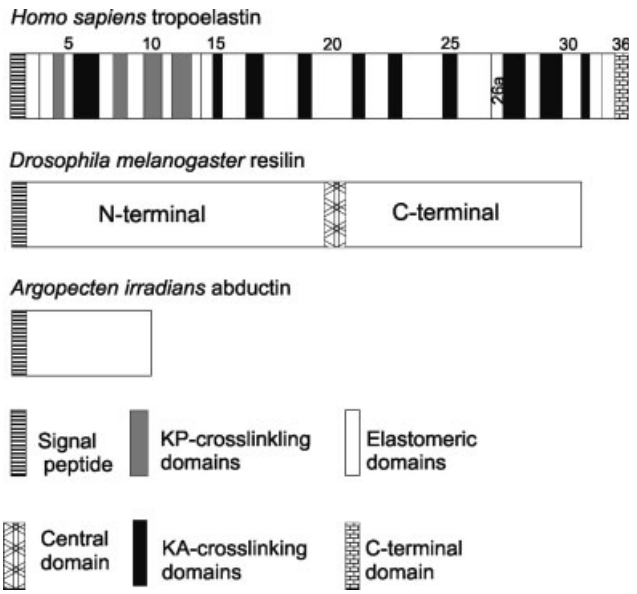

Fig. 1. Domain structures of the discussed elastomeric proteins.

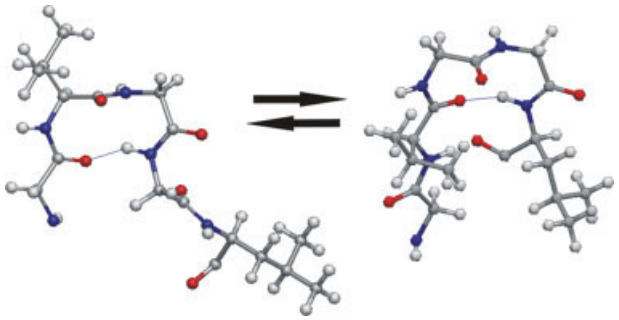

Fig. 2. Sliding β-turns of the sequence GVGGL. [Color figure can be viewed in the online issue, which is available at www.interscience.wiley.com.]

synthetic poly(VPGVG), a repeating sequence of elastin, he introduced a structural model supporting a new mechanism of elasticity. With Urry's model of poly(VPGVG), there is one type II β-turn per pentameric unit with PG at the corner of the bend and a 4 → 1 hydrogen bond connecting the C=O group of the first valine to the NH of the fourth valine along the sequence. The repetition of this conformational unit gives rise to a helical arrangement called the β-spiral. The β-turns act as spacers between the turns of the spiral. Between the β-turns are suspended dipeptide (VG) segments within which large-amplitude, low frequency librations can occur. The decrease in amplitude of the librations on extension causes a large decrease in the entropy of the segment, providing the driving force for return to the relaxed state. It is to be noted that this model, at variance with the classical theory of rubber elasticity, implies fixed end-to-end chain lengths[37,38] and references therein. The model has been apparently validated by molecular dynamics simulations in vacuum[39] and in explicit aqueous solvent.[40] However, in both cases the end-to-end distance was fixed; when this parameter was allowed to freely fluctuate, the recurring β-turns of the β-spiral were lost during the trajectory[41] and extended structures now appear. Quite interestingly, the X-ray structure of Boc-VPGVG-OH, which comprises the monomeric sequence of poly(VPGVG) constituting the ideal model for the β-spiral, shows an antiparallel β-sheet conformation.[42]

More recently, Tamburro et al. put forward a new model[43] where nonrecurring, isolated type II β-turns are proposed for (GXGGX) repeating sequence. These have XG or GG segments at the corners with 4 → 1 hydrogen bonds connecting the first and the fourth glycine or the second and fifth X residue, respectively. Because of the fact that G substitutes for P, the turns are rather labile and, therefore, can interconvert giving rise to dynamical β-turns sliding (Fig. 2) along the chain.[43,44] Thus a regular array of β-turns (the Urry β-spiral) cannot be stable enough for these sequences, and the polypeptide chain is freely fluctuating (variable end-to-end distance), according to the classical theory of rubber elasticity.

Urry and Tamburro structural models strictly apply to different regions of elastin. In fact, it is well known that proline in the second position stabilizes type II β-turns, because the corresponding ϕ dihedral is essentially fixed around the value of −60° typical for an ideal type II β-turn. On the contrary, when the proline is substituted by glycine or by a generic hydrophobic residue (X), the flexibility increases and the stability of the turn decreases. This is particularly true when XGG sequences are considered. The accessibility to the conformational space is a priori dramatically enhanced. It should be noted that the two models although differing in many respects, present a common conformational feature that is the presence of type II β-turns.

Very recently, Tamburro et al. refined the model by studying the polypeptide sequences coded by all the exons of human tropoelastin.[14,15] Some representative results are reported in the section below.

CD Studies

The peptides were monitored by CD spectroscopy at different temperatures. However, the conformational analysis is only qualitative. In fact, previous studies[14] demonstrated that CD deconvolution programs were not useful in establishing realistic values for the conformation of elastin peptides, because their reference databases consist predominately of CD spectra of globular proteins of known secondary structure.

What emerged from the CDPro analysis of our peptides was that the CD spectra of elastin peptides are not well represented in the reference proteins, so these programs are not suited for CD analysis of the hydrophobic and flexible peptides present in elastin sequence. For this reason, CD spectra of the different sequences were analyzed by comparing the curves with CD spectra of peptides with known secondary structures or with peptides that adopt a mixture of known structures. Furthermore, the number of CD curves acquired for each peptide is not enough for being fitted by the van't Hoff equation thus disabling the estimation of some physical parameters such as entropy, enthalpy and transition temperature.

Stated that, we report here on some CD spectra of three representative different types i.e. hydrophobic, KP, and KA domains (Table 2).

The CD spectra of hydrophobic EX7 domain in aqueous solution and in trifluoroethanol (TFE) at the indicated temperatures are shown in Figure 3. In aqueous solution at 0° and 25°C the spectra are very similar and dominated by a strong negative band at about 190 nm indicating the predominance of random coil conformation. Very different CD spectra are exhibited in TFE. At 0° and 25°C the CD spectra are characterized by a negative band at about 230 nm and by a strong positive one at about 205 nm. On increasing the temperature to 60°C, the positive band is almost reduced to zero and is also red-shifted. On the whole, the spectra are highly indicative of the presence of type-II β-turn which is less stable at high temperatures.

Figure 4a reports the CD spectra of KP EX12 domain in aqueous solution at different temperatures. The spectrum at 0°C is characterized by a strong negative band at 200 nm and by a trend toward positive values at about 225 nm suggesting the presence of PPII structure. The reduction of the negative band on increasing the temperature to 25° and 60°C, together with the adoption of more

TABLE 2. Polypeptide sequences of the analyzed exon-coded peptides of human tropoelastin

Exon	Sequence
EX7 (hydrophobic domain)	GAGLGGVPGVGGLGVSA
EX12 (KP domain)	GVGPFGGPQPGVPLGYPIKAPKLP
EX15 (KA domain)	GVGPQAAAAAAAKAAAKF
EX6 (KA domain)	GLGAFPAVTFPGALVPGGVADAAAAYKAAKA

negative ellipticities values at 225 nm, suggests the presence of random coil conformers predominant at higher temperatures. Accordingly, the isodichroic point at about 212 nm is indicative of a two-state equilibrium between PPII and random coil conformations.

Typical PPII CD spectra are characterized by a negative band around 200 nm and by a weaker positive band at about 217 nm. This positive band is shifted toward 225 nm for peptides rich in proline/hydroxyproline. This is due to wavelength shifts in electronic transitions between secondary and tertiary amides.

The CD spectra of EX12 in TFE at different temperatures are reported in Figure 4b. The CD spectrum at 0°C is dominated by a strong negative band at 203 nm and by a weaker one at 217 nm. The increase of the temperature to 25° and 60°C induces a progressive reduction and a slight red shift of the bands that are indicative of the presence of β-turns, favored at high temperature. This feature is very common to elastin peptides.

As expected, the CD spectra of the alanine-rich EX15 and EX6 domains reported in Figures 5 and 6, respectively are significantly different from those above analyzed, especially in TFE where the classic α-helix conformation appears. The conformational features in aqueous solution are somewhat different and indicative of the presence of the PPII conformation together with the α-helix structure.

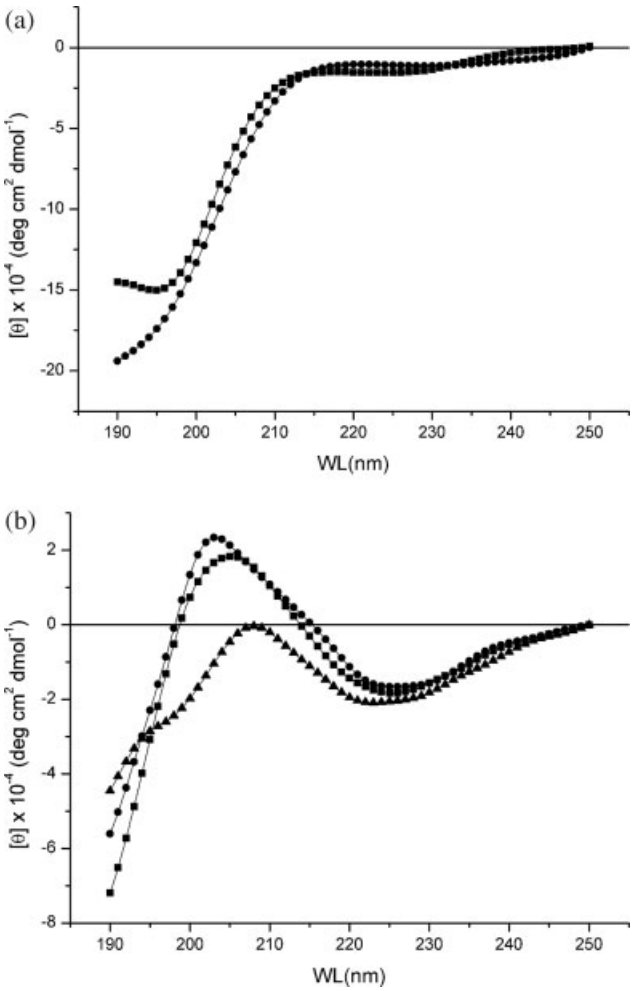

Fig. 3. CD spectra of EX7 domain in (**a**) aqueous solution at 0°C (●), 25°C (■), and in (**b**) TFE at 0°C (●), 25°C (■), 60°C (▲).

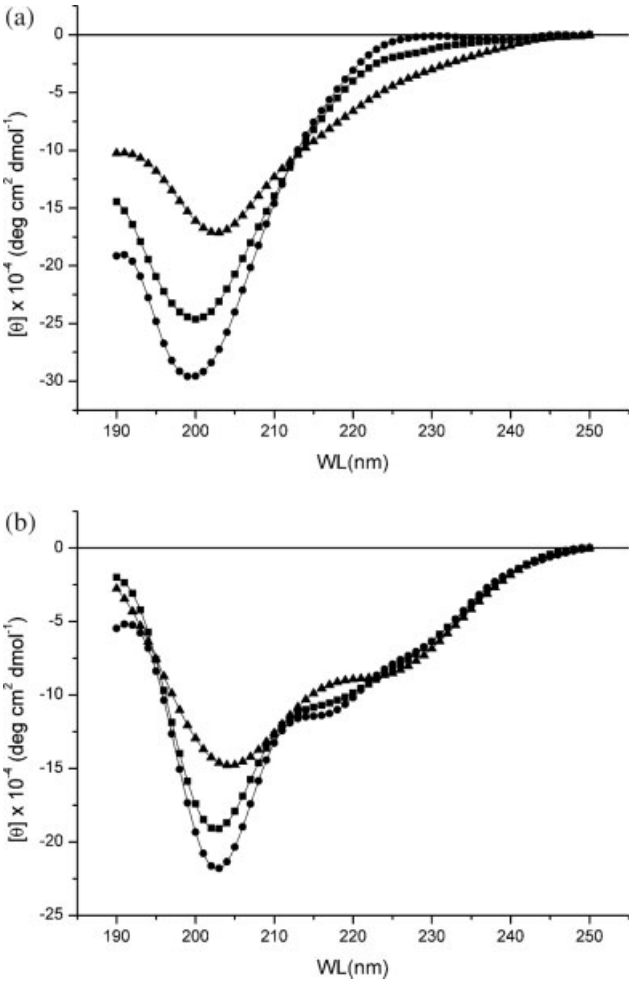

Fig. 4. CD spectra of EX12 domain at 0°C (●), 25°C (■), 60°C (▲) in (**a**) aqueous solution and (**b**) TFE.

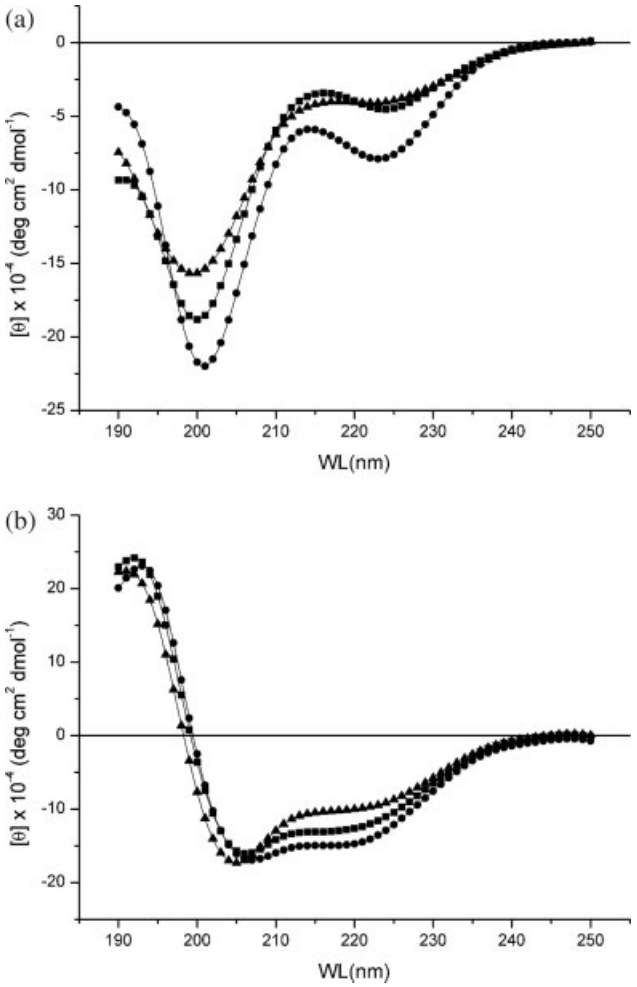

Fig. 5. CD spectra of EX15 domain at 0°C (●), 25°C (■), 60°C (▲) in (**a**) aqueous solution and (**b**) TFE.

This is more evident for EX6 where the presence of an isoelliptic point both in aqueous solution and in TFE is indicative of the presence of an equilibrium between α-helix and PPII conformations.

Summing up, the dominant conformation for the hydrophobic domains is in aqueous solution the polyproline II (PPII) often in equilibrium with the so-called "unordered" state. In the less polar solvent, such as TFE, in contrast, folded conformations, such as type I and II β-turns, are found together with unordered conformations. In regard to the regions containing lysines and polyalanine sequences (KA domains), the α-helix structure was found to dominate in TFE, but it was often present, although to a minor extend, even in water. On the contrary, the KP domains adopt either PPII or β-turns like the hydrophobic sequences.

ABDUCTIN

Abductin is a natural elastomer that serves as the primary building block for the abductor ligament in bivalves. The hydrated abductor ligament is triangular in shape with dark brown tint and rubber-like consistency. It is located in the hinge region of the bivalve and functions similar to a coil spring to open the shell upon relaxation of the abductor muscle that keeps the shell tightly closed. In addition, the ligament plays a role in the swimming of such scallops as *Aequipecten irradians* and *Placopecten magellanicus*. The abductor ligament serves to repeatedly open the shell after relaxation of the abductor muscle at a frequency of 4 Hz, causing expulsion of water dorsally enabling the scallop to swim several meters at a time to escape slow moving predators such as starfish. Abductin is a unique protein as it is the only elastomer identified in nature as having compressible elasticity whose conceptual amino acid sequence, derived from *Argopecten irradians* has been published.[45]

In the abductin extracted from the ligament of *Placopecten magellanicus*, the amino acid analysis revealed the presence, among others, of methionine and homocysteine, the last one being considered a cross-link precursor.[46] As a matter of fact, the ligament of *Pecten fumatus fumatus*, an Australian species with a similar composition to that of *Placopecten*, showed the N-terminus after cleavage with aminopeptidase M to contain a sequence, with two homocys-

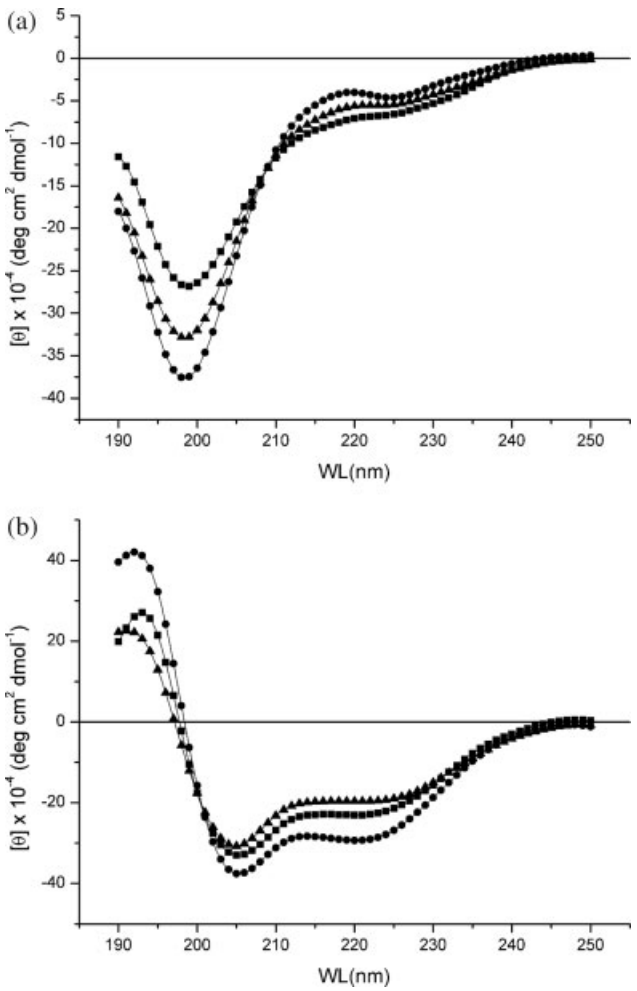

Fig. 6. CD spectra of EX6 domain at 0°C (●), 25°C (■), 60°C (▲) in (**a**) aqueous solution and (**b**) TFE.

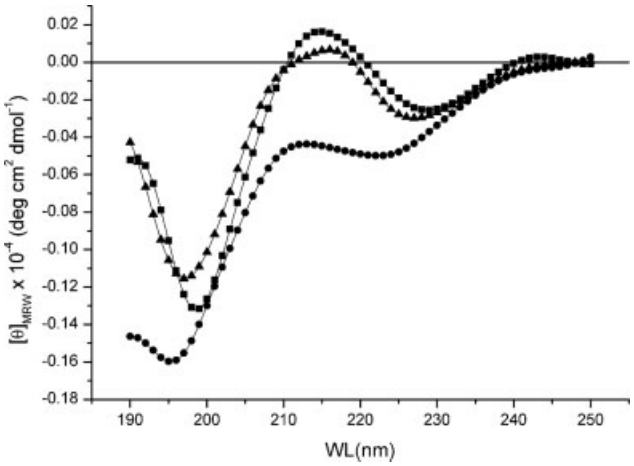

Fig. 7. CD spectra of $(FGGMGGGNAG)_2FGGMG$ in HFIP at 0°C (■), 25°C (●), 45°C (▲).

teines. Those result suggested the presence of disulfide crosslinks, originated by homocysteines, which in the oxidative environment of sea water is very stable (Table 1).

CD Studies

The CD spectra of two repeating polypeptide sequences of abductin are reported in Figures 7 and 8. In Figure 7, the CD spectra of the pentaeicosapeptide (25 amino acid residues) in hexa-fluoroisopropanol (HFIP) is shown (HFIP is the only transparent solvent in which the polypeptide is soluble). We can see that the unordered conformation is dominant at 25°C while the PPII conformation revealed by both the negative band at 198 nm and by the positive one at 215 nm is present at 0 and 45°C with a possible minor amount of type-II β turn conformers. This observation indicates that the polypeptide undergoes an inverse temperature transition in that it goes from a dominant unordered conformation to a periodic, extended PPII conformation with increasing temperature. In elastomeric proteins, able to coacervate such as elastin and abductin peptides, it is very common to observe an increase of folded conformations when the temperature is raised.

The CD spectrum of FGGMGGGNAG in aqueous solution at 0°C (Fig. 8a) shows the presence of a positive band at 220 nm and of a negative one at about 200 nm, again indicative of PPII conformation. The first one decreases on increasing the temperature, as expected for PPII conformation. A similar spectral feature is shown by the CD spectra in TFE, (Fig. 8b) although with stronger bands. Furthermore, the increase of temperature induces a slight reduction of the negative band, thus suggesting the presence of PPII conformation also in TFE. However, a contribution from β-turns or by the absorption of the phenylalanine possibly frozen in a very rigid position because of the folded conformation cannot be excluded in TFE.

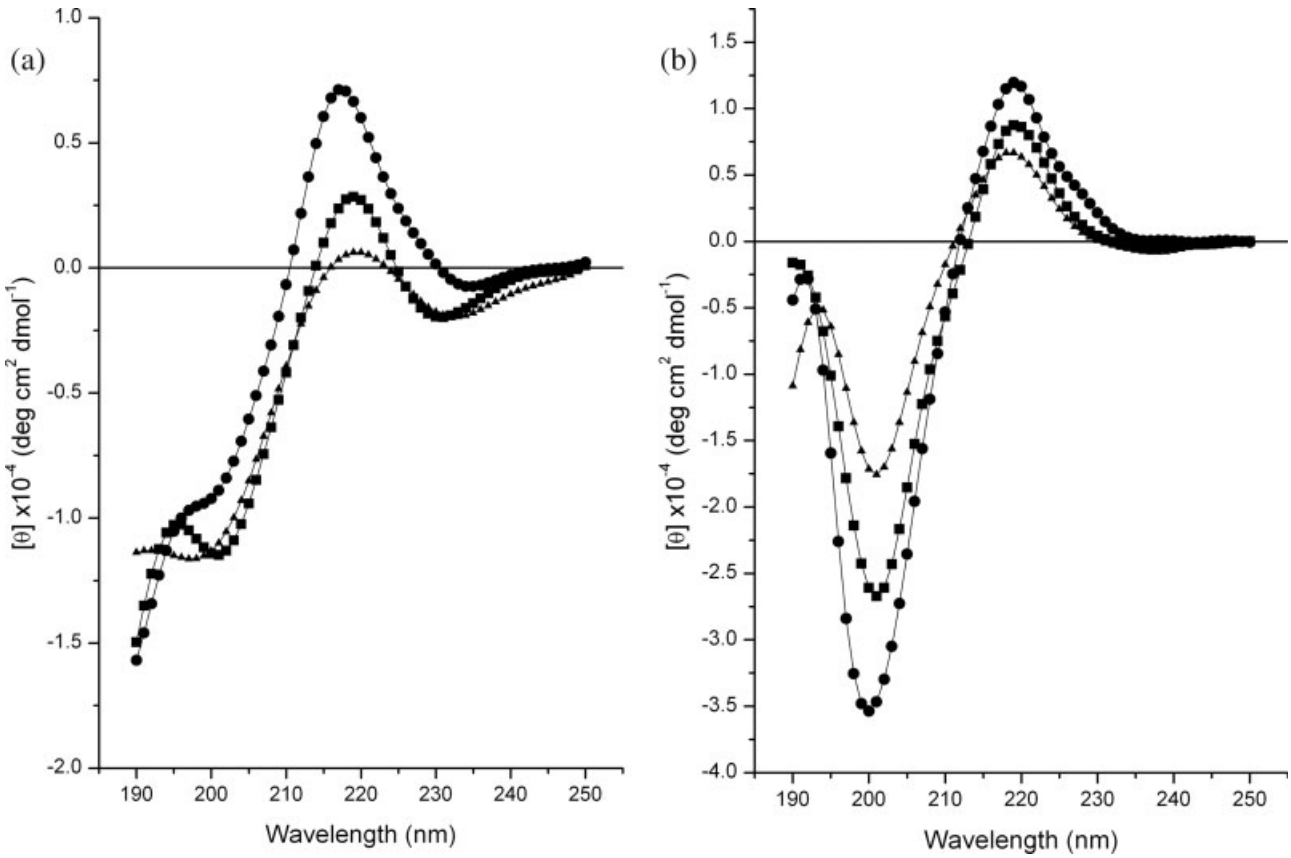

Fig. 8. CD spectra of FGGMGGGNAG at 0°C (●), 25°C (■), 50°C (▲) in (**a**) aqueous solution and (**b**) TFE.

TABLE 3. Conformational properties of the most significative repetitive sequences of Resilin as suggested by CD spectra

Peptide	H_2O	TFE
PGGGN	*B*	β2
PGGGNGGRP	U + PPII	β-turn
SDTYGAPGGGNGGRP	U + PPII	β2 + β1
PGGGNGGRPSDTYGAPGGGNGGRP	U + PPII	β2 + β1
$(PGGGN)_{10}$	U + β-turn	β2
GYSGGRPGGQDLGGYSGGRPGGQDLGGYSGGRPGGQDLG	U + PPII + β-turn(s)	β-turn(s)

RESILIN

Resilin is the major protein constituent of the elastic ligament attaching the wings to the thoraxes of insects, where it is responsible for the rapid vibration of the wings: as elastic tendons in dragonflies and as elastic wing hinges in locusts.[47] Furthermore, it has been recently demonstrated that resilin can work as a useful spring over the very wide range of speeds encountered in insect biomechanics. For example, in cicadas, where resilin acts as the elastic element in the sound-producing tymbal mechanism[48,49] ,the damped resonant vibration of the tymbal equates with energy losses in the whole system of under 20%.[50]

Weis-Fogh found that resilin shows perfect elasticity: even when strained to over twice its original length for 2 wk, a dragonfly's resilin tendon snaps back perfectly when the stress is relieved (hence the name he gave it) and that it showed neither tearing nor fatigue when stressed within its natural limits.[47]He pointed out that resilin was an ideal material for making elastic joints, such as hinges, that were subjected to repeated cyclical stress. As a matter of fact, during its life, the insect may fly for 8 h per day for about 30 days, requiring over 20 million wing beats; a cicada, singing at a frequency of 4 kHz for 2 or 3 h per day, stresses the resilin in each tymbal over 400 million times, which is more than the number of cycles per year encountered by the hairspring of a mechanical watch.

In resilin, Andersen identified the cross-links with fluorescent amino-acids dityrosine and trityrosine[6,51] (Table 1). Recently, starting from tryptic sequences identified in locust resilin, a gene putatively assigned to *Drosophila melanogaster* resilin has been detected.[8] In this protein sequence, it is possible to distinguish three different regions, apart from a 23 residue long signal peptide (see Fig. 1). The N-terminal region presents a 18 times repeated peptide sequence, while in the C-terminal domain a 13 residue sequence is repeated 11 times.

CD Studies

The CD properties of the most significative repetitive sequences of resilin are reported in Table 3.

In aqueous solution they are dominated by the coexistence of PPII, unordered conformations and β-turns. In TFE more folded structures (type-II β-turns) are populating the conformational space.

Taken together, these results are very similar to those found for the other elastomeric proteins studied by us.

CONCLUSIONS

The so-called unordered structures seem to play an important role in the structure (and elasticity) of the elastomeric proteins. For many years they were thought as statistical (mathematical) random coils according to the chain flexibility introduced by Flory[52] into the classical theory of rubber elasticity. However, more recent results (the literature on this topic is too large to be cited here) pointed out a different and more realistic picture. As a matter of fact, the structural disorder does not originate from a full exploration of the conformational hyperspace, rather it is an expression of the chain flexibility in only some selected regions of the Ramachandran map. One of these regions is that comprising the polyproline II (PPII) structure.

From a structural point of view, type II polyproline is a left-handed helix with an axial translation of 3.20 Å composed of three residues per turn, joined by transpeptide bonds with backbone dihedrals of $(\phi, \psi, \omega) = (-75^\circ, +145^\circ, +180^\circ)$.

In spite of the regularity of the PPII structure and, more precisely, of its well-defined dihedral angle values, a typical feature of PPII structure is the absence of any intrachain hydrogen bonds that renders the PPII structure almost indistinguishable from an irregular backbone structure by ^{1}H NMR spectroscopy.[53] Therefore, CD spectroscopy is a powerful tool for identify this structure in solution often confused with unordered, disordered, irregular, unstructured, extended, or random coil conformations.[54]

Actually, the absence of characteristic through-space NOEs and of low-temperature coefficients for NH protons involved in intramolecular hydrogen bonds makes NMR spectroscopy-otherwise so powerful for conformational analysis in solution-of difficult use for the identification of PPII conformation. Basically, one could do careful measuring of Noe volumes of sequential and intraresidue Hα-HN NOE crosspeaks.[3,34] This volume ratio analysis requires reduced overlap of the signals, difficult to find for glycine-rich elastomeric peptides. On the other hand, the method put forward by Lam and Hsu[55] is interesting; however it requires further validation before becoming a standard protocol. As a matter of fact, some doubts arise from the analysis of the CD spectra of the so-called "random coil" peptides reported in that paper. Spectra clearly show that a certain degree of PPII is still present in some of the "random coil" peptides. Furthermore, the NMR measurements of the so-called "random coil" peptides were recorded in 1*M* Urea, a well known PPII stabilization agent, thus suggesting that the peptides analyzed by NMR

cannot be surely considered as a standard of random coil peptides.

Accordingly, the only way to unambiguously reveal the PPII structure in solution is to use spectroscopies based on optical activity, such as circular dichroism[56](CD), vibrational circular dichroism[57,58] (VCD), and Raman optical activity[59,60] (ROA). Herein, we focus on electronic CD (ECD) identification of PPII structure, widely considered to be the most reliable methodology. In fact, CD data are invaluable as a preliminary guide to conformation and to conformational transitions under a wide range of conditions.

Polypeptides with ionized side chains and previously considered to adopt unordered conformations,[61] such as polyLys, and polyGlu at neutral pH show CD spectra with strong negative CD band below 200 nm and a positive one at 218 nm. An additional negative band near 170 nm is also observed in vacuum UV.

As a matter of fact, the theoretical work of Krimm and Mark revealed that the left-handed extended 3_1 helix (PPII) is the favored conformation for polypeptide chains with ionized side chains.[62] Accordingly, Krimm and coworkers[62,63] noted the resemblance of the CD spectra of the unordered structures to those of PPII and collagen and suggested that the so-called unordered structure consists mainly of short segments (4–7 residues) of PPII helical conformation mixed with sharp bends. Recent low-temperature CD measurements on polylysine and VCD studies of polylysine, support the Tiffany and Krimm proposal. Woody summarized[54] the experimental and theoretical studies, concluding that "unordered" systems showing positive CD absorptions near 220 nm mostly adopt PPII conformation. These left-handed helical regions are less populated at room temperature and more at low temperatures. Isoelliptic points are seen in the temperature-dependent spectra of many unordered polypeptides and should be attributed to a conformational equilibrium between the left-handed PPII and truly unordered conformation.[64]

Recently, it has been suggested that water can be an important stabilizing effect for the PPII structure.[65–67] The main question concerns the forces stabilizing this conformation in spite of the absence of both intramolecular and intermolecular hydrogen bonds, which are typical of regular conformations such as α-helix and β-pleated sheets, respectively. Actually, the water molecules can be hydrogen-bonded to the peptide backbone thus stabilizing its quasi-extended conformation.

PPII conformation is widely present in titin,[3] wheat glutenin, lamprin,[68] elastin,[14,15] abductin,[46] and resilin which are elastomeric proteins and therefore it should play a pivotal role in the genesis of elasticity. According to our studies a possible mechanism could be based on the following considerations.

PPII is a flexible conformation, the most flexible among the regular, periodic structures, almost surely due to the absence of intrachain hydrogen bonds and to its particular dihedral angles. As a matter of fact, the PPII conformation is an extended structure located very close to type II β-turns (first corner residue) and β-strand in the Ramachandran map. This allows the issue of multiconformational equilibria like the following:

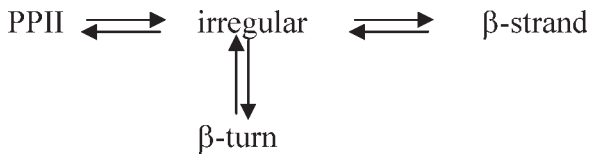

which are common to all studied elastomeric proteins. Accordingly, the high entropy of the relaxed state should originate (in addition to the sliding β-turns) from general equilibria akin open/folded. In the case of extensible proteins (elastin, titin, lamprin, resilin) the stretching should shift the equilibria toward the open, extended conformations, on the contrary, for the compressible protein abductin on compression the equilibrium extended/folded should be shifted to the folded structures, again decreasing the entropy, the uncompressed, multiconformational state being recovered by a simple increase in entropy after removal of the compression force.

Of course, the question arises as to whether the results obtained on simple and relatively short peptides might be transferred to the entire protein. Although this "reductionist approach" is of doubtful utility in the case of globular proteins, an enormous amount of experimental data, mainly obtained for elastin, may nevertheless point to a quite different scenario for elastomeric proteins.

As previously suggested, this probably originates from the intrinsic (sequence) fractality of those proteins, giving rise to the same structural pattern independently of the scale of observation.[29,36,69–71]

LITERATURE CITED

1. Debelle L, Alix AJ. The structures of elastins and their function. Biochimie 1999;81:981–994.
2. Gibson MA, Hatzinikolas G, Kumaratilake JS, Sandberg LB, Nicholl JK, Sutherland GR, Cleary EG. Further characterization of proteins associated with elastic fiber microfibrils including the molecular cloning of MAGP-2 (MP25). J Biol Chem 1996;271:1096–1103.
3. Ma K, Kan L, Wang K. Polyproline II helix is a key structural motif of the elastic PEVK segment of titin. Biochemistry 2001;40:3427–3438.
4. Robson P, Wright GM, Sitarz E, Maiti A, Rawat M, Youson JH, Keeley FW. Characterization of lamprin, an unusual matrix protein from lamprey cartilage. Implications for evolution, structure, and assembly of elastin and other fibrillar proteins. J Biol Chem 1993;268:1440–1447.
5. Shewry PR, Miles MJ, Tatham AS. The prolamin storage proteins of wheat and related cereals. Prog Biophys Mol Biol 1994;61:37–59.
6. Andersen SO. Characterization of a new type of cross-linkage in resilin, a rubber-like protein. Biochim Biophys Acta 1963;69:249–262.
7. Weis-Fogh T. A rubberlike protein in insect cuticle. J Exp Biol 1960;37:889–907.
8. Ardell D, Andersen S. Tentative identification of a resilin gene in *Drosophila melanogaster*. Insect Biochem Mol Biol 2001;31:965–970.
9. Hayashi CY, Lewis RV. Evidence from flagelliform silk cDNA for the structural basis of elasticity and modular nature of spider silks. J Mol Biol 1998;275:773–784.
10. Zhou Y, Wu S, Conticello VP. Genetically directed synthesis and spectroscopic analysis of a protein polymer derived from a flagelliform silk sequence. Biomacromolecules 2001;2:111–125.
11. Kelly RE, Rice RV. Abductin: a rubber-like protein from the internal triangular hinge ligament of pecten. Science 1967;155:208–210.

12. Coyne KJ, Qin XX, Waite JH. Extensible collagen in mussel byssus: a natural block copolymer. Science 1997;277:1830–1832.
13. Gosline J, Lillie M, Carrington E, Guerette P, Ortlepp C, Savage K. Elastic proteins: biological roles and mechanical properties. Philos Trans R Soc Lond B Biol Sci 2002;357:121–132.
14. Tamburro AM, Bochicchio B, Pepe A. Dissection of human tropoelastin: exon-by-exon chemical synthesis and related conformational studies. Biochemistry 2003;42:13347–13362.
15. Tamburro AM, Bochicchio B, Pepe A. The dissection of human tropoelastin: from the molecular structure to the self-assembly to the elasticity mechanism. Pathol Biol (Paris) 2005;53:383–389.
16. Tamburro AM, Pepe A, Bochicchio B. Localizing alpha-helices in human tropoelastin: assembly of the elastin "puzzle." Biochemistry 2006;45:9518–9530.
17. Martino M, Coviello A, Tamburro AM. Synthesis and structural characterization of poly(LGGVG), an elastin-like polypeptide. Int J Biol Macromol 2000;27:59–64.
18. Kumashiro KK, Kurano TL, Niemczura WP, Martino M, Tamburro AM. 13C CPMAS NMR studies of the elastin-like polypeptide (LGGVG)n. Biopolymers 2003;70:221–226.
19. Ohgo K, Ashida J, Okonogi M, Asakura T, Kumashiro KK. Heterogeneity in the conformation of valine in the elastin mimetic (LGGVG)6 as shown by solid-state 13C NMR SPEctroscopy. Biomacromolecules 2006;7:3306–3310.
20. Hong M, Isailovic D, Conticello VP. Structure of an elastin-mimetic polypeptide by solid-state NMR chemical shift analysis. Biopolymers 2003;70:158–168.
21. Reguera J, Fahmi A, Moriarty P, Girotti A, Rodríguez-Cabello JC. Nanopore formation by self-assembly of the model genetically engineered elastin-like polymer [(VPGVG)2(VPGEG)(VPGVG)2]15. J Am Chem Soc 2004;126:13212–13213.
22. Urry DW, Haynes B, Harris RD. Temperature dependence of length of elastin and its polypentapeptide. Biochem Biophys Res Commun 1986;141:749–755.
23. Indik Z, Yeh H, Ornstein-Goldstein N, Sheppard P, Anderson N, Rosenbloom JC, Peltonen L, Rosenbloom J. Alternative splicing of human elastin mRNA indicated by sequence analysis of cloned genomic and complementary DNA. Proc Natl Acad Sci USA 1987;84:5680–5684.
24. Rosenbloom J, Abrams WR, Mecham R. Extracellular matrix 4: the elastic fiber. FASEB J 1993;7:1208–1218.
25. Lent RW, Smith B, Salcedo LL, Faris B, Franzblau C. Studies on the reduction of elastin. II. Evidence for the presence of alpha-aminoadipic acid delta-semialdehyde and its aldol condensation product. Biochemistry 1969;8:2837–2845.
26. Partridge SM, Elsden DF, Thomas J. Constitution of the cross-linkages in elastin. Nature 1963;197:1297–1298.
27. Thomas J, Elsden DF, Partridge SM. Partial structure of two major degradation products from the cross-linkages in elastin. Nature 1963;200:651–652.
28. Piez KA. Cross-linking of collagen and elastin. Annu Rev Biochem 1968;37:547–570.
29. Gray WR, Sandberg LB, Foster JA. Molecular model for elastin structure and function. Nature 1973;246:461–466.
30. Tamburro AM, Pepe A, Bochicchio B, Quaglino D, Ronchetti IP. Supramolecular amyloid-like assembly of the polypeptide sequence coded by exon 30 of human tropoelastin. J Biol Chem 2005;280:2682–2690.
31. Pepe A, Guerra D, Bochicchio B, Quaglino D, Gheduzzi D, Pasquali Ronchetti I, Tamburro AM. Dissection of human tropoelastin: supramolecular organization of polypeptide sequences coded by particular exons. Matrix Biol 2005;24:96–109.
32. Gheduzzi D, Guerra D, Bochicchio B, Pepe A, Tamburro AM, Quaglino D, Mithieux S, Weiss AS, Pasquali Ronchetti I. Heparan sulphate interacts with tropoelastin, with some tropoelastin peptides and is present in human dermis elastic fibers. Matrix Biol 2005;24:15–25.
33. Floquet N, Pepe A, Dauchez M, Bochicchio B, Tamburro AM, Alix AJ. Structure and modeling studies of the carboxy-terminus region of human tropoelastin. Matrix Biol 2005;24:271–282.
34. Bochicchio B, Floquet N, Pepe A, Alix AJ, Tamburro AM. Dissection of human tropoelastin: solution structure, dynamics and self-assembly of the exon 5 peptide. Chemistry 2004;10:3166–3176.
35. Urry DW. Arterial mesenchyme and arteriosclerosis. Studies on the conformation and interaction of elastin. Adv Exp Med Biol 1974;43:211–243.
36. Venkatachalam CM, Urry DW. Development of a linear helical conformation from its cyclic correlate. β-Spiral model of the elastin poly(pentapeptide) (VPGVG)n. Macromolecules 1981;14:1225–1229.
37. Urry D. On the molecular structure, function, and pathology of elastin: the Gotte stepping stone. In: Tamburro AM, editor. Elastin and elastic tissue. Potenza, Italy: Armento; 1997. p 11–22.
38. Urry DW. Entropic elastic processes in protein mechanisms. I. Elastic structure due to an inverse temperature transition and elasticity due to internal chain dynamics. J Protein Chem 1988; 7:1–34.
39. Chang DK, Urry DW. Molecular dynamics calculations on relaxed and extended states of the polypentapeptide of elastin. Chem Phys Lett 1988;147:395–400.
40. Wasserman ZR, Salemme FR. A molecular dynamics investigation of the elastomeric restoring force in elastin. Biopolymers 1990;29:1613–1631.
41. Kasarda DD, King G, Kumosinky TF. Comparison of spiral structures in wheat high-molecular-weight glutenin subunits and elastin by molecular modeling. In: Kumosinski TF, Liebman MN, editors. Molecular modeling—from virtual tools to real problems, Vol. 576, Washington: ACS Symp. Ser: ACS Publ; 1994. p 203–220.
42. Ayato H, Tanaka I, Ashida T. Crystal structures of repeating peptides of elastin. 1. *N*-(tert-Butoxycarbonyl)-L-valyl-L-prolylglycyl-L-valylglycine. J Am Chem Soc 1981;103:5902–5905.
43. Tamburro AM, Guantieri V, Pandolfo L, Scopa A. Synthetic fragments and analogues of elastin. II. Conformational studies. Biopolymers 1990;29:855–870.
44. Lelj F, Tamburro AM, Villani V, Grimaldi P, Guantieri V. Molecular dynamics study of the conformational behavior of a representative elastin building block: Boc-Gly-Val-Gly-Gly-Leu-OMe. Biopolymers 1992;32:161–172.
45. Cao Q, Wang Y, Bayley H. Sequence of abductin, the molluscan "rubber" protein. Curr Biol 1997;7:R677–R678.
46. Bochicchio B, Jimenez-Oronoz F, Pepe A, Blanco M, Sandberg LB, Tamburro AM. Synthesis of and structural studies on repeating sequences of abductin. Macromol Biosci 2005;5:502–511.
47. Bailey K, Weis-Fogh T. Amino acid composition of a new rubber-like protein, resilin. Biochim Biophys Acta 1961;48:452–459.
48. Young D, Bennet-Clark H. The role of the tymbal in cicada sound production. J Exp Biol 1995;198(Part 4):1001–1020.
49. Bennet-Clark H. The first description of resilin. J Exp Biol 2007;210 (Part 22):3879–3881.
50. Bennet-Clark H. Tymbal mechanics and the control of song frequency in the cicada Cyclochila australasiae. J Exp Biol 1997;200(Part 11):1681–1694.
51. Andersen SO. The cross-links in resilin identified as dityrosine and trityrosine. Biochim Biophys Acta 1964;93:213–215.
52. Flory J. Principles of polymer chemistry. Ithaca, NY: Cornell University Press; 1953.
53. Shi Z, Woody RW, Kallenbach NR. Is polyproline II a major backbone conformation in unfolded proteins? Adv Protein Chem 2002;62:163–240.
54. Woody RW. Circular dichroism and conformation of unordered polypeptides. Adv Biophys Chem 1992;2:37–79.
55. Lam SL, Hsu VL. NMR identification of left-handed polyproline Type II helices. Biopolymers 2003;69:270–281.
56. Sreerama N, Woody RW. Poly(pro)II helices in globular proteins: identification and circular dichroic analysis. Biochemistry 1994;33:10022–10025.
57. Dukor RK, Keiderling TA. Reassessment of the random coil conformation: vibrational CD study of proline oligopeptides and related polypeptides. Biopolymers 1991;31:1747–1761.

58. Keiderling TA, Silva RA, Yoder G, Dukor RK. Vibrational circular dichroism spectroscopy of selected oligopeptide conformations. Bioorg Med Chem 1999;7:133–141.
59. Smyth E, Syme CD, Blanch EW, Hecht L, Vasak M, Barron LD. Solution structure of native proteins with irregular folds from Raman optical activity. Biopolymers 2001;58:138–151.
60. Zhu F, Isaacs NW, Hecht L, Tranter GE, Barron LD. Raman optical activity of proteins, carbohydrates and glycoproteins. Chirality 2006; 18:103–115.
61. Holzwarth G, Doty P. The ultraviolet circular dichroism of polypeptides. J Am Chem Soc 1965;87:218–228.
62. Krimm S, Mark JE. Conformations of polypeptides with ionized side chains of equal length. Proc Natl Acad Sci USA 1968;60:1122–1129.
63. Tiffany ML, Krimm S. Effect of temperature on the circular dichroism spectra of polypeptides in the extended state. Biopolymers 1972;11: 2309–2316.
64. Bochicchio B, Tamburro AM. Polyproline II structure in proteins: identification by chiroptical spectroscopies, stability, and functions. Chirality 2002;14:782–792.
65. Martino M, Bavoso A, Guantieri V, Coviello A, Tamburro AM. On the occurrence of polyproline II structure in elastin. J Mol Struct 2000; 519:173–189.
66. Stapley BJ, Creamer TP. A survey of left-handed polyproline II helices. Protein Sci 1999;8:587–595.
67. Makarov AA, Lobachov VM, Adzhubei IA, Esipova NG. Natural polypeptides in left-handed helical conformation. A circular dichroism study of the linker histones' C-terminal fragments and beta-endorphin. FEBS Lett 1992;306:63–65.
68. Bochicchio B, Pepe A, Tamburro AM. On (GGLGY) synthetic repeating sequences of lamprin and analogous sequences. Matrix Biol 2001;20:243–250.
69. Villani V, Tamburro AM. Conformational chaos of an elastin-related peptide in aqueous solution. Ann N Y Acad Sci 1999;879:284–287.
70. Gotte L. Recent observations on the structure and composition of elastin. Adv Exp Med Biol 1977;79:105–117.
71. Tamburro AM, De Stradis A, D'Alessio L. Fractal aspects of elastin supramolecular organization. J Biomol Struct Dyn 1995;12:1161–1172.

CHIRALITY 20:995–1008 (2008)

Fast Generation of Nonresonant and Resonant Optical Rotatory Dispersion Curves with the Help of Circular Dichroism Calculations and Kramers-Kronig Transformations

MARK RUDOLPH AND JOCHEN AUTSCHBACH*

Department of Chemistry, University at Buffalo, State University of New York, Buffalo, New York 14260-3000

Presented at the 11th International Conference on Circular Dichroism, 2007, Groningen, Netherlands

ABSTRACT It can be computationally expensive to compute smooth, well resolved, optical rotation (OR) dispersion (ORD) curves from first principles theory. Instead of computing the OR at a large number of frequency points, similar results can be obtained by combined use of a computed circular dichroism (CD) spectrum along with a few OR calculations by using subtractive Kramers-Kronig transformations. We have tested various subtractive schemes for simulated (analytical) CD/ORD and for time-dependent density functional computations for dimethyloxirane, fenchone, and [4]triangulane. Nonresonant ORD can be obtained with as few as two OR and one CD calculation. For resonant ORD we found that between 7 and 15 OR computations plus the CD spectrum were typically sufficient, depending on the number of excitations within the frequency window of interest. *Chirality 20:995–1008, 2008.*

KEY WORDS: optical activity; density functional theory; Kramers-Kronig transformations; circular dichroism; optical rotatory dispersion

INTRODUCTION

It is now well recognized that first-principles based computations of optical activity are very valuable in the study of chiral organic molecules[1–5] and metal complexes.[6,7] We will focus on electronic optical activity here [optical rotation (OR) and circular dichroism (CD)] and refer the reader to the literature for computational work on vibrational optical activity.[8–11] One of the important applications of computed CD and OR is to determine the absolute configuration (AC) of a chiral molecule by matching experimental data with computational data for one of the possible enantiomers. Because of its relatively easy and inexpensive measurement the OR at the sodium D-line (589.3 nm, 16969 cm^{-1}, 2.104 eV, 0.07732 au) has been used extensively for assignment of ACs with the help of computations. However, because there is only a single data point available for comparison, and because approximations in the computational model necessarily lead to some deviations between theory and experiment, care must be taken that the assignment is statistically meaningful.[12,13] Additional confidence in the AC assignment can also be gained by considering part of the OR dispersion (ORD), the CD spectrum, or both. See the aforementioned reviews and Refs. 14–16 for computational approaches to CD using time-dependent density functional theory (TDDFT), which are now mainly used in this field, and a selection of case studies. The more information about the chiroptical response of a molecule that can be obtained and brought to a match between theory and experiment, the higher the likelihood of a correct computational-based assignment of the AC. Concerted studies that include the D-line OR or a larger range of the ORD as well as electronic CD have been undertaken by a number of authors.[5,17–21] If a large enough range of the ORD can be accessed experimentally, comparison with computed data should also allow for a more reliable assignment of the AC than using the OR at just a single wavelength.[21–23] There is also a renewed interest in studying OR as a function of wavelength/frequency for chiral molecules, and to investigate rovibrational effects on the OR,[24–29] since gas-phase measurements have become possible using cavity ring-down polarimetry.[30]

Chirality and optical activity are of interest for very fundamental chemical and physical research.[31–34] Along with the application of chiroptical response calculations for AC assignments, the study of CD and ORD is interesting and important in its own right because it gains detailed insight into the electronic structure of chiral organic molecules and metal complexes. A physically meaningful response function is complex. In chiroptical response, the optical rotation angle φ (ORD) is the real part and the ellipticity θ (CD) is the imaginary part of the complex OR angle Φ,

$$\Phi = \varphi + \imath\theta. \quad (1)$$

Contract grant sponsor: CAREER program of the National Science Foundation; Contract grant number: CHE-0447321.
*Correspondence to: Jochen Autschbach, Department of Chemistry, University at Buffalo, State University of New York, Buffalo, NY 14260-3000. E-mail: jochena@buffalo.edu
Received for publication 31 October 2007; Accepted 10 January 2008
DOI: 10.1002/chir.20547
Published online 11 March 2008 in Wiley InterScience (www.interscience.wiley.com).

Therefore, concerted studies of CD and ORD investigate the full, complex, electronic chiroptical linear response (LR). In principle, only the real or the imaginary part needs to be known since φ can be obtained from θ, and vice versa, through the Kramers-Kronig (KK) transformation.[35,36] However, the KK integral transformation requires the complete spectrum including all continuum states up to infinite frequency. See the Appendix for details. Since in practice only a finite range of frequencies is accessible, knowledge of both the CD and ORD in the low-frequency range may yield useful information about the inaccessible parts of the spectrum/dispersion. This issue has recently been addressed by Polavarapu who suggested computational protocols that make use of combined CD and ORD measurements and computations along with the use of KK transformations.[37–39] Our group has recently studied the conversion of ORD into CD and vice versa in detail from a theoretical point of view, using LR calculations with empirical damping to obtain φ and θ from the complex response along with direct computations of rotatory strengths R_{0j} and excitation frequencies ω_{0j} to obtain the same quantities.[40]

One of the disadvantages of calculating a well-resolved ORD over a large frequency range (with or without use of damping) is that the LR computations have to be repeated at each frequency point. Depending on the level of theory and the intended resolution of the ORD this may require significant computational time.[21,23,40,41] The purpose of this study is to investigate several protocols involving KK transformations which combine LR computations of ORD at a relatively small number of frequencies with computations of rotatory strengths R_{0j} and excitation frequencies ω_{0j} (from which CD spectra are usually simulated). The goal is to obtain well resolved ORD curves that do not contain large truncation errors from finite frequency range KK transformations of the CD. Further, we apply these methods to address a conceptual issue in computations of resonant ORD: Without applying any damping, the ORD diverges at the excitation energies and can therefore not be compared to experiment. Damping leads to smooth ORD that has the correct qualitative peak/trough pattern around the excitation.[21,41] As it is commonly implemented[4,21,42] the damping appears as an empirical Lorentzian broadening of the excited states whereas typically in spectroscopy one would rather approximate the broadening with Gaussian functions. The combination of LR computations of ORD with CD calculations allows the removal of such implicit line-shape from the computed results and therefore to model the resonant ORD with any desired broadening. In this work, we will consider a Gaussian broadening and show the differences compared to resonant ORD based on Lorentzian broadening.

This study is organized as follows: In Computational Details and Methodology, we will summarize the computational details for the optical response calculations performed for the selected molecules, and discuss methods of performing the modified KK transformations and recovering lineshapes from dampened OR dispersion calculations. In Results and Discussion, we catalogue the results of our calculations and transformations. We will first discuss an analytic model CD/ORD for a hypothetical molecule, and then perform KK transformations on computational data for three molecules: dimethyloxirane (DMO), fenchone, and (P)-[4]triangulane. Comparisons with experiment will be made for fenchone and [4]triangulane. We summarize our findings in Summary and Conclusions section. Some additional information about KK and Hilbert transformations is given in the Appendix.

COMPUTATIONAL DETAILS AND METHODOLOGY

Density Functional Computations

We have used TDDFT for all response computations. For (2*R*,3*R*)-DMO, and (1R)-(−)-fenchone, the ORD and CD were calculated with the Amsterdam density functional (ADF) package[43] using the chiroptical response methods described in Refs. 15, 21, 44 and 45. Optimized structures for fenchone and DMO were taken from Refs. 21 and 45. We have used the asymptotically correct statistical average of orbital potentials (SAOP) exchange-correlation (XC) potential developed by Baerends and coworkers[46] along with the adiabatic local density approximation for the XC response kernel. For DMO, we have used the TZ2P+ basis from the ADF basis set library,[43] which is a valence triple-ζ doubly-polarized Slater-type basis (TZ2P) that has been augmented with additional diffuse functions (two sets of p functions for H and one set of s, p, d functions for C, O). See Ref. 45 for further details. A global damping parameter of 0.007 Hartree atomic units (au, ∼0.2 eV or 1.5×10^3 cm^{-1}) was used in the LR computations of the ORD. The CD was computed from rotatory strengths and excitation energies[15] for a few dozen excitations which were subsequently broadened with the same linewidth of 0.007 au. See Refs. 15, 21 and the Appendix for further details. The ORD and CD of fenchone were calculated for a large frequency range with a polarized double-ζ (DZP) basis with a damping/linewidth parameter of 0.007 au. Calculations for fenchone were also done with the TZ2P+ basis. For benchmark computational data for these molecules using the same functionals and Slater-type basis sets see Refs. 15, 21 and 45. The Turbomole 5.7 package,[47] using Becke's 3-parameter hybrid functional BHLYP (50% exact exchange) and the aug-cc-pVDZ Gaussian-type basis, was used to compute the ORD and CD of (P)-(+)-[4]triangulane and its structure was optimized using the hybrid functional B3LYP and a polarized triple-ζ (TZVP) basis. We decided to use a Gaussian-type basis and a hybrid functional for compatibility with previously published data for this molecule.[23] The computed ORs are based on a common gauge origin (CGO, here the center of nuclear charge). Although the CGO results are in principle origin dependent we have previously shown that qualitatively the same results are obtained in studies of the performance of KK

transformation when the CGO is used instead of an origin independent modified velocity gauge, for example.[40] For computations with the doubly polarized diffuse basis sets the origin dependence is relatively weak.[45,48] In the spectra/ORD for the molecules, we use an energy scale (in eV), which is proportional to the wavenumber (1 eV $\approx$ 8066 cm^{-1}). For the three molecules we also show a wavelength scale for convenience.

KK Transformations and Subtractive Methods

For Gaussian and Lorentzian functions, the KK (or Hilbert) transformations are known analytically. See the Appendix for details and the expressions for Lorentzian and Gaussian transform pairs. For experimental spectra, or other more complicated broadening functions, KK-, Hilbert-, and the subtractive KK-transformations investigated here are more easily performed by numerical integration. Polavarapu recently recommended the use of the Maclaurin's Formula for the numerical integration in KK transformations of CD and ORD.[37] Ohta and Ishida have previously tested several numerical integration methods for KK transformations,[49] and found that Maclaurin's Formula outperformed the others investigated. It has also been extensively tested in our previous work on KK transformations.[40] Maclaurin's numerical integration formula employs an evenly spaced grid and divides it into sets of odd (o) and even points (e), as shown in eq. 2 below, which is done to avoid the singularity at $\mu = \omega$. When an odd point is being evaluated, the summation goes over all of the even points and vice versa. As Ohta and Ishida pointed out, this method of avoiding the singularity at $\mu = \omega$ produces excellent results. For instance, the KK transformation of the imaginary part of the OR parameter β (proportional to θ/ω^2) to its real part (proportional to φ/ω^2) the numerical formula reads

$$\mathrm{Re}[\beta](\omega_i) \approx \frac{2}{\pi} 2h \sum_{j \in o,e}^{\mathrm{grid}} \frac{\mathrm{Im}[\beta](\mu_j)\mu_j}{\mu_j^2 - \omega_i^2} \qquad (2)$$

where h is the spacing of the data grid and the summation goes over the odd (o) set when grid point ω_i is even (e) and vice versa. ω and μ are frequency-like variables (frequency, energy, or wavenumber). The multiply subtractive KK transformation (MSKK) is an adaptation of the KK transformation to include a number of "anchor points" at which the transform is known exactly. One subtracts the known value from the KK equation to get the singly-subtractive KK transformation (SSKK). A second known value can then be subtracted from the SSKK equation to give a doubly-subtractive equation (DSKK), and so forth. This has been proposed to eliminate the cut-off errors when the integration is truncated at low frequencies[50] since the transform can be "anchored" to the exact values. Applications to computed molecular properties were not tested in Ref. 50. More information about KK and MSKK transformations is given in the Appendix and in Ref. 40, where we have studied the performance of a singly-subtractive method for CD-to-ORD transformations. Given the knowledge of N such anchor values of the OR at frequencies $\omega_i, i = 1 \ldots N$, the Nth order subtractive KK transformation can be written conveniently in closed form as

$$\mathrm{Re}[\beta](\omega) = \sum_i^N \mathrm{Re}[\beta](\omega_i) \prod_{j \neq i}^N \frac{(\omega^2 - \omega_j^2)}{(\omega_i^2 - \omega_j^2)} + \frac{2}{\pi}\left[\prod_i^N (\omega^2 - \omega_i^2)\right] \int_0^\infty \frac{\mathrm{Im}[\beta](\mu)\mu}{(\mu^2 - \omega^2)\left[\prod_i^N (\mu^2 - \omega_i^2)\right]} \mathrm{d}\mu. \qquad (3)$$

That is, the anchor values of the OR are the $\mathrm{Re}[\beta](\omega_i)$, which can be calculated from LR using the same basis set and methods used to compute a truncated CD. For the present work we have implemented the MSKK of eq. 3 using numerical integration as in eq. 2. The software is available free of charge from the authors upon request.

The MSKK is useful in situations where the complete CD spectrum is not known (which is almost always the case). Regardless of the integration range in eq. 3, right at an anchor point where $\omega = \omega_k$ the product in front of the integral vanishes and the first term on the right hand side of (3) will be equal to $\mathrm{Re}[\beta](\omega_k)$. This ensures that the MSKK transform will always be exact at the anchor points regardless of a truncation of the CD spectrum as long as the exact value of β is known. The computational cost of the numerical MSKK integrations is negligible compared with those for state-of-the-art response computations on chiral molecules. We may therefore exploit this fact to generate accurate ORD curves quickly from a MSKK transformation by calculating a small set of OR anchor points by LR, along with the CD over the frequency range of interest. For small to medium sized molecules, calculating a few dozen CD transitions is roughly as costly as computing the OR at one to several frequencies. Therefore, as we will show with typically 10 OR points plus one CD computation, one can obtain a well resolved ORD curve that may otherwise require on the order of 50–100 LR computations (here this corresponds to a speedup of roughly one order of magnitude). In the off-resonance regime, where no oscillations of the ORD occur, fewer ORD points from LR would be needed to obtain a reasonably smooth curve. However, in this case the MSKK yields very good results with only 2 or 3 anchor points and therefore still offers a substantial speedup.

Although Maclaurin's formula avoids the singularity in the regular KK transformation, the MSKK will introduce a new singularity at each anchor point where $\mu = \omega_k$. Previously we applied this method with a single anchor point outside the integration range to avoid this problem.[40] Unfortunately, in this form the singly-subtractive KK turned out to not be very useful since the effect of the anchor point disappears further away from the anchor frequency. Here, we propose that one creates a set of anchor points covering the range of frequencies that the ORD is to be studied, and also uses a rather tight numerical integration grid for the MSKK transformation (on the order of 10^3 to 10^4 points). The integration grid should be dense

enough such that adjacent points afford approximately the same OR value when compared with the magnitude of the ORD. With this in effect, the anchor point may span two adjacent points on the integration grid; $\omega_{odd} \approx \omega_i \approx \omega_{even}$. Now when evaluating the MSKK at an odd/even grid point, the integration goes over the even/odd grid and we use the corresponding odd/even-point anchors. This technique avoids the singularity in the same way as the original Maclaurin formula for the standard KK transform. Since the same $\varphi(\omega_i)$ is used for odd/even anchor point pairs, it should be noted that the larger the true $\varphi(\omega_{odd}) - \varphi(\omega_{even})$ for adjacent grid points is, a more strongly pronounced odd–even oscillation (ringing) will be obtained in the MSKK transform.

Anchor point placement. As Palmer has pointed out,[50] the collection of terms in the multiply subtractive KK transformation, other than the integral itself, has the form of an *N*th degree Lagrange interpolating polynomial, in powers of ω^2, that joins the *N* anchor points. There is a well known problem when using interpolating polynomials of high degree called Runge's phenomenon: the higher degree of the polynomial used, the more the interpolation oscillates towards the ends of the interval. Such oscillations can be minimized by using the Chebyshev nodes, instead of an equally spaced grid of anchors for instance, as in this case the maximum error diminishes with increasing polynomial order. These nodes can be found with the equation

$$\omega_q^{Ch} = \frac{1}{\sqrt{2}}\left((\omega_{upper}^2 - \omega_{lower}^2)\cos\left[\frac{(2q+1)\pi}{2N}\right] + (\omega_{upper}^2 - \omega_{lower}^2)\right)^{\frac{1}{2}} \quad (4)$$

where *N* is the number of anchor points, *q* goes from 0 to $N-1$, and $\omega_{upper/lower}$ are the upper and lower boundaries the nodes are to be generated in between. Here, $\omega_{upper/lower}$ define the frequency window of interest for a spectrum being transformed. Since the multiply subtractive KK transformation has the form of an interpolating polynomial, placing the anchor points at the Chebyshev nodes should minimize oscillations between the bounds. One must also consider that the Chebyshev nodes represent a nonlinear distribution that are dependent on *N* and $\omega_{upper/lower}$, i.e. they are independent of what the spectrum may look like. One should choose the Chebyshev-zeros such that the anchor points will fall onto frequencies where important ORD features should be reproduced as accurately as possible. To find these important spectral features, should experimental data not be known, we suggest to calculate a CD spectrum spanning the desired frequency region and then perform a regular (nonsubtractive) KK transformation on it. This will show the main peak/trough pattern of the ORD apart from the relatively smooth truncation error (see below).

Chained subtractive transformations. Another possibility is to perform transformations of low polynomial order and "chain" them back together; herein we propose a chained doubly-subtractive KK transformation (CDKK). To our knowledge, this version of the subtractive KK has not yet been considered. To picture this method, one should imagine anchor points $\omega_1, \omega_2, \omega_3, \ldots, \omega_N$ where $N-1$ doubly subtractive transformations of the CD use anchors ω_1 to ω_2, then ω_2 to ω_3 and so forth. The resulting transformations are stitched back together at the common anchor points and the data outside the $[\omega_i, \omega_{i+1}]$ interval for transformation *i* is discarded. The resulting transformation polynomial is of low order, which will also reduce the interpolation error. The CDKK has properties that are more akin to a spline fit (along with the advantages of spline fits) than a polynomial fit.

Lineshape-replacement KK method. The dampened ORD computed from LR has an intrinsic Lorentzian absorptive lineshape with a constant linewidth built into itself (as a result of the implementation[21,42]). However, we may still obtain ORD based on other lineshapes, such as Gaussian, and/or other linewidths with the help of Lorentzian and Gaussian broadened CD spectra along with a smooth ORD curve generated either from a large number of LR calculations or, more efficiently, from MSKK/CDKK transformations. This can be achieved, for instance, with the following protocol:

1. Select a frequency window for the ORD.
2. Calculate the ORD within the frequency window, either on many frequency points, or using subtractive KK methods, with a reasonable damping parameter (undamped calculations may work but would be numerically very sensitive near the resonance frequencies).
3. Covering at least this frequency window, calculate a CD spectrum with a Lorentzian broadening consistent with step 2. Alternatively, one may use peak fitting for the imaginary part of the LR OR of step 2.
4. Subtract the KK transformation of the CD of step 3 from the ORD of step 2. The difference, ΔORD, represents the contribution to the ORD from CD transitions outside the frequency window of interest (the KK truncation error).
5. Add that difference, ΔORD, to the KK transformation of a Gaussian or otherwise broadened CD spectrum.

By KK-transforming the Lorentzian CD spectrum and then subtracting it from the ORD we remove the information specific to the lineshape and line-width. What is left, ΔORD, is the influence from higher excitations that constitutes the cut-off error made when transforming a truncated spectrum. The CD cut-off should be high enough such that the line-shape of these high-lying excitations has no effect on ΔORD, which for practical purposes we assume to be the case if the cut-off for the CD is several eV (several 10^4 cm^{-1}) above the frequency range for which the ORD is to be studied. The information contained in ΔORD can then be added to the KK of a Gaussian or otherwise broadened CD, which yields an ORD corresponding to line shapes that are more consistent with lineshapes observed experimentally.

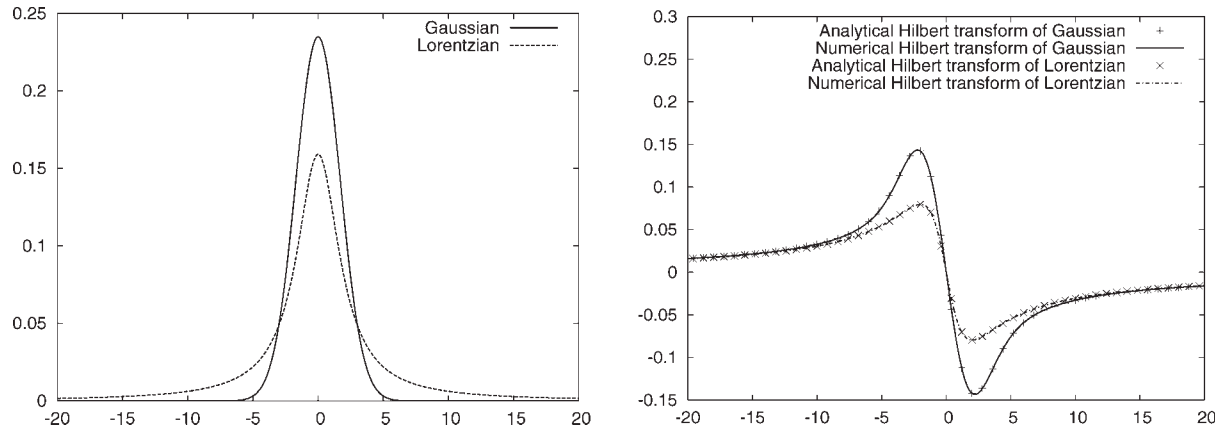

Fig. 1. Normalized Gaussian and Lorentzian functions with the same width at half peak height (left), and their analytic and numerical Hilbert transforms (right).

RESULTS AND DISCUSSION

Analytic Model Spectra

Analytical KK-transform solutions are known for antisymmetrized Lorentzian[49] and Gaussian[51] functions (see Appendix). Since the computations on molecules involve imprecisions from numerical integrations and finite convergence thresholds, an exact "synthetic" analytic spectrum with a known lineshape is useful to test the accuracy of the transformations as well as the principal performance of the various subtractive methods. In Figure 1, we show a normalized Lorentzian and a normalized Gaussian function along with their analytical and numerical (using Maclaurin's integration) transforms. The agreement between numerical and analytical results is excellent. Because of the faster decay of the Gaussian function, when comparing the transforms of two normalized peaks with the same width at half peak height, the transform of the Gaussian has a more strongly pronounced peak and trough.

In this section, the functions and transformations shown are based on Lorentzians unless otherwise noted. The methods work equally well for Gaussian lineshapes.

An analytic "Im[β]" and corresponding "Re[β]" were generated using a linear combination of over 3000 antisymmetrized Lorentzian (or Gaussian) functions representing excitations with a broadening (half width at half peak height) of $\gamma = 0.007$ au to represent the real and imaginary part of the OR parameter β for a hypothetical molecule. We note that the spectral data is typical for a molecule described computationally by a finite atomic orbital basis set. A truncated version of this spectrum generated from the lowest 16 excitations as illustrated in Figure 2 was then taken to study the performance of the MSKK, CDKK, and the lineshape-replacement methods. Regular (non-anchored) KK transformations of the full and the truncated spectrum are shown in Figure 3. The error from truncation is clearly visible by comparing the transformations.

Figure 4 shows the comparison of MSKK transformations with 2, 5, and 10 anchor points at the Chebyshev zeros on the range ω between 3.5 and 10 (all quantities in arbitrary units). It is seen that with increasing number of anchoring points the accuracy of the MSKK transformation becomes better. It appears that for a CD/ORD with as many spectral features as present in our analytic model example 10 anchor points yield quite acceptable results.

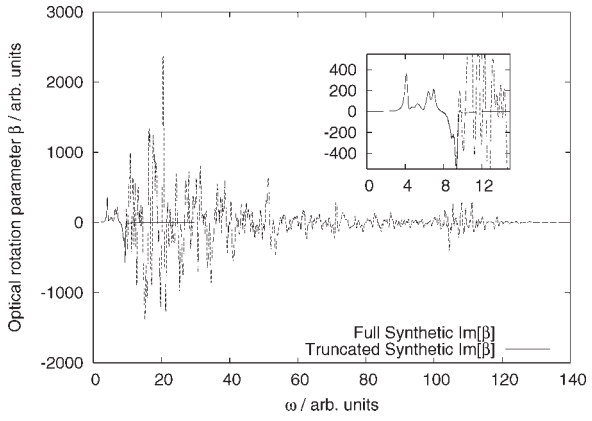

Fig. 2. Synthetic model Im[β] in its full and truncated forms.

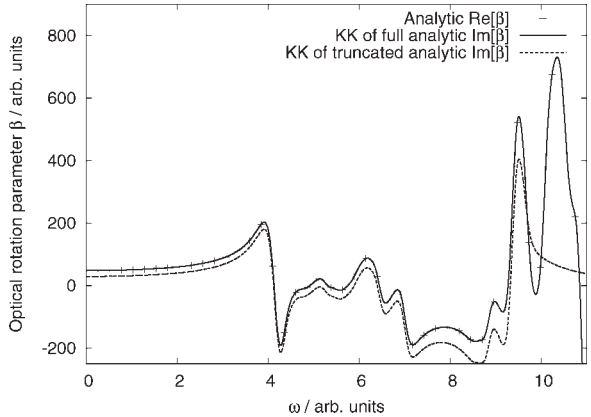

Fig. 3. Numerical KK transforms of full and truncated analytic model Im[β] spectra, respectively, along with the analytic Re[β].

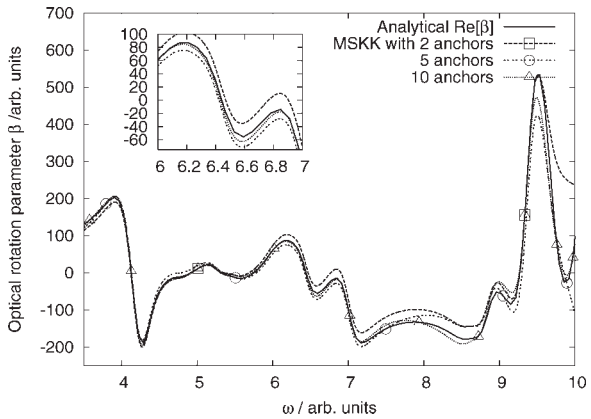

Fig. 4. Numerical MSKK of the analytic model Im[β] spectrum with varying numbers of anchor points.

An important issue for obtaining accurate MSKK transforms of truncated spectra is the placement of the anchor points. Figure 5 shows a comparison of two MSKK transformations with 10 anchor points each. One transformation has anchors at the 10 Chebychev zeroes of the interval [3.5–10], the other uses the interval [4.0–9.6]. The transformation with anchors in the [4.0–9.6] range better matches the exact result. This shows that it is not only important to choose the anchor points at the Chebychev zeros to reduce the error from the high order polynomial interpolation nature of the MSKK procedure, but also to choose a range for those points where they lie on important spectral features (as mentioned earlier). We can see that the transformation in the [4.0–9.6] interval has a point on the small peak at $\omega = 9$ and two more near the top of the larger peak at 9.5 eV. The four anchors at highest frequency for the transformation in the [3.5–10] interval have two peaks and two troughs between them, and Im[β] is rapidly changing near the anchor points, which is an undesirable situation. When choosing the placement of anchor points we therefore recommend to control the result visually as in Figure 5 to ensure an optimal placement with respect to strongly oscillating parts of the transform.

Figure 6 shows a CDKK that used 20 evenly spaced anchor points in the interval 4–10 (the anchors do not coincide with the Chebyshev zeroes). It can be seen that the transform agrees very well with the exact result. Therefore, at the cost of a somewhat larger number of anchor points one can choose an evenly spaced anchor point grid straightforwardly and does not need to worry about an accidental suboptimal anchor point placement. In a number of tests on random analytic model spectra, we have typically obtained results of the same quality as for a MSKK with well chosen anchor points when using a CDKK with a uniform grid of 1.5 to 2 times as many anchor points.

Figure 7 shows the lineshape-replacement KK method (LRKK, see Methodology section) for removing the Lorentzian lineshape that is inherently built into dampened OR computations. We have subtracted the KK transformation of the truncated Lorentzian Im[β] spectral data from the analytical Lorentzian Re[β] to obtain ΔORD. This result was then added to the KK transformation of the truncated Gaussian Im[β]. The analytical Re[β] based on the Gaussian lineshape is plotted as well for comparison. We can see that the Gaussian broadened Re[β] from the LRKK procedure is in excellent agreement with the analytical solution as it should be. Towards the high energy cut-off there is some deviation, but that is expected as noted earlier. The deviation can be reduced by extending the cut-off for the CD beyond the ORD frequency window of interest (typically >1 eV in practical computations). The cutoff for the excitations used for Figure 7 was at ~10 arb. units, i.e. the most accurate results for the lineshape-replacement method would be at frequencies below this value where tails of absorption peaks above the cut-off do not affect ΔORD.

DMO

DMO has been one of the "benchmark" molecules for chiroptical response computations because of its small number of atoms, the fact that its CD has been measured up to ~9 eV,[52] and that the CD is well reproduced by TD-

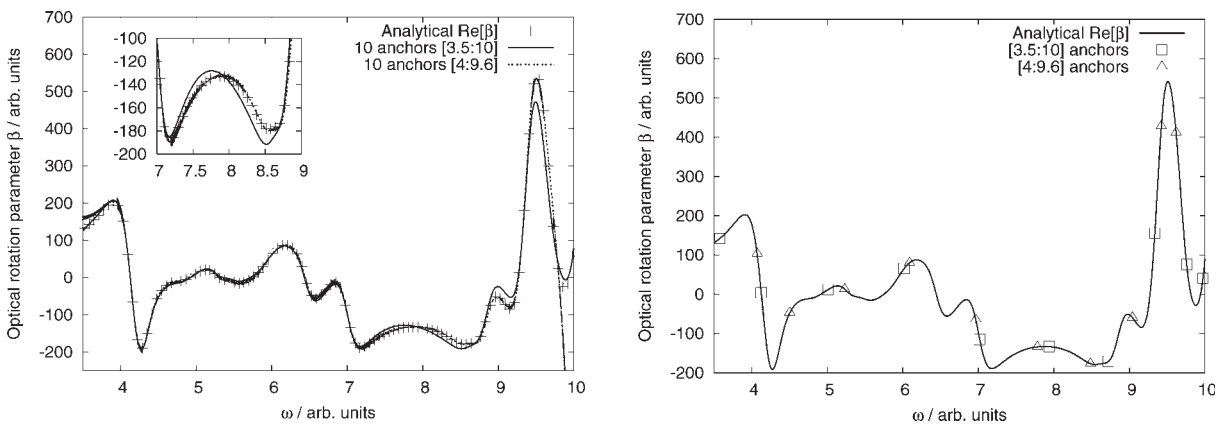

Fig. 5. Left: MSKK transformations of the analytic Im[β] using 10 anchor points within different ranges. Right: Placement of the anchor points.

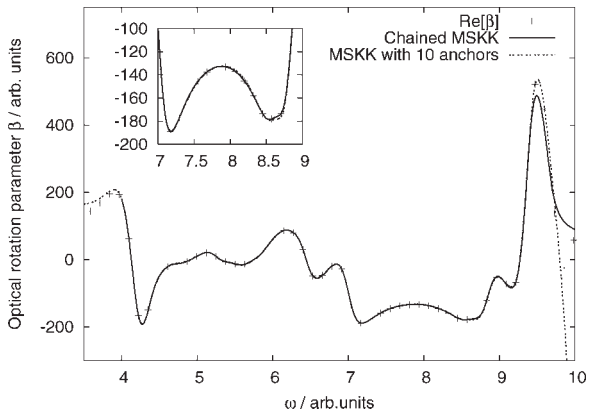

Fig. 6. Chained doubly-subtractive KK (CDKK) for the truncated analytic model Im[β] spectrum.

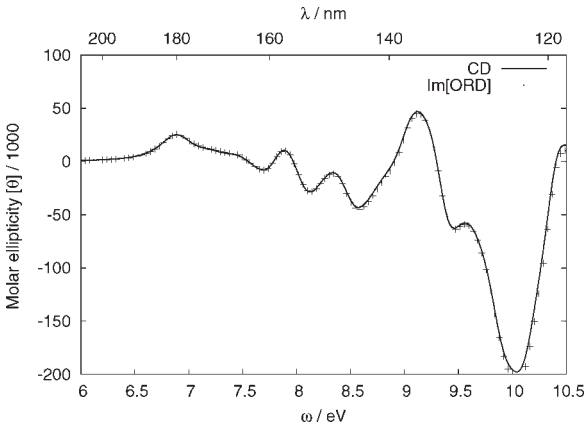

Fig. 8. Computed molar ellipticity of DMO (γ = 0.007 au Lorentzian broadening), and computed imaginary part of the molar rotation from damped linear response.

DFT computations.[53] Because of the abundance of theoretical data we decided that DMO would be a suitable test case for a first application of the various subtractive schemes using first-principles computations. Figure 8 shows a comparison of the simulated CD (from excitation energies and rotatory strengths) versus the imaginary part of the damped LR molar rotation. For the purpose of this benchmark study we have computed the LR OR with damping at a comparatively large number of frequency points. As can be seen, the molar ellipticity and the imaginary part of the molar rotation have excellent agreement up to about 10 eV whereafter slight deviations start to occur due to the high density of states.[40] For applications of the LRKK method it is important to know that the LR computations of the complex rotation angle yield the same CD as separate CD computations. Slight disagreement is typically obtained due to numerical imprecisions, finite convergence criteria, and so on.

Figure 9 shows the comparison of MSKK transformations for DMO with 2, 5, and 10 anchor points at the Chebychev zeroes in the frequency interval [6.0–10.5] eV. As with the analytic model spectrum, the use of 10 ORD anchor points turns out to be sufficient to anchor the KK transformation of the truncated CD over this frequency interval. Figure 10 shows a CDKK with 14 points in the 6–10 range in comparison with the MSKK with 10 anchor points. In this case, 14 evenly spaced points yielded about the same quality of transform as an MSKK with carefully chosen Chebychev zeros. As a rule of thumb, with multiple excitations over the desired frequency window and damping parameters on the order of 0.2 eV, 4–5 anchors per eV turned out to yield good coverage of the spectrum. In comparison, it is not always straightforward to increase the accuracy of a MSKK due to the accumulation of singular terms. Figure 11 shows the breakdown of the MSKK towards the upper and lower bounds of the frequency window when using the same 14 anchors as used in the CDKK (as expected). This illustrates that the anchor placement can be somewhat inflexible with the MSKK method, i.e. the use of the Chebychev zeros becomes mandatory at a high enough number of anchor points. Overall, however, it can be seen that both methods produce good results. The chained method is easier to apply

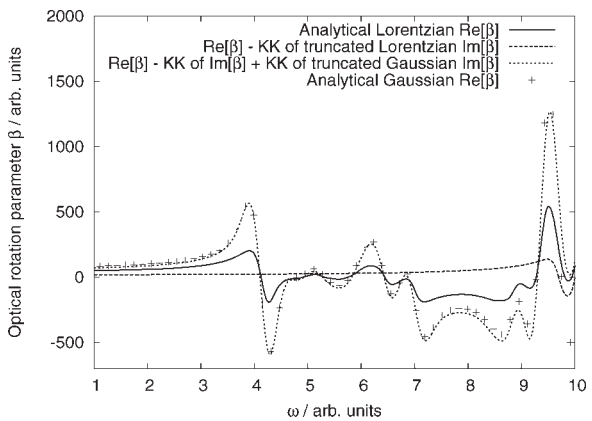

Fig. 7. The lineshape-replacement method (LRKK) described in the Methodology section applied to the analytic model Im[β] spectral data using Lorentzian and Gaussian broadening.

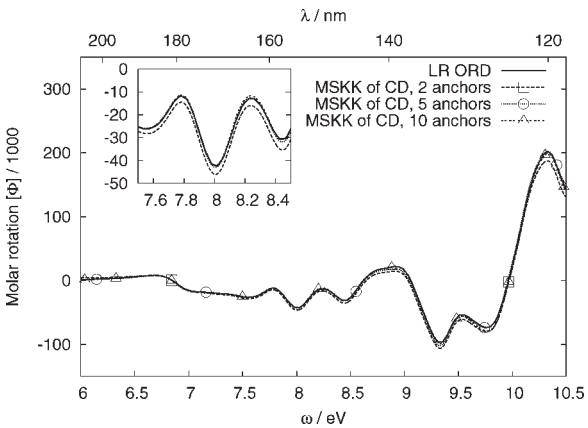

Fig. 9. Molar rotation of DMO from MSKK transformations with varying numbers of anchors (γ = 0.007 au Lorentzian broadening).

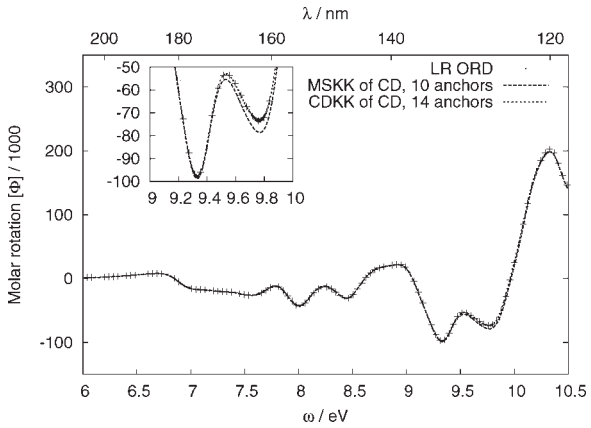

Fig. 10. Molar rotation of DMO from CDKK transformations of the CD using 14 anchor points, compared with a 10-anchor MSKK (γ = 0.007 au Lorentzian broadening).

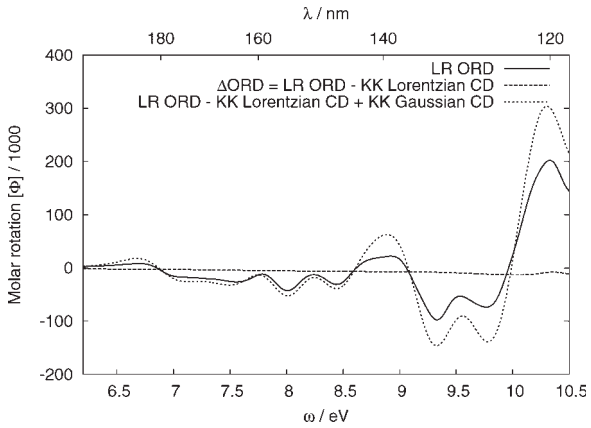

Fig. 12. Gaussian-broadening based ORD for DMO, computed with the subtractive LRKK method as outlined in Results and Discussion (γ = 0.007 au).

and appears to be more balanced, but requires somewhat more anchor points.

Using the LRKK, Figure 12 shows the ORD where a Gaussian line shape is underlying the resonant part. As already indicated in Figure 1, the peak/trough pattern of the ORD becomes more pronounced when using Gaussian broadening with the same line width at half peak height used for the Lorentzian broadening of the CD. Qualitatively, the pattern is the same, as one might expect. Since we have used a large frequency range for the CD, the KK frequency-cutoff error is relatively small compared with the peak/trough heights in the ORD at low frequencies.

Fenchone

Figure 13 shows a comparison of the computed CD versus the imaginary part of the LR molar rotation computations. The small DZP basis was chosen to facilitate benchmark calculations over a wide frequency range. However, we note that for fenchone the ORD in the near-UV range is quite well reproduced with TDDFT computations of this type.[21] As with DMO, the results agree reasonably well over the entirety of the frequency range with larger deviations occurring at higher frequencies. The deviations at higher ω are likely due to the high density of states in this frequency range.[40] For the various KK transformations we have used the 50 lowest-energy CD transitions.

Figure 14 shows the comparison of MSKK transformations with 2, 5, and 10 anchor points for the SAOP/DZP computations. As it was found for DMO, also for fenchone 10 anchor points appear to be sufficient to yield an accurate transform. Figure 15 shows a CDKK with 18 anchors (evenly spaced) along side of the MSKK with 10 anchor points. Both the CDKK and MSKK agree quite well over the observed frequency range. The largest deviations occur in the resonant region, where the ORD oscillates strongly and larger (absolute) deviations may be expected. The usefulness of the CDKK method becomes visible here, as the anchors can be chosen more freely in contrast to the nonlinear distribution of Chebyshev zeros fixed by the frequency range. To change the Chebyshev zeroes, one would have to adjust the bounds, which would in turn affect the location of every anchor point.

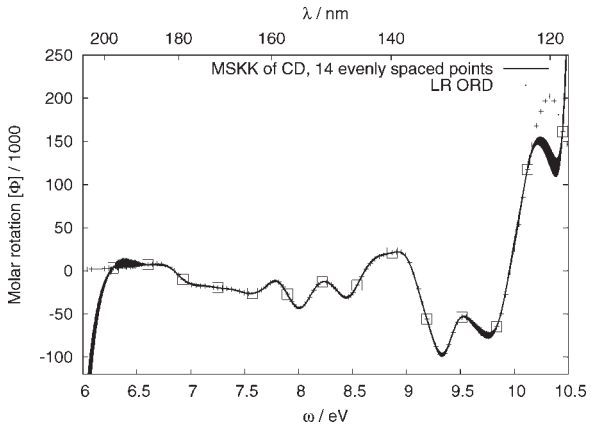

Fig. 11. MSKK of truncated CD for DMO, using 14 evenly spaced anchor points (squares). Note the breakdown of the MSKK at high frequencies and the considerable noise in the transform.

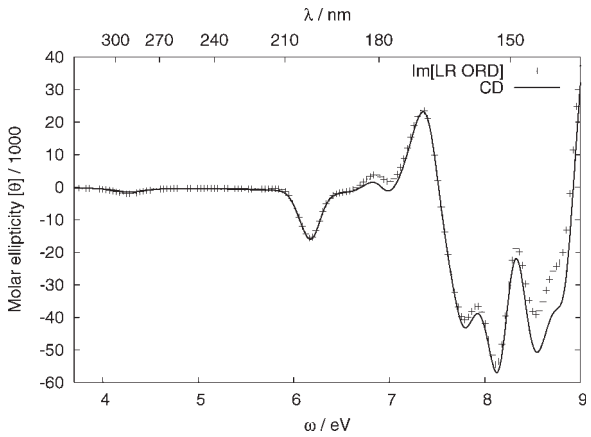

Fig. 13. Computed molar ellipticity of fenchone, and computed imaginary part of the molar rotation from damped linear response, both with DZP basis and γ = 0.007 au.

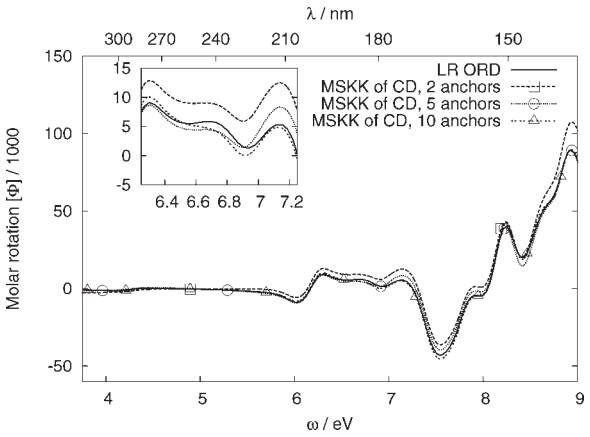

Fig. 14. Molar rotation of fenchone from MSKK transformations of SAOP/DZP computations with varying numbers of anchor points.

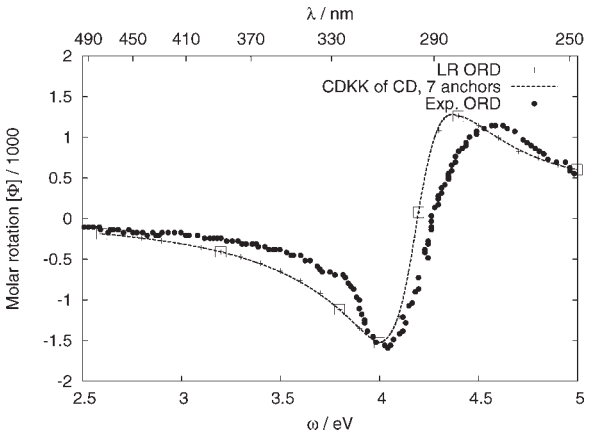

Fig. 16. Molar rotation of fenchone in the *n*-to-π* region from a CDKK transformation using 7 anchor points (squares), SAOP/TZ2P+ computations (γ = 0.007 au). Also shown is the corresponding linear response ORD and Experimental ORD. Experimental data from Ref. 22.

For direct comparisons with experimental data, we have recomputed the CD spectrum and the ORD in the *n*-to-π* region with the diffuse doubly polarized triple-ζ basis TZ2P+ (see Computational Details and Methodology). Results for a CDKK procedure are shown in Figure 16 along with a large number of LR OR points and experimental data. The use of 7 anchors with a CDKK transformation produces an ORD curve that is in excellent agreement with the computed LR OR. The agreement with experiment is also quite good, as was already noted in Ref. 21, despite the underlying Lorentzian lineshape.

Figure 17 displays the experimental CD spectrum of fenchone in the *n*-to-π* region along with computed Gaussian- and Lorentzian-broadened CD. It is easy to test different linewidths and shapes for the CD once the rotatory strengths and excitations have been calculated, to find the lineshape/linewidth combination that matches best with the experiment. One can then use the subtractive method (LRKK) to investigate lineshape effects on the ORD. Results for the LRKK method are shown in Figure 18. We have decided not to scale the computed CD intensities because this would yield a different long-wavelength limit of the molar rotation than the LR computations.

Using the LRKK subtractive method of KK transformations outlined in the Methodology section, Figure 18 shows the *n*-to-π* resonant ORD based on Gaussian line shapes (SAOP/TZ2P+ level of theory). We note that the KK truncation error is quite pronounced even with the use of 50 CD excitations (comparing the magnitude of ΔORD with the peak/trough heights), therefore the determination of ΔORD is mandatory here. Regarding the overall agreement with experiment, some improvement is obtained when using a Gaussian broadening of γ = 0.0077 au because it leads to a larger frequency separation of the ORD's peak and trough. This value for γ is also the one that leads to good agreement with the peak height of the CD in Figure 17. However, to further improve the agreement with the experimental ORD from the LRKK procedure, it would also be necessary to blue-shift the excitation energy slightly, and to use a slightly reduced rotatory

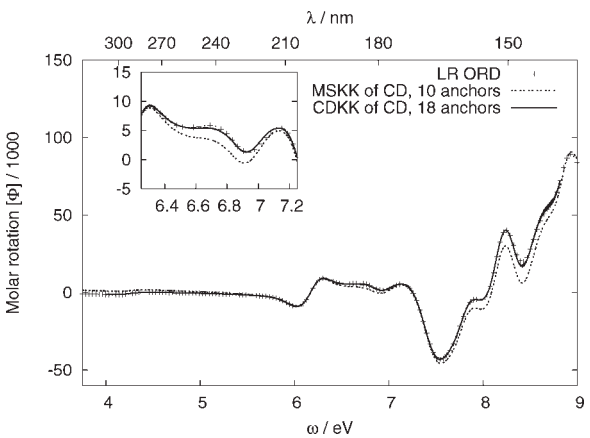

Fig. 15. Molar rotation of fenchone from CDKK transformations of the SAOP/DZP CD using 18 anchors, compared with a 10-anchor MSKK.

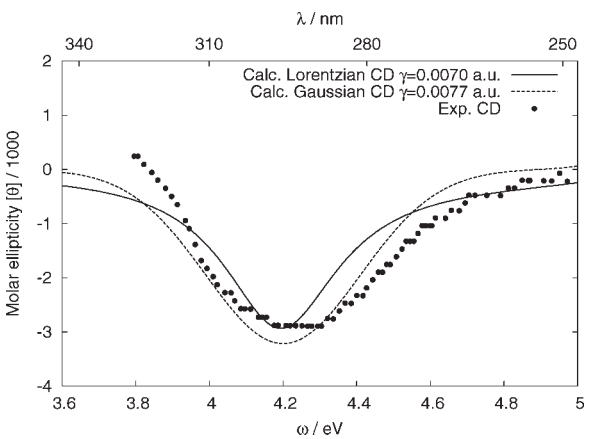

Fig. 17. Computed CD spectrum of fenchone, SAOP/TZ2P+ level of theory. Lorentzian and Gaussian broadening as indicated in the key. Experimental data from Ref. 52.

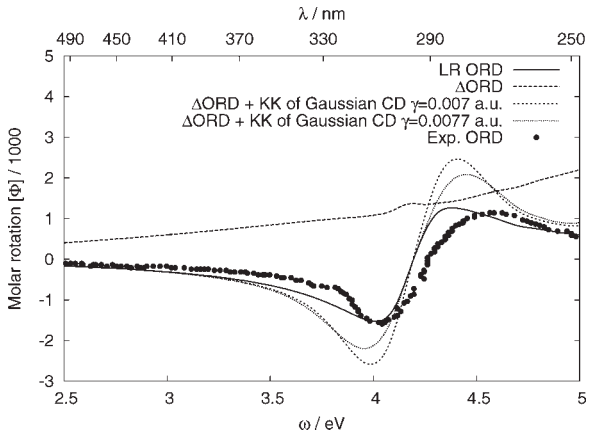

Fig. 18. Use of the subtractive method (LRKK) with Gaussian broadened CD spectra ($\gamma = 0.0070$ and $\gamma = 0.0077$ au). Subtraction based upon the 25 LR ORD points shown in Fig. 16. Alternatively, the 7-point CDKK could be used. Experimental data from Ref. 22.

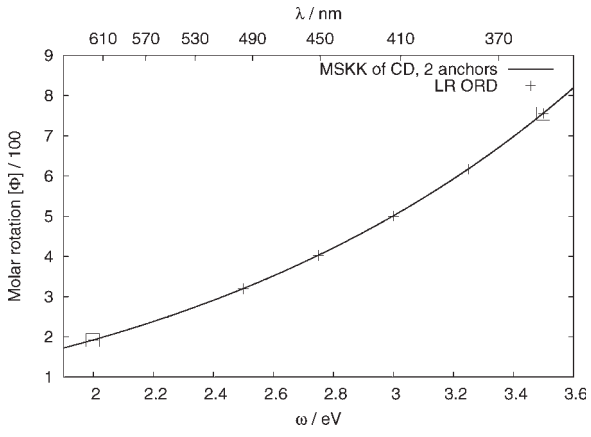

Fig. 19. Molar rotation of (P)-(+)-[4]triangulane: MSKK of the BHLYP/aug-cc-pVDZ CD with 2 LR OR anchor points (squares), and BHLYP/aug-cc-pVDZ LR optical rotations on a finer frequency grid ("+" markers).

strengths for the *n*-to-π* transition. It is likely that a more accurate computation (e.g., at a highly correlated ab-initio level with a large basis set) would yield improved excitation energies and rotatory strengths in which case a combination of CDKK and LRKK should be able to yield full agreement with the experimental ORD at affordable computational cost.

(P)-(+)-[4]Triangulane

Recently, accurate computed ORs for (P)-(+)-[4]triangulane have been showcased to demonstrate how computations can assist with the assignment of the AC.[23] The experimentally available ORD for triangulane lies in the nonresonant frequency region.[54] As Crawford et al. have shown,[23] TD-DFT yields ORs that follow the experimental trend but are somewhat too large in magnitude (most likely due to an underestimation of the lowest excitation energies). Coupled-cluster singles and doubles (CCSD) results were shown to agree very well with experiment, but the computations required a significant amount of time. The authors quoted a CPU time consumption of about one week for each frequency point. Therefore, this molecule is a good target for applying the subtractive KK methods in the nonresonant regime.

For [4]triangulane, we decided to use the BHLYP hybrid functional (50% exact exchange) along with the aug-cc-pVDZ basis since this level of theory yields ORs that agree reasonably well with experiment and with the CCSD results. To create Figure 19, we have initially used the calculated CD from the lowest 90 excitations and used 2 LR OR anchor points in the frequency range where experimental data are available to perform a MSKK transformation. Essentially the same MSKK results can be obtained with as few as the lowest 2 or 3 excitations in this case. We note that the lowest excitations are 4–5 eV above the frequency range where the ORD has been measured. The transformation with only 2 anchor points reproduces the calculated OR values with excellent agreement. No separate CDKK transformation was performed here, as with only 2 anchor points the two methods are equivalent. Provided that a CD spectrum can be obtained at relatively low computational cost (for instance from TD-DFT) or computational cost comparable with one LR OR point (which we would expect for a few excitations calculated at the CCSD level) the savings in computational time are potentially quite significant despite the fact that in the nonresonant region fewer LR points are needed to produce a smooth ORD curve.

For Figure 20, we have used the calculated CD (BHLYP/aug-cc-pVDZ), along with two of the five CCSD ORs from Ref. 23 for anchoring. Once again, the use of only 2 anchors produces a smooth ORD curve that encompasses all 5 calculated values. Since the CCSD results of Crawford et al. are very close to the experimental values, no separate MSKK transformation is shown using experimental anchors. We assume that the CD spectrum from the TD-DFT computations is moderately accurate because of the reasonable performance of BHLYP/aug-cc-pVDZ to reproduce the ORD. In this case, it is seen that a few accu-

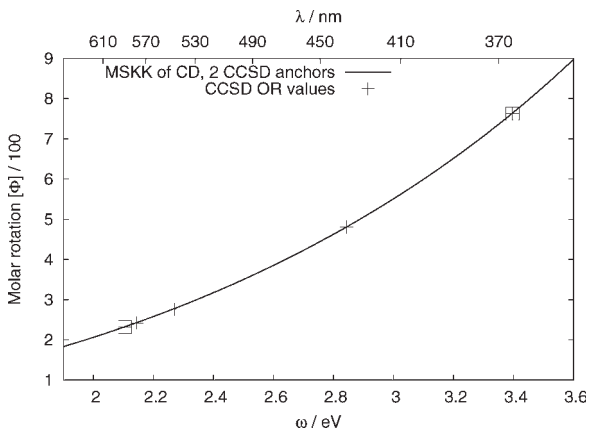

Fig. 20. Molar rotation of [4]triangulane. Same as Figure 19, but using two CCSD data-points for anchoring (squares). Other CCSD results indicated by "+" markers.

rate OR computations at a correlated ab-initio level along with the MSKK transformation of the CD computed with TD-DFT may yield excellent agreement with experiment over the whole range where the ORD is known. Upon transformation, the anchoring appears to eliminate most of the errors in the computed CD from approximations in the density functional (i.e., we obtain the same results as what one would expect from an anchored transformation of the CD spectrum calculated at the CCSD level of theory). Although it would be preferable to compute the CD with a consistent method (here CCSD), a mixed-level approach may perhaps be useful in cases where CD spectra cannot be obtained at the same level of theory or would be too costly to determine.

SUMMARY AND CONCLUSIONS

We have tested the accuracy and principal performance of subtractive KK transformations for the purpose of generating smooth ORD curves from a combination of damped LR computations of ORD at selected frequencies (anchor points) with simulated CD spectra (obtained from computations of excitation energies and rotatory strengths). Both CD and ORD were obtained from first-principles computations. The results are very promising and show that such transformations are a feasible way to produce smooth accurate dispersion curves with a small number of LR OR points, while avoiding the truncation error of the unmodified KK transformation when using a truncated CD spectrum. The advantages are obvious for the case of resonant ORD. However, the case of [4]triangulane has shown that potentially large savings of computer time are also possible for nonresonant ORD because the subtractive methods yield very good results here with just two anchor points, one at the beginning and one at the end of the frequency range of interest. It also seems possible to use a subtractive method based on anchor points calculated with a highly accurate method to eliminate (modest) errors from TD-DFT approximations along with the cut-off error when using TD-DFT CD spectra to obtain the OR dispersion. In most cases, however, it would be preferred to use theoretical methods for OR and CD that are as consistent as possible.

As Palmer has pointed out, a MSKK with N anchor points has features similar to that of an Nth degree interpolating polynomial. Therefore, the Chebychev zeros (eq. 4) should be used to minimize the interpolation error.[50] These zeroes are determined from N and the frequency range of interest, and are therefore independent of the features of the spectrum being transformed. We found that 10 anchor points typically yielded good results, but one should select a frequency range and number of anchor points so that the Chebychev zeroes lie on important spectral features. To select the anchor points for the OR computations, it would be advisable to compute the CD first, and visually inspect the anchor point locations with respect to a nonsubtractive KK transform of the CD spectrum.

Alternatively, by performing a series of doubly-subtractive KK transformations, the results can be "chained" back together to yield a transformation that has properties more similar to a spline fit than a polynomial fit (CDKK). With this method, the placement of anchor points is more easily manageable; anchor points can be added or removed at any time (as opposed to selecting Chebychev zeros where the addition anchor points renders the previously used set of anchors obsolete). For the examples investigated here the CDKK needed a somewhat larger number of anchor points as a MSKK with well chosen anchors. We believe that the advantage of the simple choice of anchor points and the possibility of easily adding points would make the CDKK procedure the preferred choice in most cases.

With the help of standard or subtractive KK transformations, the Lorentzian line shape information that is implicit in the damped OR computations can be subtracted out of the damped LR. Afterwards, the KK transform of an arbitrarily broadened CD spectrum can be added back into the ORD. We have termed this method the LRKK, which allows to take advantage of the nonsingular behavior of the damped LR computations near and at resonances without being restricted to simulations that are implicitly based on Lorentzian lineshapes. In many cases, it would be preferred to use a Gaussian-broadened CD spectrum, for instance. In the future work, we will explore the possibility of using the even more realistic line shapes obtained from simulations of the vibronic structure of the CD spectrum in the LRKK protocol.[53]

ACKNOWLEDGMENTS

The authors would like to acknowledge support from the center for computational research at the University at Buffalo. We thank Prof. Harry F. King for helpful discussions regarding the Hilbert transformation of a Gaussian function.

LITERATURE CITED

1. Polavarapu PL, Optical rotation: recent advances in determining the absolute configuration. Chirality 2002;14:768–781.
2. Pecul M, Ruud K, The ab initio calculation of optical rotation and electronic circular dichroism. In: Jensen H, editor. Advances in quantum chemistry, Vol. 50. San Diego: Elsevier; 2005. p 185–212.
3. Crawford TD. Ab initio calculation of molecular chiroptical properties. Theor Chem Acc 2006;115:227–245.
4. Autschbach J. Computation of optical rotation using time-dependent density functional theory. Comp Lett 2007;3:131–150.
5. Polavarapu PL. Renaissance in chiroptical spectroscopic methods for molecular structure determination. Chem Rec 2007;7:125–136.
6. Autschbach J, Ziegler T. Double perturbation theory: a powerful tool in computational coordination chemistry. Coord Chem Rev 2003;238/239:83–126.
7. Autschbach J. Density functional theory applied to calculating optical and spectroscopic properties of metal complexes: NMR and optical activity. Coord Chem Rev 2007;251:1796–1821.
8. Stephens PJ. Theory of vibrational circular dichroism. J Phys Chem 1985;89:748–752.
9. Nafie LA, Freedman TB. Vibronic coupling theory of infrared vibrational transitions. J Chem Phys 1983;78:7108–7116.
10. Yang D, Rauk A. Vibrational circular dichroism intensities by ab initio second-order Møller-Plesset vibronic coupling theory. J Chem Phys 1994;100:7995–8002.

11. Haesler J, Schindelholz I, Riguet E, Bochet CG, Hug W. Absolute configuration of chirally deuterated neopentane. Nature 2007;446:526–529.
12. Stephens PJ, Devlin FJ, Cheeseman JR, Frisch MJ, Bortolini O, Besse P. Determination of absolue configuration using ab initio calculation of optical rotation. Chirality 2003;15:S57–S64.
13. Stephens PJ, McCann DM, Cheeseman JR, Frisch MJ. Determination of absolute configurations of chiral molecules using ab-initio time-dependent density functional theory calculations of optical rotation: how reliable are absolute configurations obtained for molecules with small rotations. Chirality 2005;17:S52–S64.
14. Furche F, Ahlrichs R, Wachsmann C, Weber E, Sobanski A, Vögtle F, Grimme S. Circular dichroism of helicenes investigated by time-dependent density functional theory. J Am Chem Soc 2000;122:1717–1724.
15. Autschbach J, Ziegler T, van Gisbergen SJA, Baerends EJ. Chiroptical properties from time-dependent density functional theory. I. Circular dichroism spectra of organic molecules. J Chem Phys 2002;116:6930–6940.
16. Diedrich C, Grimme S. Systematic investigation of modern quantum chemical methods to predict electronic circular dichroism spectra. J Phys Chem A 2003;107:2524–2539.
17. Giorgio E, Minichino C, Viglione RG, Zanasi R, Rosini C. Assignment of the molecular absolute configuration through the ab-initio Hartree-Fock calculation of the optical rotation: can the circular dichroism data help in reducing basis set requirements? J Org Chem 2003;68:5186–5192.
18. Stephens PJ, McCann DM, Butkus E, Stoncius E, Cheeseman JR, Frisch MJ. Determination of absolute configuration using concerted ab initio DFT calculations of electronic circular dichroism and optical rotation: bicyclo3.3.1.nonane diones. J Org Chem 2004;69:1948–1958.
19. McCann DM, Stephens PJ. Determination of absolute configuration using density functional theory calculations of optical rotation and electronic circular dichroism: chiral alkenes. J Org Chem 2006;71:6074–6098.
20. Kowalczyk TD, Abrams ML, Crawford TD. Ab initio optical rotatory dispersion and electronic circular dichroism spectra of (S)-2-chloropropionitrile. J Phys Chem A 2006;110:7649–7654.
21. Autschbach J, Jensen L, Schatz GC, Tse YCE, Krykunov M. Time-dependent density functional calculations of optical rotatory dispersion including resonance wavelengths as a potentially useful tool for determining absolute configurations of chiral molecules. J Phys Chem A 2006;110:2461–2473.
22. Giorgio E, Viglione RG, Zanasi R, Rosini C. Ab initio calculation of optical rotatory dispersion (ORD) curves: a simple and reliable approach to the assignment of the molecular absolute configuration. J Am Chem Soc 2004;126:12968–12976.
23. Crawford DT, Owens LS, Tam MC, Schreiner PR, Koch H. Ab initio calculation of optical rotation in (P)-(+)-4.triangulane. J Am Chem Soc 2005;127:1368–1369.
24. Kongsted J, Pedersen TB, Strange M, Osted A, Hansen AE, Mikkelsen KV, Pawlowski F, Jorgensen P, Hattig C. Coupled cluster calculations of the optical rotation of S-propylene oxide in gas phase and solution. Chem Phys Lett 2005;401:385–392.
25. Ruud K, Zanasi R. The importance of molecular vibrations: the sign change of the optical rotation of methyloxirane. Angew Chem Int Ed 2005;44:3594–3596.
26. Tam MC, Russ NJ, Crawford TD. Coupled cluster calculations of optical rotatory dispersion of (S)-methyloxirane. J Chem Phys 2004;121:3550–3557.
27. Wiberg KB, Wang Y, Murphy MJ, Vaccaro PH. Temperature dependence of optical rotation: α-pinene, β-pinene, cis-pinane,ecamphene, camphor, and fenchone. J Phys Chem A 2004;108:5559–5563.
28. Mort BC, Autschbach J. Temperature dependence of the optical rotation in six bicyclic organic molecules calculated by vibrational averaging. Chem Phys Chem 2007;8:605–616.
29. Mort BC, Autschbach J. A pragmatic recipe for the treatment of hindered rotations in the vibrational averaging of molecular properties. Chem Phys Chem 2008;9:159–170.
30. Muller T, Wiberg KB, Vaccaro PH. Cavity ring-down polarimetry (CRDP): a new scheme for probing circular birefringence and circular dichroism in the gas phase. J Phys Chem A 2000;104:5959–5968.
31. Barron LD. Molecular light scattering and optical activity, 2nd ed. Cambridge, UK: Cambridge University Press; 2004.
32. Berova N, Nakanishi K, Woody RW, editors. Circular dichroism. Principles and applications. New York: VCH; 2000.
33. Quack M. How important is parity violation for molecular and biomolecular chirality. Angew Chem Int Ed 2002;41:4618–4630.
34. Zavattini E, Zavattini G, Ruoso G, Polacco E, Milotti E, Karuza M, Gastaldi U, Di Domenico G, Della Valle F, Cimino R, Carusotto S, Cantatore G, Bregant M. Experimental observation of optical rotation generated in vacuum by a magnetic field. Phys Rev Lett 2006;96:110406–5.
35. Kramers HA. The theory of absorption and refraction of X-rays. Nature (London) 1926;117:775.
36. Kronig RdL. The theory of dispersion of X-rays. J Opt Soc Am 1926;12:547–557.
37. Polavarapu P. Kramers-Kronig transformation for optical rotatory dispersion studies. J Phys Chem A 2005;109:7013–7023.
38. Polavarapu PL. Protocols for the analysis of theoretical optical rotations. Chirality 2006;18:348–356.
39. Polavarapu PL, Petrovic AG, Zhang P. Kramers-Kronig transformation of experimental electronic circular dichroism: application to the analysis of optical rotatory dispersion in dimethyl-L-tartrate. Chirality 2006;18:723–732.
40. Krykunov M, Kundrat MD, Autschbach J. Calculation of CD spectra from optical rotatory dispersion, and vice versa, as complementary tools for theoretical studies of optical activity using time-dependent density functional theory. J Chem Phys 2006;125:194110–194113.
41. Polavarapu PL, He J, Crassous J, Ruud K. Absolute configuration of C76 from optical rotatory dispersion. ChemPhysChem 2005;6:2535–2540.
42. Jensen L, Autschbach J, Schatz GC. Finite lifetime effects on the polarizability within time-dependent density functional theory. J Chem Phys 2005;122:224115–11.
43. Baerends EJ, Autschbach J, Bérces A, Bickelhaupt FM, Bo C, Boerrigter PM, Cavallo L, Chong DP, Deng L, Dickson RM, Ellis DE, van Faassen M, Fan L, Fischer TH, Fonseca Guerra C, van Gisbergen SJA, Groeneveld JA, Gritsenko OV, Grüning M, Harris FE, van den Hoek P, Jacob CR, Jacobsen H, Jensen L, van Kessel G, Kootstra F, van Lenthe E, McCormack DA, Michalak A, Neugebauer J, Osinga VP, Patchkovskii S, Philipsen PHT, Post D, Pye CC, Ravenek W, Ros P, Schipper PRT, Schreckenbach G, Snijders JG, Solà M, Swart M, Swerhone D, te Velde G, Vernooijs P, Versluis L, Visscher L, Visser O, Wang F, Wesolowski TA, van Wezenbeek E, Wiesenekker G, Wolff S, Woo T, Yakovlev A, Ziegler T. ADF2006.01, SCM, Theoretical Chemistry, Vrije Universiteit, Amsterdam, The Netherlands. Available at http://www.scm.com.
44. Autschbach J, Ziegler T. Calculating electric and magnetic properties from time dependent density functional perturbation theory. J Chem Phys 2002;116:891–896.
45. Autschbach J, Ziegler T, Patchkovskii S, van Gisbergen SJA, Baerends EJ. Chiroptical properties from time-dependent density functional theory. II. Optical rotations of small to medium sized organic molecules. J Chem Phys 2002;117:581–592.
46. Schipper PRT, Gritsenko OV, van Gisbergen SJA, Baerends EJ. Molecular calculations of excitation energies and (hyper)polarizabilities with a statistical average of orbital model exchange-correlation potentials. J Chem Phys 2000;112:1344–1352.
47. Quantum Chemistry Group. Universitaet Karlsruhe, Turbomole, Ver. 5.7.1.
48. Kundrat MD, Autschbach J. Time dependent density functional theory modeling of chiroptical properties of small amino acids in solution. J Phys Chem A 2006;110:4115–4123.
49. Ohta K, Ishida H. Comparison among several numerical integration methods for Kramers-Kronig transformations. Appl Spectrosc 1988;42:952–957.
50. Palmer KF, Williams MZ, Budde BA. Multiply subtractive Kramers-Kronig analysis of optical data. Appl Opt 1998;37:2660–2673.

51. King F. Efficient numerical approach to the evaluation of Kramers-Kronig transforms. J Opt Soc Am B 2002;19:2427–2436.
52. Pulm F, Schramm J, Hormes J, Grimme S, Peyerimhoff S. Theoretical and experimental investigations of the electronic circular dichroism and absorption spectra of bicyclic ketones. Chem Phys 1997;224:143–155.
53. Neugebauer J, Baerends EJ, Nooijen M, Autschbach J. Importance of vibronic effects on the circular dichroism spectrum of dimethyloxirane. J Chem Phys 2005;122:234305–234307.
54. de Meijere A, Khlebnikov A, Kostikov R, Kozhushkov S, Schreiner P, Wittkopp A, Yufit D. The first enantiomerically pure triangulane (M)-trispiro2.0.0.2.1.1.nonane is a sigma-4.helicene. Angew Chem Int Ed 1999;38:3474–3477.
55. Ahrenkiel RK. Modified Kramers-Kronig analysis of optical spectra. J Opt Soc Am 1971;61:1651–1655.

APPENDIX

Hilbert and KK Transformations

For a complex function, which represents the Fourier transform of a linear and causal physical response,

$$f(\omega) = f^{R}(\omega) + \imath f^{I}(\omega) \tag{A1}$$

the real (f^R) and imaginary (f^I) part of $f(\omega)$ constitute a Hilbert transform pair. The Hilbert transformations (forwards and backwards) are given as

$$f^{R}(\omega) = \frac{1}{\pi} P \int_{-\infty}^{\infty} \frac{f^{I}(\mu)}{\mu - \omega}\, d\mu \tag{A2}$$

$$f^{I}(\mu) = -\frac{1}{\pi} P \int_{-\infty}^{\infty} \frac{f^{R}(\omega)}{\omega - \mu}\, d\omega \tag{A3}$$

where P stands for the Principal Value of the integral, as there is a pole at $\omega = \mu$. For our optical response calculations $f^R(\omega)$ would be representative of the dispersive ORD and $f^I(\omega)$ would be the absorptive CD. For reasons of causality the ORD is an even function and the CD is an odd function, which is to say

$$f^{R}(-\omega) = f^{R}(\omega) \tag{A4}$$

$$f^{I}(-\omega) = -f^{I}(\omega) \tag{A5}$$

With this symmetry, one can eliminate negative frequencies from eqs. A2 and A3 to obtain the well known KK transformations

$$f^{R}(\omega) = \frac{2}{\pi} P \int_{0}^{\infty} \frac{f^{I}(\mu)\mu}{\mu^2 - \omega^2}\, d\mu \tag{A6}$$

$$f^{I}(\mu) = -\frac{2\mu}{\pi} P \int_{0}^{\infty} \frac{f^{R}(\omega)}{\omega^2 - \mu^2}\, d\omega \tag{A7}$$

Line Shapes

In this section, we will consider Gaussian and Lorentzian functions for f_1 in the Hilbert transformations. Let f_2 be the imaginary part of the complex OR angle in eq. 1, represented by a single peak centered at frequency ω_0, the Hilbert transform pairs for Lorentzian and Gaussian shapes are

- Lorentzian

$$\theta(\omega) = \frac{\kappa}{\pi} \frac{\gamma}{(\omega - \omega_0)^2 + \gamma^2} \tag{A8}$$

$$\varphi(\omega) = -\frac{\kappa}{\pi} \frac{(\omega - \omega_0)}{(\omega - \omega_0)^2 + \gamma^2} \tag{A9}$$

- Gaussian

$$\theta(\omega) = \frac{\kappa}{\sigma\sqrt{2\pi}} \exp\left(-\frac{(\omega - \omega_0)^2}{2\sigma^2}\right) \tag{A10}$$

$$\varphi(\omega) = \imath \frac{\kappa}{\sigma\sqrt{2\pi}} \exp\left(-\frac{(\omega - \omega_0)^2}{2\sigma^2}\right) \mathrm{erf}\left(\imath \frac{(\omega - \omega_0)}{\sigma\sqrt{2}}\right) \tag{A11}$$

The Lorentzian and Gaussian functions are normalized for $\kappa = 1$. Here, 2γ is the full peak width at half peak height for the Lorentzian, and the Gaussian function has the same width at half height for $\sigma = \gamma/(\sqrt{\ln 4})$. For the numerically accurate and rapid calculation of the error function along the imaginary axis in the Hilbert transform of the Gaussian function one may employ readily available code for the so-called Dawson integral

$$\exp(-\omega^2) \int_{0}^{\omega} \exp(\mu^2) d\mu = -\imath \frac{\sqrt{\pi}}{2} \exp(-\omega^2) \mathrm{erf}(\imath\omega) \tag{A12}$$

(e.g. at www.netlib.org). The transform pairs in eqs. A8–A11 can be easily symmetrized/antisymmetrized as

$$f_{\pm} = f(\omega) \pm f(-\omega) \tag{A13}$$

to yield analytic KK transform pairs for f_1 and f_2 in eq. A1. Using numerical software for KK transformation implies that the functions to be transformed are properly symmetrized/antisymmetrized, and the resulting transform will have the corresponding symmetry imposed onto it. To transform an unmodified Lorentzian/Gaussian the Hilbert transformation should be used instead.

Multiply Subtractive Kramers-Kronig Relations

Subtractive KK transformations have been used in various fields of science and engineering for some time and are fairly straightforward to derive.[55] The principle has been applied further to provide multiply subtractive KK transformations (MSKK) by Palmer[50] for reflectance and transmittance spectra. MSKK transformations are straightforward to adapt to CD and ORD.[40] The assumption is that for a given frequency, ω_1, if the value of the ORD, i.e., the real part $[\beta^R(\omega_1)]$ of the OR parameter, is known then it

can be used to "anchor" a truncated KK transformation around that point in the form of a subtractive KK transformation to reduce or eliminate the errors from truncation of the absorptive spectrum. With the KK relations already given in eqs A6 and A7, we will show such adaptations for the singly, doubly and then multiply subtractive KK equations.

The singly subtractive Kramers-Kronig transformation. One begins with eq. A6 at $\omega = \omega_1$ to yield

$$[\beta^R(\omega_1)] = \frac{2}{\pi}\int_0^\infty \frac{[\beta^I(\mu)]\mu}{\mu^2-\omega_1^2}\,d\mu. \tag{A14}$$

Here, $\beta^R = \mathrm{Re}[\beta]$ and $\beta^I = \mathrm{Im}[\beta]$. Then one subtracts eq. A14 from eq. A6 to give

$$[\beta^R(\omega)] - [\beta^R(\omega_1)] = \frac{2}{\pi}\int_0^\infty \frac{[\beta^I(\mu)]\mu}{\mu^2-\omega^2}\,d\mu - \frac{2}{\pi}\int_0^\infty \frac{[\beta^I(\mu)]\mu}{\mu^2-\omega_1^2}\,d\mu\,. \tag{A15}$$

The integrals on the right hand side of eq. A15 can be combined to yield the SSKK equation, as shown in eqs. A16 and A17.

$$\begin{aligned}[\beta^R(\omega)] - [\beta^R(\omega_1)] &= \frac{2}{\pi}\int_0^\infty [\beta^I(\mu)]\mu\left(\frac{1}{\mu^2-\omega^2} - \frac{1}{\mu^2-\omega_1^2}\right)d\mu \\ &= \frac{2}{\pi}\int_0^\infty [\beta^I(\mu)]\mu\left(\frac{(\mu^2-\omega_1^2)-(\mu^2-\omega^2)}{(\mu^2-\omega^2)(\mu^2-\omega_1^2)}\right)d\mu \end{aligned} \tag{A16}$$

$$[\beta^R(\omega)] = [\beta^R(\omega_1)] + \frac{2}{\pi}(\omega^2-\omega_1^2)\int_0^\infty \left(\frac{[\beta^I(\mu)]\mu}{(\mu^2-\omega^2)(\mu^2-\omega_1^2)}\right)d\mu \tag{A17}$$

The doubly subtractive Kramers-Kronig transformation. The doubly subtractive transformation is derived in the same manner as the singly subtractive: one takes a second anchor point, ω_2, and considers the SSKK equation at that frequency. This result is then subtracted from the SSKK equation. For higher-orders, the *n*th subtractive transformation is derived from the (*n*-1)th equation. Note that the derivation is easier after division of eq. A17 by $(\omega^2-\omega_1^2)$:

$$\frac{[\beta^R(\omega)] - [\beta^R(\omega_1)]}{\omega^2-\omega_1^2} = \frac{2}{\pi}\int_0^\infty \left(\frac{[\beta^I(\mu)]\mu}{(\mu^2-\omega^2)(\mu^2-\omega_1^2)}\right)d\mu \tag{A18}$$

$$\frac{[\beta^R(\omega_2)] - [\beta^R(\omega_1)]}{\omega_2^2-\omega_1^2} = \frac{2}{\pi}\int_0^\infty \left(\frac{[\beta^I(\mu)]\mu}{(\mu^2-\omega_2^2)(\mu^2-\omega_1^2)}\right)d\mu \tag{A19}$$

Subtracting eq. A19 from eq. A18 yields the DSKK equation (eqs. A20 and A21):

$$\begin{aligned}&\frac{[\beta^R(\omega)] - [\beta^R(\omega_1)]}{\omega^2-\omega_1^2} - \frac{[\beta^R(\omega_2)] - [\beta^R(\omega_1)]}{\omega_2^2-\omega_1^2} \\ &= \frac{2}{\pi}\int_0^\infty \left(\frac{[\beta^I(\mu)]\mu}{(\mu^2-\omega^2)(\mu^2-\omega_1^2)}\right)d\mu - \frac{2}{\pi}\int_0^\infty \left(\frac{[\beta^I(\mu)]\mu}{(\mu^2-\omega_2^2)(\mu^2-\omega_1^2)}\right)d\mu \\ &= \frac{2}{\pi}(\omega^2-\omega_2^2)\int_0^\infty \left(\frac{[\beta^I(\mu)]\mu}{(\mu^2-\omega^2)(\mu^2-\omega_1^2)(\mu^2-\omega_2^2)}\right)d\mu \end{aligned} \tag{A20}$$

which can be rewritten as

$$\begin{aligned}[\beta^R(\omega)] &= [\beta^R(\omega_1)]\frac{(\omega^2-\omega_2^2)}{(\omega_1^2-\omega_2^2)} + [\beta^R(\omega_2)]\frac{(\omega^2-\omega_1^2)}{(\omega_2^2-\omega_1^2)} \\ &+ \frac{2}{\pi}(\omega^2-\omega_1^2)(\omega^2-\omega_2^2)\int_0^\infty \left(\frac{[\beta^I(\mu)]\mu}{(\mu^2-\omega^2)(\mu^2-\omega_1^2)(\mu^2-\omega_2^2)}\right)d\mu. \end{aligned} \tag{A21}$$

The multiply subtractive Kramers-Kronig transformation. One may have noticed that for every anchor point ω_i a factor of $(\mu^2-\omega_i^2)$ appears in the denominator of the integral and a factor of $(\omega^2-\omega_i^2)$ appears outside of the integral. This trend follows through the 3rd, 4th, 5th and so on transformations to give the general multiply subtractive KK transformation (MSKK) equation for *N* anchors points as shown in eq. 3 in Computational Details and Methodology. It is noted that the Hilbert transformation can be successfully adapted for subtractive equations through the same process. One can prove eq. 3 by induction.

Calculation of Conformational Energies and Optical Rotation of the Most Simple Chiral Alkane

STEFAN GRIMME* AND CHRISTIAN MÜCK-LICHTENFELD
Theoretische Organische Chemie, Organisch-Chemisches Institut der Universität Münster, Münster, Germany

Presented at the 11th International Conference on Circular Dichroism, 2007, Groningen, Netherlands

ABSTRACT Quantum chemical calculations have been performed to investigate the conformer distribution of 4-ethyl-4-methyloctane and its optical rotation. With the reference methods MP2 and SCS-MP2, the energies of seven conformers are found within a range of about 1.5 kcal mol^{-1}. It is demonstrated that the relative energies cannot be reliably predicted with conventional GGA or hybrid density functionals, Hartree-Fock, semiempirical AM1, and classical force field (MM3) calculations. An empirical dispersion correction to GGA (PBE-D), hybrid (B3LYP-D), or double hybrid (B2PLYP-D) functionals corrects these errors and results in very good agreement with the reference energies. Optical rotations have been calculated for all seven conformers at the TDDFT(BHLYP/aTZV2P) level. The computed macroscopic rotation is derived from a classical Boltzmann average. The result (1.9–3.2 deg dm^{-1} $(g/mL)^{-1}$) is very close to the experimental value of 0.2 deg dm^{-1} $(g/mL)^{-1}$ for the (*R*)-enantiomer and has the right sign. Because six conformers are significantly populated at room temperature and the rotations of individual conformers differ in sign and magnitude, the calculated average rotation is rather sensitive to the conformer population used. From the electronic structure point of view, this example emphasizes the effect of long-range dispersion effects for the evaluation of population averaged quantities in large molecules. Computations based on free enthalpies are in worse agreement with experiment that is attributed to artefacts of the harmonic approximation used to compute the vibrational entropy terms. *Chirality 20:1009–1015, 2008.*

KEY WORDS: quantum chemical calculations; intramolecular dispersion; optical rotation; conformational energies

INTRODUCTION

The conformation of a molecule has a substantial influence on its physical and chemical properties. When several conformers of a compound are present in rapid equilibrium, many spectroscopic properties of the substance will appear as the average over the most abundant conformers. In these cases, calculations using quantum chemical methods simultaneously have to reliably predict the right relative energy of each conformer and its molecular properties.

Beside the inherent torsional potentials that are typical for the atom types and bonding situations in a molecule, different types of noncovalent intramolecular and intermolecular (solvent) interactions contribute to the relative energies of conformational isomers. Electrostatic (ES) and orbital interactions are of high importance for polar molecules with functional groups including heteroatoms. These are typically assumed to be negligible for non-polar alkanes where the dominant parts are Pauli-exchange repulsion (EXR) and attractive dispersion (DISP, also called van-der-Waals) interactions.[1] In any case, sufficient accuracy of a theoretical method is only achieved when it renders a reliable quantitative contribution of all the aforementioned forces.

Despite their appealingly simple structure and nonpolar character, energies of linear and branched alkanes have been shown to represent a kind of pitfall for the widely used density functional theory (DFT) methods. Because of some inability to correctly describe the mid- and long-range behavior of electron correlation, common GGA and hybrid functional even qualitatively fail to reproduce isomerization energies of alkanes.[2] It is shown here for the first time that related problems of nonlocal electron correlation effects also occur for seemingly simple conformational processes in alkanes, and that common force fields are not free of inconsistencies.

This problem came to our attention while studying the chiral alkane 4-ethyl-4-methyloctane that represents the

Contract grant sponsor: Deutsche Forschungsgemeinschaft ("Molekulare Orientierung als Funktionskriterium in chemischen Systemen"); Contract grant number: SFB 424
*Correspondence to: Stefan Grimme, Theoretische Organische Chemie, Organisch-Chemisches Institut der Universität Münster, Corrensstraße 40, D-48149 Münster, Germany. E-mail: grimmes@uni-muenster.de
Received for publication 13 November 2007; Accepted 14 January 2008
DOI: 10.1002/chir.20551
Published online 11 March 2008 in Wiley InterScience (www.interscience.wiley.com).

most simple unbranched saturated hydrocarbon with a quaternary stereogenic center.[3]

(*R*)-4-ethyl-4-methyloctane

The optical rotation (OR) of the (*R*)-enantiomer had earlier been assigned to be positive but very small ($[\alpha]^{25}_{578}$ = 0.185 [for 85% ee, i.e., $[\alpha]^{25}_{578}$ = 0.22]).[4] In the more recent synthesis of the title compound, similar values were found ($[\alpha]^{25}_{D}$ = 0.19, $[\alpha]^{23}_{365}$ = 0.70) and the absolute configuration assigned also by VCD and other spectroscopical methods.[3] In the following, all specific OR are reported in the usual units $deg \cdot [dm \cdot (g/mL)]^{-1}$. The theoretical ab inito computation of such a small OR for a flexible and rather large compound clearly represents a challenge for quantum chemistry. We furthermore propose this compound as a suitable test case for the evaluation of conformational energies of a nonpolar organic compound with several conformers in a rather narrow energy window. For recent theoretical studies on related chiroptical problems, see for example, Ref. 5–11.

Two theoretical schemes that can accurately compute noncovalent intermolecular and intramolecular interactions have been successfully elaborated by us recently. The first is the systematic correction of GGA and hybrid density functionals for the largely missing dispersion forces by an empirical (classical) correction term ("DFT-D").[12] The second approach improves DFT energies by including a second-order perturbation term that introduces nonlocal electron correlations to a hybrid functional ("double hybrid density functionals").[13] A density functional that combines both approaches is B2PLYP-D, that shows outstanding performance for the S22 (noncovalent complexes) and G3/99 (heats of formation) test sets.[14] The B2PLYP-D approach also yields for the conformational energies of a tripeptide model results that are very close to accurate CCSD(T) reference data.[14] Standard functionals like PBE[15] and B3LYP[16] have also been included in this study with and without dispersion correction to assess their performance. Alkanes have been extensively studied in the past with force field methods and for this reason, MM3[17] was also used for comparison. As reference methods for the conformational energies, we use second-order perturbation theory in standard form (MP2[18]) or in the spin-scaled variant (SCS-MP2[19]) that improves in almost all cases on MP2.

METHODS AND TECHNICAL DETAILS

The (SCS)-MP2 and DFT calculations have been performed with slightly modified versions of the TURBOMOLE suite of programs.[20] As AO basis triple-zeta (TZV) sets of Schäfer et al.[21,22] (The basis sets are available from the TURBOMOLE homepage via the FTP Server Button (in the subdirectories basen, jbasen, and cbasen) have been used. If not mentioned otherwise, we use two sets of polarization functions (2d for carbon and 2p for hydrogen) and a set of diffuse spd-functions on the carbon atoms. The exponents of these functions were taken from the corresponding correlation consistent sets aug-cc-pVTZ.[23,24] This AO basis yields typically results very close to the basis set limit in DFT calculations and is termed aTZV2P (in standard notation [5s3p2d + 1s1p1d/3s2p]). As most accurate quantum chemical methods for large systems, we use the mentioned MP2 methods[18,19] and the B2PLYP double hybrid density functional.[13] As computationally cheap methods (with resolution-of-the-identity (RI, also called density-fitting) integral approximation they scale as $O(N^3_{el})$ with system size), semilocal (nonhybrid) functionals like PBE[15] or B97-D[25] are used. The B97-D functional is a recent reparametrization of Beckes GGA ansatz from 1997[26] but now including damped, atom-pairwise $C_6 \cdot R^{-6}$ corrections to account for dispersion (van der Waals) effects. When other density functionals are used together with the dispersion correction, we add the suffix "-D" to the functional name in order to distinguish from conventional DFT computations (that are occasionally also reported to illustrate the effect of dispersion).

In all second-order perturbative treatments (MP2, SCS-MP2, and B2-PLYP) the RI approximation for the two-electron integrals has been used.[27] As RI-auxiliary basis, the sets of Weigend et al.[28] that were optimized for the cc-pVTZ AO basis have been employed. The RI-approximation has also been used in DFT treatments with pure GGA functionals[29] employing the corresponding optimized auxiliary basis sets.[30] In general, the RI-approximation speeds up calculations by about a factor of 3–15 depending on system/basis size albeit at insignificant loss of accuracy (errors for $\Delta E < 0.02$–0.03 kcal mol^{-1} compared to non-RI treatments). In the (SCS)-MP2 computations, we employ the frozen-core (FC) approximation for the correlation energy.

All geometry optimizations have been performed at the B97-D/TZV(d,p) level and these structures have been used in all subsequent single-point computations of energies and optical rotations (OR). The OR values at the sodium-D-line wavelength (589 nm) were obtained from time-dependent density functional theory (TDDFT[31]) calculations using the BHLYP[32] or BLYP[33,34] functional, and also employing the aTZV2P AO basis set. BHLYP calculations were additionally performed for a wavelength of 365 nm. The calculated OR at 589 nm was also used to compare with the experimental $[\alpha]^{25}_{578}$, because the change of $[\alpha]$ would be only minor. For a general overview about chiroptical calculations, see Ref. 35, 36 for the particular application of TDDFT methods for OR computations see Ref. 37–41 and for examples that include also several conformers and Boltzmann averaging see Ref. 5–11.

Because of technical reasons, the TDDFT/BHLYP calculations could be performed only in the coordinate origin-dependent dipole-length representation for the rotatory strengths (denoted L). Test calculations employing the pure BLYP functional[33,34] and the origin-independent velocity gauge representation[42] (denoted V) show, how-

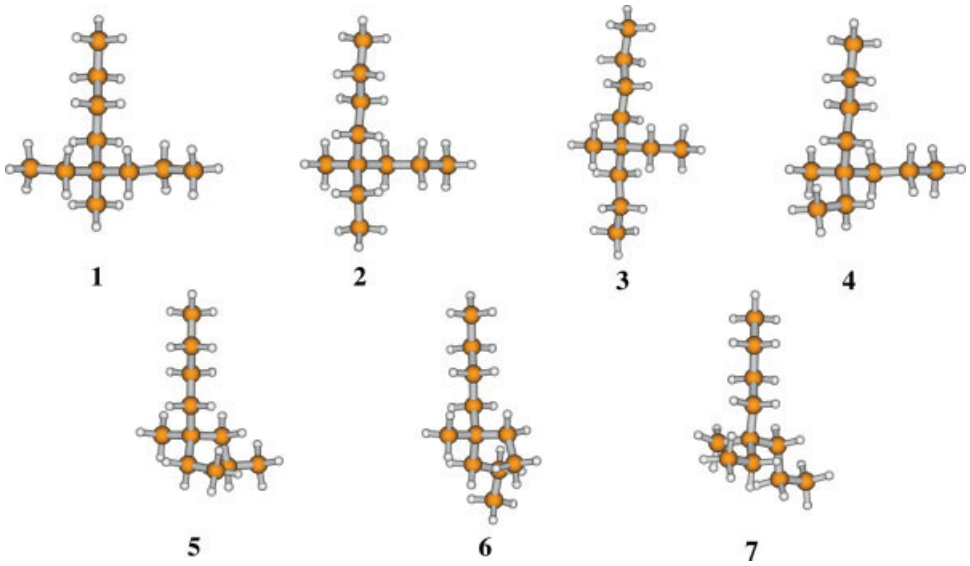

Fig. 1. Investigated conformations of (*R*)-4-ethyl-4-methyloctane. [Color figure can be viewed in the online issue, which is available at www.interscience.wiley.com.]

ever, that the differences between the two forms are rather small (see below).

RESULTS AND DISCUSSION

The seven energetically lowest-lying conformers from a search employing the MMX force field[43] are depicted in Figure 1. We first discuss their relative energies (based on B2PLYP-D results) and their methodological dependence and finally consider thermal and entropy effects and the Boltzmann averaging of individual OR values. Note that this classical procedure (opposed to a quantum mechanical average over the low-frequency, anharmonic vibrations) is the main limitation of our attempt to compute the experimentally observed OR. Solvent effects to the OR can be large in special cases,[44] but they are usually smaller than 5–10% of the computed OR and furthermore should be similar for all conformers studied.

As shown in Figure 2 (see also Table 1), the relative energies of the conformers fall in three main groups: 1–3 are within 0.2 kcal mol^{-1}, 4–6 are between 0.6 and 0.7 kcal mol^{-1} and 7 is highest with a relative energy of about 1.5 kcal mol^{-1}. As can be seen in Figure 1, this is related to the number of gauche-type torsions in each group, but a distinction between the conformers in the groups is not possible by simple reasoning. This gradual increase of the conformational energy in a sub-kcal range leads to a significant population of the first six conformers. As shown

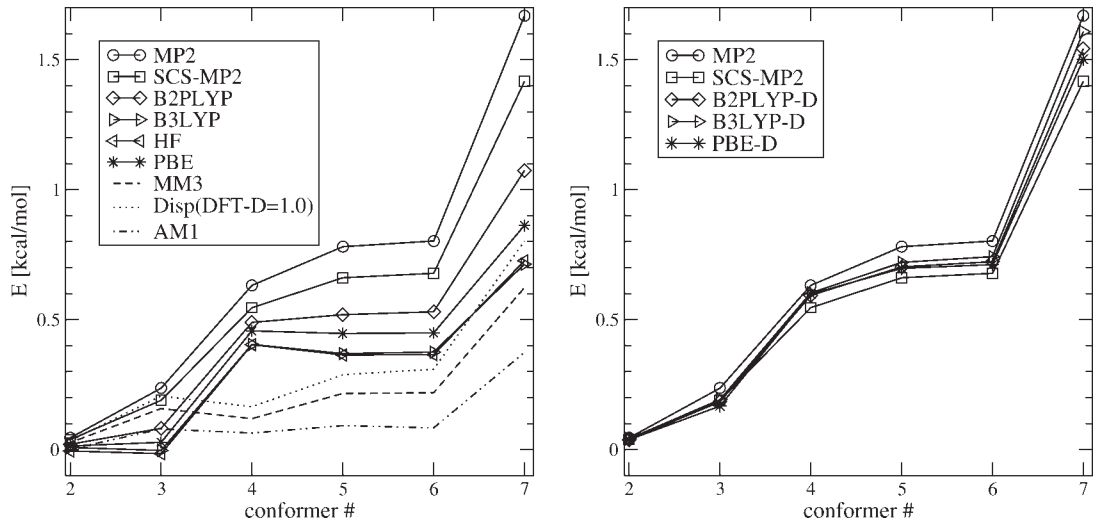

Fig. 2. Relative energies (/aTZV2P//B97-D/TZVP, energy of conformer 1 set to zero) of the investigated conformations. The left plot shows uncorrected methods, while in the right figure the dispersion correction has been used. The MP2 and SCS-MP2 values serve as reference values and the mark upper and lower limits, respectively, of the true conformational energy. The MM3 values refer to MM3 optimized structures.

TABLE 1. Computed (B2PLYP-D/aTZV2P) relative energies (ΔE, not ZPVE corrected), enthalpies (ΔH) and free enthalpies (ΔG) including vibrational corrections (B97-D/TZVP) at 298 K in kcal mol^{-1}

Conformer	ΔE	ΔH (298 K)	ΔG (298 K)
1	0.0 (26.9)	0.0 (27.3)	0.0 (28.9)
2	0.04 (25.1)	0.05 (25.1)	0.12 (23.6)
3	0.18 (19.8)	0.23 (18.5)	0.49 (12.6)
4	0.59 (9.9)	0.56 (10.6)	0.46 (13.3)
5	0.70 (8.2)	0.73 (7.9)	0.93 (6.0)
6	0.72 (8.0)	0.68 (8.6)	0.50 (12.4)
7	1.54 (2.0)	1.55 (2.0)	1.33 (3.1)

Computed Boltzmann populations (percent, 298 K) are given in parentheses.

below, even conformer 7 with a population of about 2% should be considered in this case for property evaluation.

The relative energies of conformers 2–7 are qualitatively not equally described by uncorrected DFT, and the semiempirical and MM3 methods. According to previous experience,[45] the true result should fall in between that of MP2 and SCS-MP2 that mark upper and lower limits for noncovalent interactions in main-group species. With HF and B3LYP, 3 is incorrectly lower-lying than 1, and also the energetic ordering of 5 and 6 relative to 4 is wrong. The situation is a bit better with PBE (as expected, see Ref. 46) and significant improvement is seen for the B2PLYP functional. This clearly indicates that missing intramolecular dispersion effects are important here and thus, quantitative accuracy can only be achieved by adding the dispersion correction. The results for B2PLYP-D, B3PLYP-D, and PBE-D are shown in Figure 2, right. They now almost exactly fall between MP2 and SCS-MP2 for all conformers. These results are in line with previous reports on DFT problems reproducing the energy changes during folding of long alkanes.[47]

Although the problem of DFT seems to be dispersion, the situation is exactly opposite for the MM3 force field (and this may hold for other classical approaches as well). Interestingly, the MM3 energy profile looks qualitatively different than those of the accurate quantum chemical methods, but parallels the plot of the pure dispersion energy as calculated with our DFT-D correction scheme.[12] This is understandable because, the molecule is nonpolar and the conformers differ mainly in their molecular shape. Hence, the difference of the force field energies mainly results from the nonbonded terms that are described by Lennard-Jones-type van der Waals potentials, whose attractive part is similar to that used in DFT-D. This example shows that even in this seemingly simple case, the repulsive part of the potential (Pauli-exchange repulsion) discriminates between the conformers. Missing induction (intramolecular polarizability) and electrostatic terms seem to be less important. Note that the balance between torsional potentials and nonbonding terms cannot be the reason, because also the relative energies of conformers 1–3 (which do not have any torsional strain) are not well described with MM3. The results with the semiempirical AM1 method are even worse, because it generally underestimates all conformational energies and even adding the dispersion correction would not solve the problems.

To compare with experiment, we have calculated harmonic vibrational corrections to the relative energies at the B97-D/TZVP level. As can be concluded from Table 1, the populations are only changed to minor extent if ΔH values are considered. However, the picture changes significantly when entropic contributions are taken into account. The relative free enthalpies (ΔG) are different from the electronic energies, now predicting 3, 4, and 6 to be almost at the same level. This can be explained by the many low-frequency vibrational torsional modes that enter the formulas for the entropy in a highly nonlinear (inverse) fashion. Because in such cases the harmonic approximation is rather bad, we expect big errors for the final ΔG.

Computed optical rotations (OR) are given in Table 2 at different levels. As the small difference of the aTZV2P(L) and aTZV2P(V) data with the BLYP functional shows, the basis set used is quite complete, and we can discuss the most reliable BHLYP/TZV2P(L) results as follows. Note that for the smaller TZVP AO basis significant differences between the L- and V-forms for the OR occur (cf. the last two columns).

The computed $[\alpha]_D$ values at the BHLYP/aTZV2P(L) level span a large range from −8.8 for conformer 3 to 41.1 for conformer 7 that has the highest number of helical tor-

TABLE 2. Computed optical rotations $[\alpha]_D$ (in brackets: $[\alpha]_{365}$) for (*R*)-4-ethyl-4- methyloctane

	BHLYP	BLYP			
Conformer	aTZV2P (L)	aTZV2P (L)	aTZV2P (V)	TZVP (L)	TZVP (V)
1	10.7 (29.9)	11.7	13.6	18.6	5.2
2	−2.9 (−9.4)	−5.0	−5.4	−11.6	4.8
3	−8.8 (−24.2)	−8.6	−10.2	−9.9	−11.5
4	2.4 (2.7)	0.3	2.5	−6.7	4.5
5	4.9 (11.1)	5.3	7.7	1.1	−0.1
6	−0.1 (2.3)	0.6	0.2	5.0	10.6
7	41.1 (123.4)	50.2	52.1	35.6	9.2
Average	1.9 (4.7)	1.7	2.2	0.7	1.8

The labels L and V refer to the length and velocity dipole form for the computation of optical rotations. Averaged values are based on Boltzmann populations at 298 K (ΔE(B2PYLP-D)).

TABLE 3. Computed average optical rotations $[\alpha]_D$ based on the BHLYP/aTZV2P data from Table 2 and populations calculated from relative conformer energies in Table 1

	Average based on		
Method	ΔE	ΔH_{298}	ΔG_{298}
Exp.		0.2	
B2PLYP-D	1.9	2.0	3.2
SCS-MP2	2.1	–	–
MP2	1.9	–	–
B3PLYP-D	1.8	–	–
B3PLYP	3.1	–	–
MM3	4.0	4.0	5.6

The vibrational corrections to *H* and *G* are taken from B97-D/TZVP computations.

sions. More simple reasoning is not possible to explain these values.

Taking the Boltzmann distribution of the conformers into consideration, we have calculated population averaged OR based on different ΔE, ΔH, and ΔG values (Table 3). The total OR of $[\alpha]_D$ falls in the range of 1.9–3.2 with B2PLYP-D, which is (as expected) similar to the results that are based on (SCS)-MP2 or B3LYP-D energy data. Compared to the experimental value of about 0.2, this is the right sign and correct order of magnitude for the OR.

Conformer 3 has similar absolute OR but opposite sign than 1. Its relative energy is therefore important for the total OR, as is the energy of conformer 7. Because of the rather different OR of 3 and 7 compared to that of 1, the total $[\alpha]_D$ is more sensitive to the population of these conformers than of 2, 4, 5, and 6. The resulting OR increases when taking ΔG into account, because the population of conformer 3 is increased by the entropic contributions, while conformer 7 is lowered compared to 1. Thus, the ΔG based average is in worse agreement with experiment that (as discussed above) probably results from artefacts of the harmonic approximation in the vibrational treatment. In the light of the good agreement of the averaged OR with experiment using ΔH or only ΔE, we conclude that enthalpy or energy calculations are sufficient to get a reasonable conformer distribution of this molecule. For comparison, OR values are also given for populations based on MM3 energies. They are much too high, because the force field predicts a much too low relative energy for conformer 7. Similar observations (but to a lesser extent) are made for uncorrected density functionals like B3LYP. As an extreme case, we obtain an average $[\alpha]_D$ with the AM1 based populations of 8.1 that emphasizes the sensitivity of the present example and thus the importance of using accurate energies.

Because it seems somewhat arbitrary only to include one higher-lying conformer (7) and to ignore many others that will appear in the 1.5–3.0 kcal mol^{-1} range, we have also computed an average $[\alpha]_D$ only including conformers 1–6. Under this assumption (that the effects of all higher-lying ones cancel) we obtain (using B2PLYP-D populations) $[\alpha]_D = 1.1$, which is in even better agreement with experiment.

The calculated optical rotation at the shorter wavelength ($[\alpha]_{365}$) is positive and larger than $[\alpha]_D$ as expected for a conventional ORD. The experimental value ($[\alpha]_{365} = 0.7$) is also larger at the shorter wavelength and the ratio between the two OR values at 365 and 578 nm is computed in the right ballpark (exp.: 3.5, theor.: 2.5).

SUMMARY AND CONCLUSIONS

In this work, we have shown that both dispersion-corrected GGA, hybrid-GGA (PBE-D, B3LYP-D), and double hybrid (B2PLYP-D) density functional methods are able to correctly reproduce relative energies of seven conformers of 4-ethyl-4-methyloctane with an accuracy of about 0.1–0.2 kcal mol^{-1}, when compared to accurate SCS-MP2 and MP2 reference energies. This is also the estimated error range compared to the "true" conformational energies. Regarding B2PLYP-D, this estimation confirms previous conclusions based on dipeptide conformational analysis compared to accurate CCSD(T) reference data.[14] The optical rotations (OR) of these conformers have been computed at the TDDFT level employing large AO basis sets. These values show a large span (and different signs) that is more than one order of magnitude larger than the experimental value. Because of significant differences in the individual OR values, this makes accurate relative energy evaluations necessary.

The Boltzmann distribution of these conformers gives rise to a predicted total optical rotation of about 1.8–2.1 deg dm^{-1} $(g/mL)^{-1}$ at 589 nm, which is in good qualitative (right order of magnitude) agreement with the experimental value of about 0.2. Improving the theoretical description of the conformational energies always leads to an improved computed OR compared to experiment. For the molecule presented here, opposite signs of α for different, inherently rather chiral conformers sum up to a very small total optical rotation. In summary, a determination of the absolute configuration of this molecule based on our analysis would have been correct. However, other systems with conformational effects on the OR may be more challenging, because distinct chromophores (that are absent here) lead to a more complicated dependence of $[\alpha]$ on structure. Thus, although our positive results allow no general conclusions regarding the assignment of AC by computation for flexible systems, we could at least show, that very small ORs can also be computed correctly when the electronic structure is simple and reliable relative energies are used.

It is often argued that the errors of a theoretical method cancel when only conformers, not isomers are investigated. We have reported here a case for which the optical rotation is sensitive to the population of several conformers that have relative energies within 1.5 kcal mol^{-1} range. Quite surprisingly, standard methods for conformational problems, such as B3LYP or MM3, do not provide sufficient accuracy to reproduce the conformer distribution. This is even more intriguing, because alkanes and their conformations are usually considered as electronically being very simple. The problems of standard DFT are

once again attributed to missing long-range electron correlations, while semiempirical and force field methods seem to be inaccurate due to missing molecule-specific exchange repulsion effects. Caution is therefore advised if very small energy differences of conformers are found with these methods, because persisting intrinsic errors may lead to quantitatively and qualitatively wrong conclusions. However, the future for conformational analysis seems bright. Using reasonable integral approximations and reliable AO basis sets, accurate B2PLYP-D computations are routinely possible for systems with about 100 atoms and for 10–100 conformations that is out of reach for any other quantum chemical method of similar accuracy and broad range of applicability.

LITERATURE CITED

1. Stone AJ. The theory of intermolecular forces. Oxford; Oxford University Press: 1997.
2. Grimme S. Seemingly simple stereoelectronic effects in alkane isomers and the implications for Kohn-Sham density functional theory. Angew Chem Int Ed Engl 2006;45:4460–4464.
3. Fujita T, Obata K, Kuwahara S, Miura N, Nakahashi A, Monde K, Decatur J, Harada N. (R)-(+)-[VCD(+)945]-4-Ethyl-4-methyloctane, the simplest chiral saturated hydrocarbon with a quaternary stereogenic center. Tetrahedron Lett 2007;48:4219–4222.
4. Hoeve WT, Wynberg H. Chiral tetraalkylmethanes. Two syntheses of optically active butylethylmethylpropylmethane of known and high optical purity. J Org Chem 1980;45:2754–2763.
5. Grimme S, Bahlmann A, Haufe G. Ab initio calculations for the optical rotations of conformationally flexible molecules: a case study on six-, seven- and eight-membered fluorinated cycloalkanol esters. Chirality 2002;14:793–797.
6. Pecul M, Ruud K, Rizzo A, Helgaker T. Conformational effects on the optical rotation of alanine and proline. J Phys Chem A 2004;108:4269–4276.
7. Lattanzi A, Viglione RG, Scretti A, Zanasi R. Time dependent density functional response theory calculation of optical rotation as a method for the assignment of absolute configuration of camphor-derived furyl hydroperoxide and alcohol. J Phys Chem A 2004;108:10749–10753.
8. Stephens PJ, McCann DM, Cheeseman FJDJR, Frisch MJ. Determination of the absolute configuration of [32](1,4)barrelenophanedicarbonitrile using concerted time-dependent density functional theory calculations of optical rotation and electronic circular dichroism. J Am Chem Soc 2004;126:7514–7521.
9. Wiberg KB, Wang Y-G, Vaccaro PH, Cheeseman JR, Luderer MR. Conformational effects on optical rotation. 2-substituted butanes. J Phys Chem A 2005;109:3405–3410.
10. Kundrat MD, Autschbach J. Time dependent density functional theory modeling of chiroptical properties of small amino acids in solution. J Phys Chem A 2006;110:4115–4123.
11. Tam MC, Abrams ML, Crawford TD. Chiroptical properties of (R)-3-chloro-1-butene and (R)-2-chlorobutane. J Phys Chem A 2007;111:11232–11241.
12. Grimme S. Accurate description of van der Waals complexes by density functional theory including empirical corrections. J Comput Chem 2004;25:1463–1473.
13. Grimme S. Semiempirical hybrid density functional with perturbative second-order correlation. J Chem Phys 2006;124:034108.
14. Schwabe T, Grimme S. Double-hybrid density functionals with long-range dispersion corrections: higher accuracy and extended applicability. Phys Chem Chem Phys 2007;9:3397–3406.
15. Perdew JP, Burke K, Ernzerhof M. Generalized gradient approximation made simple. Phys Rev Lett 1996;77:3865–3868.
16. Becke AD. Density-functional thermochemistry. III. The role of exact exchange. J Chem Phys 1993;98:5648–5652.
17. Allinger NL, Yuh YH, Lii J-H. Molecular mechanics. The MM3 force field for hydrocarbons. J Am Chem Soc 1989;111:8551–8566.
18. Møller C, Plesset MS. Note on an approximation treatment for many-electron systems. Phys Rev 1934;46:618–622.
19. Grimme S. Improved second-order Møller-Plesset perturbation theory by separate scaling of parallel- and anti-parallel-spin pair correlation energies. J Chem Phys 2003;118:9095–9102.
20. Ahlrichs R, Bär M, Baron H-P, Bauernschmitt R, Böcker S, Crawford N, Deglmann P, Ehrig M, Eichkorn K, Elliott S, Furche F, Haase F, Häser M, Hättig C, Hellweg A, Horn H, Huber C, Hunian U, Kattannek M, Khn A, Kölmel C, Kollwitz M, May K, Nava P, Ochsenfeld C, Öhm H, Patzelt H, Rappoport D, Rubnen O, Schäfer A, Schneiden U, Sierka M, Treutlen O, Unterreinen B, Arnim M von, Weigend F, Weis P, Weiss H, TURBOMOLE (Vers. 5.9) Universität Karlsruhe, 2006. Available at http://www.turbomole.com. Ahlrichs R, Bär M, Häser M, Horn H, Kölmel C. Electronic structure calculations on workstation computers: the program system turbomole. Chem Phys Lett 1989;162:165–169.
21. Schäfer A, Huber C, Ahlrichs R. Fully optimized contracted Gaussian basis sets of triple zeta valence quality for atoms Li to Kr. J Chem Phys 1994;100:5829–5835.
22. http://www.turbomole.com.
23. Dunning TH Jr. Gaussian basis sets for use in correlated molecular calculations. I. The atoms boron through neon and hydrogen. J Chem Phys 1989;90:1007–1023.
24. Kendall RA, Dunning TH, Harrison RJ. Electron affinities of the first-row atoms revisited. Systematic basis sets and wave functions. J Chem Phys 1992;96:6796–6806.
25. Grimme S. Semiempirical GGA-type density functional constructed with a long-range dispersion correction. J Comput Chem 2006;27:1787–1799.
26. Becke AD. Density-functional thermochemistry. V. Systematic optimization of exchange-correlation functionals. J Chem Phys 1997;107:8554–8560.
27. Weigend F, Häser M. RI-MP2: first derivatives and global consistency. Theor Chem Acc 1997;97:331–340.
28. Weigend F, Köhn A, Hättig C. Efficient use of the correlation consistent basis sets in resolution of the identity MP2 calculations. J Chem Phys 2002;116:3175–3183.
29. Eichkorn K, Treutler O, Öhm H, Häser M, Ahlrichs R. Auxiliary basis sets to approximate Coulomb potentials. Chem Phys Lett 1995;240:283–289.
30. Eichkorn K, Weigend F, Treutler O, Ahlrichs R. Auxiliary basis sets for main row atoms and transition metals and their use to approximate Coulomb potentials. Theor Chem Acc 1997;97:119–124.
31. Marques M, Ulrich C, Nagueira F, Rubio A, Burke K, Gross EKU, editors. Time-dependent density functional theory, Lecture Notes Phys. 706. Berlin-Heidelberg: Springer; 2006.
32. Becke AD. A new mixing of Hartree-Fock and local density-functional theories. J Chem Phys 1993;98:1372–1377.
33. Becke AD. Density-functional exchange-energy approximation with correct asymptotic behavior. Phys Rev A 1988;38:3098–3100.
34. Lee C, Yang W, Parr RG. Development of the Colle-Salvetti correlation-energy formula into a functional of the electron density. Phys Rev B 1988;37:785–789.
35. Polavarapu PL. Optical rotation: recent advances in determining the absolute configuration. Chirality 2002;14:768–781.
36. Crawford TD. Ab initio calculation of molecular chiroptical properties. Theor Chem Acc 2006;115:227–245.
37. Cheeseman JR, Frisch MJ, Devlin FJ, Stephens PJ. Hartree-Fock and density functional theory ab initio calculation of optical rotation using GIAOs: basis set dependence. J Phys Chem A 2000;104:1039–1046.
38. Grimme S. Calculation of frequency dependent optical rotation using density functional response theory. Chem Phys Lett 2001;339:380–388.
39. Autschbach J, Patchkovskii S, Ziegler T, van Gisbergen S, Baerends EJ. Chiroptical properties from time-dependent density functional

theory. II. Optical rotations of small to medium sized organic molecules. J Chem Phys 2002;117:581–592.

40. Ruud K, Helgaker T. Optical rotation studied by density-functional and coupled-cluster methods. Chem Phys Lett 2002;352:533–539.
41. Stephens PJ, McCann DM, Cheeseman JR, Frisch MJ. The determination of absolute configurations of chiral molecules using ab initio time-dependent density functional theory calculations of optical rotation: how reliable are absolute configurations obtained for molecules with small rotations? Chirality 2005;17:52–64.
42. Grimme S, Furche F, Ahlrichs R. An improved method for density functional calculations of the frequency-dependent optical rotation. Chem Phys Lett 2002;361:321–328.
43. PCmodel 9.1; Serena Software: Bloomington, 2005.
44. Müller T, Wiberg KB, Vaccaro PH. Cavity ring-down polarimetry (CRDP): a new scheme for probing circular birefringence and circular dichroism in the gas phase. J Phys Chem A 2000;104:5959–5968.
45. Antony J, Grimme S. Is spin-component scaled second-order Møller-Plesset perturbation theory an appropriate method for the study of noncovalent interactions in molecules? J Phys Chem A 2007;111:4862–4868.
46. Hyla-Kryspin I, Haufe G, Grimme S. Weak hydrogen bridges: a systematic theoretical study on the nature and strength of C-H···F-C interactions. Chem Eur J 2004;10:3411–3422.
47. Grimme S, Antony J, Schwabe T, Mück-Lichtenfeld C. Density functional theory with dispersion corrections for supramolecular structures, aggregates and complexes of (bio) organic molecules. Org Biomol Chem 2007;5:741–758.

C_3-Symmetrical Self-Assembled Structures Investigated by Vibrational Circular Dichroism

MAARTEN M. J. SMULDERS,[1] THIERRY BUFFETEAU,[2] DOMINIQUE CAVAGNAT,[2] MARTIN WOLFFS,[1] ALBERTUS P. H. J. SCHENNING,[1] AND E. W. MEIJER[1]*

[1]*Laboratory of Macromolecular and Organic Chemistry, Eindhoven University of Technology, 5600 MB Eindhoven, The Netherlands*
[2]*Institut des Sciences Moléculaires, Université de Bordeaux I (UMR CNRS 5255), Talence Cedex, France*

Presented at the 11th International Conference on Circular Dichroism, 2007, Groningen, Netherlands

ABSTRACT We demonstrate by using vibrational circular dichroism (VCD) spectroscopy that it is possible to investigate the chirality of a supramolecular polymeric system in relatively dilute solutions. Chiral C_3-symmetrical discotic molecules, based on a trialkylbenzene-1,3,5-carboxamide, form supramolecular columnar stacks with a right-handed helical structure in solution due to intermolecular hydrogen bonds. The handedness of the supramolecular chirality is determined using electronic spectroscopy measurements. Under dilute conditions (at 10^{-3} M concentrations), it was also possible to probe the hydrogen bonding moieties with IR and VCD spectroscopy on these self-assembled structures. In combination with density functional theory (DFT) calculations, we could verify the preference for a right-handed chirality in the helical stacks and the nonplanar orientation of the carbonyl groups present in the molecule. This chiral arrangement is in agreement with the structure determined for a related benzene-1,3,5-tricarboxamide by X-ray diffraction. *Chirality 20:1016–1022, 2008.*

KEY WORDS: vibrational circular dichroism; DFT calculations; supramolecular assembly; helical structure; nonplanar amide bonds; spectroscopy

INTRODUCTION

The investigation of helically self-assembled organic molecules in solution has typically relied on electronic spectroscopic techniques, such as UV/vis absorption, circular dichroism (CD) and fluorescence spectroscopy, as well as NMR and IR techniques.[1] Most of these self-assembled systems are based on noncovalent interactions including π–π interactions, van der Waals interactions, hydrogen bonding, and electrostatic interactions. Detailed information on the organization of the chromophores in these self-assembled structures can be obtained by these techniques.[2] To obtain more information about the internal structure of self-assembled structures, that involve hydrogen bonds, vibrational circular dichroism (VCD) spectroscopy, in combination with density functional theory (DFT) calculations, can be applied as a complementary technique next to electronic spectroscopy. In the last decades, VCD spectroscopy has been used to study the conformation of chiral molecules,[3] such as determination of absolute configuration,[4–7] and to elucidate larger, more complex structures, including biopolymers (and oligomers),[8–11] synthetic polymers,[12–15] structural chiral complexes,[16–19] and also foldamers.[20,21] More recently, VCD spectroscopy was also used to elucidate the structure of concrete, supramolecular assemblies.[22,23] Furthermore, Setnička et al. have shown that it was possible to study the sol–gel phase transition, at 10^{-1} to 10^{-2} M concentration, by VCD spectroscopy.[24] This concentration regime is already considerably low for VCD spectroscopy, due to its low sensitivity compared with CD spectroscopy, where concentrations can be used as low as 10^{-6} M. Here we show that is possible to extend the use of VCD spectroscopy to supramolecular polymeric systems in relatively dilute solutions, i.e., as low as 1.8×10^{-3} M and to study the intermolecular hydrogen bonding events in the supramolecular polymer.

The self-assembled system we have investigated is based on the C_3-symmetrical *N*,*N*′,*N*″-Tris-[(*R*)-3,7-dimethyloctyl]benzene-1,3,5-tricarboxamide, (*R*)-**1** (Scheme 1).

Recently, we reported on the self-assembly of (*R*)-**1** in dilute alkane solution, in which temperature-dependent CD and UV/vis absorption spectroscopy was used to elucidate the self-assembly of (*R*)-**1** from monomers into one-dimensional columnar stacks.[26] CD spectroscopy confirmed the presence of helical stacks of (*R*)-**1** with

Additional Supporting Information may be found in the online version of this article.

Contract grant sponsors: NRSC-Catalysis, CNRS (Chemistry Department), Région Aquitaine, Conseil Régional d'Aquitaine, French Ministry of Research and Technology.

*Correspondence to: E. W. Meijer or Albert Schenning, Laboratory of Macromolecular and Organic Chemistry, Eindhoven University of Technology, P.O. Box 415, 5600 MB Eindhoven, The Netherlands.
E-mail: e.w.meijer@tue.nl or a.p.h.j.schenning@tue.nl

Received for publication 8 November 2007; Accepted 22 February 2008
DOI: 10.1002/chir.20568
Published online 12 May 2008 in Wiley InterScience (www.interscience.wiley.com).

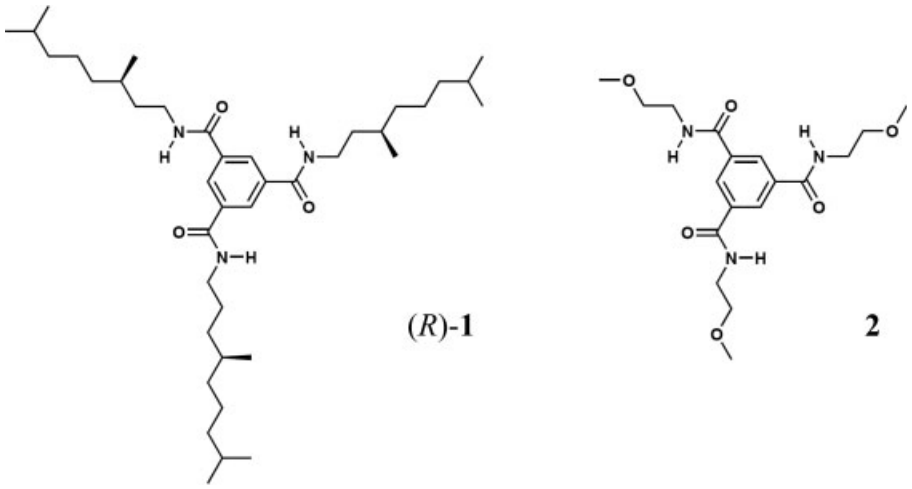

Scheme 1. The C_3-symmetrical discotic (*R*)-**1** (left) and the related discotic **2** studied by Lightfoot[25] (right).

a preferred handedness in solution, as a result of the enantiomerically pure alkyl chains. We assumed a conformation of (*R*)-**1** in solution similar to that of achiral benzene-1,3,5-tricarboxamide **2** (*N*,*N*′,*N*″-Tris-[2-methoxyethyl]benzene-1,3,5-tricarboxamide, Scheme 1). X-ray diffraction studies by Lightfoot et al. on **2** revealed a helical, columnar crystal structure without a preferred handedness,[25] in which intermolecular hydrogen bonding was present, with the amide functionalities making a 45° angle with respect to the benzene ring. The intermolecular hydrogen bonds within the stacks were confirmed by infrared spectroscopy on the aggregates in solution, which were absent for the molecularly dissolved monomers in solution.[27] Using VCD spectroscopy, combined with DFT calculations, we set out to obtain more insight into the hydrogen bonds involved in the self-assembled aggregate of (*R*)-**1**.

MATERIALS AND METHODS

Materials

The synthesis of *N*,*N*′,*N*″-Tris-[(*R*)-3,7-dimethyloctyl]-benzene-1,3,5-tricarboxamide, (*R*)-**1**, has been reported previously.[27] Decahydronaphthalene was obtained from Merck as a mixture of cis and trans isomers and used as received.

UV/vis and CD Measurements

UV/vis and CD measurements were performed on a Jasco J-815 spectropolarimeter with a response time set at 1 sec and a scan rate of 50 nm/min. The spectropolarimeter was equipped with a PFD-425S/15 Peltier-type temperature controller with a temperature range of 263–383 K and adjustable temperature slope.

IR and VCD Measurements

The infrared and VCD spectra were recorded with a ThermoNicolet Nexus 670 FTIR spectrometer equipped with a VCD optical bench.[28] In this optical bench, the light beam was focused on the sample by a BaF_2 lens (191 mm focal length), passing an optical filter (1850–800 cm^{-1} spectral range), a BaF_2 wire grid polarizer (Specac), and a ZnSe photoelastic modulator (Hinds Instruments, Type II/ZS50). The light was then focused by a ZnSe lens (38.1 mm focal length) onto a 1 × 1 mm^2 HgCdTe (ThermoNicolet, MCTA* E6032) detector. IR absorption and VCD spectra were recorded at a resolution of 4 cm^{-1}, by coadding 50 scans and 24,000 scans (8-h acquisition time), respectively. Samples were held in a fixed path length (45 μm) cell with CaF_2 windows. Baseline corrections of the VCD spectra were performed by subtracting the raw VCD spectra of the solvent. The photoelastic modulator was adjusted for a maximum efficiency at 1600 cm^{-1}. Calculations were performed via the standard ThermoNicolet software, using Happ and Genzel apodization, de-Haseth phase-correction and a zero-filling factor of one. Calibration spectra were recorded using a birefringent plate (CdSe) and a second BaF_2 wire grid polarizer, following the experimental procedure previously published.[29]

Theoretical Calculations

Regarding the long computational time necessary to fully optimize the geometry of self-assembled stacking of (*R*)-**1** within DFT, and further to determine the frequencies, the dipolar and rotational strengths, it was necessary to simplify the system prior to the calculations. To this end, the three chiral aliphatic side chains were replaced by methyl groups in self-assemblies of two, three, five or seven molecules. Moreover, to take into account the molecular chirality of (*R*)-**1**, the dimer with three (*R*)-3-methylpentyl chains were also considered.

The geometry optimizations, vibrational frequencies, and absorption and VCD intensities were calculated by Gaussian 03 program[30] on the CIS-IBM (on eight or sixteen processors) at the M3PEC computing center of the University Bordeaux 1. Calculations of the optimized geometries of self assembly of increasing size were performed at the density functional theory level using B3PW91 func-

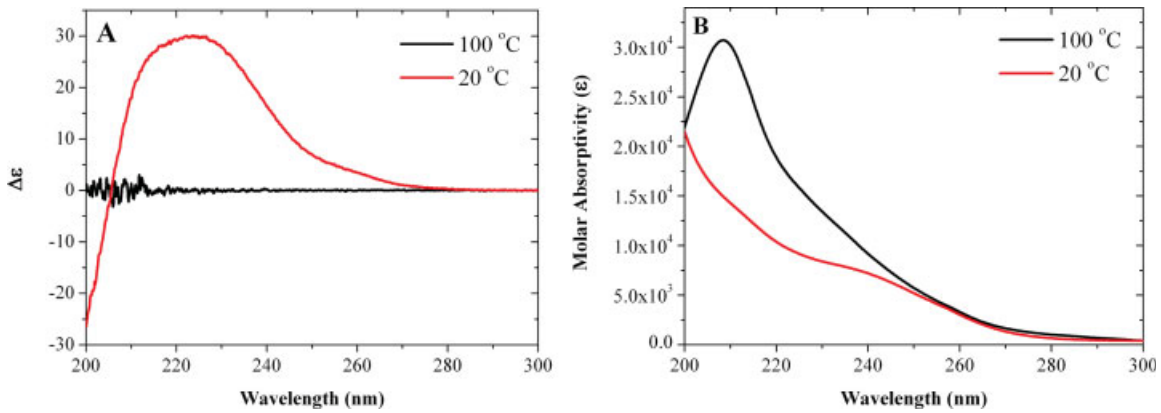

Fig. 1. CD (**A**) and UV/vis spectrum (**B**) for (*R*)-**1** in decahydronaphthalene (0.9×10^{-3} M) at 20 and 100°C. [Color figure can be viewed in the online issue, which is available at www.interscience.wiley.com.]

tional and 6-31G* basis set. Each molecule was rotated by 60° from the others to favor intermolecular hydrogen bonding between the C=O and N—H groups. As determined from the CD measurements, we considered a right-handed helical stacking, defined by the clockwise direction of the intermolecular hydrogen bonds. No tight convergence of the optimization was reached after a few days, possibly due to the presence of multiple local energy minima states due to weak interactions between the molecules. Therefore we decided to use the "nearly-optimized" geometry (optimization convergence criteria in the range 10^{-6} to 10^{-7}) to calculate the frequencies and the dipolar and rotational strengths. Vibrational frequencies and IR and VCD intensities were calculated at the same level of theory, utilizing the magnetic field perturbation method with gauge-invariant atomic orbitals.[31] For comparison with the experimental data, the calculated frequencies were scaled by 0.965, and the calculated intensities were converted to Lorentzian bands with half-width of 7 cm^{-1}. Moreover, the calculated IR and VCD spectrum were divided by the number of molecules to compare with the experimental molar absorptivity ε and $\Delta\varepsilon$, respectively.

RESULTS AND DISCUSSION

UV/vis and CD Results

Typically, the self-assembly of (*R*)-**1** is studied in heptane solutions at 10^{-4} to 10^{-5} M concentration.[26] However, as for VCD spectroscopy higher concentrations are required, decahydronaphthalene was selected as solvent, since in this solvent (*R*)-**1** is better soluble and hence the self-assembly occurs at higher concentration (vide infra). Figure 1 shows the CD and UV/vis absorption spectra of (*R*)-**1** in decahydronaphthalene at 0.9×10^{-3} M recorded at 20 and 100°C.

At 100°C, the absence of a CD effect and the UV/vis absorption maximum at 208 nm both indicate that (*R*)-**1** is molecularly dissolved at this temperature.[27] At room temperature, the hypsochromic shift of the maximum in UV/vis absorption and the appearance of a positive couplet in CD indicate the formation of right-handed helical assemblies.[32]

IR and VCD Results

The IR and VCD spectra of (*R*)-**1** in decahydronaphthalene, in the amide I (carbonyl stretching) and amide II (coupling of N—H bending and C—N stretching) regions, are presented in Figure 2. Similar molar absorptivities were obtained for the three different concentrations that were investigated, i.e., 1.8, 6.3, and 9.2×10^{-3} M (see also Figure 1 in the supporting information for IR spectra in the N—H stretching region). Only at the highest concentration we observed that after sample preparation (heating to dissolve the molecule followed by cooling to room temperature), a turbid gel was obtained instead of a transparent, homogeneous solution.

The N—H stretching vibration at 3235 cm^{-1} and the carbonyl stretching vibration at 1642 cm^{-1} indicate the presence of hydrogen-bonded species in solution, and correspond with the values measured in the solid state for (*R*)-**1**, 3225 and 1636 cm^{-1}, respectively (see Fig. 2 in the supporting information). Furthermore, the N—H stretching vibration at 3235 cm^{-1}, measured in decahydronaphthalene, corresponded nicely to the value of 3242 cm^{-1} that was previously reported for (*S*)-**1** in hexane (at 10^{-4} M).[27]

The formation of a right-handed helical structure, which was concluded from the CD measurements, was further studied by VCD spectroscopy, since the preferred handedness of the stacks implies that the hydrogen-bonded amide groups in these stacks also must have a chiral orientation.

At concentrations as low as 1.8×10^{-3} M, we still could observe the VCD signal, although at this concentration, the signal-to-noise ratio is rather low. At 6.3×10^{-3} M, we observed a VCD spectrum with a better signal-to-noise ratio for the carbonyl stretching vibration, which presents a (+,−,+) pattern. The two positive components at 1648 and 1628 cm^{-1} exhibit lower intensities than the negative component at 1640 cm^{-1}. The VCD spectrum observed for the highest concentration (9.2×10^{-3} M) is significantly

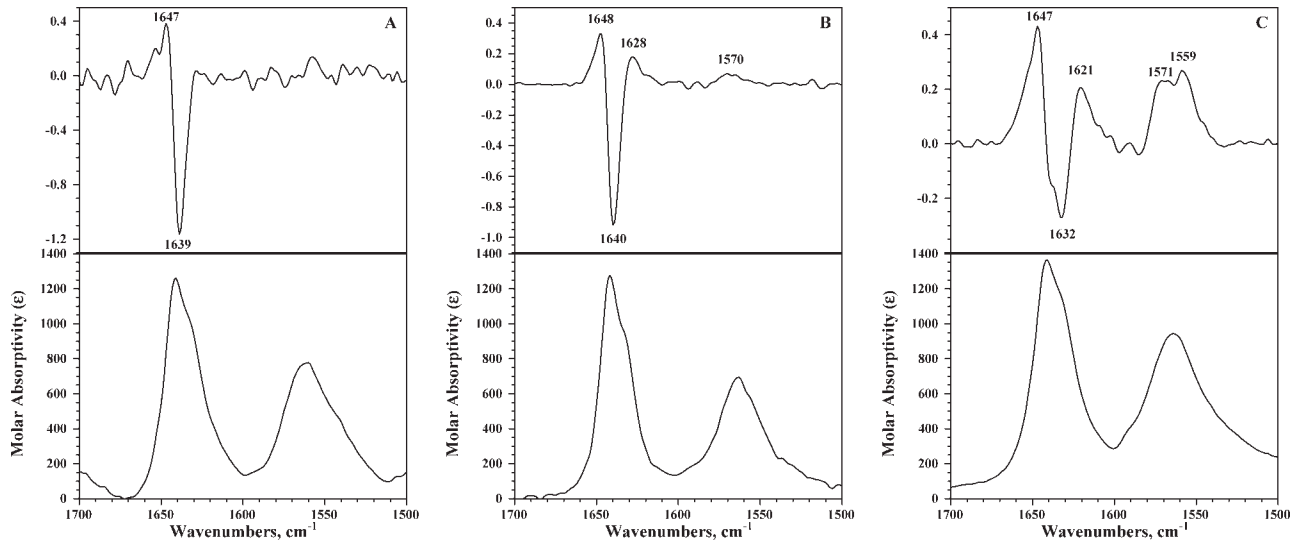

Fig. 2. VCD (top) and IR (bottom) spectra, recorded in amide I and amide II region of solutions of (*R*)-**1** in decahydronaphthalene, at 1.8×10^{-3} M (**A**), 6.3×10^{-3} M (**B**), and 9.2×10^{-3} M (**C**).

different from the spectra obtained for the transparent solutions. Indeed, the negative component is observed at 1632 cm^{-1} (a shoulder at 1640 cm^{-1} is also observed) with a lower intensity. This feature is most likely related to the gelation process that had occurred in solution and possibly also to orientation effects during sample preparation, which could lead to contribution of vibrational linear dichroism to the measured vibrational circular dichroism spectrum.[28] We have observed similar artifacts in electronic circular dichroism spectra due to alignment of fibers in solution.[33]

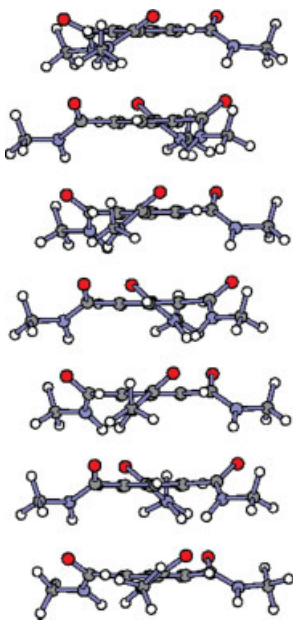

Fig. 3. Side view of stacking with seven molecules of (*R*)-1. [Color figure can be viewed in the online issue, which is available at www.interscience.wiley.com.]

Structural Parameters

The cartesian coordinates of the "nearly-optimized" geometries of dimers (with and without asymmetric centers), trimer, pentamer, and heptamer are reported in the supporting information. As an example, the optimized geometry of the heptamer is shown in Figure 3, while the relevant structural parameters for all considered oligomers are reported in Table 1. In Figure 3, one can see the right-handed helix by following the intermolecular hydrogen bonds between the amide groups.

The molecules are closer in the dimer containing the three aliphatic side chains with the asymmetric centers (labeled "dimer with *C" in Table 1). Indeed, the inter-ring distance, d_{ring}, is 3.64 Å whereas this distance is slightly higher (3.68 Å) for the simpler dimer with three methyl groups (labeled "dimer without *C" in Table 1). Since the mean planes of the three amide units make similar angles α with the aryl mean plane for the two dimers, the O—H distance, $d_{\text{O–H}}$, of the hydrogen bond is lower for the dimer containing the three aliphatic side chains with the asymmetric centers. On the other hand, the inter-ring distance increase with the size of the stacking. This increase of d_{ring} is associated with the increase of the α angle and the decrease of the $d_{\text{O–H}}$ (or $d_{\text{O–N}}$) distances. The values of α and $d_{\text{O–N}}$ for the pentamer and the heptamer are in

TABLE 1. Structural parameters of the optimized structures of the dimers, trimer, pentamer, and heptamer of (*R*)-1

Stacking	d_{ring} (Å)	α (°)	$d_{\text{O–H}}$ (Å)	$d_{\text{O–N}}$ (Å)
Dimer with *C	3.64	25	2.04	3.00
Dimer without *C	3.68	26	2.07	3.05
Trimer[a]	3.72	36	2.01	3.01
Pentamer[a]	3.73	42.5	1.95	2.95
Heptamer[a]	3.76	43	1.92	2.92

[a]Excluding the top and bottom molecule in the stack.

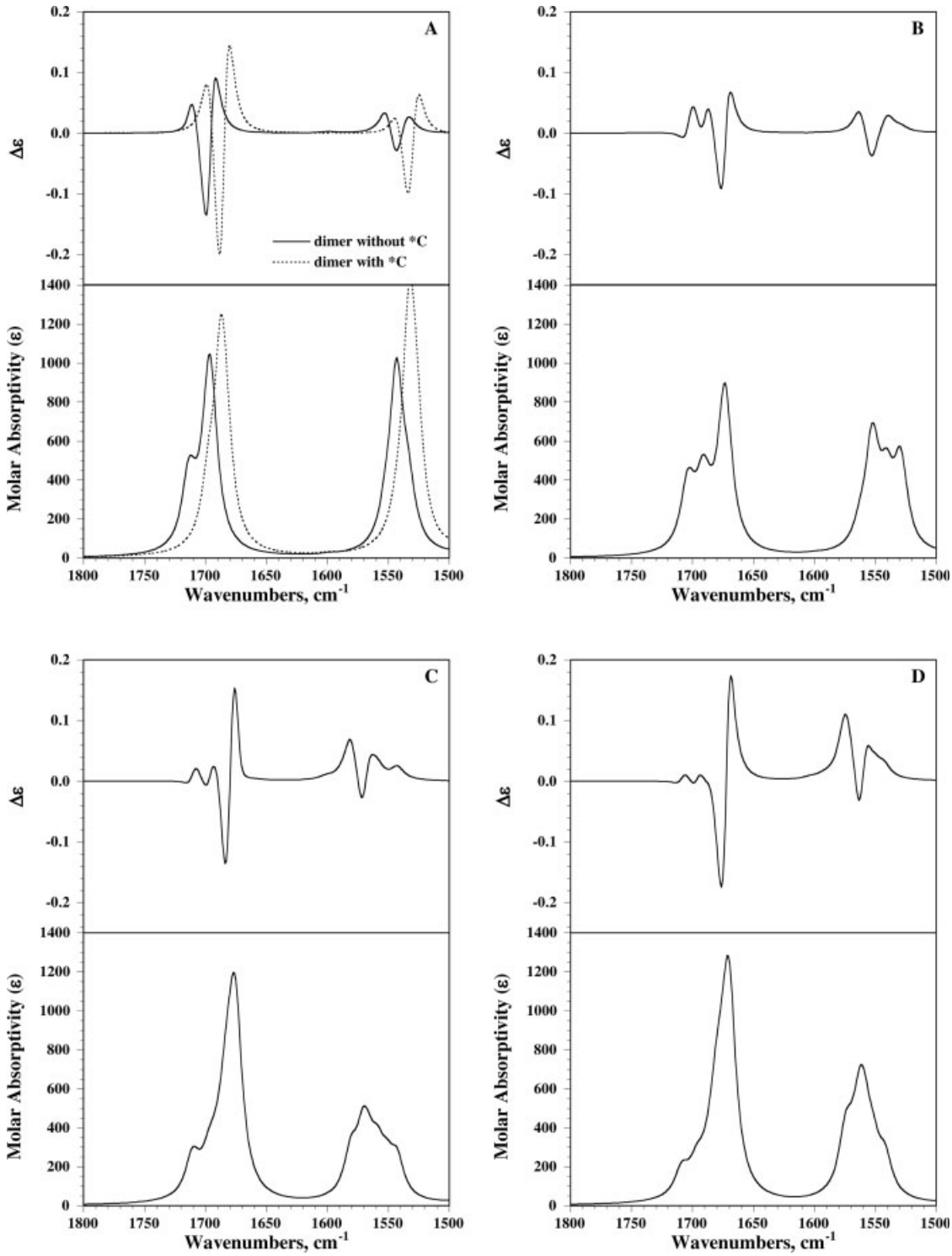

Fig. 4. Calculated VCD and IR spectra of the dimers with (dashed line) and without (solid line) chiral centers in the three aliphatic side chains (**A**) and of the trimer (**B**), pentamer (**C**), and heptamer (**D**).

accordance with the values determined by X-ray for structure **2** (Scheme 1).[25] These results show that a minimum of five molecules is necessary to obtain accurate structural parameters on helical, hydrogen-bonded amide stacks. For self-assemblies of lower size, the amide groups of the first and the last molecule are hydrogen-bonded by only one dipole (C=O or N—H), which decrease the value of the α angle.

Calculated IR and VCD Spectra

The calculated VCD and IR spectra of dimers (with and without asymmetric centers), trimer, pentamer, and heptamer are presented in Figure 4. The calculated IR spectra of pentamer and heptamer reproduce very well the molar absorptivities of the amide I and amide II modes measured in the experimental spectrum. Nevertheless, the frequency calculated for the amide I mode is higher than that observed in the experimental spectrum. This discrepancy may originate from (i) the computational method (DFT) and the modest basis set (6-31G*) used in this study, which do not calculate correctly the frequency of hydrogen bonded C=O groups; (ii) the calculations were done for the stacking in the gas phase, whereas experiments were performed in decahydronaphthalene solution; and (iii) the calculations were performed for simpler molecules (the three aliphatic side chains with the asymmetric centers were replaced by methyl groups). The effect of this last point can be estimated in the calculation of the IR spectra of the two dimers (with and without the three aliphatic side chains with the asymmetric centers) presented in Figure 4A.

As observed in Figure 4A, the shape of the VCD spectrum of dimer seems to be independent on the presence of the aliphatic side chains containing asymmetric centers. Indeed, the same (+,−,+) pattern is calculated in amide I region for the two dimers. Nevertheless, the intensity is significantly higher for the dimer containing the aliphatic side chains with asymmetric centers. This calculated VCD spectrum reproduces very well the sign of the bands observed in the experimental spectrum recorded at a concentration of 6.3×10^{-3} M. The VCD spectrum calculated for the trimer in the amide I region exhibits two positive bands at higher wavenumbers and a positive couplet at lower wavenumbers. This couplet arises from the coupling of C=O dipoles of the central molecule for which the amide groups are hydrogen-bonded with the amide groups of the upper and lower molecules. The two positive bands calculated at higher wavenumbers are due to the C=O groups of the first and the last molecules for which the amide groups are hydrogen-bonded by only one dipole (C=O or N—H). The positive couplet becomes the main contribution for self-assemblies of increasing size (pentamer and heptamer) since the number of amide groups hydrogen-bonded with neighboring amide groups increases. It is noteworthy that this positive couplet is observed in the experimental spectrum recorded at higher concentrations.

Although we have considered only relatively short stacks, the calculated VCD spectra are in satisfactory qualitative agreement with the experimental VCD spectrum. The discrepancies observed between experimental and calculated spectra may originate from specific interactions of (*R*)-**1** molecules with decahydronaphthalene and possible aggregation effects. However, together with the electronic absorption, CD and IR data, this VCD study confirms that the stacks of (*R*)-**1** in solution have a similar organization as the helical structure determined by Lightfoot et al. for **2** (Scheme 1) by X-ray analysis,[25] i.e., a helical organization of the molecules, with an offset of 60° between neighboring molecules and intermolecular hydrogen bonds, due to the nonplanarity of the amides bonds with respect to the benzene core.

CONCLUSION

In conclusion, we have shown the complementarity of VCD and CD spectroscopy to study self-assembled structures of (*R*)-**1** molecules in solution. VCD spectra with a good signal-to-noise ratio have been obtained at relatively low concentration. VCD spectroscopy combined with DFT calculations resulted in a structure for the stacks of (*R*)-**1** that is in agreement with the structure determined by X-ray for a related benzene-1,3,5-tricarboxamide.[25] We could conclude that in the stack, there is a preference for a chiral and nonplanar orientation of the carbonyl groups, which are involved in the hydrogen bonding event, present in the molecule.

ACKNOWLEDGMENTS

T.B. and D.C. acknowledge computational facilities provided by the M3PEC-Mésocenter of the University Bordeaux 1 (http://www.m3pec.u-bordeaux1.fr). M.W. thanks the Council for Chemical Sciences of the Netherlands Organization for Scientific Research (NWO-CW).

LITERATURE CITED

1. Hoeben FJM, Jonkheijm P, Meijer EW, Schenning APHJ. About supramolecular assemblies of π-conjugated systems. Chem Rev 2005;105:1491–1546.
2. Jonkheijm P, van der Schoot P, Schenning APHJ, Meijer EW. Probing the solvent-assisted nucleation pathway in chemical self-assembly. Science 2006;313:80–83.
3. Nafie LA, Freedman TB. Circular dichroism: principles and applications. 2nd ed. New York: John Wiley & Sons; 2000. p 97–132.
4. Freedman TB, Cao X, Dukor RK, Nafie LA. Absolute configuration determination of chiral molecules in the solution state using vibrational circular dichroism. Chirality 2003;15:743–758.
5. Tarczay G, Magyarfalvi G, Vass E. Towards the determination of the absolute configuration of complex molecular systems: matrix isolation vibrational circular dichroism study of (R)-2-amino-1-propanol. Angew Chem Int Ed 2006;45:1775–1777.
6. Monde K, Miura N, Hashimoto M, Taniguchi T, Inabe T. Conformational analysis of chiral helical perfluoroalkyl chains by VCD. J Am Chem Soc 2006;128:6000–6001.
7. Stephens PJ, Devlin FJ. Determination of the structure of chiral molecules using ab initio vibrational circular dichroism spectroscopy. Chirality 2000;12:172–179.
8. Tang HZ, Garland ER, Novak BM, He J, Polavarapu PL, Sun FC, Sheiko SS. Helical polyguanidines prepared by helix-sense-selective polymerizations of achiral carbodiimides using enantiopure binaphthol-based titanium catalysts. Macromolecules 2007;40:3575–3580.
9. Silva RAGD, Kubelka J, Bour P, Decatur SM, Keiderling TA. Site-specific conformational determination in thermal unfolding studies of helical peptides using vibrational circular dichroism with isotopic substitution. Proc Natl Acad Sci USA 2000;97:8318–8323.
10. Keiderling TA, Silva RAGD, Yoder G, Dukor RK. Vibrational circular dichroism spectroscopy of selected oligopeptide conformations. Bioorg Med Chem 1999;7:133–141.
11. Blagoi Y, Gladchenko G, Nafie LA, Freedman TB, Sorokin V, Valeev V, He Y. Phase equilibrium in poly(rA) poly(rU) complexes with Cd^{2+} and Mg^{2+} ions, studied by ultraviolet, infrared, and vibrational circular dichroism spectroscopy. Biopolymers 2005;78:275–286.
12. Nafie LA, Keiderling TA, Stephens PJ. Vibrational circular dichroism. J Am Chem Soc 1976;98:2715–2723.

13. Andrushchenko V, McCann JL, van de Sande JH, Wieser H. Determining structures of polymeric molecules by vibrational circular dichroism (VCD) spectroscopy. Vib Spectrosc 2000;22:101–109.
14. Wang F, Polavarapu PL, Lebon F, Longhi G, Abbate S, Catellani M. Absolute configuration and conformational stability of (*S*)-(+)-3-(2-methylbutyl)thiophene and (+)-3,4-di[(*S*)-2-methylbutyl)]thiophene and their polymers. J Phys Chem A 2002;106:5918–5923.
15. McCann J, Tsankov D, Hu N, Liu G, Wieser H. VCD study of synthetic chiral polymers: stereoregularity in poly-menthyl methacrylate. J Mol Struct 1995;349:309–312.
16. Freedman TB, Cao X, Rajca A, Wang H, Nafie LA. Determination of absolute configuration in molecules with chiral axes by vibrational circular dichroism: a C_2-symmetric annelated heptathiophene and a D_2-symmetric dimer of 1,1′-binaphthyl. J Phys Chem A 2003;107:7692–7696.
17. Freedman TB, Cao X, Oliveira RV, Cass QB, Nafie LA. Determination of the absolute configuration and solution conformation of gossypol by vibrational circular dichroism. Chirality 2003;15:196–200.
18. Burgi T, Urakawa A, Behzadi B, Ernst K-H, Baiker A. The absolute configuration of heptahelicene: a VCD spectroscopy study. New J Chem 2004;28:332–334.
19. Brotin T, Cavagnat D, Dutasta JP, Buffeteau T. Vibrational circular dichroism study of optically pure cryptophane-A. J Am Chem Soc 2006;128:5533–5540.
20. Buffeteau T, Ducasse L, Poniman L, Delsuc N, Huc I. Vibrational circular dichroism and ab initio structure elucidation of an aromatic foldamer. Chem Commun 2006:2714–2716.
21. Ducasse L, Castet F, Fritsch A, Huc I, Buffeteau T. Density functional theory calculations and vibrational circular dichroism of aromatic foldamers. J Phys Chem A 2007;111:5092–5098.
22. Urbanová M, Setnička V, Devlin FJ, Stephens PJ. Determination of molecular structure in solution using vibrational circular dichroism spectroscopy: the supramolecular tetramer of *S*-2,2′-dimethyl-biphenyl-6,6′-dicarboxylic acid. J Am Chem Soc 2005;127:6700–6711.
23. Setnička V, Urbanová M, Volka K, Nampally S, Lehn J-M. Investigation of guanosine-quartet assemblies by vibrational and electronic circular dichroism spectroscopy, a novel approach for studying supramolecular entities. Chem Eur J 2006;12:8735–8743.
24. Setnička V, Urbanova M, Pataridis S, Kral V, Volka K. Sol-gel phase transition of brucine-appended porphyrin gelator: a study by vibrational circular dichroism spectroscopy. Tetrahedron: Asymmetry 2002;13:2661–2666.
25. Lightfoot MP, Mair FS, Pritchard RG, Warren JE. New supramolecular packing motifs: p-stacked rods encased in triply-helical hydrogen bonded amide strands. Chem Commun 1999:1945–1946.
26. Smulders MMJ, Schenning APHJ, Meijer EW. Insight into the mechanisms of cooperative self-assembly; the "Sergeants-and-Soldiers" principle of chiral and achiral C_3-symmetrical discotic triamides. J Am Chem Soc 2008;130:606–611.
27. Brunsveld L, Schenning APHJ, Broeren MAC, Janssen HM, Vekemans JAJM, Meijer EW. Chiral amplification in columns of self-assembled N,N′,N″-tris[(S)-3,7-dimethyloctyl]benzene-1,3,5-tricarboxamide in dilute solution. Chem Lett 2000:292–293.
28. Buffeteau T, Lagugne-Labarthet F, Sourisseau C. Vibrational circular dichroism in general anisotropic thin solid films: measurement and theoretical approach. Appl Spectrosc 2005;59:732–745.
29. Nafie LA, Vidrine DW. In: Ferraro JR, Basile LJ, editors. Fourier transform infrared spectroscopy. Vol 3. New York: Academic Press; 1982. p 83–123.
30. Frisch MJ, Trucks GW, Schlegel HB, Scuseria GE, Robb MA, Cheeseman JR, Montgomery JA Jr, Vreven T, Kudin KN, Burant JC, Millam JM, Iyengar SS, Tomasi J, Barone V, Mennucci B, Cossi M, Scalmani G, Rega N, Petersson GA, Naktasuji H, Hada M, Ehara M, Toyota K, Fukuda R, Hasegawa J, Ishida M, Nakajima T, Honda Y, Kitao O, Nakai H, Klene M, Li X, Knox JE, Hratchian HP, Cross JB, Adamo C, Jaramillo J, Gomperts R, Statmann RE, Yazyev O, Austin AJ, Cammi R, Pomelli C, Ochterski JW, Ayala PY, Morokuma K, Voth GA, Salvador P, Dannenberg JJ, Zakrzewski VG, Dapprich S, Daniels AD, Strain MC, Farkas O, Malick DK, Rabuck AD, Raghavachari K, Foresman JB, Ortiz JV, Cui Q, Baboul AG, Clifford S, Cioslowski J, Stefanov BB, Liu G, Liashenko A, Piskorz P, Komaromi I, Martin DJ, Fox T, Keith MA, Al-Laham CY, Peng A, Nanayakkara M, Challacombe RL, Gill PMW, Johnson B, Chen W, Wong MW, Gonzalez C, Pople JA. Gaussian 03, Revision B. 04. Gaussian Inc.: Pittsburgh, PA; 2003.
31. Cheeseman JR, Frisch MJ, Delvin FJ, Stephens PJ. Ab initio calculation of atomic axial tensors and vibrational rotational strengths using density functional theory. Chem Phys Lett 1996;252:211–220.
32. Eliel EL, Wilen SH, Mander LN. Stereochemistry of organic compounds. Chichester: Wiley-Interscience; 1994. p 1267.
33. Wolffs M, George SJ, Tomovic Z, Meskers SCJ, Schenning APHJ, Meijer EW. Macroscopic origin of CD-effects by alignment of self-assembled fibers in solution. Angew Chem Int Ed 2007;46:8203–8205.

CHIRALITY 20:1023–1028 (2008)

Compact Optical Cell System for Vacuum Ultraviolet Absorption and Circular Dichroism Spectroscopy and its Application to Aqueous Solution Sample

MASAHITO TANAKA,[1]* KAZUTOSHI YAGI-WATANABE,[1] FUSAE KANEKO,[2] AND KAZUMICHI NAKAGAWA[2,3]

[1]*Research Institute of Instrumentation Frontier, National Institute of Advanced Industrial Science and Technology (AIST), Tsukuba Tyuou-2, Umezono 1-1-1, Tsukuba, Ibaraki, 305-8568, Japan*

[2]*Graduate School of Science and Technology, Kobe University, Tsurukabuto 3-11, Nada-ku, Kobe, 657-8501, Japan*

[3]*Graduate School of Human Development and Environment, Kobe University, Tsurukabuto 3-11, Nada-ku, Kobe, 657-8501, Japan*

Presented at the 11th International Conference on Circular Dichroism, 2007, Groningen, Netherlands

ABSTRACT We have designed a compact optical cell for studying the absorption and circular dichroism (CD) of a solution sample in the vacuum ultraviolet (VUV) region using a temperature control unit. The cell size was 34 mm in diameter and 14 mm in length. Such compactness was obtained by coating the VUV scintillator onto the outside of the back window. Because this scintillator converts the transmitted VUV light to visible light, the outside of this cell is operated under atmospheric pressure. The temperature of the sample solution was maintained in the range of 5°C to 80°C using a temperature control unit with a Peltier thermoelectric element. Changes in the sample temperature were observed by monitoring the absorption intensity of water. Through the study of VUV-CD spectra of ammonium camphor-10-sulfonate aqueous solutions and the transmitted spectrum of an empty cell, it was concluded that this cell unit has sufficient performance for use in VUV spectroscopy. *Chirality 20:1023–1028, 2008.*

KEY WORDS: synchrotron radiation; linear dichroism; polarization spectroscopy; undulator; temperature control; absorption of water; transmitted spectra

INTRODUCTION

Circular dichroism (CD) spectroscopy in the vacuum ultraviolet (VUV) region allows more precise protein secondary structure analysis[1–3] and provides chiral and structural information on molecules comprising only σ-electrons, such as sugars.[4] However, the absorption of a solvent, usually water in the case of biomolecules, increases drastically with photon energy in this region. Therefore, the vacuum ultraviolet circular dichroism (VUV-CD) as well as the absorption spectroscopy of an aqueous solution requires an optical cell with a short optical path length (less than 100 μm) for minimizing absorption of the solvent. For example, a demountable thin quartz cell with 120 μm spacers has been designed by Gray et al.[5] Recently, a well-established micro cell for VUV-CD measurements has been developed by Wien and Wallace.[6] This cell has some advantages in that it has a very short path length (as small as 2 μm), and requires fairly small sample volumes. However, it is available only in a nitrogen gas atmosphere.

The VUV-CD spectra of aqueous solutions have successfully been measured using a combination of synchrotron radiation and photo-elastic modulators (PEMs) at several synchrotron radiation facilities such as beamline CD12 in SRS (UK),[7] beamline UV1 in ASTRID (Denmark), beamlines U9b and U11 in NSLS (USA), beamline 3m_NIM1_C in BESSY2 (Germany), beamline BL-15 in HiSOR (Japan),[8] beamline DISCO in SOLEIL (France),[9] and beamline 4B8 in BSRF (China). These facilities have adopted PEM for the modulation of circular polarization. Recently, we have developed a unique VUV-CD measurement system[10–13] using a polarizing undulator instead of PEMs as a polarized light source. The polarizing undulator can irradiate bright polarized light. It is therefore the most suitable polarized light source and has been utilized to obtain VUV-CD and linear dichroism (LD) spectra.[10,11]

Our VUV-CD measurement system[10–13] using the polarizing undulator required the evacuation of the whole optical path including the optical cell in high vacuum. This is because it is difficult to use this system with transparent-type optics such as windows, owing to its polarization characteristic as well as its absorbance. In the case of the other VUV-CD instrument, the PEM is usually located between

Contract grant sponsor: Budget for Nuclear Research of the Ministry of Education, Culture, Sports, Science and Technology (MEXT), Japan, based on screening and counseling by the Atomic Energy Commission; Grant-in-Aid of MEXT, Japan (to M. T.); and Sumitomo foundation (to M. T.); Contract grant number: Young Scientists (B), 17750020 (to M.T.)

*Correspondence to: Masahito Tanaka, National Institute of Advanced Industrial Science and Technology (AIST), Tsukuba Tyuou-2, Umezono 1-1-1, Tsukuba, Ibaraki, 305-8568, Japan. E-mail: masahito-tanaka@aist.go.jp

Received for publication 31 October 2007; Accepted 12 March 2008
DOI: 10.1002/chir.20579
Published online 12 May 2008 in Wiley InterScience (www.interscience.wiley.com).

the monochromator or linear polarizer and sample cell. In contrast, in our system, the polarization light source, that is, the polarizing undulator, is located in the storage ring, and the polarization of incoming light can then be modified using the polarization characteristic of the optics. If the windows have linear anisotropy, the recorded CD and LD spectra may be disturbed because of their anisotropy, and the description of the recorded signal based on the Mueller matrix calculation may be too complicated to extract the true CD and/or LD signals.[10] Therefore, superfluous optics such as windows should be not used if possible, because high vacuum is required to prevent the change in the polarization of incident light in this system and the optical cell.

A vacuum-proof optical cell system with a temperature control unit was constructed by Matsuo et al.[14] Because this cell system needs to be loaded in a vacuum chamber evacuated under 10^{-4} Pa, it requires large-scale equipment such as a vacuum chamber with vacuum pumps and liquid-nitrogen temperature control unit. In addition, it is difficult to evaluate the contribution of linear anisotropy.

In this study, a compact optical cell with a temperature control unit was designed to study CD and absorption spectroscopy in the VUV region. The performance of this cell system was evaluated by measuring the absorption spectra of H_2O at several temperatures, the VUV-CD spectra of ammonium camphor-10-sulfonate (ACS) aqueous solutions, and the transmitted spectrum of an empty cell. We also found that the temperature dependence of water absorption intensity is useful for monitoring the temperature of the sample solution.

This article is organized as follows. In the first section, we explain the design of the optical cell and the temperature control unit developed in this study. In the second section, we describe the temperature dependence of the H_2O absorption spectra and the method for estimating the temperature of the sample solution. Finally, in the third section, we demonstrate the performance of this cell unit by measuring the VUV-CD of the ACS aqueous solution and the transmitted spectra of an empty cell.

DESIGN OF THE COMPACT OPTICAL CELL WITH THE TEMPERATURE CONTROL UNIT

Figure 1a and b shows the schematic views of the designed optical cell and temperature control unit, respectively. The size of the cell is 34 mm in diameter and 14 mm in length. The cell volume is about one-fifth that of the vacuum-installed optical cell designed by Matsuo et al.[14] and almost the same as that of the micro cell with a cell holder developed by Wien and Wallace.[6] By coating a VUV scintillator on the outside of the back window, the outside of the cell can be operated under atmospheric pressure, but not in vacuum. The temperature of the cell is maintained in the range of 5°C to 80°C using the temperature control unit equipped with a Peltier thermoelectric element.

As shown in Figure 1a, the optical cell consists of two stainless steel blocks (2) and (3), two O-rings (4), two flat

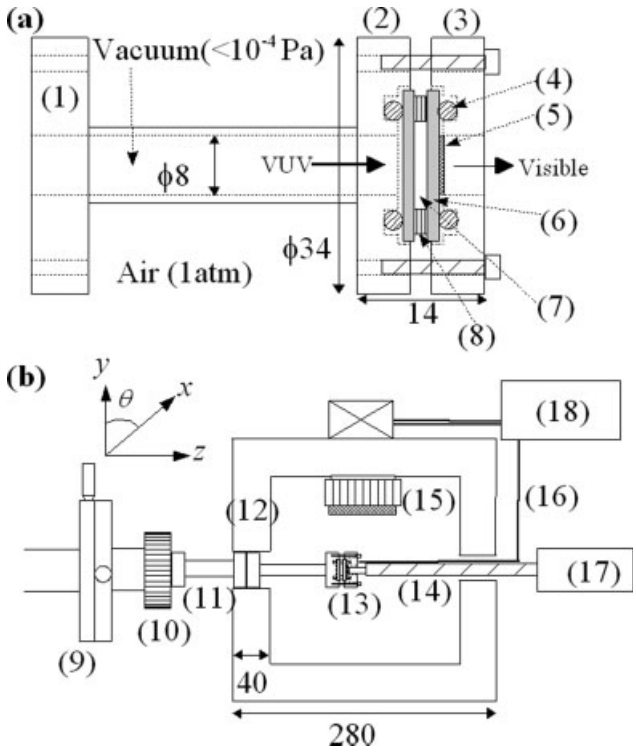

Fig. 1. (**a**) Schematic drawing of a compact optical cell. The linear dimensions are in mm. (1) 34 mm OD flange; (2) stainless-steel block; (3) stainless-steel cover; (4) P-12 type O-rings; (5) coated sodium salicylate; (6) CaF_2 optical windows (diameter, 20 mm, thickness t = 1.5 mm); (7) solution sample; and (8) Teflon spacer (t = 5–500 μm). (**b**) Schematic drawing of the temperature control unit and apparatus for adjusting the cell position. The linear dimensions are in mm. (9) dual-axis *x-y* stage; (10) rotatable axis stage; (11) 34 mm OD nipple; (12) box consisting of a vacuum insulation panel; (13) optical cell; (14) optical fiber; (15) Peltier thermoelectric element; (16) Pt thermistor; (17) photomultiplier; and (18) Peltier thermo-controller.

CaF_2 optical windows of radius 10 mm and thickness 1.5 mm (6), and a ring-shaped spacer made of Teflon (8). The sample solution (7) is sealed between the two CaF_2 windows by tightening the screws with a torque-controlled screwdriver. The cell is easily attached to the vacuum system with a 34 mm flange (1). The optical path length of the cell is adjusted by changing the spacers, which are of various thicknesses (5–500 μm). In the case of the cell without any spacers, the optical path length is estimated to be 2 μm from the interference pattern in the transmitted spectrum of the empty cell, and the required sample volume is approximated to be as low as 1 μl. Optical pathlength estimation will be detailed in a later section. The upper section of the front window is evacuated to less than 10^{-4} Pa within about 1 h, which is sufficient to permit the synchrotron radiation experiment, and to less than 10^{-5} Pa within about one day.

The main advantage of this cell is its compactness. The cell size was reduced by coating sodium salicylate on the outside of the back window (5). Sodium salicylate is usually employed as a VUV scintillator.[15] The VUV light transmitted through the two windows and sample solution is converted to visible light, centered around 420 nm, by the sodium-salicylate scintillator. The converted visible light

is easily detected with a conventional photomultiplier (R6249, HAMAMATSU Photonics K.K. was used in this work). Because the outside of this cell is under atmospheric pressure, it can be said that we successfully developed a simple and compact optical cell system. In addition, apparent CD signal derived from the linear anisotropy of the detector can be ignored, as discussed in the next paragraph. Most other SR-CD instruments use a photomultiplier with VUV transparent windows rather than phosphors.

The linear anisotropy of the cell windows is evaluated by measuring the rotation angle θ dependence of CD and LD spectra. If the window has linear anisotropy, the observed CD signal consists of not only a real CD signal but also a signal originating from the linear anisotropy.[16] To measure the θ dependence, the cell is rotated around the *z*-axis using a rotatable axis stage (10), and its center is adjusted to the light spot using a dual-axis *x*-*y* stage (9), as shown in Figure 1b. The definitions of the *x*, *y*, and *z* directions and the rotational angle θ are illustrated in Figure 1b. Figure 2 shows the rotation angle θ dependence of the LD spectra of the empty CaF_2 cell. This result clearly indicates that the LD spectra are independent of θ. The absence of angle dependence of the LD spectra is direct evidence that the contribution of linear anisotropy can be ignored in this cell system.

In addition, the absence of angle dependence of the LD spectra shown in Figure 2 directly indicates that our phosphor-based detector is also free from linear anisotropy. A conventional photomultiplier occasionally acts as a partial polarizer, and therefore, one can observe the angle dependence of CD and LD spectra.[16] An apparent signal induced from the anisotropic detector occasionally becomes a serious problem.[17] From the result shown in Figure 2, our cell system was confirmed as an isotropic optical component.

As shown in Figure 1b, the temperature control unit is composed of a thermal insulated box (12), a Pt thermistor (16), Peltier thermoelectric elements (15), and a Peltier thermo-controller (18). The cell (13) is inserted in the box, which consists of a vacuum insulating panel (12). The Pt thermistor (16) is used for monitoring the temperature of the cell surface. The temperature of the cell surface is adjusted by blowing temperature-regulated air into the box. The air temperature is controlled using Peltier thermoelectric elements (15) and the Peltier thermo-controller (18) by the conventional PID method. The temperature control unit can maintain the cell temperature in the range of 5°C to 80°C to a precision of ± 0.1°C. The estimation of the precision will be described in the next section. The Peltier element (15) is air-cooled by a fan. Since it is not necessary to evacuate the outside of the cell, the design of the temperature control unit is relatively simple.

The converted visible light is propagated out of the box through an optical fiber (30 cm in length) (14) and detected with a photomultiplier (17). The photomultiplier (17) is placed outside the box because its efficiency is dependent on the ambient temperature. The optical fiber (14) attenuates approximately half of the converted visible light intensity. Thus, in the experiment without a temperature control, the photomultiplier can be connected directly to the cell.

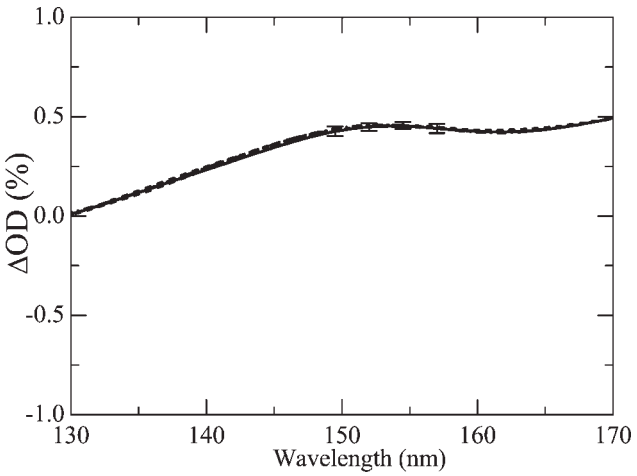

Fig. 2. LD spectrum of the empty CaF_2 cell without a spacer at the rotation angles θ = 0°, 45°, 90°, and 135°. In this figure, four lines overlap each other.

ABSORPTION OF WATER AS A MONITOR OF THE SAMPLE TEMPERATURE

The absorption spectra of H_2O at several temperatures were measured using a conventional VUV monochromator (Acton, VM-502) equipped with a D_2 lamp as a light source. Ultra-pure water (Wako chemical, LC/MS grade) was carefully dropped into the cell with a 20 μm spacer. The absorption spectra at a given temperature were recorded in thermal equilibrium between the cell surface and water, that is, about 1 h after setting the cell temperature.

Figure 3a shows the absorption spectra of liquid H_2O at cell temperatures of 20°C, 35°C, and 80°C. It is clear that the absorption spectra of H_2O are red-shifted with increasing temperature, as reported elsewhere.[18,19] This shift is explained by a lower shift of the electronic transition energy.[19] This temperature dependence indicates that temperature regulation is essential for accurately measuring absorption spectra in the VUV region. That is, the contribution of H_2O absorption is determined from the observed VUV absorption spectra of the sample solution recorded at the same temperature.

Varying the absorption of water with temperature is considered to be useful for monitoring the temperature of the sample solution and not the cell surface. In general, it is difficult to monitor the temperature of a sample solution at micrometer-scale path length. Figure 3b shows the absorbance of water at a wavelength of 173 nm as a function of cell temperature. It is clear that the absorbance is almost proportional to the cell temperature while increasing and decreasing the temperature. Therefore, one can observe the variation of the temperature of the sample solution by measuring the absorbance of water.

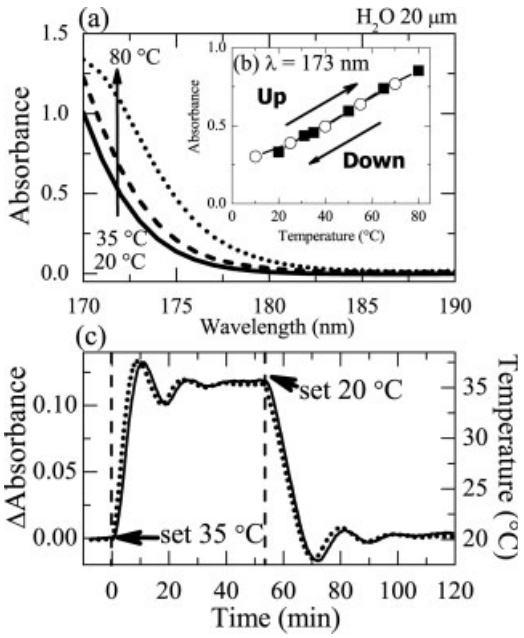

Fig. 3. (**a**) Absorption spectra of liquid H_2O with a 20 μm spacer at temperatures of 20°C (solid line), 35°C (broken line), and 80°C (dotted line). (**b**) Absorbance of liquid H_2O with a 20-μm spacer at a wavelength of 173 nm as a function of temperature during rising temperature (closed square) and falling temperature (open circle). (**c**) The relationship between the difference in H_2O absorbance at a wavelength of 173 nm (solid line) and the temperature of the cell surface (dotted line) as a function of time. Here, the difference in absorption is defined as the subtraction of absorbance at 20°C. The Peltier thermo-controller was set to 35°C and 20°C at 0 and 52 min, respectively.

Figure 3c shows the time-dependence of the cell temperature and the difference in the absorbance of water at a wavelength of 173 nm. When the Peltier thermo-controller was set to a given temperature, the cell temperature changed immediately and then oscillated around the set-point as a decaying sinusoid. The absorption intensity followed the change in cell temperature with some time lag. This time lag corresponds to the heat transfer from the cell surface to the sample solution. Both the cell temperature and the absorption intensity were stable after about 40 min in this case. While the cell temperature is stabilized, the temperature of the sample solution is considered to be the same as that of the cell surface. In addition, from the distribution of the absorbance before the temperature was set at 35°C, the precision of the sample temperature was also estimated to be about ±0.1°C.

VUV-CD AND TRANSPARENT-SPECTRA MEASUREMENT

To evaluate the performance of this cell system, we measured the absorption and VUV-CD spectra of a standard sample. These spectra of the ACS aqueous solution were measured at the TERAS BL-5[10–13] of the National Institute of Advanced Industrial Science and Technology and calibrated using the calibration method recently developed by us.[20] Powders of *S*- and *R*-ACS were purchased from Kanto Kagaku and Sigma Aldrich Japan, respectively, and dissolved in distilled water. The VUV-CD and absorption spectra of the 240 m*M* ACS aqueous solutions with a 5 μm spacer were measured at 25°C in the wavelength range down to 175 nm. Here, measurement of the θ-dependence of the VUV-CD and LD spectra confirmed that the cell was isotropic. To compensate for a little non-chiral baseline, the VUV-CD spectrum of *R*-ACS was subtracted from that of *S*-ACS.[21] Details of VUV-CD measurements at the TERAS BL-5 and the calibration method have been reported elsewhere.[10–13] The calibrated CD spectrophotometer (J720WI, JASCO) was also used to obtain the standard CD spectra of ACS aqueous solutions.[22]

The optical path length was calculated by following the Lambert-Beer law using values for the observed optical density, concentration (240 m*M*), and molar absorption coefficient. The molar absorption coefficients in the range of greater than 190 nm were determined by another absorption measurement recorded with a conventional UV spectrophotometer (Shimadzu Co, UV1200), quartz cell (optical path length 3 mm), and 2.4 m*M* ACS aqueous solution. Using these values, the optical path length in this VUV-CD measurement was determined to be 8.2 μm.

Figure 4a and b shows the absorption and VUV-CD spectra of the *S*-ACS aqueous solution, respectively. The obtained VUV-CD spectrum is in good agreement with the standard spectrum,[18] which is also shown in Figure 4b. The determination of the optical path length by measuring the absorption spectrum is necessary to obtain accurate VUV-CD spectra, because of the variations in the optical path length between loadings of the sample solution.

Figure 5 shows the transmitted spectrum of the empty CaF_2 cell without the spacer. This spectrum was also measured at the TERAS BL-5. It is clear that this cell can

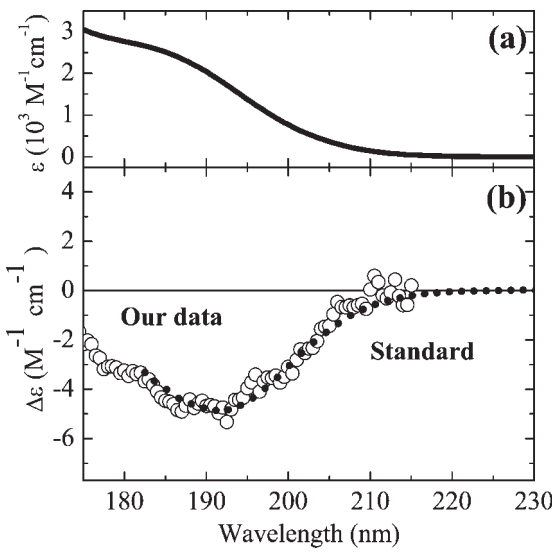

Fig. 4. (**a**) Absorption spectrum of *S*-ACS aqueous solution at 25°C. (**b**) VUV-CD spectra of *S*-ACS aqueous solution measured at TERAS BL-5 at 25°C (open circle) and that measured with a conventional CD spectrophotometer (dotted line).

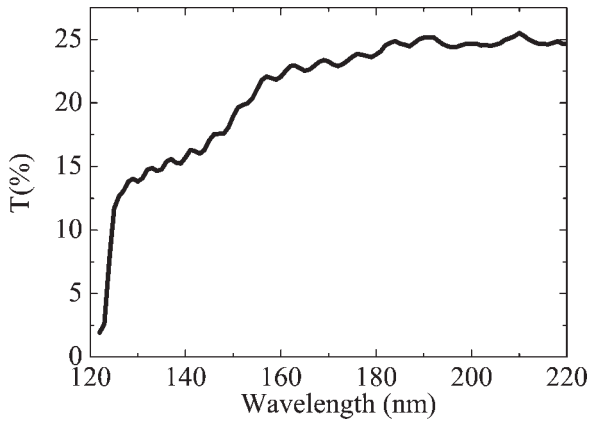

Fig. 5. Transmitted spectrum of the empty CaF_2 cell without a spacer.

transmit VUV light in the wavelength range of greater than 130 nm. This limit is due to the cut-off of the CaF_2 windows. It should be noted that this transparency includes the attenuation by the optical fiber. Excluding this attenuation, the transparency was approximated to be 80% at a wavelength of 200 nm and 60% at 140 nm. These results clearly indicate that our phosphor-based cell can be used for the VUV region. A clear interference pattern is found in this spectrum. Using this interference pattern,[23] the optical path length in the empty cell was estimated to be 2.4 μm.

From these results, it was concluded that this compact optical cell system has sufficient performance to measure VUV-CD and absorption spectra. The VUV-CD measurement of chiral liquids such as saturated chiral alcohols as well as that of solutions of biomolecules is in the planning stage.

CONCLUSION

A compact optical cell for measuring VUV-CD and absorption spectra was successfully developed. The adoption of a VUV scintillator coated on the outside of the back window allowed the outside of the cell to work under atmospheric pressure. The cell, 34 mm in diameter and 14 mm in length, was easily attached to the conventional 34 mm flange. The cell was confirmed to be free of any contribution from linear anisotropy. A simple temperature control unit including the cell successfully maintained the temperature of the cell surface in the range of 5°C to 80°C using a Peltier thermoelectric element. We found that the temperature dependence of the absorbance of water corresponded to the sample temperature, which is useful for monitoring the temperature of a sample solution even at micrometer-scale path lengths. The recorded VUV-CD spectra of the ACS aqueous solution showed good consistency with standard spectra. The cell with CaF_2 windows transmitted VUV light greater than 130 nm. Therefore, regardless of its compactness, this cell system is suitable for use in VUV spectroscopy.

ACKNOWLEDGMENTS

The authors would like to thank Dr. Hiroyuki Toyokawa and Mr. Takeshi Kaihori for their technical help in the TERAS operation, and the staff of the AIST Linac Group for help with the operation of the machinery.

LITERATURE CITED

1. Wallace BA, Janes RW. Synchrotron radiation circular dichroism spectroscopy of proteins: secondary structure, fold recognition and structural genomics. Curr Opin Chem Biol 2001;5:567–571.
2. Matsuo K, Yonehara R, Gekko K. Secondary-structure analysis of proteins by vacuum-ultraviolet circular dichroism spectroscopy. J Biochem 2004a;135:405–411.
3. Brahms S, Brahms J. Determination of protein secondary structure in solution by vacuum ultraviolet circular dichroism. J Mol Biol 1980; 138:149–178.
4. Matsuo K, Gekko K. Vacuum-ultraviolet circular dichroism study of saccharides by synchrotron radiation spectrophotometry. Carbohydr Res 2004b;339:591–597.
5. Gray DM, Lang D, Kuner E, Vaughan M, Sutherland J. A thin quartz cell for suitable for vacuum ultraviolet absorption and circular dichroism measurements. Anal Biochem 1984;136:247–250.
6. Wien F, Wallace BA. Calcium fluoride micro cells for synchrotron radiation circular dichroism spectroscopy. Appl Spectrosc 2005;59: 1109–1113.
7. Clarke DT, Jones G. CD12: a new high-flux beamline for ultraviolet and vacuum-ultraviolet circular dichroism on the SRS, Daresbury. J Synchrotron Rad 2004;11:142–149.
8. Ojima N, Sakai K, Matsui T, Fukazawa T, Namatame H, Taniguchi M, Gekko K. Vacuum-ultraviolet circular dichroism spectrophotometer using synchrotron radiation: optical system and on-line performance. Chem Lett 2001;30:522–523.
9. Miron S, Refregier M, Gilles AM, Maurizot JC. New synchrotron radiation circular dichroism end-station on DISCO beamline at SOLEIL synchrotron for biomolecular analysis. Biochim Biophys Acta 2005; 1724:425–431.
10. Tanaka M, Yagi-Watanabe K, Yamada T, Kaneko F, Nakagawa K. Development of vacuum-ultraviolet circular dichroism measurement system using a polarizing undulator. Chirality 2006;18:196–204.
11. Yagi-Watanabe K, Yamada T, Tanaka M, Kaneko F, Kitada T, Ohta Y, Nakagawa K. Design and implementation of VUV-CD and LD measurements using an ac modulated polarizing undulator. J Electron Spectrosc Relat Phenom 2005a;144-147:1015–1018.
12. Yamada T, Yagi-Watanabe K, Tanaka M, Kaneko F, Kitada T, Ohta Y, Nakagawa K. VUV circular dichroism spectroscopy using an AC modulated polarizing undulator. Rev Sci Instrum 2005;76: 093103.
13. Yagi-Watanabe K, Tanaka M, Kaneko F, Nakagawa K. Recent progress in vacuum-ultraviolet polarization modulation spectroscopy using polarizing undulator at the TERAS BL5 beamline. Rev Sci Instrum 2007;78:123106.
14. Matsuo K, Sakai K, Matsushima Y, Fukuyama T, Gekko K. Optical cell with a temperature-control unit for a vacuum-ultraviolet circular dichroism spectrophotometer. Anal Sci 2003;19:129–132.
15. Samson JAR. Technique of vacuum ultraviolet spectroscopy. New York: John Wily & Sons; 1967. p 212–217.
16. Shindo Y, Nishio M, Maeda S. Problems of CD Spectrometers (V): Can we measure CD and LD simultaneously? Comments on differential polarization microscopy (CD and linear dichroism). Biopolymers 1990;30:405–413.
17. Kuroda R, Harada T, Shindo Y. A solid-state dedicated circular dichroism spectrophotometer: development and application. Rev Sci Instrum 2001;72:3802–3810.
18. Williams F, Varma SP, Hillenius S. Liquid water as a lone-pair amorphous semiconductor. J Chem Phys 1976;64:1549–1554.

19. Marin TM, Takahashi K, Bartels DM. Temperature and density dependence of the light and heavy water ultraviolet absorption edge. J Chem Phys 125:104314, 2006.
20. Yagi-Watanabe K, Tanaka M, Yamada T, Kaneko F, Nakagawa K, Yuri M. A vacuum ultraviolet polarimeter with quadruple-reflectors: polarization measurements at the TERAS BL-5 beamline. Nucl Instrum Methods Phys Res A. 2005b;553:620–626.
21. Nakagawa K, Tanaka M, Kaneko F, Kitada T, Ohta Y, Agui A, Fujii K, Yokoya A, Yagi-Watanabe K, Yamada T. Natural circular dichroism of amino acid films observed in soft X-ray and VUV region using polarizing undulator. J Electron Spectrosc Relat Phenom 2005;144-147:271–273.
22. Takakuwa T, Konno T, Meguro H. A new standard substance for calibration of circular dichroism: ammonium d-10-camphorsulfonate. Anal Sci 1985;1:215–218.
23. Miles AJ, Wien F, Lees JG, Wallace BA. Calibration and standardisation of synchrotron radiation and conventional circular dichroism spectrometers. Part 2: Factors affecting magnitude and wavelength. Spectroscopy 2005;19:43–51.

CHIRALITY 20:1029–1038 (2008)

A New Reference Material for UV–visible Circular Dichroism Spectroscopy

ANGELIKI DAMIANOGLOU,[1] EDWARD J. CRUST,[1] MATTHEW R. HICKS,[1] SUZANNE E. HOWSON,[1] ALEX E. KNIGHT,[2] JASCINDRA RAVI,[2] PETER SCOTT,[1] AND ALISON RODGER[1]*

[1]*Department of Chemistry, University of Warwick, Coventry, United Kingdom*
[2]*Quality of Life Division, National Physical Laboratory, Teddington, Middlesex, United Kingdom*

Presented at the 11th International Conference on Circular Dichroism, 2007, Groningen, Netherlands

ABSTRACT To obtain accurate and consistent measurements from circular dichroism (CD) instruments over time and from different laboratories, it is important that they are properly calibrated. The characteristics of the available reference materials are not ideal to ensure proper calibration as they typically only give peaks in one or two spectral regions, and often have issues concerning purity and stability. Currently either camphor sulfonic acid or ammonium camphor sulfonate are used. The latter can be an unstable, slightly hygroscopic secondary standard compound with only one characterized CD band. The former is the very hygroscopic primary standard for which only one enantiomer is readily available. We have synthesized a new reference material for CD, Na[Co(EDDS)]·H_2O (EDDS = *N*,*N*-ethylenediaminedisuccinic acid) which addresses these problems. It is extremely stable and available in both enantiomeric forms. The CD spectrum of Na[Co(EDDS)]·H_2O has nine distinct peaks between 180 and 599 nm. It thus fulfils the principal requirements for CD calibration chemical standards and has the potential to be used to ensure good practice in the measurement of CD data, providing two spectra of equal magnitude and opposite sign for a given concentration and path length. We have carried out an interlaboratory comparison using this material and show how it can be used to improve CD comparability between laboratories. A fitting algorithm has been developed to assess CD spectropolarimeter performance between 750 and 178 nm. This could be the basis of a formal quality control process once criteria for performance have been decided. *Chirality 20:1029–1038, 2008.*

KEY WORDS: circular dichroism; calibration; enantiomers; standard

INTRODUCTION

Circular dichroism (CD) is a powerful spectroscopic technique with many applications in organic chemistry and biochemistry. For example, one can qualitatively and quantitatively assess the purity of two enantiomers of a chiral molecule; one can sensitively detect changes in the structure of protein molecules; and one can predict the secondary structure of proteins. It is important, prior to the analysis, to establish quality assurance for factors affecting the reliability of the data. This is especially true when spectra are crucial evidence of the structure and stability of a protein component of a pharmaceutical product, but it is also important when spectra are to be reported for almost any purpose.

To achieve comparability of CD spectra between instruments, it is important that the instruments are well-maintained and used correctly.[1,2] However, even where this is done, differences between instruments will mean that data are typically not comparable.[3,4] One route to the comparability of data is to characterize CD instruments in terms of both CD intensity calibration and wavelength calibration across the spectral range of interest. However, currently available "standard" materials typically only provide a single CD peak, and are often poorly characterized, as is discussed below. The lack of confidence that data can meaningfully be compared when they are measured in different laboratories, or at different times, undermines the usefulness of CD as a technique. This is particularly true in heavily regulated areas such as biopharmaceutical quality control.

In the past decades, a series of optically active substances have been identified and used extensively for the calibration of CD spectropolarimeters. D-10-camphorsulfonic acid (CSA) in water at 290.5 nm has been regarded as the primary standard and has been the one used extensively throughout the world. However, differences in the magni-

Additional Supporting Information may be found in the online version of this article.

Contract grant sponsors: Project PC4 of the National Measurement System's "Measurements for Biotechnology" Programme; EPSRC.

*Correspondence to: Alison Rodger, Department of Chemistry, University of Warwick, Gibbet Hill Road, Coventry CV4 7AL, United Kingdom.
E-mail: a.rodger@warwick.ac.uk

Received for publication 5 December 2007; Accepted 13 February 2008
DOI: 10.1002/chir.20566
Published online 27 May 2008 in Wiley InterScience (www.interscience.wiley.com).

tude of its spectra due to its hygroscopic nature have repeatedly been reported in the literature.[5] Other substances such as androsterone and isoandrosterone in dioxane have also been considered[5,6] as well as glucurono-γ-lactone and D-pantolactone in other organic solvents.[7] Glucurono-γ-lactone was found to be less suitable than the D-pantolactone that became commercially available as optically pure crystals having relatively high optical rotation with weak UV absorption and less water uptake than CSA.[7] A study was also conducted by Chen and Yang[6] comparing CSA in water at 290.5 nm, D-pantolactone in methanol at 222 nm and (+)-*tris*-(ethylenediamine) Co(III) iodide monohydrate in water at 490 nm. The study revealed deviations in molar ellipticity of up to 30% for D-pantolactone and (+)-*tris*-(ethylenediamine) Co(III) iodide monohydrate[8] between measurements carried by different spectropolarimeters. That study may suggest that [Co(ethylenediamine)$_3$]$^{3+}$ would make a good standard. It is certainly chemically and enantiomerically stable. However, it is challenging to make up solutions accurately for UV measurements (literature extinction coefficient data is all for the visible region and the UV intensity is orders of magnitude larger). In addition, a single solution cannot be used from the visible region to the UV region. The final nail in its coffin is that it is not commercially available and it extremely difficult to produce 100% enantiomerically pure as it is resolved by repeated co-crystallization with chiral anions.[9]

Ammonium D-10-camphorsulfonate (ACS) (see Fig. 1), which is less hygroscopic, but much more expensive, than CSA, has been widely adopted as a secondary standard. ACS was found to be essentially non-hygroscopic, easily handled and to have the same spectrometric behavior as CSA because of the fact that both compounds form the same ion in solution.[2,5] Calibration with both CSA and ACS routinely involves using only the 290.5 nm peak. Thus, there is no calibration of the visible region and none at lower wavelength. CSA does have a CD band at 191.5 nm, however, there is still some debate as to what its magnitude is (the consensus is that the 192.5 nm:290.5 nm ratio should be about 2.0).[3] A further concern with ACS is that its stability is variable. Jones et al.[10] showed its intensity can change within 2 wk even when refrigerated. Thus fresh standards need to be made regularly and accurately to a standardized protocol.[1,2] The material used also needs to be of a known chemical purity and enantiomeric purity. In a recent interlaboratory comparison study coordinated by the National Physical Laboratory (NPL),[11] it became apparent that the current single point calibration even with an externally provided standard did not ensure instrument comparability or even provide enough data to indicate whether instruments recorded comparable data.[4] For all types of measurement, the ideal is that standards should be traceable to the International System of Units (the SI)[12] with a known uncertainty.[13,14] This means that all measurements that are made in this way can be compared within a known uncertainty; moreover this is recognized as an efficient means of achieving comparability. Traceability is typically established through a chain of measurements, starting from a primary, absolute measurement (often made by a National Measurement Institute, such as NPL) and disseminated through primary and secondary standards. No such chain exists for CD, and therefore the absolute values of the CD of the standard compounds are not known with any confidence. However, where such a chain cannot be established, it may be sufficient for practical purposes to establish the comparability of measurements by other means, and this is what we have set out to achieve.

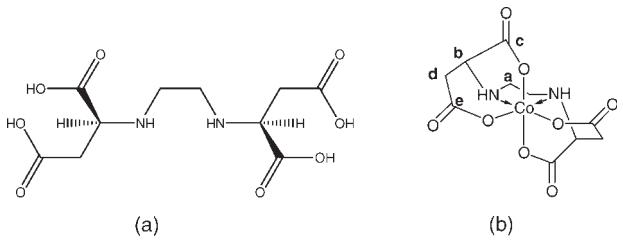

Fig. 1. (**a**) *S,S-N,N*-ethylenediaminedisuccinic acid (EDDS); (**b**) Co-EDDS with proton labeling indicated.

What impacts do uncertainties in the measurement of CD have? A good example is the use of CD spectra to predict the secondary structure of proteins. With some algorithms, errors in the intensity and wavelength scales of CD spectrometers have a significant effect on the predicted structures.[15] Similar problems arise when CD is used to measure enantiomeric purity since CD intensity is proportional to enantiomeric excess. In empirical applications such as comparing the spectra of biopharmaceutical formulations, the comparisons between data measured on different occasions and/or in different laboratories are only valid if the instruments can be relied on to produce consistent data. Thus it is essential that, even in the absence of an absolute standard for CD, all instruments used would produce essentially the same data for the same sample. Furthermore we need a measure of what we mean by 'the same'.

There has been a long running project at Warwick University to find an alternative CD secondary standard with the following prerequisites: chemical stability in solution; enantiomeric stability in solution; availability of bands across the full UV–visible region (including below 200 nm) that can be measured on the same concentration solution; and availability of both enantiomers. One of the issues with low wavelength instrument performance is that in most instruments stray light becomes a significant problem. Instrument problems, in this or any other region of the spectrum, apart from a simple magnitude scaling, are likely to result in enantiomers not having mirror image spectra. The availability of both enantiomers and a requirement for equal magnitude and opposite signed CD signals at all wavelengths were therefore among the requirements of this work. We have screened many compounds over the years and have finally selected and tested *R,R*- and *S,S*-Na[Co(EDDS)]·H_2O ((EDDS = *N,N*-ethylenediaminedisuccinic acid), henceforth referred to as *R,R*-CoEDDS and *S,S*-CoEDDS, respectively). CoEDDS is a transition metal complex with d→d transitions which was first synthesized by Neal and Rose in 1968.[16] Its visible region CD spectrum

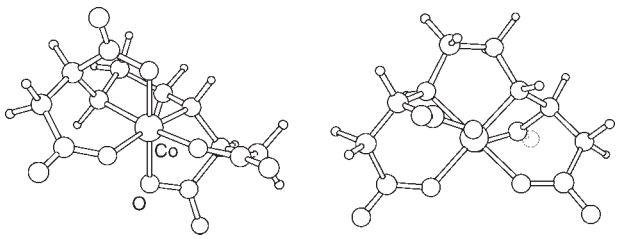

Fig. 2. Stereogenic arrangements of the five- and six-membered rings in the EDDS complex $Li(H_2O)_3[Co^{III}(S,S\text{-EDDS})]$.[18]

has been previously published[16,17] though no UV CD data were available prior to this study. With modern instruments, it is now possible to collect data for this compound from the visible to well into the far UV region with the same sample in the cuvette as shown later. In fact by using both bench top and synchrotron radiation instruments we have acquired data from the visible down to 165 nm. Together with its stability (see later) and the availability of both enantiomers this makes it an attractive calibration standard.

For both enantiomers of $Na[Co(EDDS)]\cdot H_2O$ we have considered the effects of temperature and concentration on the CD spectra line shapes and also tested the chemical and enantiomeric stability of the compounds over a period of 12 mo. In addition we undertook a small interlaboratory comparison (including Warwick University, National Physical Laboratory, the National Institute for Biological Standards and Control, and Chiralabs). Data were also collected at the synchrotron source at Aarhus University to determine low wavelength spectral shape. The aim of the comparison study was to investigate the utility of the new material in achieving comparability between laboratories and to confirm the spectral characterization performed at Warwick. We also investigated the use of the material in instrument performance verification testing.

MATERIALS AND METHODS

Optically pure *S,S*-EDDS (see Fig. 2) was donated by Innospec. Other materials were obtained from Sigma-Aldrich and used without further purification. 18.2 MΩ water was used throughout.

R,R-*EDDS*[16]

A mixture of D-aspartic acid (50.73 g, 0.38 mol, ee = 98%), NaOH (30 ml, 50% aqueous solution), $Ca(OH)_2$ (13.94 g, 0.19 mol), and deionized water (70 ml) was placed in a 1-liter three-necked flask fitted with a reflux condenser and 50 ml pressure-equalized dropping funnel and large magnetic follower. 1,2-dibromoethane (28 ml, 61.0 g, 0.33 mol) was added carefully with stirring via the third side-arm and the mixture was heated to gentle reflux. A further portion of NaOH (24 ml, 50% aqueous) was added dropwise over about 6 hr, maintaining the reflux. Water (100 ml) was added and the solution was heated at reflux for 1 hr. The reaction mixture was left to cool with stirring for 1 hr. The mixture was acidified with concentrated HCl until pH 3 by which time a copious white precipitate had formed. The filtrate was collected and added to water (225 ml) followed by NaOH (50% aqueous) to pH 11. The solution was carefully acidified with HCl to pH 3.5 and the subsequent precipitate was collected, washed with dilute HCl and dried in air at 65°C in vacuo. Yield 17.9 g (32%). Anal. Found (Calcd. for $C_{10}H_{16}N_2O_8$) %C 41.02 (41.10), H 5.50 (5.52), N 9.31 (9.59). ^{1}H NMR (400 MHz, 293 K, NaOH/D_2O ref. 4.79) δ ca. 2.35 (dd, 2H, CH_2CO_2), 2.51 (dd, 2H, CH_2CO_2) 2.64 (m, 4H, CH_2CH_2), 3.39 (dd, 2H, CH) (NH and CO_2H not observed at this pH). ^{13}Cpp NMR δ 41.5 (CH_2), 46.8 (CH), 61.5 (CH_2—CH_2), 179.9 (C_q), 181.6 (C_q). MS (FAB) *m/z* 292 (M^+).

$Na_3[Co(CO_3)_3]\cdot 3H_2O$[16]

$Co(NO_3)_2.6H_2O$ (29.1 g, 0.1 mol) in water (50 ml) and H_2O_2 (10 ml, 30%) was added dropwise to a cold slurry of $NaH(CO_3)$ (42.0 g, 0.5 mol) in water (50 ml). The mixture was allowed to stand for 1 hr at 0°C with continuous stirring. The resultant green product was filtered, washed with cold water (thrice in 10 ml), ethanol, and diethyl ether, and then dried in vacuo. Yield 29 g, 80%.

*Na[Co(*S,S*-EDDS)]H$_2$O (*R,R*-Isomer Prepared Similarly)*[16]

S,S-EDDS (3.10 g, 10 mmol) was added with stirring to an ice cold slurry of $Na_3[Co(CO_3)_3]\cdot 3H_20$ (3.63 g, 10 mmol) and activated charcoal (3 g) in water (75 ml). The reaction mixture was allowed to warm to ambient temperature and was stirred until CO_2 evolution ceased. The mixture was then heated to 80°C and stirred for 20 min, followed by slow addition of small amounts of acetic acid (5% aqueous, total 10 ml) to complete evolution of CO_2. The solution was heated again to 80°C for 5 min and allowed to cool. Acetic acid solution was added to pH 4.25. The solution was filtered through Celite to remove the charcoal and the volume of the solution was reduced to about 30 ml. Slow addition of ethanol (ca. 100 ml) resulted in precipitation of a purple solid which was isolated by filtration. The solid was suspended in ethanol (ca. 100 ml) and sufficient water was added to dissolve the solid. The solution was filtered and ethanol was slowly added with stirring until a solid began to precipitate. The mixture was then heated to redissolve the complex and was left to cool. The fine crystals of $Na[Co(EDDS)]\cdot H_2O$ (see Fig. 2) obtained were isolated by filtration and left to dry in air overnight (yield 1.7 g, 44%). Intriguingly drying the crystals in a vacuum oven removed the water of crystallization. However, on exposure to the atmosphere (most obviously on a balance), one molecule of water per Co was reincorporated. *S,S*-isomer: Anal. found (Calcd. for $C_{10}H_{14}O_9CoN_2Na$) % C 30.17 (30.94), H 3.75 (3.64), N 7.00 (7.22). ^{1}H NMR (400 MHz, 298 K, D_2O) δ 3.51 (2H, dd, $^3J_{HH}$ = 5.5 Hz, $^3J_{HH}$ = 1.5 Hz, H_c), 3.16 (2H, d, $^2J_{HH}$ = 10.5 Hz, H_a/H_b), 3.09 (2H, dd, $^2J_{HH}$ = 24 Hz, $^3J_{HH}$ = 5.5 Hz, H_e), 2.84 (2H, dd, $^2J_{HH}$ = 24 Hz, 1.5 Hz, H_d), 2.71 (2H, d, $^2J_{HH}$ = 10.5 Hz, H_a/H_b). ^{13}C {} NMR (100 MHz, 298 K, D_2O) δ_C 183.1 (C_c/C_e), 183.0 (C_c/C_e), 66.6 (C_b), 52.6 (C_a) 40.0 (C_d, observed at 353 K). MS (ESI negative) m/z 346.9 ($[M]^-$), 302.9 ($[M]^-$, CO_2), 259.0 ($[M]^-$, 2 × CO_2). IR ν cm^{-1}:

1563 s (COO asymmetric stretch), 1383 s (COO symmetric stretch), 1209 m, 1134 w, 1040 m, 925 w, 879 m.

Circular Dichroism Analysis

The spectral characterization and stability study spectra of the CoEDDS compounds were all obtained using the Jasco J-715 spectropolarimeter at Warwick (calibrated using 0.060% ACS for intensity and a neodymium filter for wavelength) or the Jasco J-810 at NPL (calibrated using 0.060% ACS for intensity and a holmium filter for wavelength). As a rule of thumb, with the Jasco's photomultiplier tubes we choose sample concentrations to keep the high tension voltage below 600 V. The standard parameters used were: bandwidth 1 nm; response time 1 sec; wavelength scan range 190–750 nm; data pitch 0.5 nm; and scanning speed 100 nm/min. These parameters gave spectra that overlaid with those collected at slower scan speeds and narrower bandwidth and so were deemed satisfactory. If one wishes only to calibrate in the visible region then a concentration of ~2 mM is appropriate (higher concentrations can be used but with Jasco instruments require the low sensitivity setting to be selected, otherwise the signal goes off scale); in the UV region a smaller concentration (0.05 mM) is required to ensure the sample's absorbance is not too high.

All cuvettes used in this study were washed three times with water (18.2 MΩ) and three times with ethanol and dried with compressed air. Before establishing the stability study, the instrument-only (i.e. air only in the sample compartment) baseline and the water baseline of each cuvette used were collected. Instrument-only baselines were then collected at each time point. Thus at intermediate time points, *t*, the baseline that was subtracted from the sample spectrum was the water baseline of the cuvette at time 0 plus the difference between the instrument-only baseline at time *t* and the instrument-only baseline at time 0. Samples of each of the *R,R* and *S,S*-[Co(EDDS)] at a concentration of 0.05 mM in water were stored at 4°C, at room temperature in the dark, and at room temperature in the light for 12 mo.

Interlaboratory Comparison

The interlaboratory comparison followed a "star" design where samples were distributed from the coordinating laboratory to the participants. The study participants are listed in Table 1. The samples that were distributed included both the *R,R*- and the *S,S*-CoEDDS enantiomers of the standard (of concentrations 0.067 mM) and a racemic mixture of the two; an ACS solution for comparison, and a water blank. The participants were provided with a common protocol for measurements. All spectra were acquired in 10 mm path length cuvettes provided by the participant laboratory; CoEDDS spectra were collected from 180 to 800 nm and ACS spectra from 200 to 360 nm. The spectra were collected with a 1 nm bandwidth, 0.1 nm data pitch, and 6 accumulations. The reference spectra collected at NPL were collected at a scan speed of 10 nm/min with a 4 sec response time. Participants were left to choose the scan speed they felt most appropriate, but 50 nm/min with a 1 sec response was suggested. Baseline and sample spectra were then returned to the organizing laboratory for baseline subtraction and further analysis. To investigate the use of the standards for instrument performance verification, one participant (designated 4) intentionally used an instrument that was known to be in need of calibration and with a poorly performing lamp.

TABLE 1. Participants in the interlaboratory comparison

Institution	Participants
NPL (Coordinator)	Alex Knight; Jascindra Ravi
University of Warwick	Alison Rodger; Angeliki Damianoglou
National Institute for Biological Standards and Control	Christopher Jones
Chiralabs	George Tranter; Delphine LePevelen; Ann Talbert

Curve Fitting

Manipulation and analysis of the interlaboratory comparison data was performed in MATLAB (The MathWorks, Natick, MA). Curve fitting of the spectra was performed using the MATLAB Curve Fitting Toolbox. The model chosen for the interlaboratory comparison data was a sum of 9 Gaussians (reflecting the 9 maxima in the observed spectra), with constraints applied to peak position, height, and width to ensure an accurate fit. The equation used was of the form:

$$a_1 e^{-((x-b_1)/c_1)^2} + a_2 e^{-((x-b_2)/c_2)^2} + \cdots + a_9 e^{-((x-b_9)/c_9)^2}$$

where for the *n*th Gaussian peak a_n corresponds to the peak height, b_n to the peak (or center) wavelength, and c_n is related to the peak width (with the full width at half maximum given by $2\sqrt{2\ln(2)}c$). To achieve accurate fitting of the spectra it was necessary to include constraints in the fitting method, and these are listed in Table 2. The peak heights (*a* parameters) were constrained to be either positive (0 to $+\infty$) or negative ($-\infty$ to 0); the peak wavelengths (*b* parameters) were constrained to a 10 nm or 15 nm window. In addition, the *c* (width) parameters were constrained to a minimum of 10 nm for all peaks except 1, which was constrained to a minimum of 5 nm. These constraints were developed empirically by iteratively adding terms to the model until the residuals approached a flat line. Additionally, spectra were truncated at short wavelengths to exclude noisy data.

RESULTS

Structure of the Complexes

EDDS (EDDS = *N,N*-ethylenediaminedisuccinic acid) is a hexadentate chelating agent, isomeric with EDTA, and forms an octahedral complex with two nitrogen and four oxygen donors; the latter are typically deprotonated under basic conditions.[16] A key structural difference between H_4EDDS and H_4EDTA is that the former contains two

TABLE 2. Constraints used in Gaussian fitting of CoEDDS and fit coefficients for NPL data

	Fit constraints				Fit parameters					
	Wavelength (nm)		Sign		Wavelength (nm)		Height (mdeg)		Width (nm)	
Peak	Min	Max	*S,S*	*R,R*	*S,S*	*R,R*	*S,S*	*R,R*	*S,S*	*R,R*
1	175	185	+	−	179.2	181.4	25.494	−19.650	8.770	7.804
2	205	215	+	−	211.0	211.0	61.189	−62.025	12.120	12.117
3	225	240	−	+	234.9	233.6	−11.691	12.165	26.215	26.479
4	260	275	+	−	267.6	268.6	9.985	−9.577	28.034	27.307
5	367	377	+	−	368.0	370.3	1.740	−1.919	23.656	25.343
6	399	409	+	−	406.8	409.0	2.129	−2.016	29.775	27.371
7	478	488	+	−	482.6	484.2	1.719	−1.791	32.972	36.096
8	540	550	−	+	544.9	545.4	−5.947	6.170	31.572	33.284
9	595	610	+	−	598.8	595.0	1.188	−1.382	30.218	34.488

Confidence limits for these data are available in Supplementary Information. Additionally, minimum width constraints were applied to the peaks to ensure an accurate fit. Note that *S,S-* and *R,R-* data are in most cases consistent within 95% confidence limits (see Supplementary Information). Where peaks are not well constrained by the data they may show differences but these peaks would not be used for calibration purposes.

stereogenic carbon atoms which retain their stereochemistry upon chelation. However, unlike with EDTA where the four carboxyl arms all form five-membered rings upon coordination, EDDS forms two five-membered rings and two six-membered rings (see Fig. 2). When the two stereogenic carbon atoms have the same absolute configuration (i.e. both *S,S-* or both *R,R-*), only one arrangement, that with the five-membered rings in the axial positions and the six-membered rings in the equatorial positions has been observed.[16,17,19,20] This is a result of excessive strain energy associated with having the five-membered rings in equatorial positions.[16,18,20] As a result, all homochiral EDDS complexes are diastereomerically pure; the chirality of the ligand is expressed perfectly in the absolute configuration of the metal atom such that e.g. *S,S*-EDDS gives only the complexes Δ-[M(*S,S*-EDDS)]$^{n-}$. It is this stereogenic arrangement of the ligand around the metal atom that leads to the observed CD spectrum.

Characterization and Purity by NMR

The cobalt complexes produced by the methods described in this article were chemically, diasteriomerically, and enantiomerically pure within limits of detection. After the reaction there is at most 0.01% of any *R,R*-EDDS in the *S,S-* product due to the high enantiomeric purity of the starting materials. (The aspartic acid is >98% ee (er = 99:1), but the product diastereomer is homochiral. Any heterochiral (*R,S*) is crystallized out, and is absent according to NMR. Chances of any homochiral product of wrong handedness is thus 1% of 1%, i.e. 0.01%.) Recrystallization will have further reduced this. The ^{1}H-NMR spectra of Na[Co(*S,S*-EDDS)]·H_2O and Na[Co(*R,R*-EDDS)]·H_2O in D_2O (see Fig. 3) were superposable on one another. They showed no detectable impurities; small apparent fluctuations in the baselines in Figure 3 (e.g. about 3.1 and 3.4 ppm) are due to ^{13}C satellites. The spectra showed the expected five sets of multiplets, the NH groups having been deuteriated by the solvent. The assignments given in the experimental section were made via ^{1}H—^{1}H and ^{13}C—^{1}H correlation spectra and other standard methods. The H atoms on the ethylene backbone, H_a and H_b, gave two second-order doublets of doublets centered at 2.81 and 3.28 ppm. H_d and H_e gave two sets of mutually coupled doublets centered at 2.98 ppm and 3.22 ppm with the smaller and inequivalent couplings to H_c (3.59 ppm) allowing their assignment via the Karplus equations. In the ^{13}C spectrum the resonance for the C atom bonded to $H_{d/e}$ was observed only at high temperature or via ^{1}H observed heteronuclear correlation, presumably as a result of an exchange between conformers of this 6-membered ring. We note that the corresponding ^{1}H resonances are also relatively broad. Unfortunately, the freezing point of

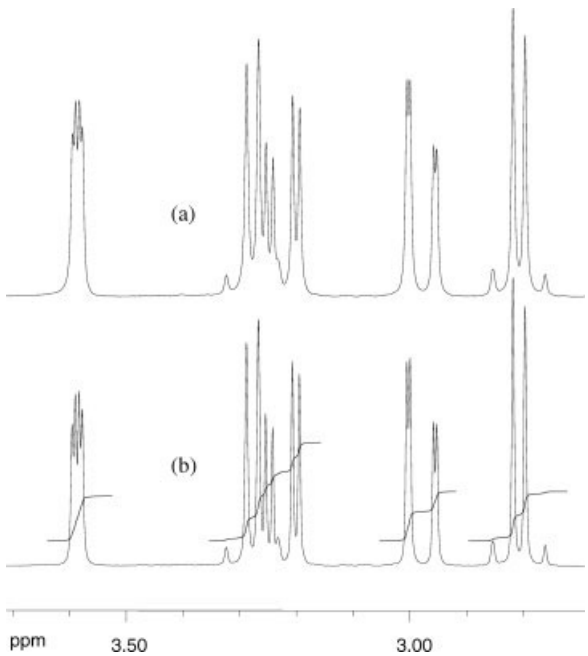

Fig. 3. ^{1}H NMR spectra of **(a)** Na[Co(*R,R*-EDDS)]·H_2O and **(b)** Na[Co(*S,S*-EDDS)]·H_2O.

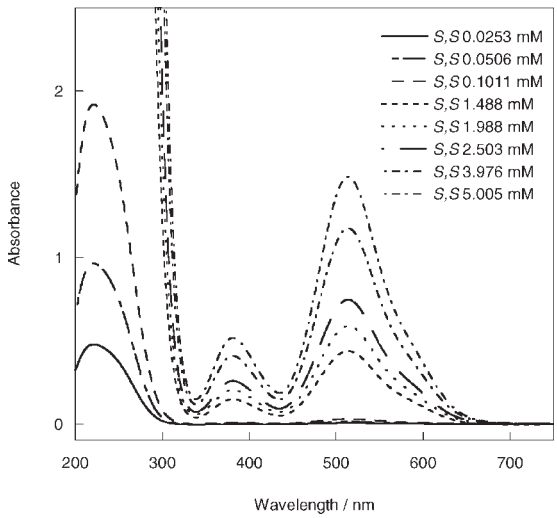

Fig. 4. Absorbance spectra (1 cm path length) as a function of increasing sample concentration (indicated in figure) for *S,S*-CoEDDS.

the solvent precluded measurement of low temperature spectra.

Extinction Coefficient Determination

Most laboratories with CD machines have UV/visible absorption instruments but not all have high quality balances. Thus, accurate values for the extinction coefficients of CoEDDS are required in all application wavelength ranges. Absorbance data were collected over a series of separately prepared samples of each enantiomer at a range of concentrations (determined by weighing four independent samples and making to volume in a volumetric flask, then diluting these samples) (see Fig. 4). Data at the wavelength maxima were extracted and plotted to determine extinction coefficients as summarized in Table 3.

CD Spectra of R,R- *and* S,S-*CoEDDS*

A full wavelength spectrum of *R,R*-CoEDDS is given in Figure 5a. It is a concatenation of data collected at Warwick, NPL, and the synchrotron source at Aarhus (calibrated using 0.060% ACS for intensity and benzene vapor for wavelength) to give the best signal-to-noise at each wavelength and to ensure significant overlap of the different instruments (spectra in common wavelength regions were identical within the noise envelope of the data). The spectra for the two enantiomers are equal and opposite in sign at each wavelength, as illustrated in Figure 5b where the spectra of the *R,R* and $-S,S$ (minus 1 times the *S,S* spectrum) spectra overlay within instrument noise. $\Delta\varepsilon$ values are given in Table 3. The low wavelength spectra collected with a 1 cm cell overlaid those collected with 100 μm and 18 μm pathlengths, when scaled to account for the pathlengths and concentrations (data not shown).

Stability Studies by CD

The CD spectral shapes of the two enantiomers show that the samples are stable for at least 1 yr even at room temperature exposed to light. All storage conditions retained the same spectral shapes over the 12 mo period (most data not shown) as illustrated in Figure 6. Despite sealing the cuvettes with Teflon tape, a slight degree of evaporation occurred for one sample, which has been corrected for in Figure 6 by a scaling factor determined from the change in the absorbance.

Curve Fitting

Comparison of spectra by eye is sufficient for many purposes. However, if we wish to use CD to, for example, Good Laboratory Practice (GLP) standard, a more rigorous and quantitative evaluation of instrument performance is required. To this end, we first showed that the CoEDDS CD spectra could be fitted using a sum of 9 Gaussian functions (see methods). To illustrate the fitting results, fits and residuals for the NPL data from the round robin study are shown in Figure 7. The constraints and fit parameters are given in Table 2. It is clear that the model fits the data accurately from 185 to 800 nm. The residuals are small and randomly distributed, although greater noise in the spectra is evident at the wavelength extrema. The R^2 for the *S,S* enantiomer was 0.9998 and for the *R,R* enantiomer, 0.9997. Once a data set has been reduced to a sum of Gaussians, comparison with a similarly represented standard spectral data set is straightforward.

Interlaboratory Comparison

The interlaboratory comparison (see Supplementary Information for details) clearly illustrated the value of the fitting methodology. It was possible to show pictorially with spectra (Supplementary Information Fig. S3) and quantitatively with residual plots (Supplementary Information Fig.

TABLE 3. Extinction coefficient and delta epsilon values for both enantiomers, fitted using Kaleidagraph

Wavelength (nm)	$\varepsilon_{S,S}$ (mol^{-1} dm^3 cm^{-1})	$\varepsilon_{R,R}$ (mol^{-1} dm^3 cm^{-1})	$\Delta\varepsilon_{S,S}$ (mol^{-1} dm^3 cm^{-1})	$\Delta\varepsilon_{R,R}$ (mol^{-1} dm^3 cm^{-1})
545	209 ± 0.4	211+0.9	**−2.40 ± 0.05**	**+2.33 ± 0.05**
515	**296 ± 0.4**	**299 ± 0.3**		
480			**+0.68 ± 0.015**	**−0.67 ± 0.015**
382	**103 ± 0.5**	**104 ± 0.6**	**−0.95 ± 0.025**	**+0.93 ± 0.025**
274	6142 ± 20	6131 ± 33	**+3.35 ± 0.10**	**−3.30 ± 0.10**
237			**+3 ± 0.3**	**+4 ± 0.3**
221.5	**18,997 ± 24**	**18,985 ± 32**	**+0.665 ± 0.10**	**−0.675 ± 0.10**
210	17,490 ± 35	17,500 ± 60	**+24.0 ± 0.3**	**−22.5 ± 0.3**

Error quoted is standard deviation. Data and its analysis are given in Supplementary information. Data in bold are peak maxima.

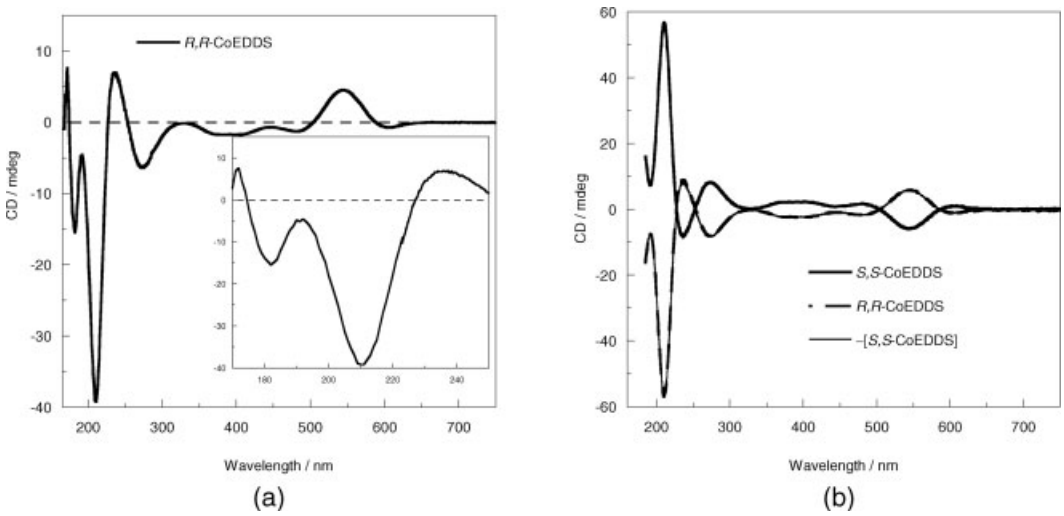

Fig. 5. (**a**) CD spectrum in millidegrees of *R,R*-CoEDDS in water (concentration of 0.056 mM, 1 cm path length and 0.56 mM, 100 μM pathlength). *S,S*-CoEDDS is equal in magnitude and opppsite in sign at each wavelength but is not shown for clarity. The insert shows the low wavelength part of the spectrum. (**b**) Overlaid CD spectra of *R,R*-, *S,S*-CoEDDS and minus *S,S*-CoEDDS (0.072 mM, 1 cm path length) illustrating the equal magnitude and opposite sign of the two enantiomers.

S4) that 3 of the 4 laboratories were giving consistent data. As expected Laboratory 4 clearly had problems, giving R^2 values with respect to the standard of 0.44 (*S,S*) and 0.79 (*R,R*). This implies that "rogue" spectra can be automatically rejected by software based on fit quality statistics such as the R^2 value. The 211 nm peak is particularly useful for instrument validation as it typically gives the narrowest confidence intervals, shown by the error bars in the plots in Supplementary Information Figure S4.

A more subtle application of the standards and the fitting method to analyze instrument performance is provided by the spectra of Figure 8. These *R,R*- and *S,S*- spectra should match the ones in Figures 5 and 6 as the samples were the same but the data collected with a 2 nm bandwidth. Our expectation with a 2 nm bandwidth was that most of the spectra should be of reasonable quality (and usually better than with 1 nm bandwidth, as more light passes through the sample with wider slits) but that the sharp peak at 210 nm might show some flattening. In practice, however, on the Warwick J-715 instrument when these spectra were collected, it is apparent from the overlay of the two enantiomers and more clearly from the *R,R*- plus *S,S*- spectrum (which should be a flat line of zero magnitude), that below 300 nm the instrument performance with 2 nm bandwidth would not be satisfactory for many applications.

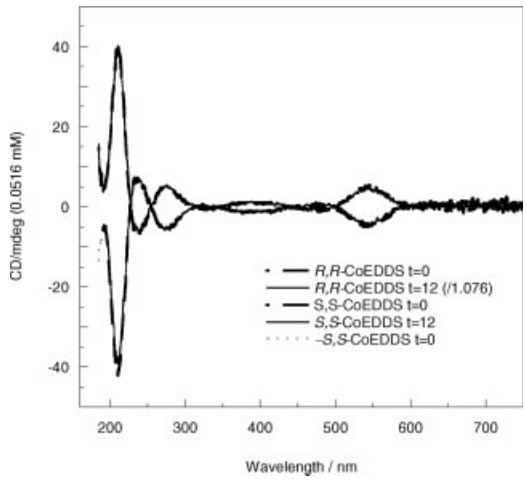

Fig. 6. CD spectra of *R,R*- and *S,S*-Co EDDS (0.56 mM in water, 1 cm pathlength) obtained at time = 0 and time = 12 mo (labeled $t = 0$ and $t = 12$, respectively) and stored on the bench at room temperature in the light between measurements which were using the Jasco J-715 instrument. A water baseline measured on the same day as the sample was subtracted from the initial and final spectra. *R,R*-CoEDDS at $t = 12$ mo has been scaled to account for a slight increase in concentration (as determined from absorbance measurements) of the sample due to evaporation.

CONCLUSIONS

To meet the pressing requirement for better consistency and comparability of circular dichroism measurements, we have set out, in the program reported in this article, to synthesize and characterize a suitable reference material. The synthesis of the two enantiomers of the metal complex $Na[Co(EDDS)]\cdot H_2O$ (EDDS = *N,N*-ethylenediaminedisuccinic acid) has been accomplished and its properties assessed. The stereochemistry of EDDS ensures that the metal complexes adopt only one diastereomeric form, thus the enantiomeric purity of the ligand determines the enantiomeric purity of the final complex. ε and $\Delta\varepsilon$ values have been determined for a number of wavelengths. We have shown that both enantiomers remain stable in solution at room temperature on the bench for at least 12 mo (in contrast to ACS which can often be surprisingly unstable[10]). Greater care does need to be taken to prevent evaporation and we recommend sealing the cuvettes to be used. We have also demonstrated that consistent results can be obtained with these standards (when used according to good practice recommenda-

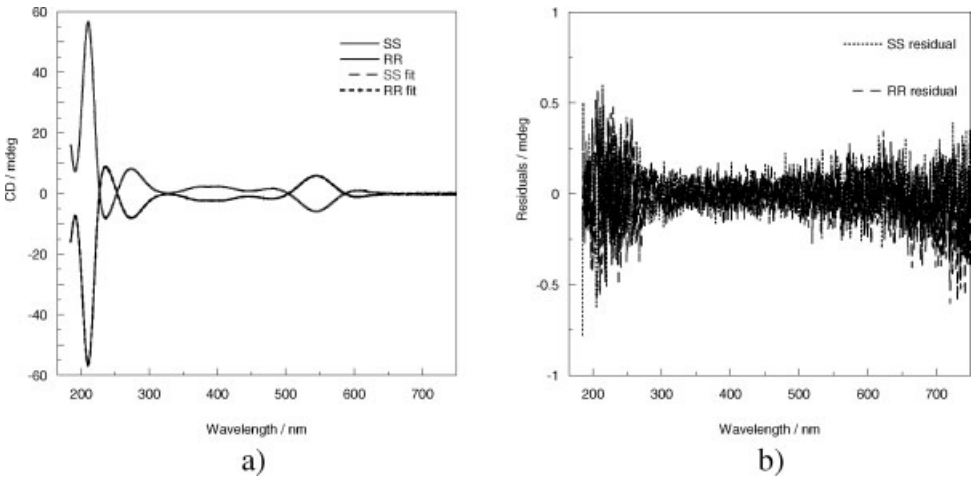

Fig. 7. (**a**) Overlay of NPL experimental CD data for *R,R*- and *S,S*-CoEDDS (0.067 mM) with its fit to a sum of 9 Gaussian curves; (**b**) the fit residuals.

tions)[1,2] between laboratories, particularly between conventional instruments and the synchrotron CD instrument at Aarhus in Denmark. By combining data from different instruments we have produced a standard spectrum from a single solution of concentration ~0.05 mM which can be used as an instrument performance verification tool and to compare the calibration status of CD instruments from 750 to 168 nm. For more critical work, however, higher concentrations could be used for measurements of the longer wavelength peaks.

The broad spectral range of this standard means that it will be useful for a wide range of applications. For example, if we consider only proteins, in conventional CD, the far UV range (typically 180 to 260 nm) is primarily used for protein secondary structure measurements. The main peak of ACS or CSA is at 290.5 nm, which lies outside this range. However, CoEDDS has intense peaks at 210 and 237 nm; it also has a peak at around 179 nm, which is readily accessible on synchrotron CD instruments. The near UV region (typically 240 to 320 nm) provides information on the aromatic side-chains and disulfide bridges in proteins, and can be calibrated using the CoEDDS peak at 270 nm. Further, peaks are found at 370, 410, 480, 545, and 599 nm, extending well into the visible region. In protein work this spectral region is principally used for studies of prosthetic groups such as haems. This wide spectral range should prove to be of similar benefit in other applications.

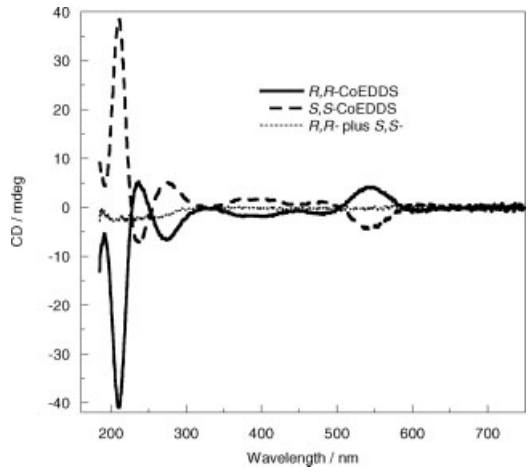

Fig. 8. CD spectra of *R,R*-CoEDDS and *S,S*-CoEDDS (0.056 mM and 1 cm path length) collected with 2 nm bandwidth. Also show is the sum of the two enantiomeric spectra.

The CD spectrum of CoEDDS thus has a number of peaks across the spectral range from the far UV to the visible region, all of which can be measured with a single solution. Furthermore, we noted that the spectrum can be accurately modeled as a summation of nine Gaussian functions. This means that the characteristics of the instrument across the spectral range where virtually all electronic CD measurements are made can be reduced down to a set of a few numbers, which greatly facilitates the comparison across instruments. Indeed, such a set of parameters could be used to "correct" for differences between instrument sensitivity profiles, as previously described by Miles et al.[3] but with the benefit that only one standard is required rather than three. We have therefore developed a protocol for CD wavelength and intensity calibrations using a method for 'automatic' instrument validation. The data from participant 4 and also the Warwick data collected with a 2 nm bandwidth provided a test of the standard material in instrument performance verification. Automated pass/fail testing based on this standard could readily be implemented in software used as part of a quality control regime, for example in industrial applications. Criteria could include a threshold for fit quality, and acceptable ranges for the wavelength and intensity of each peak.

We would suggest the following procedure for the use of the standard:

1. Certified samples of both enantiomers of CoEDDS are distributed to users in sealed cuvettes, together with

appropriate documentation, a protocol for their use, software for analysis of the resulting spectra, and the cuvette baseline. The certification would indicate the cell path length, peak parameters (intensity and wavelength), and recalibration intervals.

2. A spectrum is acquired from each of the two enantiomers of CoEDDS using appropriate parameters, together with baseline spectra (determined from the local instrument baseline and the provided cuvette baseline). If desired, the spectra can be truncated to the range of wavelengths of interest.
3. The spectra are imported into the analysis software, baselines are subtracted, and the curve fitting method described earlier is applied to the spectra.
4. The parameters of the fit are then compared to reference values. If the values fall outside a predefined range, the instrument will be considered to have failed the test. These parameters would include:
   (a) The R^2 (coefficient of determination) of the fit should exceed 0.99. If the value is less than this, it indicates poor quality spectra, for example due to severe wavelength errors, noise, or other distortions. This also serves as a check that the correct spectrum is being used.
   (b) The peak wavelength parameters should fit the reference values to within a defined range, for example ± 1 nm. (This should only be applied to peaks within the measured range. This would also take into account the confidence limits of the fit, and should only be applied to peaks which have positions well constrained by the data.)
   (c) The peak heights should match the reference values to within a predefined limit. For example, for critical work we recommend the value of the 211 nm peak should be correct to within, say 0.5% (in which case the above quoted 2 nm bandwidth spectrum of Figure 8 would 'fail') or less critically to within 5% (in which case it would pass). Again, this criterion would only apply to these peaks within the measured spectral range and that are sufficiently well estimated by the fitting algorithm.
   (d) Implicit within the above criteria is that the two enantiomers will exhibit equal and opposite spectra, confirming that the instrument is performing correctly.
5. The software would then generate a report, including the measured and reference spectra, the results of the curve fitting, and a parameter-by-parameter pass/fail assessment of the spectrum. Finally, the software would generate an overall pass/fail decision and a recommendation for the next action in the event of a failure:
   (a) In the event that the spectra pass on the fit quality and wavelength checks, but fail on the peak intensities, the user will be first recommended to remeasure the spectra, checking all instrument parameters. If this situation still holds, the software will offer the option of generating a calibration correction curve. This curve can be applied to data to make them comparable to data measured on the reference instrument. This option serves to accommodate the scenario where a simple single-wavelength intensity calibration adjustment (as available on most instruments) is insufficient to achieve comparability; for example, where instruments exhibit wavelength-dependent variation in sensitivity.
   (b) If the spectra fail on fit quality or wavelength checks, or if the intensity correction option is not appropriate, the user will be recommended to perform further calibration checks or adjustments, or call in a service engineer.

We believe that this new standard, when used as described above, will greatly improve the reproducibility and comparability of circular dichroism spectroscopy. Although we anticipate most users will want calibration in the UV region, CoEDDS has already been used by physicists at Durham who were building a visible region CD machine and could not find a commercially available standard.[21] The usefulness of this material could be greater still if its absolute, traceable spectral characteristics were determined. It could then be used to disseminate traceable CD to end-user laboratories. However, this will require the development of CD reference instruments by a National Measurement Institute.

ACKNOWLEDGMENTS

The authors are extremely grateful to the participants in the interlaboratory comparison (see Table 1) and Søren Vrønning-Hoffman of Aarhus University who established the beamline for the synchrotron data collection. Funding for this work was provided under project PC4 of the National Measurement System's "Measurements for Biotechnology" Programme and by the EPSRC.

LITERATURE CITED

1. Jones C, Schiffmann D, Knight A, Windsor S. Val-CiD Best Practice Guide: CD spectroscopy for the quality control of biopharmaceuticals; Report nr DQL-AS 008; National Physical Laboratory: Teddington, 2004.
2. Kelly SM, Jess TJ, Price NC. How to study proteins by circular dichroism. Biochimica et Biophysica Acta 2005;1751:119–139.
3. Miles AJ, Wien F, Lees JG, Rodger A, Janes RW, Wallace BA. Calibration and standardisation of synchrotron radiation circular dichroism and conventional circular dichroism spectrophotometers. Spectroscopy 2003;17:653–661.
4. Schiffmann DA, Yardley RE, Butterfield DM, Knight AE, Windsor SA, Jones C. Val-CiD Appendix A: CD spectroscopy: an inter-laboratory study; Report nr DQL-AS 009. National Physical Laboratory; 2004.
5. Takakuwa T, Konno T, Meguro H. A new standard substance for calibration of circular dichroism: ammonium d-10-camphorsulfonate. Anal Sci 1985;1.
6. Chen GC, Yang JT. Two-point calibration of circular dichrometer with d-10-camphorsulfonic acid. Anal Lett 1977;10:1195–1207.
7. Konno T, Meguro H, Tuzimura K. D-Pantolactone as a circular dichroism (CD) calibration. Anal Biochem 1975;67:226–232.
8. McCaffery AJ, Mason SF. The electronic spectra, optical rotatory power and absolute configuration of metal complexes—the dextro-tris (ethylenediamine)cobalt(III) ion. Mol Phys 19636:359–371.

9. Rodger A, Sanders KJ, Hannon MJ, Meistermann I, Parkinson A, Vidler DS, Haworth IS. DNA structure control by polycationic species: polyamines, cobalt ammines, and di-metallo transition metal chelates. Chirality 2000;12:221–236.
10. Jones C, Knight A, Liordes AB, Marrington R, Rodger A, Schiffman DA, Vives OC, Windsor S, Yardley R. Val-CiD Appendix B: The use of chemical calibrants in circular dichroism spectrometers. Report nr DQL-AS 010; National Physical Laboratory: Teddington, 2004.
11. http://www.npl.co.uk/biotech/.
12. http://www.bipm.org/en/si/si_brochure/.
13. Guide to the expression of uncertainty in measurement. Geneva: International Organization for Standardization; 1995.
14. International vocabulary of basic and general terms in metrology. Geneva: International Organization for Standardization; 1993.
15. Miles AJ, Whitmore L, Wallace BA. Spectral magnitude effects on the analyses of secondary structure from circular dichroism spectroscopic data. Protein Sci 2005;14:368–374.
16. Neal JA, Rose NJ. Stereospecific ligands and their complexes. I. A cobalt(III) complex of ethylenediaminedisuccinic. Acid Inorg Chem 1968;7:2408–2412.
17. Jordan WT, Legg JI. Correlation between structure and circular dichroism in ethylenediaminetetraacetatocobaltate (Ii1) and related complexes. Inorg Chem 1974;13:2271–2273.
18. Pavelcik F, Majer J. The crystal and molecular structure of lithium [(*S,S*)-*N,N′*-ethylenediaminedisuccinato]cobaltate(III) trihydrate. Acta Crystallogr B 1978;34:3582–3585.
19. Soldanova J, Pavelcik F, Majer J. Structure of magnesium (*S,S*)-*N,N′*-ethylenediaminedisuccinato-cuprate(II) heptahydrate. Acta Crystallogr B 1981;37:921–923.
20. Kanamori K, Ino K, Maeda H, Miyazaki K, Fukagawa M, Kumada J, Eguchi T, Okamoto K. Relationship between oxo-bridged dimer formation and structure of vanadium (III) amino polycarboxylates. Inorg Chem 1994;33:5547–5554.
21. Vaughan H, Walker L. Private communication. Durham University; 2007.

CHIRALITY 20:1039–1046 (2008)

Single-Molecule Chiroptical Spectroscopy: Fluorescence Excitation of Individual Helicene Molecules in Polymer-Supported Thin-Films

RUTHANNE HASSEY, KEVIN D. McCARTHY, ELLEN SWAIN, DIPANKAR BASAK, DHANDAPANI VENKATARAMAN, AND MICHAEL D. BARNES*

Department of Chemistry, University of Massachusetts-Amherst, Amherst, Massachusetts

Presented at the 11th International Conference on Circular Dichroism, 2007, Groningen, Netherlands

ABSTRACT We present results of fluorescence excitation circular dichroism studies of the chiroptical response of single (bridged triarylamine) helicene molecules immobilized at a polymer interface. We extract directly dissymmetry parameters, and corresponding probability distributions, associated with the single-molecule fluorescence excitation associated with modulation of a circular polarized excitation field for three different excitation wavelengths (405, 440, 457 nm) showing circular dichroism in bulk films. The observed single molecule chiroptical response is anomalously large in comparison with the results of time-dependent density functional calculations, and the observed defocused emission patterns seem to indicate a higher multipole nature to the transition probed. Our results provide new insights into chiroptical properties of chiral fluorophores that are hidden under the extensive averaging associated with conventional chiroptical probes. *Chirality 20:1039–1046, 2008.*

KEY WORDS: single-molecule; fluorescence; thin-films; chiroptical response; rotatory strength tensor

INTRODUCTION

Despite nearly 200 yr of experimental investigation of the dissymmetric interaction of light with chiral materials,[1–3] very little is known experimentally of the individual molecular contributions (and the role of solvation and local dielectric environment) to a collective chiroptical response. Conventional chiroptical probes such as optical rotatory dispersion (ORD) or circular dichroism (CD) measure the cumulative differential response of large numbers of molecules, and are therefore blind to any heterogeneities or fluctuations that might be present at the single-molecule level. Using single-molecule fluorescence imaging techniques,[4] we have investigated the chiroptical response of single helicene molecules immobilized in polymer supported films to probe the distribution of chiroptical dissymmetries in fluorescence excitation. Our preliminary results indicated a broad and nonsymmetric distribution of dissymmetry parameters, suggestive of a strong orientational dependence in the individual molecular response. Here, we provide an in-depth examination of the dissymmetry parameter distributions at three different excitation wavelengths in the spectral region where strong circular dichroism in bulk films is observed. An orientational dependence on the single-molecule chiroptical response is supported here by time-dependent density functional electronic structure calculations yielding the full rotatory strength tensor, followed by numerical integration over the solid angle of our collection objective for several different selected molecular orientations.

The dissymmetry parameter, g, captures both the sign and magnitude of the light-matter interaction with chiral materials.[1,5] In CD measurements, g is quantified by the relation $g = 2\,[\varepsilon_L - \varepsilon_R]/[\varepsilon_L + \varepsilon_R]$, where ε_R and ε_L are the measured absorbances associated with right or left circular polarized excitation, respectively. In Fluorescence-Detected Circular Dichroism (FDCD),[6] the fluorescence intensity is used as a reporter of the differential absorption cross-section for right- and left-circularly polarized excitation. In contrast with absorption or scattering, fluorescence-based probes of molecular chirality, originally reported by Turner and coworkers,[7–9] offer significantly enhanced sensitivity, and have been widely used in a number of interesting applications.[10–13] In particular, the sensitivity of fluorescence signals to molecular conformation and local environment is attractive from the standpoint of recovering detailed information on the heterogeneity of chiroptical response in condensed phase systems. How-

Contract grant sponsor: US Department of Energy Office of Basic Energy Sciences; Contract grant number: #05ER15695
Contract grant sponsors: NSF-Sponsored Center for Hierarchical Manufacturing, NSF-Sponsored MRSEC
Ellen Swain is currently at Department of Chemistry, Northeastern University, Boston, Massachusetts
*Correspondence to: Michael D. Barnes Department of Chemistry, University of Massachusetts-Amherst, Amherst, Massachusetts.
E-mail: mdbarnes@chem.umass.edu
Received for publication 21 November 2007; Accepted 18 March 2008
DOI: 10.1002/chir.20584
Published online 29 May 2008 in Wiley InterScience (www.interscience.wiley.com).

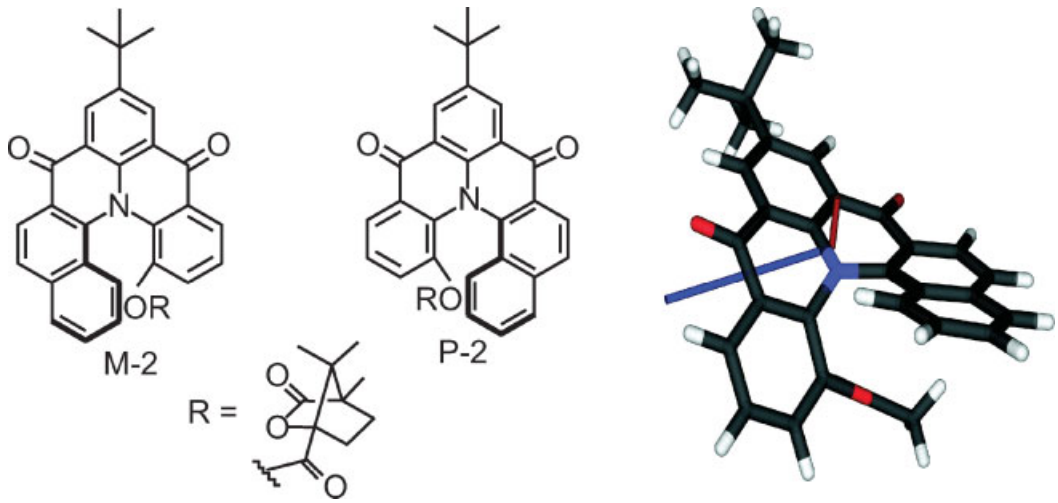

Fig. 1. Chemical structures and optimized 3D representation of M2 helicene. In the simulations, the camphanate moiety was replaced by an acetyl group to allow comparison with previous work.2 The transition electric (blue) and magnetic (red) dipoles, obtained from TD-DFT (B3LYP 6-31*g**) are shown as vectors superimposed on the molecular frame. [Color figure can be viewed in the online issue, which is available at www.interscience.wiley.com.]

ever, it is also well known that immobilized molecules (in thin solid films, for example) may exhibit an apparent dissymmetry in the light-matter interaction that is associated with orientation-dependent electric dipole/electric quadrupole interactions.[6] Such contributions to the chiroptical signature vanish in the limit where the molecule may sample all orientations on the timescale of the measurement, but can be significant even for achiral species with fixed orientations.[14]

In the context of single-molecule fluorescence measurements, our primary interest is in identifying heterogeneities (and fluctuations) in the molecular chiroptical response associated with coupling between the molecule and surrounding host medium. Vaccaro and co-workers have developed novel gas-phase polarimetry methods to probe the effect of solvation and local dielectric environment[15–17] on the cumulative chiroptical response. These results illustrate dramatically how the chiroptical response is tied to solvation and the nature of the local molecular environment. In the condensed phase, Kahr and coworkers have developed circular extinction imaging techniques to probe chiral properties of organic[18] and inorganic crystals[19] and mechanisms for chiral meso- and microstructure evolution in thin-film growth.[20]

In the past several years, single-molecule spectroscopy has emerged as a powerful tool to disentangle heterogeneities in complex physical systems.[21,22] For example, many elegant published works on orientational dynamics,[23] spectroscopy of conjugated polymers,[24,25] and quantum dot systems,[26] have shown how a single emitter approach can provide detailed information on the photophysics of complex systems. In the biophysics communities, for example, single molecule spectroscopy has offered fascinating new insights into a multitude of problems including molecular transport, kinetics,[21] and macromolecular structural dynamics.[27] Single-molecule spectroscopy holds the potential to answer important questions such as effects of local environment using different polymer hosts, and fluctuations (and associated timescales) in a single-molecule chiroptical response.

Recently, Venkataraman and Riehl demonstrated the synthesis and bulk chiroptical characterization of bridged triarylamine helicenes (Fig. 1B) where a specific-handedness in the molecular frame is enforced by the presence of a camphanate group at the indicated position.[28] A weak dissymmetry in the circular polarized luminescence ($|g_{lum}| \approx 0.001$) was observed from solution-phase samples of these species,[28] which was similar in magnitude and sign to the circular dichroism at the same excitation wavelengths. Our approach here was to use ultradilute thin polymer films doped with helicenes to image the dichroic response of a single molecule using fluorescence-excitation. By modulating the circular polarization of the excitation field, we were able to record the fluorescence intensity as a function of input (Right/Left) circular polarization, thus allowing direct access to the dissymmetry (in fluorescence excitation) from a single molecule. From sets of several hundred different single-molecule measurements, we were able to construct probability distributions of the single-molecule dissymmetry parameters for three different excitation wavelengths in the lowest energy electronic transitions for these species.

EXPERIMENTAL

Figure 1 shows structural schematics of the M2/P2 helicenes, and a 3D structure adapted from crystal structure determination. The molecules were synthesized using previously reported procedures.[29] The pure M- and P-type diastereomers of helicenes (as verified by ^{1}H NMR) were derivatized with a camphanate moiety to sterically enforce a specific chirality.[28]

Figure 2 shows a schematic of our experimental apparatus, along with bulk absorption and emission spectra indi-

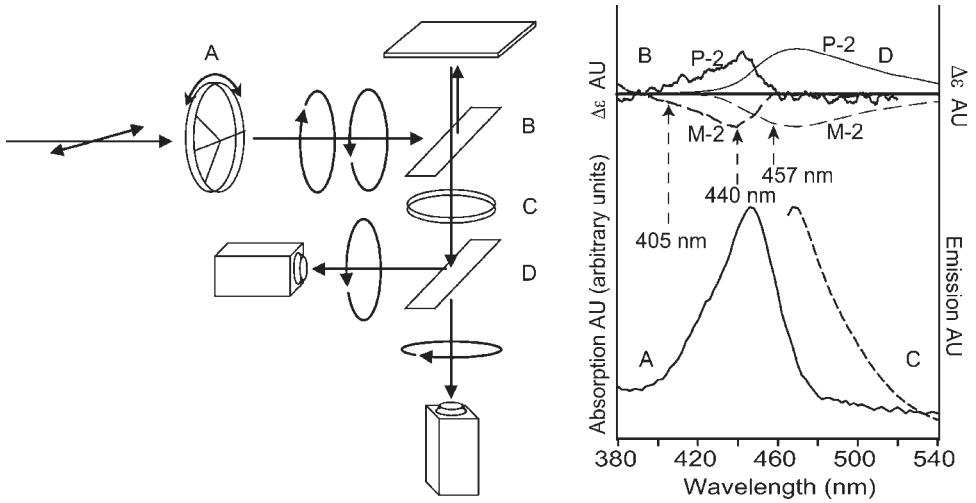

Fig. 2. (Left) Experimental setup for single-molecule fluorescence excitation measurements. (**A**) Quarter waveplate Melles Griot (**B**) Dichroic 2027 DRLP Omega (**C**) 460 nm or 480 nm long pass filter Omega. (**D**) Combined sheet polarizer and quarter waveplate. (Right) Bulk solid state absorption (A), CD (B), and emission (C) of M2/P2 helicene. CPL (D) adapted from Field et al. 1 Solid (dashed) P2 (M2) Spectral positions of (fixed-wavelength) laser sources indicated with arrows.

cating the spectral positions of our excitation sources and fluorescence integration. Our experimental design used an epi-illumination configuration on a Nikon TE300 microscope with 1.4 N.A. objective. Right- or left-hand circularly polarized light from a CW Ar^+ ion laser (457 nm; ≈100 μW nominal power) was delivered to the sample by orienting a multi-order quarter waveplate (QWP) on a rotation stage at $+/-$ 45° with respect to the (horizontal) input polarization axis. Care was taken to minimize the ellipticity of in the input polarization; typical purity of circular polarization (probed by retroreflecting the beam at the sample plane) was determined to be >98%. We acquired 5–10 sequential CCD camera exposures (Roper Scientific PhotonMax) for each QWP orientation. Individual frame exposure times were set to be between 1 and 2 sec, which averaged out most of the short-time (blinking) instabilities in the fluorescence and yielded higher signal-to-noise ratio in the fluorescence image. Only molecules with sufficient photostability to survive at least 1.5 polarization rotation cycles (e.g., L-R-L) were considered. For molecules with longer photochemical survival time, we were able to assess any cycle-to-cycle changes in the dissymmetry within the experimental observation time.

In the fluorescence-excitation measurements, three different fixed-wavelength lasers were used as excitation sources within the lowest electronic absorption band where bulk solution and solid film CD for these molecules is observed. Figure 2 (Right) shows the ensemble solid-film CD spectra for M2 and P2 helicenes in Zeonex®, and the locations of the 405, 440, and 457 nm laser lines used for excitation. Solutions of the two diastereomers were dissolved in semiconductor-grade cyclohexane, and diluted to nominal concentrations of 10^{-11} M; film-based samples were prepared by drop-casting ≈200 μl of the ultradilute solution onto a thin polycycloolefin (Zeonex) polymer film. We find that the photochemical stability of the helicenes is significantly enhanced by the use of a Zeonex supporting film over clean glass.

RESULTS

Defocused Radiation Patterns from Single Helicene Molecules

Spatial intensity patterns obtained via defocusing is a well established tool in single-molecule spectroscopy to probe orientational dynamics in condensed phase[23,30] and self-assembly on surfaces.[25] The diffraction pattern induced by the defocusing reveals the underlying "antenna" characteristics of the emitter; for a molecular system with emission wavelength 690 nm and a single linear transition dipole oriented in the *x-y* plane, these patterns appear as "cat's eye" like patterns at smaller defocus (approximately −300 to −100 nm) and as bi-lobed patterns at defocus values ∼1 μm. In contrast, multi-chromophoric sources such as dye-doped spheres yield circularly symmetric Airy spatial intensity patterns. Recently, this technique has been applied to quantum dot luminescence to explore the nature of the optical transition moments in quasi-spherical nano-confined systems.[31–33]

The defocused helicene images shown in Figure 3 (panels A–F) are similar to numerically predicted point dipole radiation patterns but with some subtle and perhaps important differences in image symmetry. While theory predicts that a linear 1-d dipole emission pattern will always possess a line of bilateral symmetry, we can see that the experimental images show a pronounced breaking of this symmetry. Panels G and H illustrate results of our numerical simulations (extending earlier work[34,35]) in which two radiating dipoles at different orientations and with a relative phase difference produce defocused images that lack the clear bilateral symmetry of a single dipole. Simulations of the defocused image of such a source is

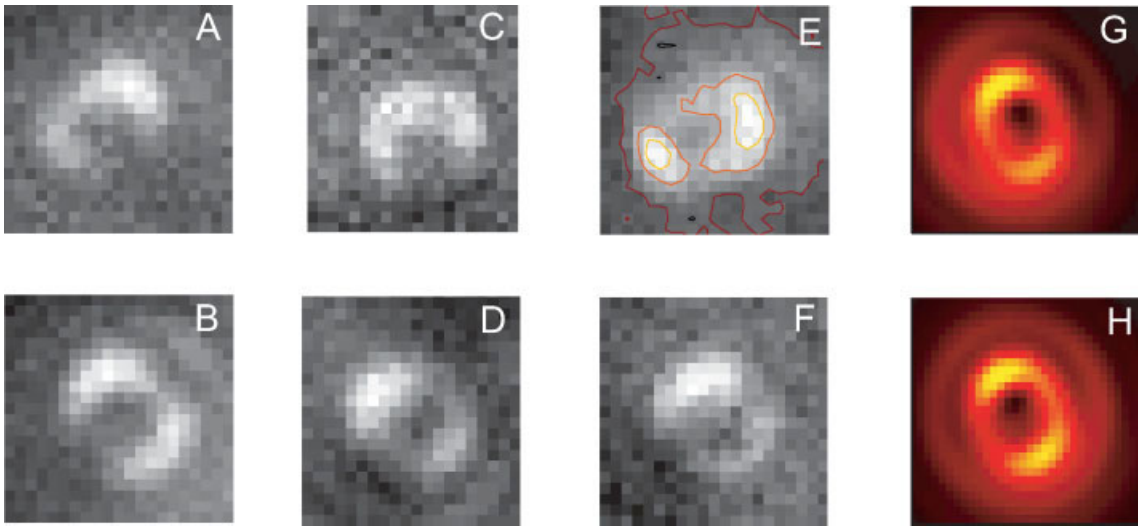

Fig. 3. Panels A–F: Defocused fluorescence images from (different) single M2 molecules using right circular excitation. The contours on E emphasize the asymmetry of the emission pattern. Panels G and H depict simulated defocused images of two noncoplanar dipoles with a relative phase difference, to illustrate the effects of a slight elliptical polarization of the fluorescence emission. [Color figure can be viewed in the online issue, which is available at www.interscience.wiley.com.]

intended as a crude approximation to a higher order multipole source, and is motivated by the large dissymmetry values observed in the individual helicene measurements. We speculate that the complexities of the local molecular environment may serve to enhance the higher multipole transition matrix elements, resulting in larger dissymmetries and a somewhat distorted radiation pattern. Ongoing experimental and theoretical investigations seek to address these possibilities.

Fluorescence Excitation of Single Helicene Molecules

Figure 4 shows representative fluorescence intensity traces from the M2 and P2 helicenes under excitation with right- and left-circularly polarized laser radiation. In these examples, the sample is illuminated with alternating right and left-circular polarized laser radiation every 10 frames, with an integration time of 2 sec per frame. The dissymmetry factor, g, in the single-molecule fluorescence excitation signal was defined as $2\,[(I_L - I_R)/(I_L + I_R)]$ where I_L, I_R are the measured fluorescence intensities associated with left or right circularly polarized excitation, respectively.[36,37] While some variations in g are observed within a given single-molecule intensity trajectory, the gross value of g appears to be well defined for a given molecule during the measurement duration suggesting that a particular single-molecule g-factor is determined primarily by a predominantly static orientation or local environment.

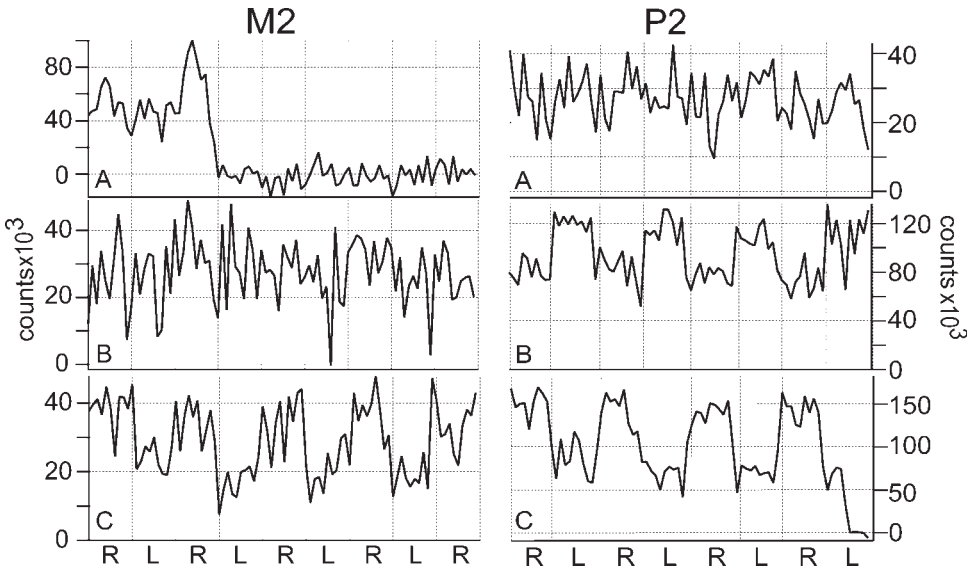

Fig. 4. Fluorescence intensity trajectories from different selected M2 and P2 molecules during FECD measurements. Here a 2-second exposure time was used, rotating between right and left circular polarized excitation every 10 frames.

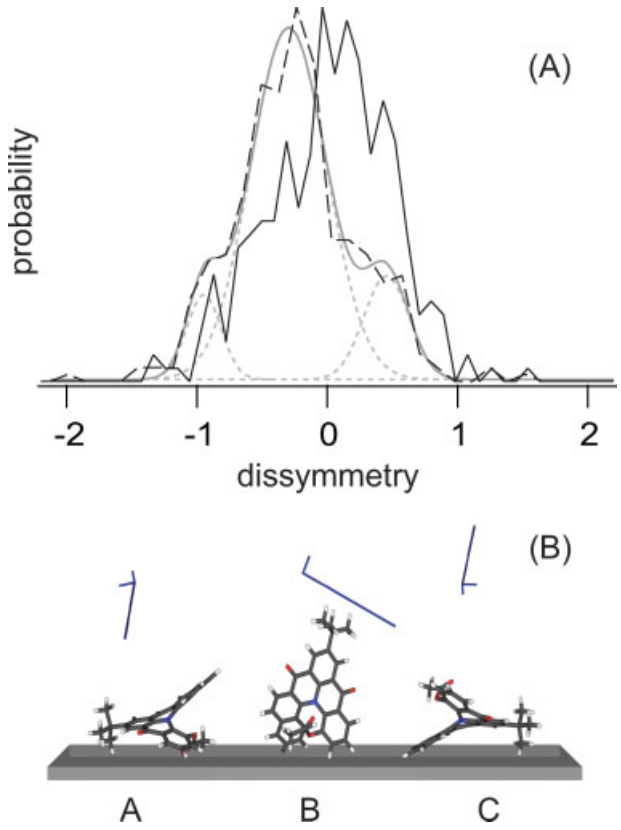

Fig. 5. Normalized histograms of FECD dissymmetry parameters determined from single M-2 (dashed) and P-2 (solid) fluorescence measurements. The solid gray curve is a fit of three Gaussians to the M-2 dissymmetry histogram data. The lower graphic illustrates three different molecule orientations on a surface along with relative orientations of the transition electric dipole components. [Color figure can be viewed in the online issue, which is available at www.interscience.wiley.com.]

Several different control experiments were performed to ensure that experimental artifacts associated with linear polarization bias did not contribute to our results. Our primary control experiment was to probe dissymmetry in fluorescence excitation from 20-nm dye-doped polymer nanospheres. After sonication and dilution, individual fluorescent nanospheres were interrogated by AFM and circular polarized excitation using the same experimental protocol as for the helicenes. In all cases, the distribution of dissymmetry parameters, P(g), obtained for the nanospheres was symmetric about $g = 0$, with a small width $\sigma_g \approx 0.05$. We performed similar measurements on (achiral) linear dipole systems (DiI-18), and obtained results similar to the dye-doped nanospheres in terms of the distribution of apparent dissymmetry parameters, indicating that any linear bias in the experiment was negligible.

Figure 5 shows the distribution of the dissymmetry parameter, g, obtained from single M2 and P2 molecules. The structure of the histograms for M2 and P2 are striking mirror images of each other, with each distribution spanning a significant range of positive and negative g-values for a given diastereomer. Despite the fact that the compounds were isolated as pure diastereomers, we considered the possibility that this component could be associated with the opposite enantiomer formed by partial racemization while in methanol solution or by reaction with condensed water vapor on the film during sample preparation. However, further experiments starting from pure M2 powder under strict anhydrous conditions within a solvent such as cyclohexane showed that distribution remained approximately the same, and therefore not a result of sample degradation.

Analysis of the M2 and P2 dissymmetry parameter distributions are suggestive of three distinct components, with similar amplitudes but opposite signs for the two diastereomers. We originally proposed that these three components are associated with three distinct stable molecular frame orientations at the surface shown in Figure 5B: Camphanate-down, camphanate-up, and "tripod" (chiral axis perpendicular to the optical axis).[4] We speculated that the two in-plane orientations ("camphanate-up" orientation, placing the helicene frame in direct contact with (or solvated by) the polymer film, vs. "camphanate-down") might be distinguishable from each other. To examine this effect

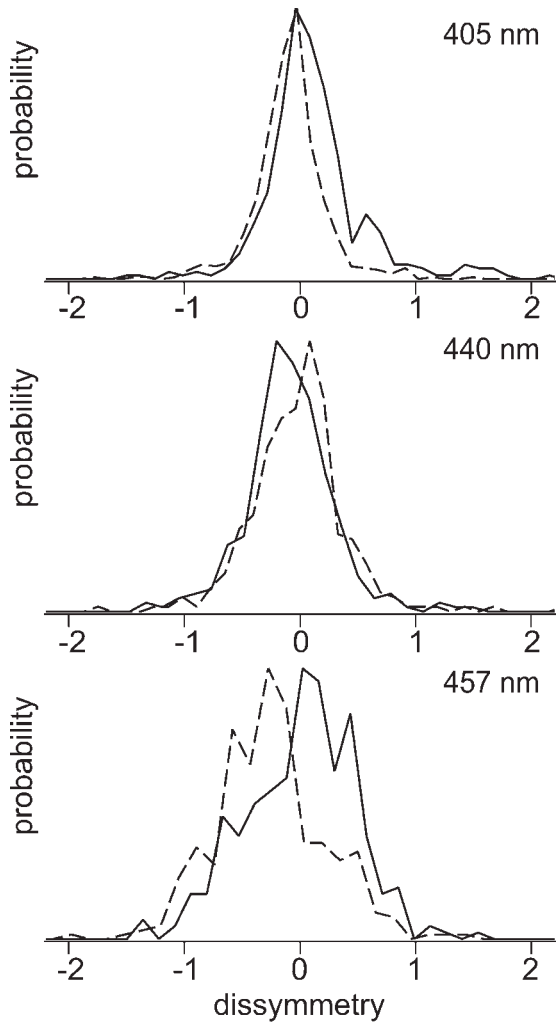

Fig. 6. Normalized P(g) determined from single molecule fluorescence measurements at different excitation wavelengths (M2, dashed; P2, solid).

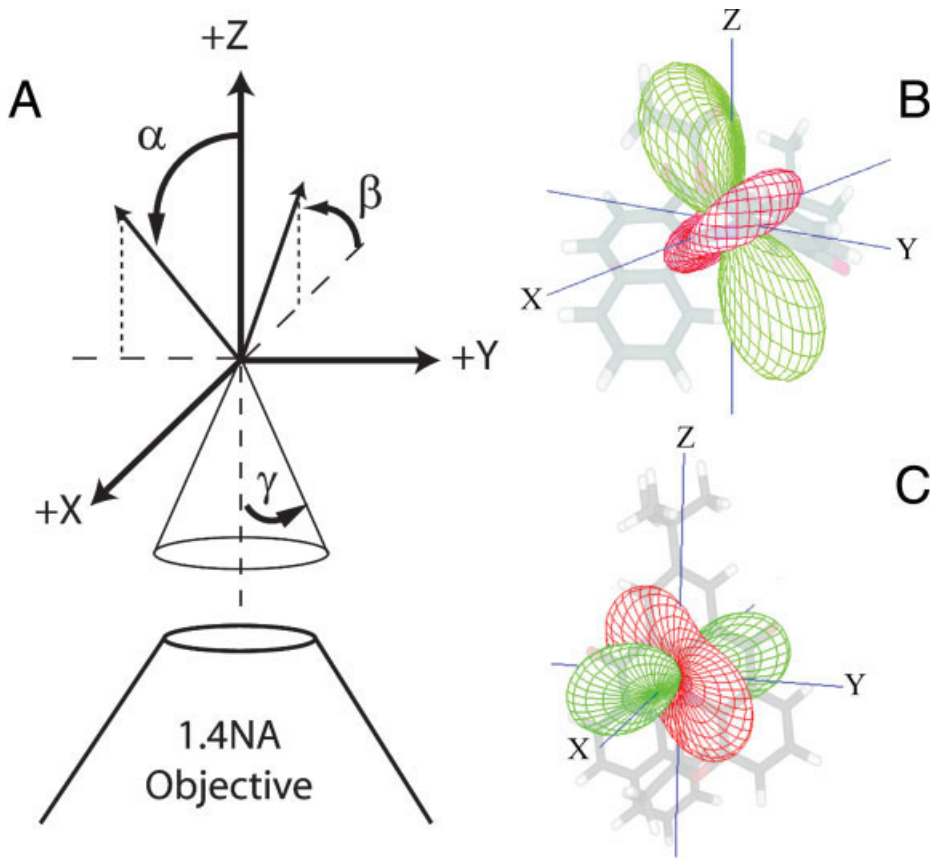

Fig. 7. (**A**) Geometry of the lab frame with respect to the 1.4NA objective. The objective is located at _z. y (≈67°) describes the solid angle of collection. α and β correspond to counter clockwise rotations of the molecule and Γ(θ,φ) about the *x* and *y* axis, respectively. (**B**) M2 overlaid with Γ(θ,φ) in the lab frame with α = 0° and β = 0°. This orientation of M2 and Γ(θ,φ) corresponds to camphanate up. (**C**) M2 and Γ(θ,φ) have been rotated by *F* = 90° corresponding to the tripod orientation. The green and red in the plots of Γ(θ,φ) corresponds to positive and negative values, respectively. [Color figure can be viewed in the online issue, which is available at www.interscience.wiley.com.]

more closely, we investigated the excitation wavelength dependence of the single-molecule response.

Figure 6 summarizes the results obtained using 405-, 440- and 457-nm excitation wavelengths. Interestingly, the shapes of the distributions are slightly different at each excitation wavelength. At 405 and 457 nm excitation, the signs of the first moments are consistent with bulk CD/CPL measurements, although the magnitudes are significantly larger. However, with 440-nm excitation—the wavelength that generates maximum dichroic response in the bulk—the signs of the first moments of P(*g*) become inverted with respect to the bulk. Normalized P(*g*) determined from single molecule fluorescence measurements at different excitation wavelengths (M2, dashed; P2, solid). The first moments of the distributions were $< g >_{405\ \mathrm{nm}} = -0.03$(M-2), 0.17(P-2); $< g >_{440\ \mathrm{nm}} = 0.03$(M-2), −0.01(P-2); $< g >_{457\ \mathrm{nm}} = -0.18$(M-2), 0.06(P-2). Efforts are currently underway to understand the interplay between orientation with respect to the interface and excitation wavelength, and the resulting measurements of single molecule CD.

Computational Modeling

We performed time-dependent density functional (TDFT) calculations using the B3LYP 6-31*g** basis on the structure of M2 (substituting an acetyl group for the camphanate group for computational convenience).[38,39] From representations of the electronic states involved in the lowest energy optical transition, we determined the components of the rotatory strength tensor, which in turn was used to compute angle-integrated dissymmetry values for a particular molecular orientation. According to Pederson,[40] the dissymmetry in circular dichroism associated with a specific k-vector aligned along an arbitrary direction $\hat{n}$ relative to the chiral axis of the molecule is given by the scalar product:

$$\Gamma_{n0}(\theta,\phi) = \hat{n}\cdot\vec{R}\cdot\hat{n} = \sin^2\theta\left[R_{xx}^{n0}\cos^2\phi + R_{yy}^{n0}\sin^2\phi + \frac{1}{2}\left(R_{xy}^{n0}+R_{yx}^{n0}\right)\sin 2\phi\right] + \sin 2\theta\left[\frac{1}{2}\left(R_{xz}^{n0}+R_{zx}^{n0}\right)\cos\phi + \frac{1}{2}\left(R_{yz}^{n0}+R_{zy}^{n0}\right)\sin\phi\right] + \cos^2\theta R_{zz}^{n0} \quad (1)$$

where θ and φ are spherical polar angles for $\hat{n}$ in the molecular frame. The predicted dissymmetry values are then calculated from the circular dichroism for various orientations, assuming a high numerical aperture for collection of radiation.

TABLE 1. Computed dissymmetry values obtained for M2 by numerical integration of the scalar product, $\Gamma_{n,0}(\theta,\phi)$, over a solid angle with a half angle of $\sim 67^\circ$ corresponding to the collection angle of the 1.4NA objective

Orientation	α	β	Dissymmetry (*g*)
Camph up	300°	0	+0.0021
Camph up	315°	0	+0.0034
Camph up	0°	0	+0.0022
Camph up	45°	0	−0.0026
Tripod	0	90°	−0.0025
Camph down	120°	0	+0.0021
Camph down	135°	0	0.0034
Camph down	180°	0	0.0022
Camph down	225°	0	−0.0026

In Figure 7(B,C) $\Gamma_{n,0}(\theta,\varphi)$ is pictorially displayed by the green/red mesh spherical plot representing positive and negative values (respectively) of the scalar product. Figure 7 represent the camphanate up and tripod orientation of M2 in the lab frame. The dissymmetries for these and other orientations are displayed in Table 1. The total dissymmetry, calculated by integration over 4π steradians, is −0.0016, in agreement with the ensemble value of −0.0010. We note that these values are all much smaller in magnitude than those observed in our measurements, and speculate that the same environmental effects on multipolar transition matrix elements may be responsible.

From Table 1 note the dissymmetry values are the same for camphanate up and down when the molecular frame orientation is the same relative to the objective. As the angle of observation is shifted slightly the dissymmetry calculated for camphanate up and down is observed to be positive or negative. In previous work,[4] we postulated it would be possible to differentiate between camphanate up and down. From an initial look at the dissymmetry values there is no difference between camphanate up and down. Taking into account the effect of the camphanate group on orientation a difference could be predicted. In camphanate up, the molecular frame will orient almost flat on the surface with the chiral axis is almost perpendicular to the surface. In camphanate down, camphanate prevents the molecular frame from orienting flat on the surface so the chiral axis is at an angle to the surface. These differences and contributions of surface interactions may allow distinguishing between camphanate up and down.

The dissymmetry values calculated for each of the orientations support the idea of a discrete set of orientations contributing to the distribution of single molecule dissymmetry values. We stress once again that such a multimodal distribution is unique to fixed orientation molecules, and unlike directionally averaged measurements (i.e., in solution), reflects rotatory strength contributions from not only the magnetic dipolar, but also from the electric quadrupolar properties of the electronic transition.

SUMMARY AND CONCLUSIONS

In summary, we have investigated the chiroptical response of individual helicene molecules immobilized in polymer-supported films. Both short- and long-time fluorescence instabilities (blinking and discrete photobleaching) provide evidence that we are indeed interrogating single-molecules. In addition, the defocused fluorescence images obtained from single-helicene molecules show spatial intensity patterns that appear to be associated with a bi-directional transition moment and are qualitatively different from the well-known patterns associated with linear dipoles. From the single-molecule fluorescence intensity trajectories, we are able to extract dissymmetry parameters, *g*, associated with fluorescence excitation and emission. From these measurements, we are able to construct probability distributions P(*g*) as a function of excitation wavelength. Interestingly, P(*g*) spans a relatively large range of positive *and* negative *g* values for a given diastereomer, at each of the excitation wavelengths studied. We also observe that the sign of the first moment of P(*g*)—consistent with bulk measurements at the red (457 nm) and blue (405 nm) edge of the specific electronic transition being probed—is inverted with respect to the ensemble when excited at 440 nm. These results have provided a new insight into the asymmetric light-matter interaction with chiral organic molecules, and we hope this will spark further experimental and theoretical efforts in the study of individual chiral fluorophores.

ACKNOWLEDGMENTS

The authors thank Karl Hammond, Justin Fermann, and Scott Auerbach for their assistance with the computational modeling. The authors thank Dr. James Cheeseman for helpful discussions.

REFERENCES

1. Berova N, Nakanishi K, Woody RW. Circular dichroism: principles and applications. New York: Wiley-VCH; 2000.
2. Berova N, Di Bari L, Pescitelli G. Application of electronic circular dichroism in configurational and conformational analysis of organic compounds. Chem Soc Rev 2007;36:914–931.
3. Polavarapu PL. Renaissance in chiroptical spectroscopic methods for molecular structure determination. Chem Rec 2007;7:125–136.
4. Hassey R, Swain EJ, Hammer NI, Venkataraman D, Barnes MD. Probing the chiroptical response of a single molecule. Science 2006;314:1437–1439.
5. Barron LD. Molecular light scattering and optical activity. New York: Cambridge University Press; 2004.
6. Tinoco I, Ehrenberg B, Steinberg IZ. Fluorescence detected circular-dichroism and circular-polarization of luminescence in rigid media—direction dependent optical-activity obtained by photoselection. J Chem Phys 1977;66:916–920.
7. Turner DH, Tinoco I, Maestre M. Fluorescence detected circular-dichroism. J Am Chem Soc 1974;96:4340–4342.
8. Tinoco I, Turner DH. Fluorescence detected circular-dichroism—theory. J Am Chem Soc 1976;98:6453–6456.
9. Lobenstine EW, Turner DH. Photo-selected fluorescence detected circular-dichroism. J Am Chem Soc 1979;101:2205–2207.
10. Tanaka K, Pescitelli G, Nakanishi K, Berova N. Fluorescence detected exciton coupled circular dichroism: development of new fluorescent reporter groups for structural studies. Monatsh Chem 2005;136:367–395.
11. Riehl JP, Richardson FS. General theory of circularly polarized emission and magnetic circularly polarized emission from molecular systems. J Chem Phys 1976;65:1011–1021.

12. Gunde KE, Richardson FS. Fluorescence-detected 2-photon circular-dichroism of $Gd^{3}+$ in trigonal $Na_3[Gd(C_4H_4O_5)_3]$ $2NaClO_4$ $6H_2O$. Chem Phys 1995;194:195–206.
13. Muller G, Muller FC, Maupin CL, Riehl JP. The measurement of the fluorescence detected circular dichroism (FDCD) from a chiral Eu(III) system. Chem Commun 2005;28:3615–3617.
14. Isborn C, Claborn K, Kahr B. The optical rotatory power of water. J Phys Chem A 2007;111:7800–7804.
15. Muller T, Wiberg KB, Vaccaro PH. Cavity ring-down polarimetry (CRDP): a new scheme for probing circular birefringence and circular dichroism in the gas phase. J Phys Chem A 2000;104:5959–5968.
16. Sfeir MY, Beetz T, Wang F, Huang LM, Huang XMH, Huang MY, Hone J, O'Brien S, Misewich JA, Heinz TF, Wu LJ, Zhu YM, Brus LE. Optical spectroscopy of individual single-walled carbon nanotubes of defined chiral structure. Science 2006;312:554–556.
17. Fasel R, Parschau M, Ernst KH. Amplification of chirality in two-dimensional enantiomorphous lattices. Nature 2006;439:449–452.
18. Claborn K, Puklin-Faucher E, Kurimoto M, Kaminsky W, Kahr B. Circular dichroism imaging microscopy: application to enantiomorphous twinning in biaxial crystals of 1,8-dihydroxyanthraquinone. J Am Chem Soc 2003;125:14825–14831.
19. Kaminsky W, Claborn K, Kahr B. Polarimetric imaging of crystals. Chem Soc Rev 2004;33:514–525.
20. Gunn E, Sours R, Benedict JB, Kaminsky W, Kahr B. Mesoscale chiroptics of rhythmic precipitates. J Am Chem Soc 2006;128:14234–14235.
21. Xie XS. Single-molecule approach to dispersed kinetics and dynamic disorder: probing conformational fluctuation and enzymatic dynamics. J Chem Phys 2002;117:11024–11032.
22. Moerner WE, Fromm DP. Methods of single-molecule fluorescence spectroscopy and microscopy. Rev Sci Instrum 2003;74:3597–3619.
23. Bartko AP, Xu KW, Dickson RM. Three-dimensional single molecule rotational diffusion in glassy state polymer films. Phys Rev Lett 2002;89:026101.
24. Yu ZH, Barbara PF. Low-temperature single-molecule spectroscopy of MEH-PPV conjugated polymer molecules. J Phys Chem B 2004;108:11321–11326.
25. Kumar P, Mehta A, Dadmun MD, Zheng J, Peyser L, Bartko AP, Dickson RM, Thundat T, Sumpter BG, Noid DW, Barnes MD. Narrow-bandwidth spontaneous luminescence from oriented semiconducting polymer nanostructures. Phys Chem B 2003;107: 6252–6257.
26. Nirmal M, Dabbousi BO, Bawendi MG, Macklin JJ, Trautman JK, Harris TD, Brus LE. Fluorescence intermittency in single cadmium selenide nanocrystals. Nature 1996;383:802–804.
27. Michalet X, Weiss S, Jager M. Single-molecule fluorescence studies of protein folding and conformational dynamics. Chem Rev 2006;106:1785–1813.
28. Field JE, Muller G, Riehl JP, Venkataraman D. Circularly polarized luminescence from bridged triarylamine helicenes. J Am Chem Soc 2003;125:11808–11809.
29. Field JE, Hill TJ, Venkataraman D. Bridged triarylamines: a new class of heterohelicenes. J Org Chem 2003;68:6071–6078.
30. Bartko AP, Dickson RM. Three-dimensional orientations of polymer-bound single molecules. J Phys Chem B 1999;103:3053–3056.
31. Schuster R, Barth M, Gruber A, Cichos F. Defocused wide field fluorescence imaging of single CdSe/ZnS quantum dots. Chem Phys Lett 2005;413:280–283.
32. Patra D, Gregor I, Enderlein J, Sauer M. Defocused imaging of quantum-dot angular distribution of radiation. Appl Phys Lett 2005;87:101–103.
33. Brookman X, Coolen L, Hermier JP, Dahan M. Emission properties of single CdSe/ZnS quantum dots close to a dielectric interface. Chem Phys 2005;318:91–98.
34. Hellen EH, Axelrod D. Fluorescence emission at dielectric and metal-film interfaces. J Opt Soc Am B Opt Phys 1987;4:337–350.
35. Bohmer M, Enderlein J. Orientation imaging of single molecules by wide-field epifluorescence microscopy. J Opt Soc Am B Opt Phys 2003;20:554–559.
36. Riehl JP, Richardson FS. Circularly polarized luminescence spectroscopy. Chem Rev 1986;86:1–16.
37. Richardson FS, Riehl JP. Circularly polarized luminescence spectroscopy. Chem Rev 1977;77:773–792.
38. Spassova M, Asselberghs I, Verbiest T, Clays K, Botek E, Champagne B. Theoretical investigation on bridged triarylamine helicenes: UV/visible and circular dichroism spectra. Chem Phys Lett 2007;439:213–218.
39. Frisch MJ, Trucks GW, Schlegel HB, Scuseria GE, Robb MA, Cheeseman JR, Montgomery J, JA, Vreven T, Kudin KN, Burant JC, Dapprich S, Millam JM, Daniels AD, Kudin KN, Strain MC, Farkas O, Tomasi J, Barone V, Cossi M, Cammi R, Mennucci B, Pomelli C, Adamo C, Clifford S, Ochterski J, Petersson GA, Ayala PY, Cui Q, Morokuma K, Salvador P, Dannenberg JJ, Malick DK, Rabuck AD, Raghavachari K, Foresman JB, Cioslowski J, Ortiz JV, Baboul AG, Stefanov BB, Liu G, Liashenko A, Piskorz P, Komaromi I, Gomperts R, Martin RL, Fox DJ, Keith T, Al-Laham MA, Peng CY, Nanayakkara A, Challacombe M, Gill PMW, Johnson B, Chen W, Wong MW, Andres JL, Gonzalez C, Head-Gordon M, Replogle ES, Pople. Gaussian 03 Revision C. 02. Wallingford, CT: Gaussian, Inc.; 2004.
40. Pedersen TB, Hansen AE. Ab-initio calculation and display of the rotatory strength tensor in the random-phase-approximation—method and model studies. Chem Phys Lett 1995;246:1–8.

CHIRALITY 20:1047–1052 (2008)

An Operative Approach to Correct CD Spectra Distortions due to Absorption Flattening

ETTORE CASTIGLIONI,[1,2]* FRANCE LEBON,[2,3]
GIOVANNA LONGHI,[2,3] ROBERTO GANGEMI,[2,3] AND SERGIO ABBATE[2,3]
[1]*JASCO Corporation, Hachioji-Shi, Tokyo, Japan*
[2]*Dipartimento di Scienze Biomediche e Biotecnologie, Università di Brescia, Brescia, Italy*
[3]*CNISM, Consorzio Nazionale Interuniversitario Scienze Fisiche della Materia, Roma, Italy*

Presented at the 11th International Conference on Circular Dichroism, 2007, Groningen, Netherlands

ABSTRACT We discuss the influence of absorption flattening (AF) on CD spectra, aiming at finding a simple way to compensate the induced distortions. A simple algebraic formalism is proposed based on an unconventional measuring approach, which makes use of a commercial unit. Validation of the proposed compensation method for AF is conducted not only on the already studied CD Vis spectral region of a Co chiral complex with the use of an AF emulator, but also on the far UV CD spectra of poly-L-glutamic acid suspensions with different turbidity levels. Comparison with some correction factors proposed in the literature is presented. *Chirality 20:1047–1052, 2008.*

KEY WORDS: circular dichroism; absorption flattening; poly-L-(glutamic acid); PGA

INTRODUCTION

We have recently devoted some attention to the effect on CD spectra of absorption flattening (AF), also known as Duysens effect.[1] In a previous paper,[2] we proposed a simple sampling emulator and, also by considering spectra simulations from ideal solution data, we showed that AF may induce distortions and spectral wavelength shifts in the CD spectra (particularly when CD and absorption maxima are not at the same wavelength). In a subsequent paper,[3] we showed how AF induces band splittings in the presence of excitonic features.

In our approach, solvent/buffer absorption was not taken into account and was assumed to give no contribution to the CD signal distortion, which originates only from the changes that AF induces in the sample absorption spectrum. The key open aspect is now how to correct for this effect, particularly in the UV region. In this article, we extend our previous formalism[2,3] including the possibility of solvent absorption and we intend also to define an operative "tell-me-what-to-do" protocol in terms of a simple measuring approach and postrun data treatment that allows one to estimate and to compensate AF effects even in far UV region.

We have first tested the new approach in the Vis region with Λ-$Co(en)_3Cl_3$ complex using our AF emulator[2], and then we have applied it to the far UV region for poly-L-glutamic acid (PGA), as originally proposed by Urry et al.[4,5]: needless to say, we think that the real interest and needs of adequately dealing with CD data and of correctly managing the AF artifacts is in the latter type of example.

THE ALGEBRAIC FORMALISMS

Commercial CD spectrometers are based on photoelastic modulators. The CD spectrum, which is defined as the difference in absorbance of left circularly polarized light and right circularly polarized light, may be expressed also in terms of intensities, using the fact that the difference in intensities I_L and I_R is much smaller than the corresponding sum:

$$CD = (I_L - I_R)/(I_L + I_R) \approx AC/DC$$

Usually $(I_L - I_R)$ is three to five orders of magnitude smaller than $(I_L + I_R)$. This imposes a different strategy for the measurement of the two quantities: the former quantity, appearing in the numerator of the above equation, is proportional to a modulated signal from a lock-in amplifier (AC) connected to the photoelastic modulator (PEM); the latter quantity, appearing in the denominator, corresponds to a DC signal. Normally only the AC component is measured, since the DC component is kept constant by dynode feedback circuitry of the photomultiplier tube (PM). In the following formalisms we assume, on the opposite, that the voltage on the PM is kept constant so that the DC value will change during the experiment.

Using an extension of the same approach as previously published,[2] we have

$$CD_{Exp}(\lambda) = \{f/[AC_{Sam}(\lambda, f) + AC_{Sol}(\lambda)] + (1-f)AC_{Sol}(\lambda)\}/DC_{Exp}(\lambda) \quad (1)$$

*Correspondence to: Ettore Castiglioni, JASCO Corporation, Hachioji-Shi, Tokyo, Japan. E-mail: ettore.castiglioni@jasco-europe.com
Received for publication 13 November 2007; Accepted 10 June 2008
DOI: 10.1002/chir.20639
Published online 24 July 2008 in Wiley InterScience (www.interscience.wiley.com).

where f is the ratio of the volume in which the sample is dissolved with respect to the total volume of the solution; in other words, it is the fraction of the light beam incident onto the (more concentrated) sample with respect to the total light beam; CD_{Exp} is the expected CD signal of the whole system (solvent + sample) when AF is present; $AC_{Sam}(f)$ is the AC component of just the sample in the conditions of AF; AC_{Sol} is the AC component of the solvent (or better solvent + cell windows); DC_{Exp} is the expected DC component of the whole system (solvent + sample) when AF is present.

In addition, we introduce, CD_{Sam}, the CD of the homogeneous solution, i.e. when $f = 1$; AC_{Sam}, the AC component in the homogeneous solution, i.e. when $f = 1$; $DC_{Sam+Sol}$, the DC component (sample + solvent together) in the homogeneous solution, i.e. when $f = 1$.

We now assume that $AC_{Sol}(\lambda)$ is zero, since solvent and cell are not optically active and in addition we consider that

$$AC_{Sam}(\lambda,f) = (1/f)AC_{Sam}(\lambda)$$

This allows to take into account the concentration effect, since in the inhomogeneous solution the local sample concentration is higher by a factor $1/f$ with respect to the situation of the homogeneous one. So, from eq. 1, one has

$$CD_{Exp}(\lambda) = AC_{Sam}(\lambda)/DC_{Exp}(\lambda) \qquad (1')$$

We now take into account that

$$CD_{Sam}(\lambda) = AC_{Sam}(\lambda)/DC_{Sam+Sol}(\lambda)$$

which means that CD of ideal solution is indeed simply the ratio of the lock-in amplifier output by the DC level coming from the sample dissolved in the solvent and filled in a cell. We can now rewrite (1′) as

$$CD_{Exp}(\lambda) = CD_{Sam}(\lambda)DC_{Sam+Sol}(\lambda)/DC_{Exp}(\lambda) \qquad (1'')$$

We could go further, as done in Ref. 2, and take into account that DC levels are proportional to transmittance (rather than absorbance), but we regard it as unnecessary, since our measurement strategy here is based on eq. 1″. The latter equation indicates that, to obtain a CD signal cleaned of AF, i.e. in order to obtain $CD_{Sam}(\lambda)$, we can correct the experimental distorted spectrum $CD_{Exp}(\lambda)$ simply dividing it by $DC_{Sam+Sol}(\lambda)/DC_{Exp}(\lambda)$. We call this ratio $Q_f(\lambda)$, so

$$CD_{Sam}(\lambda) = CD_{Exp}(\lambda)/Q_f(\lambda) \qquad (1''')$$

$Q_f(\lambda)$ is the ratio of the DC spectrum of the homogeneous solution versus the one obtained in AF conditions.

MATERIALS AND METHODS

Λ-Co(en)$_3$Cl$_3$ complex[6] was kindly provided by Prof. Sven E. Harnung of University of Copenhagen, different aqueous solutions (2.85, 1.95, 1.45, 1.14×10^{-3} M) were measured in standard (10-mm aperture) and in semimicro (4-mm aperture with clear walls) 10-mm path length rectangular quartz cells at room temperature.

PGA was purchased from Sigma-Aldrich and used without further purification. A PGA solution of 4 mg/ml was diluted with bi-distillated water and HCl 0.1N was added to reach pH 2.45. The final concentration of the PGA solution was 2.05 mg/ml and the spectra were taken on the freshly prepared solution. In this condition, the solution is already turbid and very probably already giving AF effects. Spectra were obtained in a 0.1-mm path cylindrical Hellma cell at room temperature on the prepared solution as it was and after repeated time-controlled sonications to increase turbidity (and AF effects).

A JASCO J-815SE spectrometer has been used with the following parameters:

- For the Co complex: SBW = 2 nm, integration time = 0.25 s, scanning speed = 100 nm/min, single scan with no further smoothing.
- For PGA: SBW = 1 nm, integration time = 1 s, scanning speed = 100 nm/min, taking the average of 5 runs with no further smoothing.

In the PGA case, the sample was placed on the side of the sample compartment as close as possible to the PM tube active surface to increase solid angle sampling viewing geometry[7] and to collect as much forward scattering as possible.

In contrast to common practice, thanks to the built-in facility of the instrument, spectra were acquired keeping the PM tube high voltage constant, at 200 and 260 V for the Vis and the UV regions, respectively, in order not to saturate the preamplifier at any wavelength.

We have collected the following in the same run: AC data (i.e., the lock-in amplifier output) and DC data.

Alternatively, after verifying that the PM tube dark current was low enough not to influence the data directly, one may collect AC/DC data (i.e., the calibrated CD data) and DC.

It is mentioned that the measuring approach adopted here for pedagogical reasons is used in NIR-CD and in VCD dispersive or FTIR instruments when dealing with fixed gain detectors (such as Si, InGaAs, InSb, MCT, . . .).

Results for the Cobalt Complex Using AF Emulator

Figure 1 (left) shows the CD molar ellipticity spectra obtained at the different concentrations in the 4-mm aperture cell compared to the one obtained in the standard one (10-mm wide). As predicted by AF theory,[2] distortions and wavelength red shift are observed to increase with the sample concentration.

Individual $Q_f(\lambda)$ were calculated for each concentration by the ratio of the two DC(λ) spectra obtained in the 10- and 4-mm wide cells, respectively, for the same solution. However, since the same sample concentration was used in the two cells, the relationship

$$AC_{Sam}(\lambda,f) = (1/f)AC_{sam}(\lambda)$$

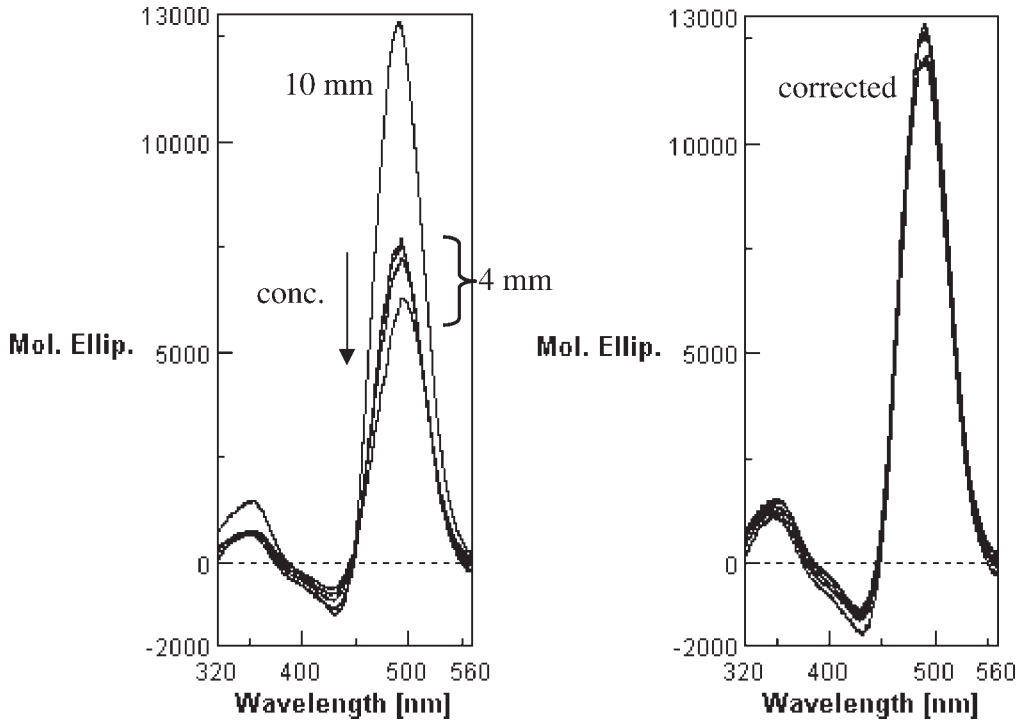

Fig. 1. Left: CD spectra of Λ-Co(en)$_3$Cl$_3$ complex in 4-mm aperture cell at different concentrations when compared with the one in standard 10-mm aperture cell. Right: same as left, but corrected by f and $Q_f(\lambda)$ factors (see text).

does not apply. Instead one has

$$AC_{Sam}(\lambda,f) = AC_{Sam}(\lambda)$$

And, as a consequence, eq. 1′ should be substituted by

$$CD_{Exp}(\lambda) = fAC_{Sam}(\lambda)/DC_{Exp}(\lambda)$$

Consequently,

$$CD_{Sam}(\lambda) = (1/f)[CD_{Exp}(\lambda)/Q_f(\lambda)] \qquad (1'''')$$

Figure 1 (right) shows the overlay of the same spectra corrected in this way. Using for f the value 0.74 (estimated from the geometric shape of our sampling beam),[2] compensation is proper and the validity of our approach is confirmed. It must be stressed that in normal situation there is no need to introduce f in the calculations, since the formation of a suspension (instead of a homogeneous solution) changes the local concentration in a way very difficult to evaluate, but roughly giving a local concentration inversely proportional to the occupied volume.

Results for PGA

Figure 2 (top) shows the obtained DC spectra of the PGA solution prepared with sonication times of $t = 0$, 30, 45, and 60 sec. On the same panel, we report the spectrum of the empty sample compartment and of the dark. The latter was obtained by inserting a screen, which traps the light before the PM tube and may be very effective in subtracting dark current of the PM tube or whatever DC offset signal from the preamplifier. This "dark" signal, when of appreciable amplitude, should be subtracted from regular DC spectra to improve accuracy.

It is noticed that while operating the CD spectrometer in the usual procedure (constant DC level by automatic change of the PM tube high voltage) there is no way to compensate the "dark." In addition, dark current of PM tubes is strongly related to the high voltage applied, so a built-in source of error may be present, when running spectra in normal procedure. In our case, the dark signal was measured as less than 0.86 mV, many times smaller than the minimum DC level from our samples, so there has been no need of subtraction.

Figure 2 (bottom) shows the AC spectra for samples obtained with sonication times of $t = 0$, 30, 45, 60 sec.

Figure 3 (top) shows the four CD spectra (obtained by the AC/DC operation); please remember they could be obtained directly (as was done for the Co complex case) using the instrument software. The presentation of the data looks more familiar to the routine CD utilizer and the AF effect, depressing more and more the CD signal for longer sonication times, is quite clear.

Figure 3 (bottom) presents the overlay of the starting spectra ($t = 0$) with the ones after 30, 45, and 60 sec sonication divided by $Q_f(\lambda)$. Matching is quite fair, even though not perfect; in addition to AF, differential scatter is present in this case as pointed out previously.[4,5]

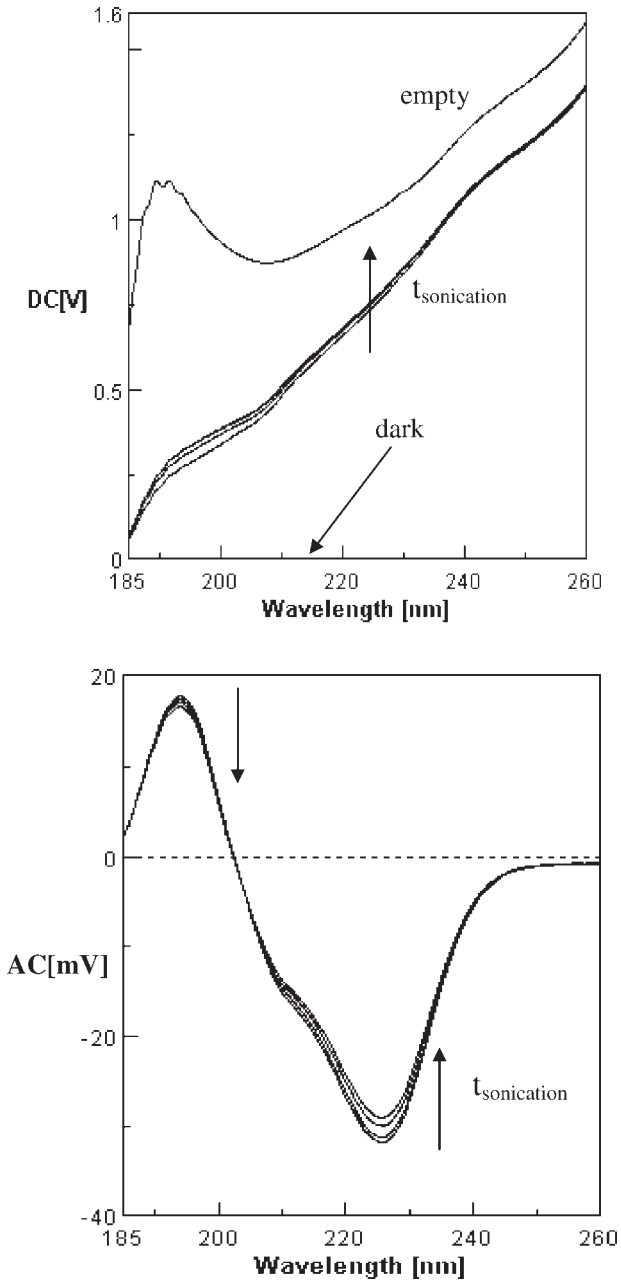

Fig. 2. Top: DC spectra at constant high voltage on PM tube of empty sample compartment, PGA solution at $t = 0$, 30, 45, 60 sec sonication times and dark (which is coincident with the wavelength axis). Bottom: AC spectra of PGA solution at $t = 0$, 30, 45, and 60 sec sonication times (PM tube voltage constant).

COMPARISON WITH PREVIOUSLY REPORTED CORRECTION FACTORS

In 1970, Urry et al.[4] proposed a model to correct CD spectra for both AF and scattering effects. They correctly pointed out that AF and scattering distort the absorption spectra in opposite directions: the presence of scattering increases apparent absorption, while AF depresses absorption maxima. Their correction model was based on Q_A and A_S, where Q_A is the Duysens flattening coefficient (ratio between absorption spectra of the suspensions and of the dispersed solution) and A_S is the part of the absorption due to scattered light.

In 1984, Wallace and Mao made a detailed analysis for the case of membrane proteins[8] and concluded that, by using a wide angle collection photomultiplier tube/sample geometry,[7] scattering component may be neglected and

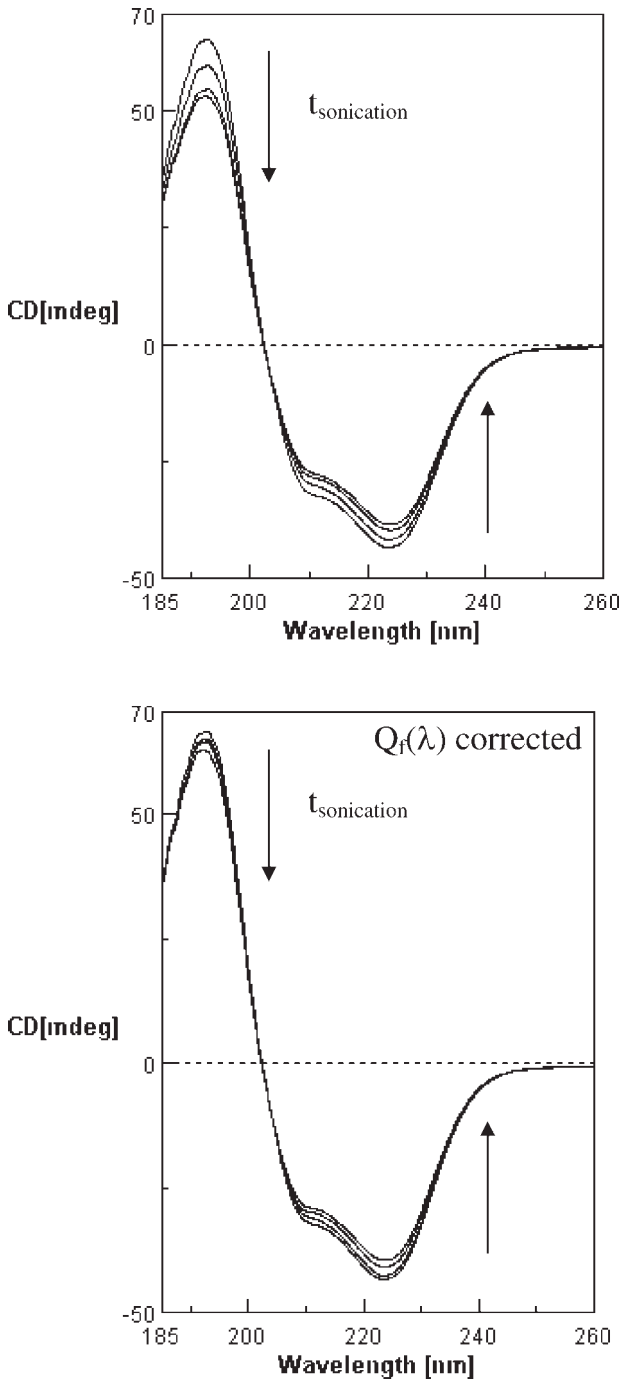

Fig. 3. Top: experimental CD spectra (AC/DC) of PGA solutions at $t = 0$, 30, 45, and 60 sec sonication times. Bottom: same as top, but corrected by $Q_f(\lambda)$ factors.

TABLE 1. Comparison of correction factors Q_A,[4,5] $K_f^{(CD)}$,[8] and Q_f (present approach) at fixed wavelength for the two absorbance values 0.4 and 1

	Outcoming photons						
	f	DC_{exp}	T_{exp}	A_{exp}	Q_A	K_f^{CD}	Q_f
A = 0.4	1	39.8	0.398	0.400	1	1	1
	0.95	5 + 36.03[a]	0.41	0.387	0.967	0.935	0.970
	0.9	10 + 32.35[b]	0.423	0.373	0.932	0.865	0.941
	0.8	20 + 25.30[c]	0.453	0.344	0.860	0.720	0.873
A = 1	1	10	0.1	1	1	1	1
	0.95	5 + 8.42[d]	0.134	0.873	0.873	0.746	0.746
	0.9	10 + 6.97[e]	0.170	0.770	0.770	0.540	0.588
	0.8	20 + 4.50[f]	0.245	0.611	0.611	0.222	0.408

[a]Since 5 pass through and 95 are attenuated by 0.421 O.D.
[b]Since 10 pass through and 90 are attenuated by 0.444 O.D.
[c]Since 20 pass through and 80 are attenuated by 0.5 O.D.
[d]Since 5 pass through and 95 are attenuated by 1.053 O.D.
[e]Since 10 pass through and 90 are attenuated by 1.111 O.D.
[f]Since 20 pass through and 80 are attenuated by 1.25 O.D.

flattening coefficient only (expressed as $Q_{(\lambda)}$ in their paper) may be used.

In 1988, Bustamante and Maestre approached again the problem treating AF as localized statistical fluctuation in the concentration of the absorbing species.[9] They showed that Q_A (named $K_f^{(abs)}$ in their paper) cannot be used to compensate the CD spectrum and proposed a flattening coefficient for CD: $K_f^{(CD)} = 2\,[K_f^{(abs)} - (1/2)]$.

How do the flattening coefficients of the literature compare with our proposed Q_f? We should first of all consider that correction factors obtained from ratios of absorbances should be intrinsically less accurate; indeed, in current CD instruments the spectra are obtained by the ratio of the AC to DC components, and the DC components are proportional to transmittance not to absorbance (see also Ref. 2). To quantify the comparison, we present a simple numerical example in Table 1. Herein, we assume to operate at a given wavelength with two samples, respectively, of 0.4 and 1 optical density, we hypothesize the situation in which samples are fed with 110 photons, 10 of which are absorbed by the solvent and the cuvette walls. Different f values (ratio of the number of photons interacting with the sample and of the total number of photons) are applied: $f = 1$ (no AF), 0.95, 0.9, 0.8. As expected, the table shows little differences in Q_f and Q_A values for moderate absorption levels, and larger differences for large absorbances, and this is related to the more rigorous meaning of Q_f. Besides, we point out that the use of Q_f versus Q_A in our proposed sample approach is more advantageous, since estimation of Q_f is very easy. Although AF effects on CD spectra are caused only by the pertinent distortion of the regular absorption profile, with our proposed sampling approach, there is no need to measure or to calculate the absorption spectra (since the relevant information is already "included" in the DC profile).

It is a common practice with CD spectrometers to extract the absorption data from the PM tube high voltage, which continuously changes to keep constant DC, but the technique is not error-free, since this practice relays on the PM tube log response stored in the instrument memory. Further calibration is possible,[10] but it is not a trivial operation. In addition, proper subtraction of buffer/solvent absorption baseline is necessary, an operation which calls for skill, particularly in the low UV range. On the contrary, our approach is very simple to apply and calls for minimum postrun data manipulation.

CONCLUSIONS

We have shown here that by a different spectra collection strategy and simple postrun data treatment it is possible to quantify a correction factor $Q_f(\lambda)$ to compensate AF spectra distortions. For complete correction, the spectrum of homogeneous solution is necessary, but even in the cases in which the latter is not available, this approach can provide quick information on whether apparent spectral modifications are caused by real conformational modifications or merely by AF.

LITERATURE CITED

1. Duysens LMN. The flattening of the absorption spectrum of suspensions, as compared to that of solutions. Biochim Biophys Acta 1956;19:1–12.
2. Castiglioni E, Abbate S, Longhi G, Gangemi R. Wavelength shifts in solid-state circular dichroism spectra: a possible explanation. Chirality 2007;19:491–496.
3. Castiglioni E, Abbate S, Longhi G, Gangemi R, Lauceri R, Purrello R. Absorption flattening as one cause of distortion of circular dichroism spectra of Δ-RuPhen$_3$ H$_2$TPPS complex. Chirality 2007;19:642–646.
4. Urry DW, Hinners TA, Masotti L. Calculation of distorted circular dichroism curves for poly-L-glutamic acid suspensions. Arch Biochem Biophys 1970;137:214–221.

5. Urry DW, Krivacic J. Differential scatter of left and right circularly polarized light by optically active particulate systems. Proc Natl Acad Sci USA 1970;65:845–852.
6. Broomhead JA, Dwyer FP, Hogarth JW. Resolution of the tris(ethylendiamine) cobalt(III) ion. In: Rochow EG, editor. Inorganic synthesis, Vol.6. New York: McGraw Hill; 1960. p 183–188.
7. Schneider AS, Harmatz D. An experimental method correcting for absorption flattening and scattering in suspensions of absorbing particles: circular dichroism and absorption spectra of hemoglobin in situ in red blood cells. Biochemistry 1976;15:4158–4162.
8. Wallace BA, Mao D. Circular dichroism analyses of membrane proteins: an examination of differential light scattering and absorption flattening effects in large membrane vesicles and membrane sheets. Anal Biochem 1984;142:317–328.
9. Bustamante C, Maestre MF. Statistical effects in the absorption and optical activity of particulate suspensions. Proc Natl Acad Sci USA 1988;85:8482–8486.
10. Arvinte T, Bui TTT, Dahab AA, Demeule B, Drake AF, Elhang D, King P. The multi-mode polarization modulation spectrometer, Part 1: simultaneous detection of absorption, turbidity, and optical activity. Anal Biochem 2004;332:46–57.

Stereoselective Synthesis of 2,3,7-Trimethylcyclooctanone and Related Compounds and Determination of Their Relative and Absolute Configurations by the MαNP Acid Method

JUNPEI NAITO,[1] SHUNSUKE KUWAHARA,[1] MASATAKA WATANABE,[1] JOHN DECATUR,[2] PIETER H. BOS,[3] RUBEN P. VAN SUMMEREN,[3] BJORN TER HORST,[3] BEN L. FERINGA,[3] ADRIAAN J. MINNAARD,[3†] AND NOBUYUKI HARADA[1,2*†]

[1]*Institute of Multidisciplinary Research for Advanced Materials, Tohoku University, Sendai, Japan*
[2]*Department of Chemistry, Columbia University, New York*
[3]*Stratingh Institute for Chemistry, University of Groningen, Groningen, The Netherlands*

Presented at the 11th International Conference on Circular Dichroism, 2007, Groningen, Netherlands

ABSTRACT The copper/chiral phosphoramidite (**L_1**)-catalyzed conjugate addition of dimethylzinc to cycloocta-2,7-dienone **4**, followed by the methylation of the intermediate enolate, yielded a single isomer of 7,8-dimethylcyclooct-2-enone (+)-**5**. Compound (+)-**5** was subjected to the second conjugate addition with ent-**L_1** giving only one stereoisomer of 2,3,7-trimethylcyclooctanone (+)-**6**, which was converted to 2,3,7-trimethylcyclooctanol **7**. To determine the relative and absolute configurations of these compounds, the ^{1}H NMR anisotropy method using (*S*)-(+)-2-methoxy-2-(1-naphthyl)-propionic acid {(*S*)-(+)-MαNP acid} **1** was applied. Racemic alcohol (±)-**7** was esterified with (*S*)-(+)-MαNP acid **1** yielding diastereomeric esters, which were efficiently separated by HPLC on silica gel affording the first-eluted MαNP ester (–)-**10a** and the second-eluted one (–)-**10b**. The relative and absolute configurations of ester (–)-**10a** were determined to be (*S*;1*R*,2*S*,3*R*,7*S*) by analyzing the ^{1}H and ^{13}C NMR spectra of (–)-**10a** and (–)-**10b**, especially their HSQC-TOCSY and NOESY spectra, and by applying the MαNP anisotropy method. The alcohol **7** formed from (+)-**6** was similarly esterified with (*S*)-(+)-MαNP acid **1** yielding an MαNP ester, which was identical with (–)-**10a**, and the relative and absolute configurations of 2,3,7-trimethylcyclooctanone (+)-**6** were determined to be (2*S*,3*R*,7*S*). *Chirality 20:1053–1065, 2008.*

KEY WORDS: chiral phosphoramidite; asymmetric conjugate addition; 2,3,7-trimethylcyclooctanone; 2,3,7-trimethylcyclooctanol; MαNP acid; 2-methoxy-2-(1-naphthyl)propionic acid; HPLC separation on silica gel; stereochemistry; absolute configuration; HSQC-TOCSY; ^{1}H NMR anisotropy

INTRODUCTION

The MαNP acid method[1–8] is very useful for the preparation of enantiopure alcohols and the simultaneous determination of their absolute configurations by the ^{1}H NMR anisotropy effect. For example, racemic alcohol (±)-**2** is esterified with a chiral ^{1}H NMR anisotropy reagent (CAR), 2-methoxy-2-(1-naphthyl)propionic acid {MαNP acid} (*S*)-(+)-**1**, yielding diastereomeric MαNP esters, which are easily separable by HPLC on silica gel (Fig. 1a). The ^{1}H NMR signals of the first-eluted ester (*S;X*)-**3a** and those of the second-eluted ester (*S;–X*)-**3b** are assigned by ^{1}H-^{1}H COSY, ^{13}C, HMQC, HMBC, and HSQC-TOCSY methods leading to the calculation of Δδ values {Δδ = δ(*R;X*) – δ(*S;X*) = δ(*S;–X*) – δ(*S;X*) = δ(2nd Fr.) – δ(1st Fr.)}, where *R* and *S* denote the absolute configuration of the MαNP acid parts, respectively, and *X* and *–X* are those of the alcoholic parts of the first-eluted ester and the second-eluted ester, respectively. By applying the MαNP sector rule, the absolute configuration *X* of the first-eluted ester **3a** can be determined (Fig. 1b). If enantiopure or enantioenriched alcohol **2** has already been obtained by asymmetric synthesis, the chiral alcohol **2** is esterified with

Additional Supporting Information may be found in the online version of this article.

Contract grant sponsor: Japan Society for the Promotion of Science; Contract grant number: 16350069.
Contract grant sponsors: Nissan Science, Mazda, Inamori Foundations, Netherlands Organization for Scientific Research (NWO-CW), Research School NRSC-C, New York State Office of Science, Technology, and Academic Research.

†These authors contributed equally to this work.

*Correspondence to: Nobuyuki Harada, Department of Chemistry, Columbia University, 3000 Broadway, MC3152, New York, NY10027, USA. E-mail: nh2212@columbia.edu or n_harada@ma.mni.ne.jp

Received for publication 23 April 2008; Accepted 10 June 2008
DOI: 10.1002/chir.20637
Published online 24 July 2008 in Wiley InterScience (www.interscience.wiley.com).

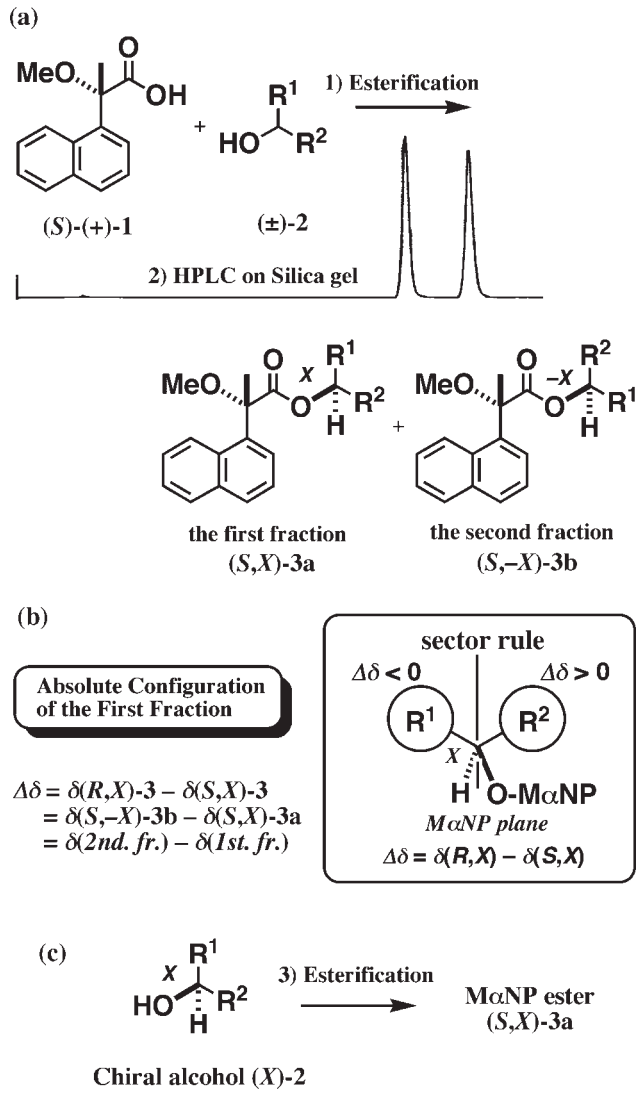

Fig. 1. Determination of the absolute configuration of chiral alcohol by the ^{1}H NMR anisotropy method using (*S*)-(+)-MαNP acid **1** (CAR)[1–3]: (**a**) synthesis of diastereomeric MαNP esters and HPLC separation, (**b**) calculation of Δδ values and application of the sector rule, and (**c**) synthesis of MαNP ester from chiral alcohol (*X*)-**2**.

acid (*S*)-(+)-**1** yielding MαNP ester **3a** or **3b**. By comparison of data from HPLC and ^{1}H and ^{13}C NMR spectra, the MαNP ester prepared from chiral alcohol **2** can be identified and, therefore, the absolute configuration of chiral alcohol **2** can be determined (Fig. 1c). The MαNP acid method is thus useful for determining the absolute configuration of chiral alcohols by the ^{1}H NMR anisotropy method.[1–8]

Stereoselective reactions on eight-membered ring compounds have not been intensively studied because of the general expectation that the reactions result mostly in mixtures of products due to the flexibility of the ring. In addition, the determination of the stereochemistry of the products is not easy due to the absence of established NMR rules such as the Karplus relation in six-membered rings. The first argument is largely incorrect as previously shown by Still and Galynker.[9] The second argument, however, is certainly valid.

Some of us have studied the copper-catalyzed asymmetric conjugate addition of dimethylzinc to cycloocta-2,7-dienone **4** as a basis to prepare synthetic chiral building blocks for natural product synthesis.[10–12] In the study, we observed that methylation of the enolate resulting from the copper/chiral phosphoramidite (**L$_1$**)-catalyzed conjugate addition of dimethylzinc was a highly stereoselective process affording only a single isomer of 7,8-dimethylcyclooct-2-enone (+)-**5** (Scheme 1). When compound (+)-**5** was subjected to the second conjugate addition with ent-**L$_1$** involving the remaining enone functionality, only one stereoisomer of 2,3,7-trimethylcyclooctanone (+)-**6** could be produced reflecting the enantiomeric structure of the catalyst. We were eager to elucidate the stereochemistry of (+)-**6** and therefore ketone (+)-**6** was converted to chiral 2,3,7-trimethylcyclooctanol **7**, to which we applied the MαNP acid method.

In this article, we report the details of stereoselective synthesis of 2,3,7-trimethylcyclooctanone (+)-**6** and related compounds. To determine the relative and absolute configurations of these compounds, the ^{1}H NMR anisotropy method using (*S*)-(+)-MαNP acid **1** has been applied to alcohol **7**. Compound **7** is a saturated eight-membered cycloalkanol, and so it is generally difficult to assign the ^{1}H NMR signals because of heavy overlap of proton signals. Therefore, it is hard to determine the relative and absolute configurations by NMR spectroscopy. However, we have overcome these difficulties by the use of its MαNP ester, the ^{1}H NMR signals of which were well separated by the diamagnetic anisotropy effect generated by the naphthalene group, especially in the case of the second-eluted MαNP ester. By the intensive use of ^{1}H-^{1}H COSY, ^{13}C, HMQC, HMBC, and HSQC-TOCSY spectra, all ^{1}H and ^{13}C NMR signals could be assigned, leading to the unambiguous determination of the relative and absolute configurations. The conformation of 2,3,7-trimethylcyclooctanol has been confirmed by NOESY as well. The applied procedure is described in detail below.

MATERIALS AND METHODS

General

Melting points are uncorrected. IR spectra were obtained as KBr disks or neat on a Jasco FT/IR-410 spectrophotometer. ^{1}H NMR spectra were recorded on Varian Gemini-200 (200 MHz), Varian VXR300 (300MHz), Varian AMX400 (400 MHz), Bruker DMX 500 (500 MHz), Jeol JNM-LA600 (600 MHz), and/or Bruker Avance 800 (800 MHz) spectrometers. ^{13}C NMR spectra were obtained on Varian Gemini-200 (50 MHz), Varian VXR300 (75 MHz), Varian AMX400 (100 MHz), DMX 500 (125 MHz), and/or Jeol JNM-LA600 (150 MHz) spectrometers. All NMR data are reported in ppm (δ) downfield from TMS. Specific rotations $[\alpha]_D$ were measured on a Jasco DIP-1000 spectropolarimeter or a Schmidt+Haensch Polartronic MH8 spectropolarimeter. Mass spectra (HRMS) were recorded on an AEI MS-902. Silica gel 60 F_{254} precoated plates on glass from Merck Ltd. were used for thinlayer chromatography

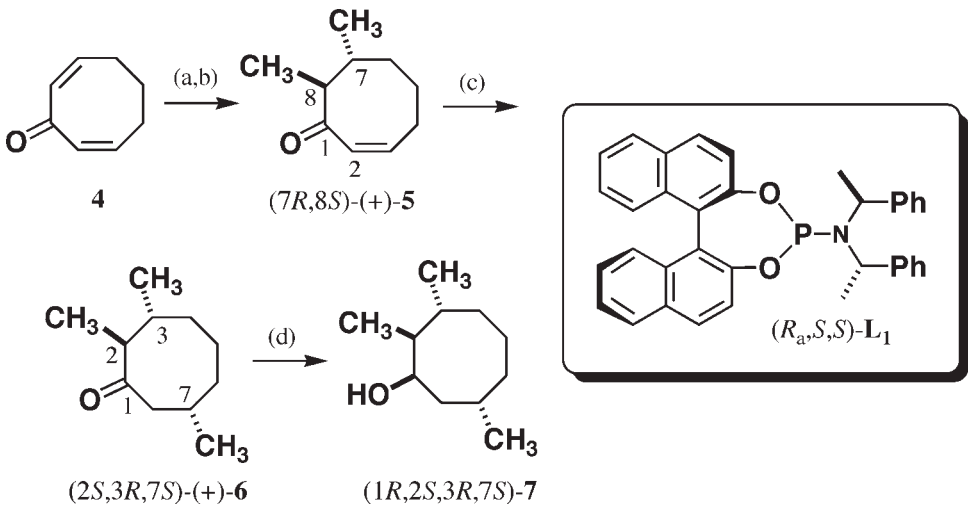

(a) $Cu(OTf)_2$ (5 mol%), (R_a,*S*,*S*)-$\mathbf{L_1}$ (10 mol%), Me_2Zn (5.0 eq), toluene, –25 °C. (b) MeI (8 eq), HMPA (8 eq). (c) $Cu(OTf)_2$ (5 mol%), (S_a,*R*,*R*)-*ent*-$\mathbf{L_1}$ (10 mol%), Me_2Zn (3.0 eq), toluene, –25 °C. (d) $NaBH_4$, MeOH/DCM.

Scheme 1. Enantioselective synthesis of enantiopure 2,3,7-trimethylcyclooctanone (2*S*,3*R*,7*S*)-(+)-**6** and related compounds, the absolute configurations of which were determined as discussed here.

(TLC). HPLC separation was performed using a prepacked glass column (22 ϕ × 300 mm, number of theoretical plates n = 9300–10,600) of silica gel (particle size, 5–10 μm) from Kusano, Tokyo. Reverse phase HPLC was carried out using a prepacked ODS column (22 ϕ × 300 mm, number of theoretical plates n = 6000–7200, particle size, 20 μm) from Kusano, Tokyo. The purities of the title compounds were shown to be ≥99% by ^{1}H NMR, TLC, and/or HPLC.

Synthesis

Cycloocta-2,7-dienone 4. Cyclooctanone (3.0 g, 23.7 mmol) was dissolved in DMSO (320 ml) and 2-iodoxybenzoic acid (IBX, 26.6 g, 95 mmol, 4.0 eq) was added. The resulting solution was slowly heated to 85°C and stirred for 6 h and then overnight at 65°C. After cooling to room temperature, the mixture was diluted with Et_2O until two layers appeared. The DMSO-layer was extracted with Et_2O (9×). The combined ether extracts were washed with aq. $NaHCO_3$ (5% w/w, 3×), water and brine (sat.), dried ($MgSO_4$), and concentrated. Purification by open column chromatography (pentane/Et_2O 5:1) gave dienone **4** (2.45 g, 20.0 mmol, 84%) as a light yellow liquid. NMR data agreed with those reported in the literature[13]: ^{1}H NMR (300 MHz, $CDCl_3$) δ 1.77 (2 H, m), 2.38 (4 H, m), 6.35 (4 H, m); ^{13}C NMR (50.3 MHz, $CDCl_3$) δ 25.0 (t), 27.1 (t), 135.9 (d), 141.5 (d), the carbonyl carbon signal was not observed.

7,8-Dimethylcyclooct-2-enone (7*R*,8*S*)-(+)-5. Cu$(OTf)_2$ (0.355 g, 0.98 mmol, 5 mol %) and (R_a,*S*,*S*)-$\mathbf{L_1}$ (1.06 g, 1.96 mmol, 10 mol %) were dissolved in dry toluene (60 ml) and stirred at room temperature for 30 min under nitrogen. The solution was cooled to –25°C and Me_2Zn (2.0 M in toluene, 39.3 ml, 78.6 mmol, 4 eq) was added over 5 min. After stirring for 10 min, dienone **4** (2.4 g, 19.6 mmol) dissolved in toluene (60 ml) was added via a syringe pump over 5 h. The resulting solution was stirred at –25°C overnight, and then HMPA (27.3 ml, 157.1 mmol, 8 eq) and MeI (9.8 ml, 157.1 mmol, 8 eq) were added to the reaction mixture, and the solution was stirred for 72 h at –25°C and then quenched with aq. NH_4Cl (sat.), extracted with Et_2O (3×), washed with brine (sat.), and dried with $MgSO_4$. The Et_2O was removed under vacuum, and the product was purified by open column chromatography (pentane/Et_2O 50:1 to 5:1) to give compound (+)-**5** (2.19 g, 14.4 mmol, 73%) as a colorless oil: $[\delta]_D^{20}$ +145.2 (*c* 1.59, $CHCl_3$); ^{1}H NMR (300 MHz, $CDCl_3$) δ 1.07 (3 H, d, J = 6.2 Hz), 1.09 (3 H, d, J = 6.2 Hz), 1.43 (2 H, m), 1.65 (2 H, m), 1.83 (1 H, m), 2.30 (1 H, m), 2.72 (2 H, m), 6.09 (1 H, dd, J = 12.4, 1.6 Hz), 6.35 (1 H, m); ^{13}C NMR (50 MHz, $CDCl_3$) δ 15.9 (q), 17.8 (q), 19.7 (t), 27.5 (t), 30.4 (t), 35.6 (d), 51.0 (d), 134.0 (d), 140.2 (d), 208.0 (s) (see Supplementary Material). MS (EI) for $C_{10}H_{16}O$: *m/z* 152 [M^+], HRMS calcd for $C_{10}H_{16}O$: 152.120, found: 152.120.

2,3,7-Trimethylcyclooctanone (2*S*,3*R*,7*S*)-(+)-6. Cu$(OTf)_2$ (0.143 g, 0.39 mmol, 5 mol %) and (S_a,*R*,*R*)-ent-$\mathbf{L_1}$ (0.425 g, 0.79 mmol, 10 mol %) were dissolved in dry toluene (50 ml) and stirred at room temperature for 30 min under nitrogen. The solution was cooled to –25°C and Me_2Zn (2.0 M in toluene, 11.8 ml, 23.6 mmol, 3 eq) was added over 5 min. After stirring for 10 min (+)-**5** (1.2 g, 7.88 mmol) dissolved in DCM (25 ml) was added via a syringe pump over 5 h. The resulting solution was stirred at –25°C overnight and then quenched with aq. NH_4Cl (sat.), extracted with Et_2O (3×), washed with brine (sat.), and dried with $MgSO_4$. The Et_2O was removed under vacuum.

To remove the remaining ligand which causes purification problems, the crude product was dissolved in DCM and *m*-CPBA (0.315 g, 1.8 mmol) was added and the mixture was stirred overnight (0°C to room temp.). The reaction was quenched with aq. $Na_2S_2O_3$ (10% w/w), extracted with DCM (3×), washed with brine (sat.), dried with $MgSO_4$. After checking the mixture for peroxides, the product was concentrated and purified by open column chromatography (pentane/Et_2O 5:1) to give (+)-**6** (1.13 g, 6.7 mmol, 85%) as a colorless liquid: $[\delta]_D^{20}$ +34.8 (*c* 0.92, $CHCl_3$); ^1H NMR (400 MHz, $CDCl_3$) δ 0.95 (3 H, d, J = 6.6 Hz), 0.98 (3 H, d, J = 6.8 Hz), 1.04 (3 H, d, J = 6.7 Hz), 1.10–1.36 (3 H, m), 1.60-1.76 (4 H, m), 2.14 (1 H, m), 2.30 (2 H, m), 2.44 (1 H, dd, J = 12.2, 3.7 Hz); ^{13}C NMR (50 MHz, $CDCl_3$) δ 16.2 (q), 20.6 (q), 23.1 (q), 23.6 (t), 33.2 (d), 36.3 (t), 36.6 (t), 39.5 (d), 49.6 (t), 54.1 (d), 219.3 (s) (see Supplementary Material) MS (EI) for $C_{11}H_{20}O$, *m/z* 168 [M^+], HRMS calcd for $C_{11}H_{20}O$: 168.151, found: 168.151.

2,3,7-Trimethylcyclooctanol (1*R*,2*S*,3*R*,7*S*)-7. Ketone (+)-**6** (0.116 g, 0.69 mmol) was dissolved in MeOH (2.0 ml) and DCM (4.0 mL), cooled to 0°C and subsequently $NaBH_4$ (130 mg, 3.45 mmol, 5 eq) was added and the mixture was stirred overnight. The reaction was quenched with aq. NH_4Cl (sat.), concentrated, and taken up in H_2O. Subsequently, aq. HCl (10%) was added and the aqueous layer was extracted with Et_2O (3×). The combined ether extracts were dried with $MgSO_4$, concentrated, and the crude product was purified by open column chromatography (pentane/Et_2O 5:1) to give **7** (88.2 mg, 0.52 mmol, 75%) as a colorless liquid: ^1H NMR (400 MHz, $CDCl_3$) δ 0.91 (3 H, d, J = 6.4 Hz), 0.96 (3 H, d, J = 6.4 Hz), 0.98 (3 H, d, J = 6.4 Hz), 1.12–1.60 (9 H, m), 1.60–1.70 (1 H, m), 1.70–1.80 (2 H, m), 4.15 (1 H, dt, J = 7.0, 3.3 Hz,); ^{13}C NMR (50 MHz, $CDCl_3$) δ 12.6 (q), 24.8 (q), 25.6 (q), 29.2 (d), 30.1 (t), 34.4 (t), 35.4 (t), 38.4 (d), 41.7 (t), 45.9 (d), 70.8 (d) (see Supplementary Material). MS(EI) for $C_{11}H_{22}O$: *m/z* 170 [M^+], HRMS calcd for $C_{11}H_{22}O$: 170.167, found: 170.167.

7,8-Dimethylcyclooct-2-enone (7*R,8*S**)-(±)-5.** To a stirring suspension of CuI (1.23 g, 6.44 mmol, 1.125 eq, pre-dried with a hotgun) in dry Et_2O (55 ml) at 0°C under nitrogen was added MeLi (8.0 ml, 12.9 mmol, 2.25 eq). After stirring for 10 min, compound **4** (0.700 g, 5.73 mmol) dissolved in Et_2O (7.0 ml) was added. After 1 h HMPA (4.98 ml, 28.65 mmol, 5 eq) and MeI (1.8 ml, 28.65 mmol, 5 eq) were added and the solution was stirred overnight at 0°C and then quenched with aq. NH_4Cl (sat.), extracted with Et_2O (3×), washed with dilute aq. ammonia, washed with brine (sat.), and dried with $MgSO_4$. The Et_2O was removed under vacuum and the product purified by open column chromatography (pentane/Et_2O 8:1) to give (±)-**5** (0.523 g, 3.44 mmol, 60%) as a colorless oil. ^1H NMR, ^{13}C NMR, MS (EI), and HRMS were identical with those of (7*R*,8*S*)-(+)-**5**.

2,3,7-Trimethylcyclooctanone (2*S,3*R**,7*S**)-(±)-6.** To a stirring suspension of CuI (0.398 g, 2.09 mmol, 1.125 eq, pre-dried with a hotgun) in dry Et_2O (18 ml) at 0°C under nitrogen was added MeLi (2.62 ml, 4.19 mmol, 2.25 eq). After stirring for 10 min, compound (±)-**5** (0.283 g, 1.86 mmol) dissolved in Et_2O (2.5 ml) was added. After full conversion the reaction was quenched with aq. NH_4Cl (sat.), extracted with Et_2O (3×), washed with dilute aq. ammonia, washed with brine (sat.), and dried with $MgSO_4$. The Et_2O was removed under vacuum and the product purified by open column chromatography (pentane/Et_2O 5:1) to give (±)-**6** (0.250 g, 1.49 mmol, 80%) as a colorless oil. ^1H NMR, ^{13}C NMR, MS (EI), and HRMS were identical with those of (2*S*,3*R*,7*S*)-(+)-**6**.

2,3,7-Trimethylcyclooctanol (1*R,2*S**,3*R**,7*S**)-(±)-7.** Racemic ketone (±)-**6** (0.238 g, 1.41 mmol) was reduced similarly as in the case of chiral ketone (+)-**6** giving alcohol (±)-**7** (0.189 g, 1.11 mmol, 79%). ^1H NMR and ^{13}C NMR were identical with those of (1*R*,2*S*,3*R*,7*S*)-**7**.

7-Methylcyclooct-2-enone (*R*)-8. $Cu(OTf)_2$ (0.151 g, 0.417 mmol, 5 mol%) and (R_a,*S*,*S*)-$\mathbf{L_1}$ (0.448 g, 0.83 mmol, 10 mol%) were dissolved in dry toluene (25 ml) and stirred at room temperature for 30 min under nitrogen. The solution was cooled to –25°C and Me_2Zn (2.0 M in toluene, 16.7 ml, 33.3 mmol, 4 eq) was added over 5 min. After stirring for 10 min, dienone **4** (1.0 g, 8.33 mmol) dissolved in toluene (37.5 ml) was added via a syringe pump over 5 h. The resulting solution was stirred at –25°C overnight and then quenched with aq. NH_4Cl (sat.), extracted with Et_2O (3×), washed with brine (sat.), and dried with $MgSO_4$. The Et_2O was removed under vacuum and the product purified by open column chromatography (pentane/Et_2O 50:1 to 10:1) to give (*R*)-**8** (0.965 g, 6.99 mmol, 84%) as a colorless liquid: ^1H NMR (400 MHz, $CDCl_3$) δ 1.01 (3 H, d, J = 6.8 Hz), 1.36 (1 H, m), 1.56–1.74 (3 H, m), 2.13 (1 H, m), 2.46 (1 H, dd, J = 13.6, 8.4 Hz), 2.42–2.62 (2 H, m), 2.70 (1 H, dd, J = 13.6, 5.6 Hz), 6.04 (1 H, d, J = 12.4 Hz), 6.35 (1 H, dt, J = 12.4, 7.2 Hz); ^{13}C NMR (50 MHz, $CDCl_3$) δ 21.5 (t), 21.8 (q), 28.0 (t), 28.8 (d), 32.0 (t), 50.0 (t), 133.3 (d), 141.5 (d), 204.4 (s).

3,7-Dimethylcyclooctanone (3*R,7*S**)-cis-9.** Cu$(OTf)_2$ (16 mg, 45 μmol, 2.5 mol %) and (S_a,*R*,*R*)-ent-$\mathbf{L_1}$ (49 mg, 90 μmol, 5 mol %) were dissolved in dry DCM (6.3 ml) and stirred at room temperature for 30 min under nitrogen. The solution was cooled to –25°C and Me_2Zn (2.0 M in toluene, 1.36 ml, 2.71 mmol, 1.5 eq) was added over 5 min. After stirring for 10 min, enone (*R*)-**8** (0.250 g, 1.81 mmol) dissolved in DCM (5 ml) was added via a syringe pump over 5 h. The resulting solution was stirred at –25°C overnight and then quenched with aq. NH_4Cl (sat.), extracted with Et_2O (3×), washed with brine (sat.), and dried with $MgSO_4$. The Et_2O was removed under vacuum and the product purified by open column chromatography (pentane/Et_2O 25:1) to give *cis*-ketone **9** (0.263 g, 1.71 mmol, 94%) as a colorless liquid: ^1H NMR (400 MHz, $CDCl_3$) δ 0.96 (6 H, d, J = 6.4 Hz), 1.27 (3 H, m), 1.47 (1 H, m), 1.66 (2 H, m), 2.16 (4 H, m), 2.50 (2 H, br d, J = 9.6 Hz); ^{13}C NMR (100.6 MHz, $CDCl_3$) δ 22.3 (q), 22.5 (t), 32.4 (d), 36.3 (t), 50.2 (t), 215.2 (s).

2,3,7-Trimethylcyclooctanone (2*S,3*R**,7*S**)-(±)-6.** To a solution of *cis*-**9** (0.247 g, 1.6 mmol) in dry THF under nitrogen at 0°C was added $LiN[Si(CH_3)_3]_2$ (1.76 ml,

1.76 mmol, 1.0 M in THF, 1.1 eq) and the mixture stirred for 1 h at 0°C. Subsequently the solution was cooled to –78°C and MeI (150 μl, 2.4 mmol, 1.5 eq) was added. The reaction mixture was allowed to slowly warm to ambient temperature and was stirred overnight. The reaction was quenched with aq. NH_4Cl (sat.), extracted with Et_2O (3×), washed with brine (sat.), and dried with $MgSO_4$. The Et_2O was removed under vacuum and purified by open column chromatography (pentane/Et_2O 9:1) to give (±)-**6** (0.204 g, 1.21 mmol, 76%) as a colorless liquid. ^1H NMR and ^{13}C NMR were identical with those of (2*S*,3*R*,7*S*)-(+)-**6**.

3,7-Dimethylcyclooctanone (3*R*,7*R*)-trans-9. Enone (*R*)-**8** was subjected to the 1,4-addition reaction with $Cu(OTf)_2$, (R_a,*S*,*S*)-**L_1**, and Me_2Zn as described for the synthesis of *cis*-ketone **9**. The reaction was quenched with aq. NH_4Cl (sat.) and the mixture was worked up. The crude product was purified by open column chromatography (pentane/Et_2O 9:1) to give *trans*-ketone **9** as a colorless oil: ^1H NMR (400 MHz, $CDCl_3$) δ 0.97 (6 H, d, J = 6.8 Hz), 1.13 (2 H, m), 1.36 (2 H, m), 1.61 (2 H, m), 2.16 (2 H, m), 2.20 (2 H, br d, J = 12.4 Hz), 2.28 (2 H, dd, J = 12.4, 12.4 Hz); ^{13}C NMR (100.6 MHz, $CDCl_3$) δ 23.3 (q), 23.7 (t), 32.1 (d), 36.1 (t), 50.3 (t), 215.9 (s).

Synthesis of diastereomeric esters (*S*;1*R*,2*S*,3*R*,7*S*)-(–)-10a and (*S*;1*S*,2*R*,3*S*,7*R*)-(+)-10b from (*S*)-(+)-MαNP acid 1 and 2,3,7-trimethylcyclooctanol (±)-7, and their HPLC separation. To a mixture of enantiopure MαNP acid (*S*)-(+)-**1** (101 mg, 0.441 mmol), 4-(dimethylamino)pyridine (DMAP, 17.9 mg, 0.147 mmol), racemic 2,3,7-trimethylcyclooctanol (±)-**7** (50.0 mg, 0.294 mmol), and 1,3-dicyclohexylcarbodiimide (DCC, 121 mg, 0.588 mmol) in CH_2Cl_2 (1.0 ml) cooled at 0°C was added 10-camphorsulfonic acid (CSA, 20 mg, 0.088 mmol), and the mixture was stirred at room temperature overnight. After addition of a small amount of water, the mixture was stirred for 1 h, diluted with EtOAc, and filtered with Celite, which was washed with EtOAc. The organic layer was evaporated under reduced pressure, and the residue was subjected to open column chromatography on silica gel (hexane/EtOAc = 1:1) yielding a diastereomeric mixture of esters.

The mixture was easily separated by HPLC on silica gel (hexane/EtOAc 8:1, separation factor α = 1.35, resolution factor R_s = 1.92), giving the first-eluted ester (*S*;1*R*,2*S*,3*R*,7*S*)-(–)-**10a** and the second-eluted one (*S*;1*S*,2*R*,3*S*,7*R*)-(+)-**10b**. The second-eluted ester was further purified by repeating HPLC with a ODS column (MeOH) to remove small amounts of impurities.

MαNP ester (*S*;1*R*,2*S*,3*R*,7*S*)-(–)-10a. Yield 37.6 mg, 33%; colorless amorphous solid; $[\alpha]_D^{25}$ –3.9 (*c* 0.83, $CHCl_3$); IR (film) ν_{max} 3048, 2953, 2925, 1723, 1509, 1458, 1397, 1370, 1258, 1181, 1135, 1065, 1054, 1030, 941, 918, 822, 779 cm^{-1}; ^1H NMR (600 MHz, $CDCl_3$) δ 0.603 (3 H, d, J = 6.2 Hz, 7-CH_3), 0.691 (3 H, d, J = 6.8 Hz, 2-CH_3), 0.858 (3 H, d, J = 6.5 Hz, 3-CH_3), 0.880 (1 H, ddd, J = 13.7, 10.3, 3.5 Hz, 8-H_{eq}), 1.20 (1 H, m, 5-H_{ax}), 1.23 (1 H, m, 3-H), 1.30 (1 H, m, 4-H_{eq}), 1.31 (2 H, m, 6-H), 1.31 (1 H, m, 7-H), 1.344 (1 H, dqd, J = ∼10.3, 6.8, 3.5 Hz, 2-H), 1.404 (1 H, ddd, J = 13.7, 10.4, 4.4 Hz, 8-H_{ax}), 1.494 (1 H, dddd, J = 14.5, 11.4, 8.6, 2.7 Hz, 4-H_{ax}), 1.680 (1 H, ddddd, J = 13.7, 5.6, 5.6, 2.8, 2.8 Hz, 5-H_{eq}), 1.978 (3 H, s, 3′-H), 3.146 (3 H, s, OCH_3), 5.276 (1 H, ddd, J = 10.4, 3.5, 3.5 Hz, 1-H_{ax}), 7.43-7.46 (3 H, m, 3″-H, 7″-H, 6″-H), 7.599 (1 H, dd, J = 7.3, 1.1 Hz, 2″-H), 7.808 (1 H, d, J = 8.2 Hz, 4″-H), 7.834 (1 H, m, 5″-H), 8.413 (1 H, m, 8″-H); ^{13}C NMR (150 MHz, $CDCl_3$) δ 13.909 (2-CH_3), 21.955 (3′-C), 23.751 (3-CH_3), 24.918 (7-CH_3), 28.658 (7-C), 28.863 (5-C), 34.011 (4-C), 35.022 (6-C), 37.334 (8-C), 37.857 (3-C), 42.616 (2-C), 51.107 (OCH_3), 75.890 (1-C), 81.723 (2′-C), 124.613 (3″-C), 125.356 (2″-C), 125.405 (8″-C), 125.547 (7″-C), 126.197 (6″-C), 128.587 (5″-C), 129.160 (4″-C), 131.323 (1″-C), 134.067 (8″a-C), 135.743 (4″a-C), 173.294 (1′-C) (see Supplementary Material).

MαNP ester (*S*;1*S*,2*R*,3*S*,7*R*)-(–)-10b. Yield 31 mg, 28%; colorless amorphous solid; $[\alpha]_D^{27}$ –14.1 (*c* 1.02, $CHCl_3$); IR (film) ν_{max} 3049, 2953, 2925, 1741, 1540, 1508, 1457, 1396, 1373, 1255, 1136, 1065, 1054, 943, 893, 805, 780 cm^{-1}; ^1H NMR (600 MHz, $CDCl_3$) δ 0.062 (3 H, d, J = 6.5 Hz, 2-CH_3), 0.655 (3 H, d, J = 6.6 Hz, 3-CH_3), 0.824 (3 H, d, J = 6.6 Hz, 7-CH_3), 0.961 (1 H, dqd, J = 9.8, 6.5, 3.5 Hz, 2-H), 1.05 (1 H, m, 3-H), 1.091 (1 H, ddd, J = 13.6, 11.1, 3.5 Hz, 8-H_{ax}), 1.234 (1 H, ddddd, J = 14.2, 11.8, 11.8, 3.6, 3.6 Hz, 5-H_{ax}), 1.31 (1 H, br d, J = 15.0 Hz, 4-H_{eq}), 1.35 (1 H, dddd, J = 14.3, 11.7, 8.5, 2.9 Hz, 6-H_{ax}), 1.42 (1 H, br d, J = 14.3 Hz, 6-H_{eq}), 1.49 (1 H, m, 4-H_{ax}), 1.52 (1 H, m, 7-H), 1.634 (1 H, ddd, J = 13.6, 10.7, 4.6 Hz, 8-H_{ax}), 1.705 (1 H, ddddd, J = 14.2, 5.6, 5.6, 2.8, 2.8 Hz, 5-H_{eq}), 1.980 (3 H, s, 3′-H), 3.118 (3 H, s, OCH_3), 5.265 (1 H, ddd, J = 10.7, 3.5, 3.5 Hz, 1-H_{ax}), 7.43-7.47 (3 H, m, 3″-H, 6″-H, 7″-H), 7.575 (1 H, dd, J = 7.2, 1.0 Hz, 2″-H), 7.809 (1 H, d, J = 8.2 Hz, 4″-H), 7.829 (1 H, m, 5″-H), 8.435 (1 H, m, 8″-H); ^{13}C NMR (150 MHz, $CDCl_3$) δ 12.650 (2-CH_3), 21.559 (3′-C), 23.688 (3-CH_3), 25.215 (7-CH_3), 28.885 (7-C), 29.224 (5-C), 34.279 (4-C), 35.163 (6-C), 37.482 (8-C), 37.702 (3-C), 42.241 (2-C), 50.917 (OCH_3), 75.501 (1-C), 81.447 (2′-C), 124.550 (3″-C), 125.462 (8″-C), 125.568 (2″-C), 125.610 (7″-C), 126.310 (6″-C), 128.488 (5″-C), 129.209 (4″-C), 131.550 (1″-C), 134.039 (8″a-C), 135.431 (4″a-C), 173.422 (1′-C) (see Supplementary Material).

Preparation of MαNP ester (*S*;1*R*,2*S*,3*R*,7*S*)-(–)-10a. Alcohol **7** (5.2 mg, 0.031 mmol) prepared from (+)-**6** was similarly esterified with MαNP acid (*S*)-(+)-**1** (35.4 mg, 0.15 mmol) yielding ester **10a** (5.0 mg, 43%), ^1H NMR of which was identical with that of the first-eluted ester (*S*;1*R*,2*S*,3*R*,7*S*)-(–)-**10a**.

RESULTS AND DISCUSSION

Stereoselective Synthesis of 2,3,7-Trimethylcyclooctanone and Related Compounds

From earlier work it is known that the copper/chiral phosphoramidite (**L_1**)-catalyzed conjugate addition of dimethylzinc to cyclic enones is highly stereoselective and has proven to be useful for the preparation of chiral building blocks for natural products syntheses.[10–12] This methodology was extended even further by combining the conjugate addition with successive methylation of the result-

ing enolate. The details of the reactions and synthesis of related compounds are described below.

The first copper-catalyzed asymmetric conjugate addition of dimethylzinc to cycloocta-2,7-dienone **4** and successive methylation of the enolate formed yielded only a single isomer of 7,8-dimethylcyclooct-2-enone (+)-**5** (73% yield, Scheme 1). The stereochemistry of the conjugate addition, i.e., the absolute configuration at position 7, was thus controlled by the chirality of a ligand, phosphoramidite (R_a,*S*,*S*)-$\mathbf{L_1}$. The stereochemistry of successive methylation of the enolate formed was governed by the chirality at position 7. The whole reaction is thus effectively controlled by the chirality of a ligand, phosphoramidite $\mathbf{L_1}$. The second conjugate addition of dimethylzinc to enone (+)-**5** was carried out using an enantiomeric ligand, phosphoramidite (S_a,*R*,*R*)-ent-$\mathbf{L_1}$, yielding a single isomer of 2,3,7-trimethylcyclooctanone (+)-**6** (85% yield). Since the copper catalyst composed of ent-$\mathbf{L_1}$ was employed, the stereochemistry at the new chiral position would take an opposite absolute configuration, as expected from the preliminary results.[10–12] Namely, the cis-configuration of 3,7-dimethyl groups was expected as shown in Scheme 1. Finally ketone (+)-**6** was reduced to alcohol **7** (75% yield).

To determine the absolute configurations of these chiral compounds **5–7** by application of the ^{1}H NMR anisotropy using MαNP acid (*S*)-(+)-**1**, racemic alcohol **7** was necessary and therefore racemic compounds **5–7** were similarly synthesized as in the case of chiral compounds described above. In this case, no chiral ligand was employed, but the product yields were similar to those of chiral reactions (see Materials and Methods).

Determination of the cis Configuration of 3,7-Dimethyl Moiety in Ketone 6

In the above syntheses, the cis-configuration of 3,7-dimethyl groups of ketone **6** was assumed based on the literature.[10–12] To confirm the cis-configuration, the chemical correlation between 3,7-dimethylcyclooctanone (3*R**,7*S**)-*cis*-**9** and ketone (±)-**6** was performed as shown in Scheme 2. The copper/chiral phosphoramidite $\mathbf{L_1}$-catalyzed conjugate addition of dimethylzinc to dienone **4** gave 7-methylcyclooct-2-enone (*R*)-**8** (84% yield), which was subjected to the second conjugate addition reaction with ent-$\mathbf{L_1}$ affording 3,7-dimethylcyclooctanone (3*R**, 7*S**)-*cis*-**9** (94% yield). Another reference compound, 3,7-dimethylcyclooctanone (3*R*,7*R*)-*trans*-**9**, was similarly synthesized from (*R*)-**8** using the copper/chiral phosphoramidite $\mathbf{L_1}$-catalyzed reaction (Scheme 2).

The ^{13}C NMR of *cis*-ketone **9** shows the signals of only six carbon atoms, reflecting the meso structure of C_s-symmetry (see Materials and Methods). Namely the 3-methyl and 7-methyl carbon atoms appear to be equivalent. It has been reported that the cyclooctane ring prefers a boat-chair (BC, ca. 94% at room temperature) or crown (CC, ca. 6%) conformation,[14] and these BC and CC conformations are of C_s-symmetry. Both BC and CC conformations are possible in 3,7-dimethylcyclooctanone *cis*-**9** keeping the structure of C_s-symmetry. Thus it is easy to interpret the observed ^{13}C NMR of *cis*-ketone **9** based on the major BC and CC conformations.

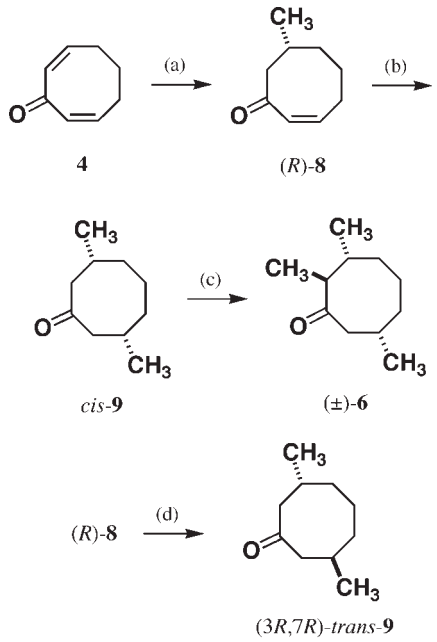

(a) $Cu(OTf)_2$ (5 mol%), (R_a,*S*,*S*)-$\mathbf{L_1}$ (10 mol%), Me_2Zn (5.0 eq), toluene, –25 °C. (b) $Cu(OTf)_2$ (5 mol%), (S_a,*R*,*R*)-*ent*-$\mathbf{L_1}$ (10 mol%), Me_2Zn (3.0 eq), toluene, –25 °C. (c) $LiN[Si(CH_3)_3]_2$, MeI, THF. (d) $Cu(OTf)_2$ (5 mol%), (R_a,*S*,*S*)-$\mathbf{L_1}$ (10 mol%), Me_2Zn (5.0 eq), toluene, –25 °C.

Scheme 2. Chemical correlation among 3,7-dimethylcyclooctanones *cis*-**9**, *trans*-**9**, and 2,3,7-trimethylcyclooctanone (±)-**6**.

It is interesting that the ^{13}C NMR of *trans*-ketone **9** also shows the signals of only six carbon atoms, indicating the chiral structure of C_2-symmetry (see Materials and Methods). Namely the 3-methyl and 7-methyl carbon atoms appear to be equivalent. Therefore, the conformation of C_2-symmetry is conceivable for *trans*-ketone **9**. If *trans*-ketone **9** adopts a BC or CC conformation, the two methyl groups become nonequivalent. The twisted conformations (TBC and TCC) of BC and CC are also reported for the cyclooctane ring,[14] and these TBC and TCC conformations are of C_2-symmetry. However, in *trans*-ketone **9**, TBC and TCC conformations cannot keep their exact C_2-symmetrical structures. Therefore, it is reasonable to consider that *trans*-ketone **9** exists as rapidly interconverting conformers that are a little deviated from the C_2-symmetrical conformation, but converge to the average conformer of C_2-symmetry.

As seen in Materials and Methods, the ^{13}C NMR data of *cis*- and *trans*-ketones **9** are very similar to each other, and therefore, it is impossible to discriminate these stereoisomers by ^{13}C NMR spectroscopy. How can the stereochemistry, i.e., relative configuration, of *cis*- and *trans*-ketones **9** be determined? This problem was unambiguously resolved as follows. The ^{1}H NMR data of *cis*- and *trans*-ketones **9** are shown in Figure 2, where the spectrum of *cis*-ketone **9** (meso-form) shows multiplets at 1.26 ppm (3 H) and 1.47 ppm (1 H). Namely, the two protons at 5-C appear at different chemical shifts, leading to the C_s-symmetrical structure, i.e., cis-configuration. The appearance

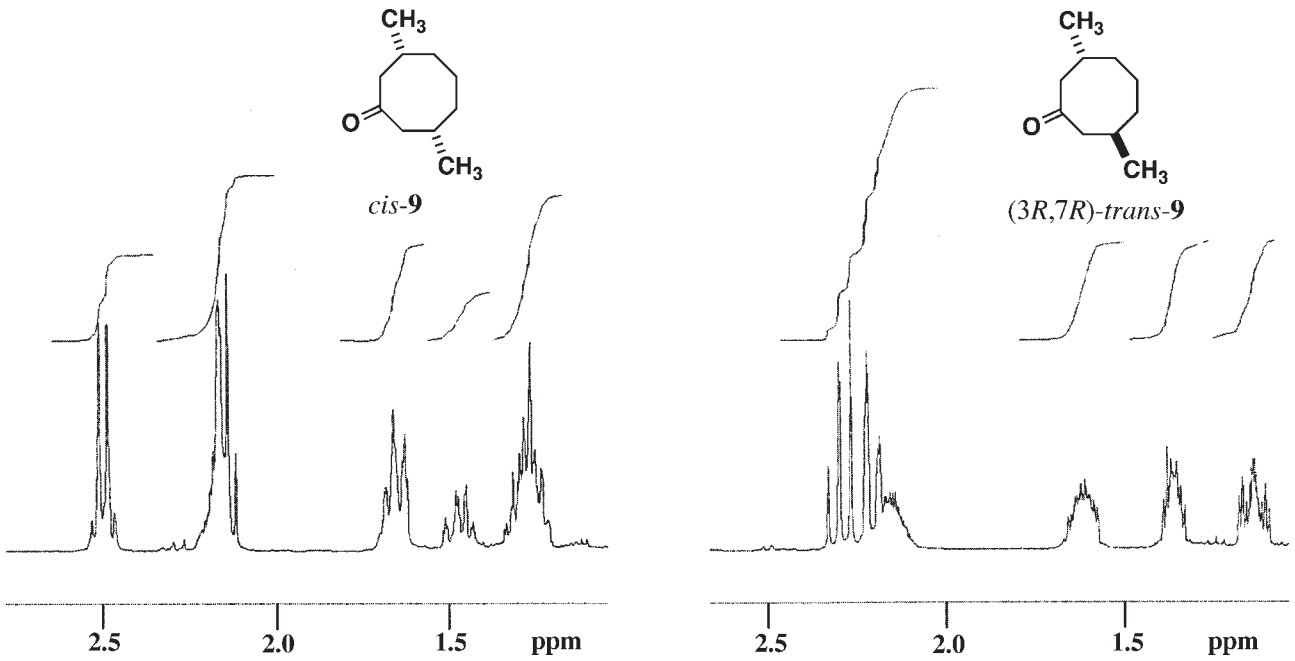

Fig. 2. ^{1}H NMR (400 MHz, $CDCl_3$) spectra of 3,7-dimethylcyclooctanones *cis*-**9** and (3*R*,7*R*)-*trans*-**9**.

of nonequivalent one-proton signals is possible only in the C_s-symmetrical structure. The relative configuration of *cis*-ketone **9** was thus established. In addition, the ^{1}H and ^{13}C NMR data of *cis*-ketone **9** agree with the literature data confirming the above assignment.[15]

If the ketone **9** has a C_2-symmetrical structure, i.e., trans-configuration, the two protons at 5-C are equivalent to each other. Therefore, they should appear at the same chemical shift as a signal of two-proton intensity. In fact, in the ^{1}H NMR of (3*R*,7*R*)-*trans*-ketone **9**, the two protons at 5-C appear as a multiplet at 1.13 ppm (2 H, m) or 1.37 ppm (2 H, m) indicating the C_2-symmetrical structure (Fig. 2). The relative configuration of *trans*-ketone **9** was thus unambiguously determined.

As shown in Scheme 2, *cis*-ketone **9** was methylated at the position 2, and only one product (±)-**6** was obtained. Its ^{1}H and ^{13}C NMR spectra were identical with those of chiral ketone (+)-**6**, indicating that the 3-methyl and 7-methyl groups have a cis configuration in chiral ketone **6** (Scheme 1). Finally, the cis configuration of the 3,7-dimethyl moiety of **6** and **7** was further confirmed by the direct observation of an NOE between 3-H and 7-H of its MαNP ester (–)-**10b**, as described below.

Preparation of Diastereomeric Esters from MαNP Acid (S)-(+)-1 and Racemic 2,3,7-Trimethylcyclooctanol (±)-7, and HPLC Separation

Racemic 2,3,7-trimethylcyclooctanol (±)-**7** was esterified with (*S*)-(+)-MαNP acid **1** as shown in Scheme 3. Alcohol (±)-**7** was treated with (*S*)-(+)-**1**, DCC, DMAP, and CSA in CH_2Cl_2 yielding a diastereomeric mixture of esters **10a/10b** (Scheme 3).

Diastereomeric MαNP esters **10a** and **10b** were easily separable by HPLC on silica gel (hexane/EtOAc = 8/1)

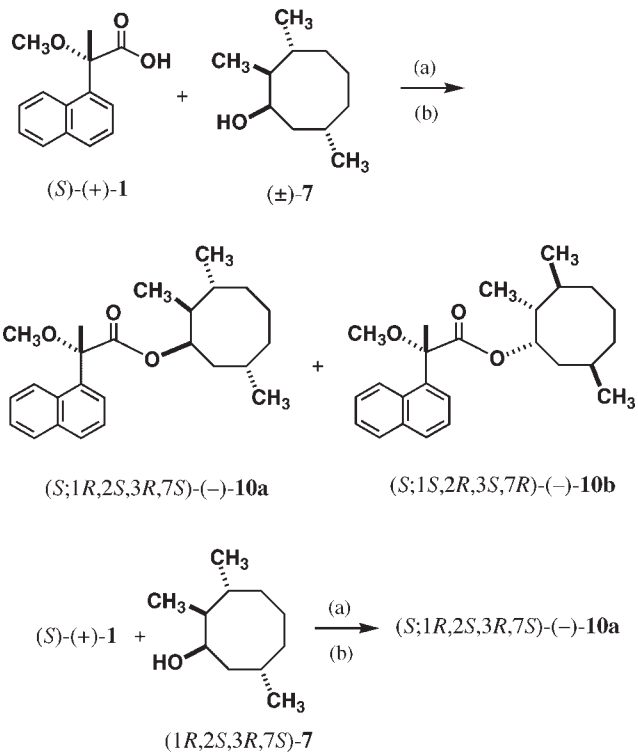

Scheme 3. Preparation of 2,3,7-trimethylcyclooctanol MαNP esters (*S*;1*R*,2*S*,3*R*,7*S*)-(–)-**10a** and (*S*;1*S*,2*R*,3*S*,7*R*)-(–)-**10b**.

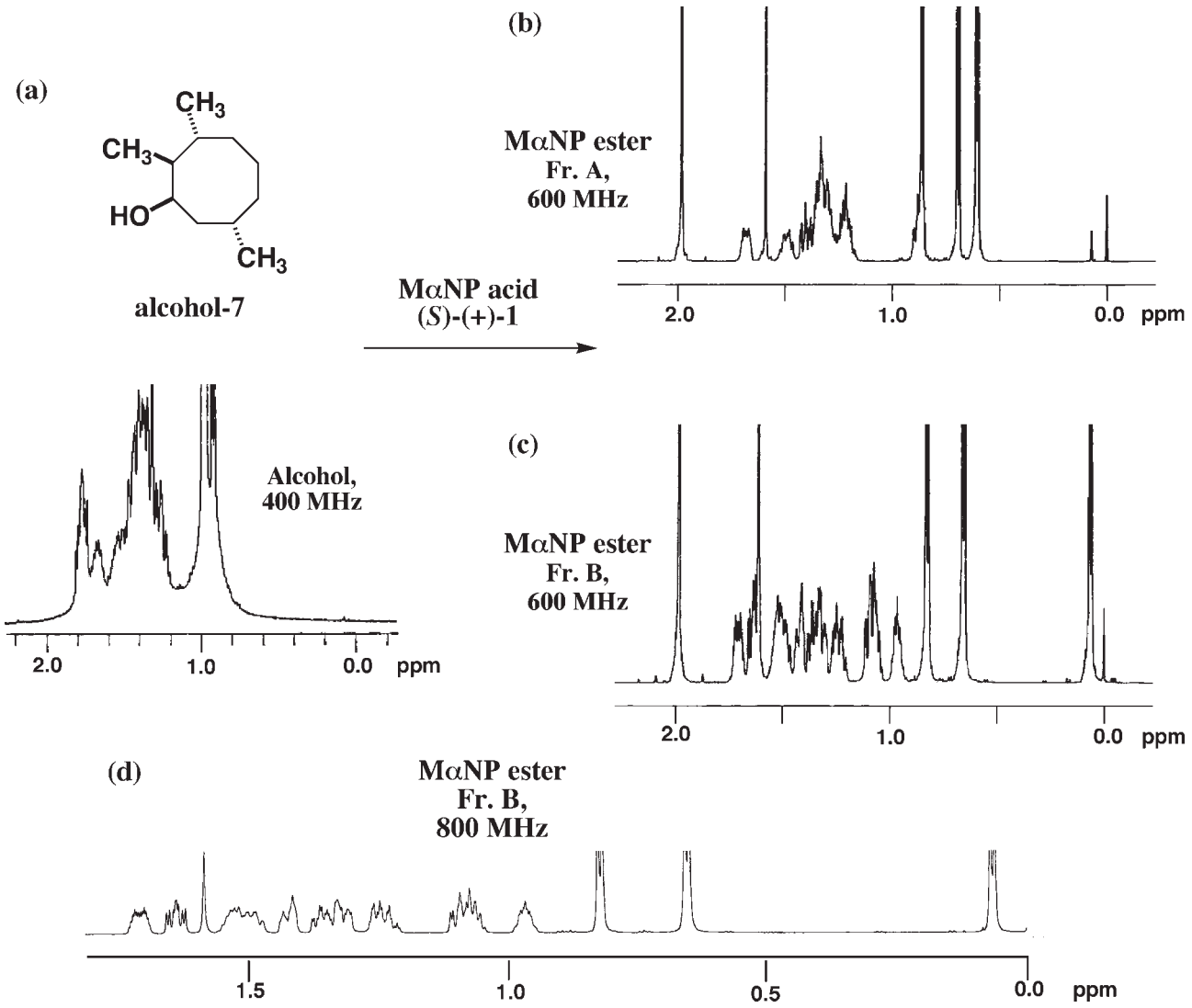

Fig. 3. Separation of ^{1}H NMR peaks by MαNP esterification ($CDCl_3$, 0.0-1.8 ppm): (**a**) 2,3,7-trimethylcyclooctanol **7** (400 MHz); (**b**) MαNP ester (*S*;1*R*,2*S*,3*R*,7*S*)-(–)-**10a** (600 MHz); (**c**, **d**) MαNP ester (*S*;1*S*,2*R*,3*S*,7*R*)-(–)-**10b** (600 and 800 MHz).

with baseline separation: separation factor $\alpha = 1.35$, resolution factor $R_s = 1.92$. The first-eluted fraction gave ester (–)-**10a** (33% yield) as an amorphous solid, the ^{1}H NMR spectrum of which indicated that the product is a single isomer. However, the ^{1}H NMR spectrum of the second-eluted fraction showed the contamination with two byproducts, which might be MαNP esters of other stereoisomers. To remove the byproducts, the second-eluted fraction was purified by repeating reverse phase HPLC using a ODS column with methanol giving pure MαNP ester (–)-**10b** (28% yield).

Determination of the Relative Configuration and Conformation of 2,3,7-Trimethylcyclooctanol Moiety by ^{1}H NMR Spectroscopy

Alcohol **7** is an eight-membered cycloalkanol, and hence in the ^{1}H NMR spectrum, methyl, methylene, and methine proton peaks largely overlap with one another as seen in Figure 3a. Therefore it is impossible to assign each proton and to deduce the relative configuration. However, it should be emphasized that in MαNP esters (–)-**10a** and (–)-**10b**, these proton peaks are largely separated from one another (Figs. 3b and 3c); especially in the second-eluted ester (–)-**10b**, most peaks appear as single protons (Fig. 3d). Hence the analysis of proton signals and determination of the relative configuration became possible. This phenomenon is of course due to the ^{1}H NMR anisotropy effect of naphthalene ring contained in the MαNP acid group. The MαNP acid method is thus useful not only for the determination of absolute configurations but also for the determination of relative configurations.

As discussed earlier, the cyclooctane ring takes a boat-chair (BC) conformation as the most stable one[14] as shown in Figure 4. Since the two methyl groups at the

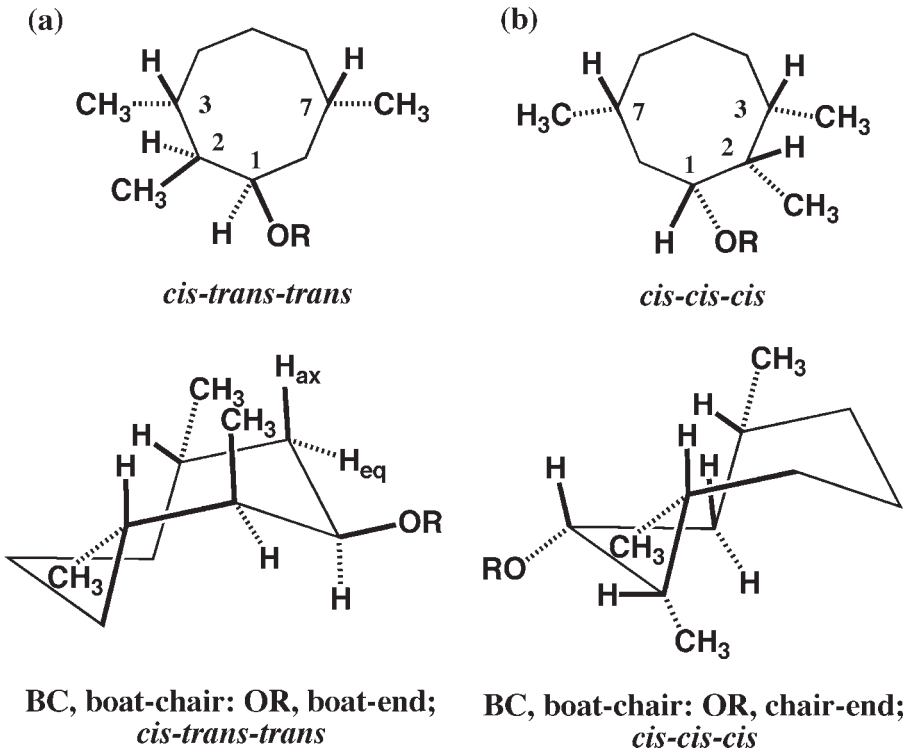

Fig. 4. Possible relative configurations and conformations of 2,3,7-trimethylcyclooctanol ester: (**a**) cis-trans-trans configuration; (**b**) cis-cis-cis configuration.

3- and 7-positions have cis-configuration, these groups are placed at the exo-positions. Therefore, 3,7-dimethylcyclooctanol takes a symmetrical conformation (a) or (b) as shown in Figure 4, where the ester moiety OR is located at the boat-end in (a) or at the chair-end in (b). This assignment is supported by the ^{1}H NMR coupling constant data of esters **10a** and **10b**: in ester **10a**, $J_{1,2}$ = 3.5 Hz, $J_{1,8ax}$ = 10.4 Hz, $J_{1,8eq}$ = 3.5 Hz (Table 1); in ester **10b**, $J_{1,2}$ = 3.5 Hz, $J_{1,8ax}$ = 10.7 Hz, $J_{1,8eq}$ = 3.5 Hz (Table 2). Namely, the ester moiety OR is located at the 1-equato-

TABLE 1. ^{13}C (125 and/or 150 MHz) and ^{1}H (500 and/or 600 MHz) NMR data of the alcohol part of the first-eluted 2,3,7-trimethylcyclooctanol MαNP ester (*S*:1*R*,2*S*,3*R*,7*S*)-(–)-10a in $CDCl_3$

Position	^{13}C	^{1}H	HSQC-TOCSY
1	75.89	5.28 (1 H, ddd, J = 10.4, 3.5, 3.5 Hz)	1-H/1-C, 1-H/8-C, 8ax-H/1-C, 8eq-H/1-C
2	42.62	1.34 (1 H, dqd, J = ~10.3, 6.8, 3.5 Hz)	2-H/2-C, 2-H/3-C, 2-H/2-CH_3, 3-H/2-C, 3-CH_3/2-C, 2-CH_3/2-C
2-CH_3	13.91	0.69 (3 H, d, J = 6.8 Hz)	2-CH_3/2-CH_3, 2-CH_3/2-C, 2-CH_3/3-C, 2-H/2-CH_3
3	37.86	1.23 (1 H, m)	3-H/3-C, 3-H/2-C, 3-H/3-CH_3, 2-CH_3/3-C, 3-CH_3/3-C, 2-H/3-C, 4-Hax/3-C
3-CH_3	23.75	0.86 (3 H, d, J = 6.5 Hz)	3-CH_3/3-CH_3, 3-CH_3/4-C, 3-CH_3/3-C, 3-CH_3/2-C, 3-H/3-CH_3
4-ax	34.01	1.49 (1 H, dddd, J = 14.5, 11.4, 8.6, 2.7 Hz)	4ax-H/4-C, 4ax-H/3-C, 4ax-H/5-C, 3-CH_3/4-C, 3-H/4-C, 4eq-H/4-C, 5eq-H/4-C
4-eq	–	1.30 (1 H, m)	4eq-H/4-C
5-ax	28.86	1.20 (1 H, m)	5ax-H/5-C, 5eq-H/5-C
5-eq	–	1.68 (1 H, ddddd, J = 13.7, 5.6, 5.6, 2.8, 2.8 Hz)	5eq-H/5-C, 5eq-H/4-C, 5eq-H/6-C
6	35.02	1.31 (2 H, m)	6-H_2/6-C, 5ax-H/6-C, 5eq-H/6-C, 7-CH_3/6-C
7	28.66	1.31 (1 H, m)	7-H/7-C, 7-H/6-C, 7-H/8-C, 7-H/7-CH_3
7-CH_3	24.92	0.60 (3 H, d, J = 6.2 Hz)	7-CH_3/7-CH_3, 7-CH_3/7-C, 7-CH_3/6-C, 7-CH_3/8-C, 7-H/7-CH_3
8-ax	37.33	1.40 (1 H, ddd, J = 13.7, 10.4, 4.4 Hz)	8ax-H/8-C, 8ax-H/7-C, 7-H/8-C, 8eq-H/8-C, 7-CH_3/8-C
8-eq	–	0.88 (1 H, ddd, J = 13.7, 10.3, 3.5 Hz)	8eq-H/8-C, 8eq-H/7-C

TABLE 2. ^{13}C (125 and/or 150 MHz) and ^{1}H (500 and/or 600 MHz) NMR data of the alcohol part of the second-eluted 2,3,7-trimethylcyclooctanol MαNP ester (*S*:1*S*,2*R*,3*S*,7*R*)-(–)-10b in $CDCl_3$

Position	^{13}C	^{1}H	HSQC-TOCSY
1	75.50	5.27 (1 H, ddd, J = 10.7, 3.5, 3.5 Hz)	1-H/1-C, 1-H/8-C, 8ax-H/1-C, 8eq-H/1-C
2	42.24	0.96 (1 H, dqd, J = 9.8, 6.5, 3.5 Hz)	2-H/2-C, 2-H/3-C, 2-H/2-CH_3, 3-H/2-C, 3-CH_3/2-C, 2-CH_3/2-C
2-CH_3	12.65	0.06 (3 H, d, J = 6.5 Hz)	2-CH_3/2-CH_3, 2-CH_3/2-C, 2-CH_3/3-C, 2-H/2-CH_3
3	37.70	1.05 (1 H, m)	3-H/3-C, 3-H/2-C, 3-H/3-CH_3, 3-H/4-C, 2-CH_3/3-C, 3-CH_3/3-C, 2-H/3-C, 4-Hax/3-C
3-CH_3	23.69	0.66 (3 H, d, J = 6.6 Hz)	3-CH_3/3-CH_3, 3-CH_3/4-C, 3-CH_3/3-C, 3-CH_3/2-C, 3-H/3-CH_3
4-ax	34.28	1.49 (1 H, m)	4ax-H/4-C, 4ax-H/3-C, 4ax-H/5-C, 3-CH_3/4-C, 3-H/4-C, 4eq-H/4-C, 5ax-H/4-C, 5eq-H/4-C
4-eq	–	1.31 (1 H, br d, J = 15.0 Hz)	4eq-H/4-C, 4eq-H/5-C, 3-CH_3/4-C
5-ax	29.22	1.23 (1 H, ddddd, J = 14.2, 11.8, 11.8, 3.6, 3.6 Hz)	5ax-H/5-C, 5ax-H/4-C, 5ax-H/6-C, 4eq-H/5-C, 6ax-H/5-C, 6eq-H/5-C, 4ax-H/5-C, 5eq-H/5-C
5-eq	–	1.71 (1 H, ddddd, J = 14.2, 5.6, 5.6, 2.8, 2.8 Hz)	5eq-H/5-C, 5eq-H/4-C, 5eq-H/6-C
6-ax	35.16	1.35 (1 H, dddd, J = 14.3, 11.7, 8.5, 2.9 Hz)	6ax-H/6-C, 6ax-H/5-C, 6eq-H/6-C, 7-CH_3/6-C 5ax-H/6-C, 5eq-H/6-C, 7-H/6-C
6-eq	–	1.42 (1 H, br d, J = 14.3 Hz)	6eq-H/6-C, 6eq-H/5-C, 6eq-H/7-C
7	28.89	1.52 (1 H, m)	7-H/7-C, 7-H/6-C, 7-H/8-C, 7-H/7-CH_3, 7-CH_3/7-C, 8-H/7-C, 6ax-H/7-C, 6eq-H/7-C, 8-ax-H/7-C
7-CH_3	25.22	0.82 (3 H, d, J = 6.6 Hz)	7-CH_3/7-CH_3, 7-CH_3/7-C, 7-CH_3/6-C, 7-CH_3/8-C, 7-H/7-CH_3
8-ax	37.48	1.63 (1 H, ddd, J = 13.6, 10.7, 4.6 Hz)	8ax-H/8-C, 8ax-H/7-C, 7-H/8-C, 8eq-H/8-C, 7-CH_3/8-C
8-eq	–	1.09 (1 H, ddd, J = 13.6, 11.1, 3.5 Hz)	8eq-H/8-C, 8eq-H/7-C

rial position, the 2-CH_3 group is at the 2-axial position, and both 3-CH_3 and 7-CH_3 groups are at the exo positions, as shown in both conformers (a) and (b).

To discriminate between the two possible stereoisomers (a) and (b), the ^{1}H NMR coupling constant data were further analyzed; in the ester **10a**, the 8eq-H shows $J_{8ax,8eq}$ = 13.7 Hz, $J_{7,8eq}$ = 10.3 Hz, $J_{1,8eq}$ = 3.5 Hz (Table 1); in ester **10b**, the 8eq-H shows $J_{8ax,8eq}$ = 13.6 Hz, $J_{7,8eq}$ = 11.1 Hz, $J_{1,8eq}$ = 3.5 Hz (Table 2). These data of the coupling constants between 7-H and 8eq-H ($J_{7,8eq}$ = 10.3–11.1 Hz) indicate that these two protons are in the trans relation {dihedral angle ϕ(7-H/8eq-H) = ca. 180°}, which is explicable only by the stereoisomer (a). On the other hand, the dihedral angle ϕ(7-H/8eq-H) is ca. 120° in the stereoisomer (b), and is not consistent with the observed coupling constant data. Therefore, the stereoisomer (a) with the cis-trans-trans configuration was assigned to esters **10a** and **10b**. We have continued further analyses by ^{1}H, ^{1}H-^{1}H COSY, ^{13}C, HMQC, and HMBC methods and came to the final assignments as shown in Tables 1 and 2.

To confirm the relative configuration and conformation of stereoisomer (a), we have studied the NOESY spectra of esters **10a** and **10b** expecting an NOE between some key protons, e.g., 3-H (endo) and 7-H (endo). In ester **10a**, however, most methylene and methine protons of the cyclooctane ring overlap with each other (Fig. 3b), and 3-H and 7-H appear at δ 1.23 and 1.31 ppm, respectively (Table 1). Therefore, it was difficult to observe the NOE between 3-H and 7-H. On the other hand, in ester **10b**, the methylene and methine protons of the cyclooctane ring are separated well by the diamagnetic anisotropy effect of the MαNP ester group as discussed earlier (Fig. 3d), and the 3-H and 7-H protons appeared at δ 1.05 and 1.52 ppm, respectively (Table 2). When the NOESY spectrum was measured with an 800 MHz NMR spectrometer, a clear cross peak was observed between 3-H and 7-H (Fig. 5 and Table 3). In addition, cross peaks were clearly observed for the following proton pairs: 2-CH_3/8ax-H, 1-H/4ax-H, and 1-H/6ax-H. The latter two NOE's, 1-H/4ax-H, and 1-H/6ax-H, clearly indicate that the ester moiety is located at the boat-end (Fig. 6). The relative configuration and conformation of the 2,3,7-trimethylcyclooctanol moiety was thus confirmed by NOESY as shown in Figure 6. It should be noted that the anisotropy effect generated by the MαNP group was thus useful for spreading and enhancing the separation of the ^{1}H NMR signals, which made the NOE measurements possible.

Determination of the Absolute Configuration of 2,3,7-Trimethylcyclooctanol by ^{1}H NMR Anisotropy

To determine the absolute configuration of 2,3,7-trimethylcyclooctanol, the MαNP acid method was next applied to esters **10a** and **10b**. The parameter Δδ representing the anisotropy effect is defined as Δδ = δ (2nd fr.) – δ (1st fr.), when (*S*)-(+)-MαNP acid is used.[1–8] The methyl, methylene, and methine protons of the cyclooctanol part in MαNP esters **10a** and **10b** were assigned by analyzing the ^{1}H NMR coupling constants, and two-dimensional ^{1}H-^{1}H COSY, ^{1}H-^{13}C COSY (HMQC and/or HSQC), and HMBC spectra. The Δδ values of all signals were calculated and plotted according to the MαNP ester sector rule.

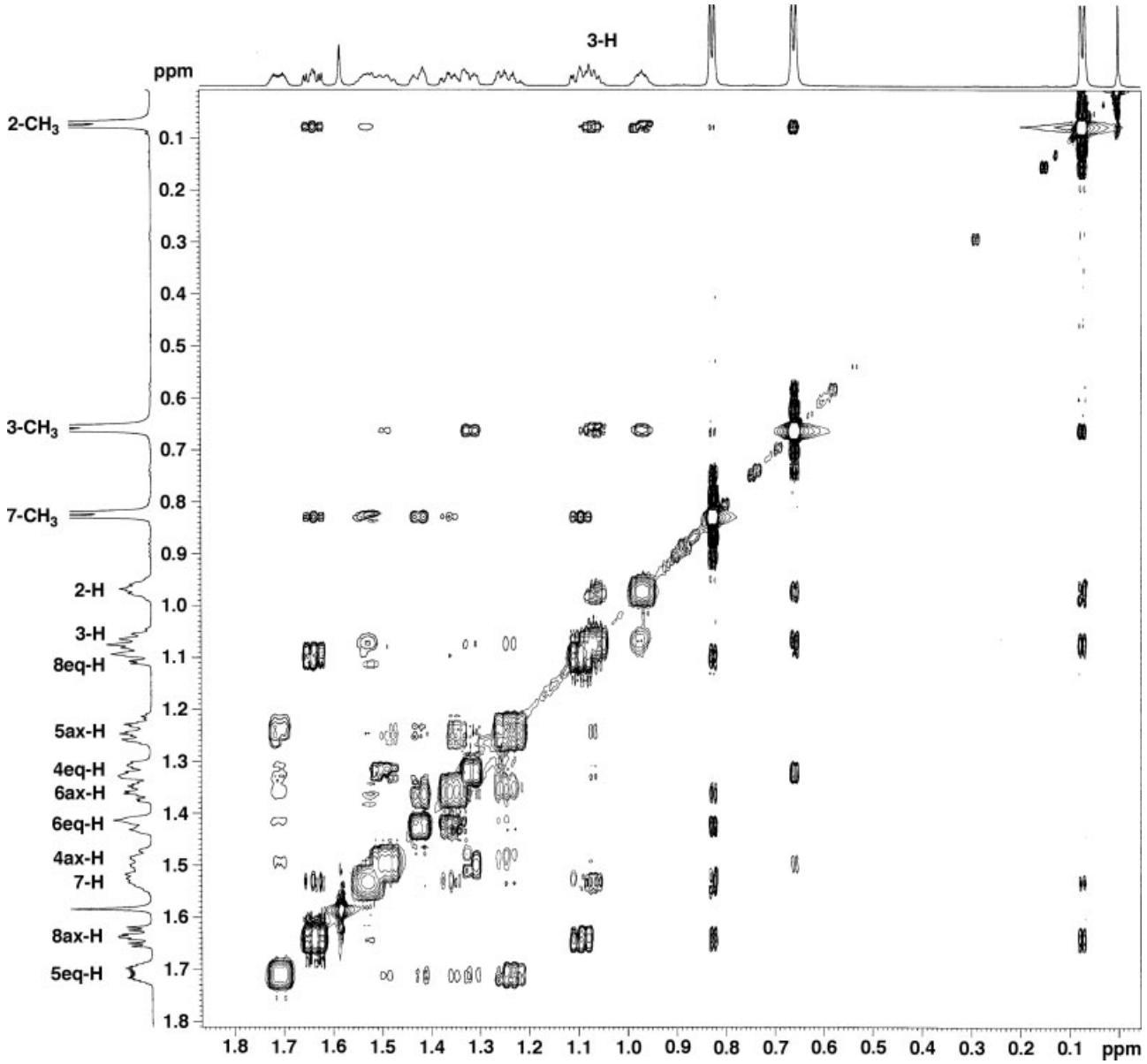

Fig. 5. ^{1}H NMR (800 MHz, $CDCl_3$) NOESY spectrum of 2,3,7-trimethylcyclooctanol MαNP ester (*S*;1*S*,2*R*,3*S*,7*R*)-(–)-**10b**.

It was found that most protons showed a reasonable distribution pattern; the right side protons showed positive Δδ values, while the left side ones negative Δδ values, obeying the MαNP sector rule. However, irregularities were found at 4ax-H and 6ax-H; 4ax-H showed as a positive Δδ value despite its location at the left side, while 6ax-H showed a negative Δδ value despite its location at the right side.

The above results clearly indicated errors in the assignment of 4ax-H and 6ax-H in MαNP ester **10a** or **10b**. So we rechecked the previous assignment and realized that 4ax-H and 6-axH in ester **10a** may be convertible. Because of the heavy overlapping of proton signals in ester **10a**, the connectivity of 4ax-H and 6ax-H was not clear, and these protons had been assigned mainly by the similarity of proton coupling pattern. Namely a signal at δ 1.49 ppm (1 H, dddd, J = 14.5, 11.4, 8.6, 2.7 Hz) in ester **10a** had been assigned to 6ax-H, because its coupling pattern was similar to that of 6ax-H in ester **10b**, δ 1.35 ppm (1 H, dddd, J = 14.3, 11.7, 8.5, 2.9 Hz) (Table 2). The remaining 6eq-H and 4-H appeared as multiplet and therefore those were not useful for assignment.

To clarify the connectivity of these protons and their attached carbons, we next measured the HSQC-TOCSY of ester **10a**, which was very useful for the assignment of ^{1}H and ^{13}C signals as discussed below. From the HMQC and HSQC, it was found that the ^{13}C signals at δ 34.01 and 35.02 ppm were assignable to 4-C or 6-C. The HSQC-TOCSY spectrum with a mixing time of 12 ms showed a weak cross peak between 3-CH_3 (δ 0.86 ppm) and C

TABLE 3. ^{1}H NMR (800 MHz) NOESY data of the alcohol part of the second-eluted 2,3,7-trimethylcyclooctanol MαNP ester (*S*:1*S*,2*R*,3*S*,7*R*)-(–)-10b in $CDCl_3$

Position	^{1}H	NOESY
1	5.27	2-H, 3-H, 4ax-H, 6ax-H
2	0.96	1-H, 2-CH_3, 3-H, 3-CH_3
2-CH_3	0.06	2-H, 3-H, 3-CH_3, 8ax-H
3	1.05	1-H, 2-H, 2-CH_3, 3-CH_3, 7-H
3-CH_3	0.66	2-CH_3, 2-H, 3-H, 4eq-H
4-ax	1.49	1-H, 4eq-H
4-eq	1.31	4ax-H, 3-CH_3
5-ax	1.23	5eq-H
5-eq	1.71	5ax-H
6-ax	1.35	1-H, 6eq-H, 7-CH_3
6-eq	1.42	6ax-H, 7- CH_3
7	1.52	3-H, 7-CH_3
7-CH_3	0.82	6eq-H, 7-H, 8ax-H, 8eq-H
8-ax	1.63	2-CH_3, 7-CH_3, 8eq-H
8-eq	1.09	7-CH_3, 8ax-H

(δ 34.01 ppm), and the cross-peak became stronger with a mixing time of 25 ms (Table 1). However, no cross-peak was found between 3-CH_3 (δ 0.86 ppm) and C (δ 35.02 ppm), Therefore, it is clear that the signal at 34.01 ppm is assignable to 4-C. On the other hand, 7-CH_3 (δ 0.60 ppm) showed a cross peak with C (δ 35.02 ppm), which was

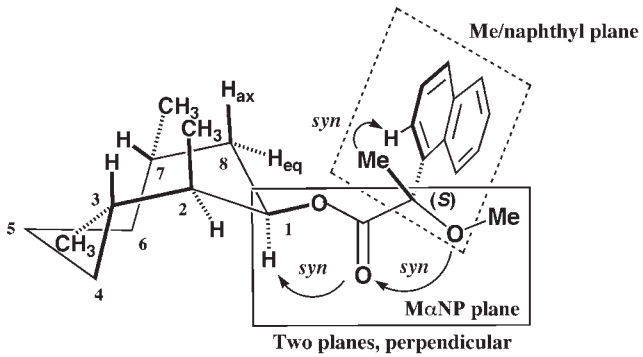

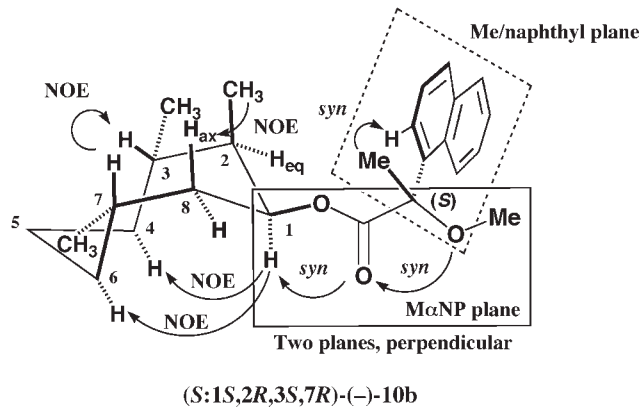

Fig. 6. Preferred conformations of 2,3,7-trimethylcyclooctanol MαNP esters (*S*;1*R*,2*S*,3*R*,7*S*)-(–)-**10a** and (*S*;1*S*,2*R*,3*S*,7*R*)-(–)-**10b**, and NOEs for ester (–)-**10b**.

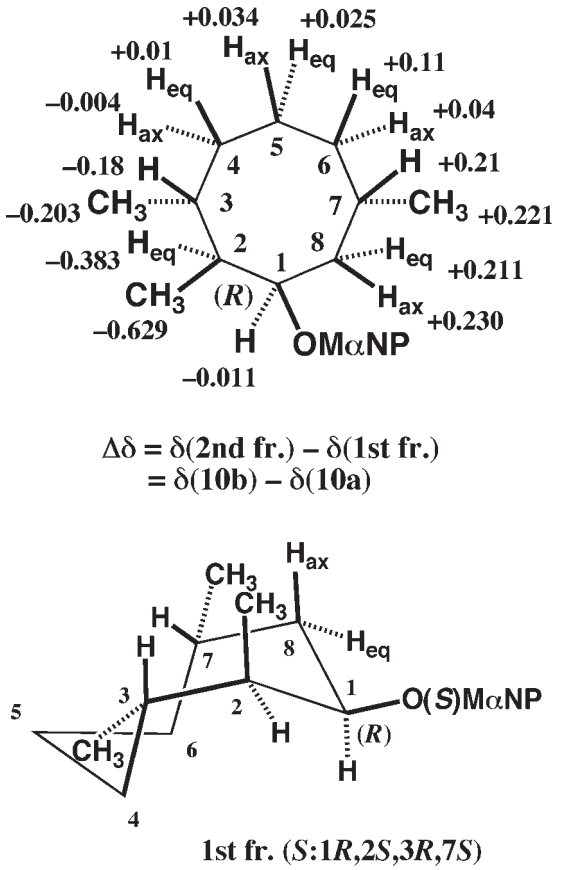

Fig. 7. Observed Δδ values (ppm), ^{1}H NMR anisotropy effects, of 2,3,7-trimethylcyclooctanol MαNP esters **10a**/**10b**, and determination of the absolute configuration of the first-eluted ester (–)-**10a**.

therefore assigned to 6-C (Table 1). From the HMQC and HSQC spectra, the proton signal at δ 1.49 ppm was assigned to 4ax-H, 1.30 ppm to 4eq-H, and 1.31 ppm to 6-H. The ^{1}H and ^{13}C signals of ester **10a** were thus established as shown in Table 1.

We next recalculated the Δδ values {Δδ = δ(2nd fr.) – δ(1st fr.) = δ(**10b**) – δ(**10a**)}; as shown in Figure 7, the right side protons show positive Δδ values, while the left side ones negative Δδ values, among which the 2-methyl group shows a large negative Δδ value. This strong anisotropy effect of the 2-methyl group is explicable by the conformation of ester **10b**, where the 2-methyl group is located just above the naphthalene ring of the MαNP group. Therefore, the strong diamagnetic anisotropy effect affected the chemical shift of 2-methyl group, and it appeared at δ 0.06 ppm (Table 2). From these results, the absolute configuration of the first-eluted fraction (–)-**10a** was determined to be (*S*;1*R*,2*S*,3*R*,7*S*). The second-eluted ester (–)-**10b** naturally takes the configuration of (*S*;1*S*,2*R*,3*S*,7*R*).

Chiral alcohol **7** synthesized from ketone (+)-**6** was esterified with (*S*)-(+)-MαNP acid **1** yielding an ester, which was identical to the first-eluted ester (–)-**10a** (Scheme 3), and therefore the absolute configurations of ketone (+)-**6** and alcohol **7** were determined to be (2*S*,3*R*,7*S*) and (1*R*,2*S*,3*R*,7*S*), respectively (Schemes 1 and 3).

CONCLUSION

The copper/chiral phosphoramidite $\mathbf{L_1}$-catalyzed conjugate addition of dimethylzinc to cyclooctadienone, followed by methylation of the resulting enolate is a highly stereoselective process affording only the trans isomer (+)-**5**. When this product was subjected to the second conjugate addition catalyzed with copper/ent-$\mathbf{L_1}$, only one stereoisomer (+)-**6** was produced reflecting the enantiomeric structure of the catalyst. The relative and absolute configurations of 2,3,7-trimethylcyclooctanone (+)-**6** and related compounds were determined by the MαNP acid method, which was applied to alcohol **7**. Diastereomeric MαNP esters **10a** and **10b** formed were easily separable by HPLC on silica gel. The strong ^{1}H NMR anisotropy effects observed in esters **10a** and **10b** were useful not only for the determination of absolute configuration but also for the determination of relative configuration by NOESY. The anisotropy method using chiral MαNP acid (*S*)-(+)-**1** (CAR) is thus very powerful for the determination of stereochemistry of aliphatic alcohols such as 2,3,7-trimethylcyclooctanol.

ACKNOWLEDGMENTS

The authors thank Drs. George A. Ellestad and Koji Nakanishi, Department of Chemistry, Columbia University, for their valuable suggestions, and the New York Structural Biology Center for the use of an 800 MHz NMR machine. One of the authors (J.D.) is a member of the New York Structural Biology Center, which is a STAR center supported by the New York State Office of Science, Technology, and Academic Research.

LITERATURE CITED

1. Harada N, Watanabe M, Kuwahara S, Sugio A, Kasai Y, Ichikawa A. 2-Methoxy-2-(1-naphthyl)propionic acid, a powerful chiral auxiliary for enantioresolution of alcohols and determination of their absolute configurations by the ^{1}H NMR anisotropy method. Tetrahedron: Asymmetry 2000;11:1249–1253.
2. Taji H, Kasai Y, Sugio A, Kuwahara S, Watanabe M, Harada N, Ichikawa A. Practical enantioresolution of alcohols with 2-methoxy-2-(1-naphthyl)propionic acid and determination of their absolute configurations by the ^{1}H NMR anisotropy method. Chirality 2002;14:81–84.
3. Kasai Y, Taji H, Fujita T, Yamamoto Y, Akagi M, Sugio A, Kuwahara S, Watanabe M, Harada N, Ichikawa A, Schurig V. MαNP acid, a powerful chiral molecular tool for preparation of enantiopure alcohols by resolution and determination of their absolute configurations by the ^{1}H NMR anisotropy method. Chirality 2004;16:569–585.
4. Kasai Y, Sugio A, Sekiguchi S, Kuwahara S, Matsumoto M, Watanabe M, Ichikawa A, Harada N. Conformational analysis of MαNP esters, powerful chiral resolution and ^{1}H NMR anisotropy tools. Aromatic geometry and solvent effects on Δδ values. Eur J Org Chem 2007;1811–1826.
5. Kuwahara S, Naito J, Yamamoto Y, Kasai Y, Fujita T, Noro K, Shimanuki K, Akagi M, Watanabe M, Matsumoto T, Watanabe M, Ichikawa A, Harada N. Crystalline state conformational analysis of MαNP esters, powerful resolution and chiral ^{1}H NMR anisotropy tools. Eur J Org Chem 2007;1827–1840.
6. Harada N. Powerful chiral molecular tools for preparation of enantiopure alcohols and simultaneous determination of their absolute configurations by X-ray crystallography and/or ^{1}H NMR anisotropy methods. In: Francotte E, Lindner W, editors. Chirality in drug research. Weinheim, Germany: Wiley-VCH; 2006. Chapter 9, p 283–321.
7. Kasai Y, Naito J, Kuwahara S, Watanabe M, Ichikawa A, Harada N. Novel chiral molecular tools for preparation of enantiopure alcohols by resolution and simultaneous determination of their absolute configurations by the ^{1}H NMR anisotropy method. J Synth Org Chem 2004;62:1114–1127.
8. Harada N. Determination of absolute configurations by X-ray crystallography and ^{1}H NMR anisotropy. Chirality 2008;20:691–723.
9. Still WC, Galynker I. Chemical consequences of conformation in macrocyclic-compounds—an effective approach to remote asymmetric induction. Tetrahedron 1981;37:3981–3996.
10. Van Summeren RP, Reijmer SJW, Feringa BL, Minnaard AJ. Catalytic asymmetric synthesis of enantiopure isoprenoid building blocks: application in the synthesis of apple leafminer pheromones. Chem Commun 2005;1387–1389.
11. Van Summeren RP. Total synthesis of enantiopure biomolecules, on mycolactones, saturated isoprenoid building blocks and beta-mannosyl phosphomycoketides. PhD thesis, University of Groningen, Groningen, 2006.
12. Van Summeren RP, Moody DB, Feringa BL, Minnaard AJ. Total synthesis of enantiopure β-D-mannosyl phosphomycoketides from *Mycobacterium tuberculosis*. J Am Chem Soc 2006;128:4546–4547.
13. Nicolaou KC, Montagnon T, Baran PS, Zhong YL. Iodine(V) reagents in organic synthesis, Part 4: *o*-iodoxybenzoic acid as a chemospecific tool for single electron transfer-based oxidation processes. J Am Chem Soc 2002;124:2245–2258.
14. Eliel EL, Wilen SH, Mander LN. Stereochemistry of organic compounds. New York: Wiley; 1994. p 765–766.
15. Berkowitz WF, Wu Y. A C-10 chiron applicable to the synthesis of archaebacterial lipids. J Org Chem 1997;62:1536–1539.

Exciton Coupling Circular Dichroism of an Allylic *N*-imidazolyl Group in Amaranzole A, a Marine Natural Product from *Phorbas amaranthus*

BRANDON I. MORINAKA[1] AND TADEUSZ F. MOLINSKI[1,2]*

[1]*Department of Chemistry and Biochemistry, University of California, San Diego, La Jolla, California*
[2]*Skaggs School of Pharmacy and Pharmaceutical Sciences, University of California, San Diego, La Jolla, California*

Presented at the 11th International Conference on Circular Dichroism, 2007, Groningen, Netherlands

ABSTRACT A new steroidal alkaloid amaranzole A (**10**) with a C24-imidazolyl group displays an unusually large split-CD spectrum at short wavelengths that we assign to exciton coupled circular dichroism (ECCD) between the polarized π-π* transitions of the C25 C=C double bond and the imidazolyl group. A model 4,5-disubstituted imidazole **11**, prepared from optically pure (*R*)-(–)-2-aminobutanol, exhibited similar ECCD and solvent and pH-dependence consistent with changes in the protonation state of the imidazole ring. Calculations and CD measurement of **12** (the dihydro-derivative of **11**) suggest that the 4-hydroxyphenyl group is not strongly conjugated to the imidazole group in **10**, and the observed ECCD is entirely accounted for by coupling between the C=C double bond and isolated imidazole π-π* transitions. *Chirality 20:1066–1070, 2008.*

KEY WORDS: circular dichroism; natural product; alkaloid; exciton coupling

INTRODUCTION

Electronic circular dichroism has a long association with the study of natural products and the assignment of their absolute configurations. Outstanding examples include the interpretation of the Cotton effects (CEs) associated with the forbidden n-π* transitions of cyclic ketones and applications to conformational analysis in steroids.[1,2] Exciton coupled circular dichroism (ECCD) is a powerful tool for assignment of configuration in natural products, and has been used to predict the configurations of cyclic diols, amino alcohols through their corresponding dibenzoates or other chromophoric diester derivatives.[3,4] Weak CEs in acyclic systems are also useful in assignment of configuration in acyclic molecules, provided there is an understanding of the origin of the CE in context of the conformation and configuration of the molecular structure. For example, we assigned the configurations of the macrolide glycosides, phorbasides A (**1**) and B (**2**) (Fig. 1a), by exploiting the CD of the remote hyperconjugated ene-yne chlorocyclopropane chromophore (λ232 nm, Δε +9.1; 241, +8.1) which relays stereochemical information within the first sphere of asymmetry of the cyclopropyl group to the allylic acyloxy-substituted carbon C13.[5] The sponge *Xestospongia muta*, common throughout the Caribbean, typically produces long-chain brominated 1,3-diene and 1,3-ene-yne unsaturated fatty acids. We recently characterized seven minor components—mutafurans A-G (**3–9**, Fig. 1b) which are the first chiral brominated lipids in this class[6]—and assigned the absolute configuration of the tetrahydrofuran ring based on interpretation of the weak ene-yne associated CEs (λ227 nm, Δε –0.46; 237, –0.5; 252, +0.26) that are asymmetrically perturbed by the propargylic center C8. In these two special cases of naturally occurring molecules with ene-yne chromophores, it is important to realize that calculations based on force field models predict the sp-sp^2 bond is essentially a free rotor with a barrier to rotation of approximately 0 kcal/mol^{-1}. The important consequence of the latter property is that accurate time-dependent DFT calculations of the CD spectra will be compromised by small inaccuracies in Boltzman-weighted distributions. In fact, as the number of degrees of freedom in an acylic system increases, the confidence level of geometry calculations may even preclude accurate CD calculations. Under these conditions, empirical approaches appear more attractive.

Recently, we reported an unusual *N*-imidazolyl steroidal alkaloid, amaranzole A (**10**) from the tropical sponge *Phorbas amaranthus* (Note that the sign of rotation given in this paper for (*R*)-2-amino-1-butanol is an error: it should be (*R*)-(–)-2-amino-1-butanol, not (+). We thank a reviewer for pointing out this error.).[7] While many imidazole and 2-aminoimidazole natural products and some steroidal alkaloids are known from marine invertebrates and microbes,[8] this is the first example of a steroidal imidazole (A 2-aminoimidizolium salt of the steroidal di-sulfate ester, halistanol, has been described).[9] The unusual structure of

Contract grant sponsor: NIH; Contract grant number: CA122256
*Correspondence to: Tadeusz F. Molinski, Department of Chemistry and Biochemistry, University of California, San Diego, 9500 Gilman Drive, La Jolla, California 92093, USA. E-mail: tmolinski@ucsd.edu
Received for publication 14 November 2007; Accepted 4 June 2008
DOI: 10.1002/chir.20636
Published online 8 August 2008 in Wiley InterScience (www.interscience.wiley.com).

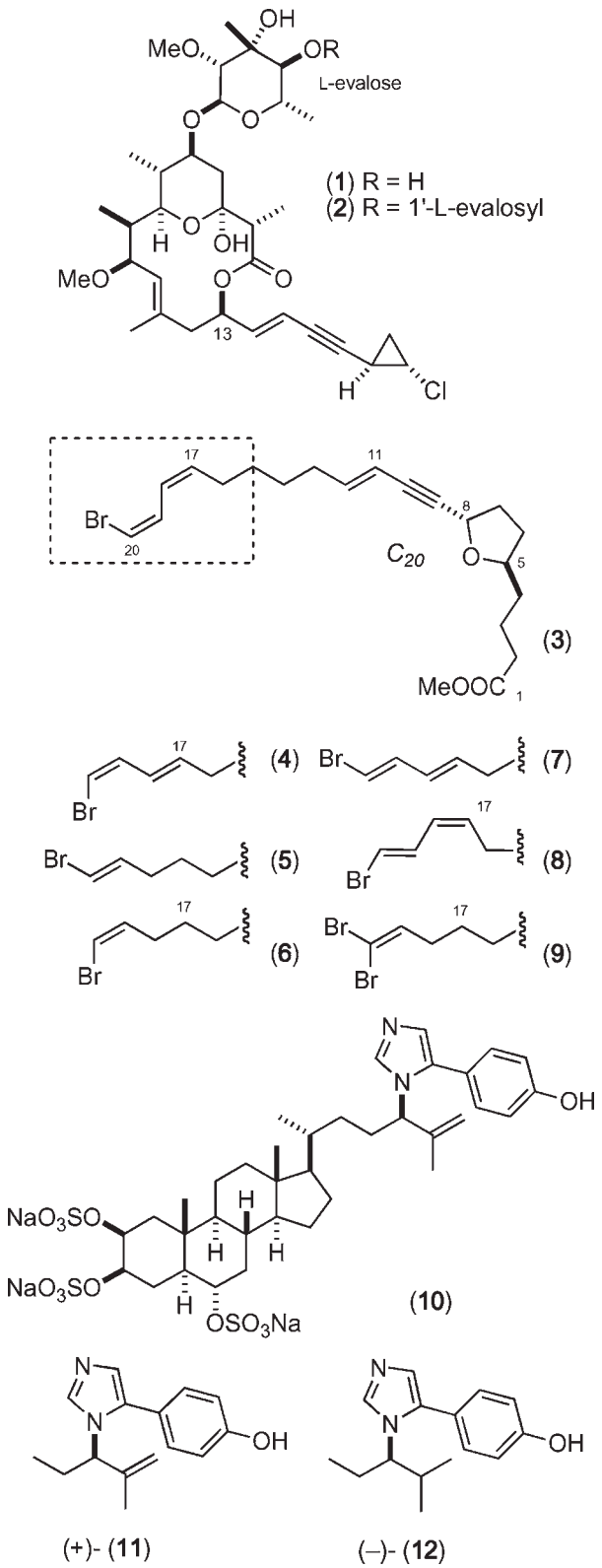

Fig. 1. Phorbasides A (**1**), B (**2**), mutafurans A-G (**3–9**), amaranzole A (**10**), and model compounds (+)-(*R*)-**11** and (–)-(*R*)-**12**.

10 implies a convergence of isoprenoid and amino acid secondary metabolism and presented a challenge for configurational assignment. Amaranzole A exhibited a positive CE at $\lambda \sim 205$ nm which we presumed to arise from ECCD between the imidazole and the 1,1-disubstituted olefin which absorbs $\lambda < 200$ nm. The C24 configuration was solved by matching the CD spectrum of **10** with that of a stereodefined model imidazole prepared from (*R*)-(–)-2-amino-1-butanol.[7] In this report we characterize the CD properties of allyl imidazole and propose an assignment of the origin of the ECCD between the isolated imidazole and the 1,1-disubstituted alkene.

EXPERIMENTAL

General

All CD spectra were acquired with a JASCO-810 spectrophotometer at 23°C using a 2 mm cell at concentrations of $\sim 1 \times 10^{-4}$ M in spectroscopic or HPLC grade solvents (Aldrich, MeOH, CH_3CN, H_2O, or CF_3CH_2OH). Each CD spectrum was acquired by averaging 20 scans with correction for background (solvent). Smoothing was applied to the CD spectra in Figures 2a and 2b. No smoothing was applied to the data in Figure 4. pH measurements were carried out using a Denver Instrument Model 220 pH-conductivity meter which was calibrated against standard buffers. The isolation and purification of amaranzole A (**10**) and synthesis of compounds (+)-(*R*)-**11** and (–)-(*R*)-**12** are described elsewhere.[7]

pH Dependence of the CD Spectrum of 11

The CD spectrum of a solution of **11** (0.1 mM, 500 μL) in 30% CF_3CH_2OH/20 mM aqueous Na_2HPO_4, pH 8.2) was measured (pH = 8.2). The solution was titrated with aqueous HCl (0.375 M, 5 μl, resultant pH = 7.2), the CD spectrum measured again, and the procedure repeated (pH = 6.4). The solution was titrated sequentially three more times with 0.125 M HCl (5 μL) and CD measurements made in between additions at resultant pHs = 5.9, 4.9, and 3.3.

Calculations

Calculations were performed at semi-empirical level (PM3) or DFT (B3LYP-/6-31G(D), Spartan 2004) on a Macintosh (G4 Motorola processor, 1.44 GHz, or iMac (Intel Core2 Duo, 2.4 GHz processor).

RESULTS AND DISCUSSION

The marine sponge *Phorbas amaranthus* occurs in waters of the Florida Keys and, less commonly, in the Bahamas. Amaranzole A (**10**) was isolated from the polar extracts *P. amaranthus* collected at Key Largo by extensive gel filtration chromatography and final purification by HPLC. The substitution pattern and stereochemistry of the sterol core was assigned using conventional NMR techniques, in particular analysis of the vicinal coupling constants and the NOESY spectra. Compound **10** is the first example of a steroidal imidazole natural product and presented a unique challenge for stereochemical analysis. The configuration of the remote C24–imidazolyl group in

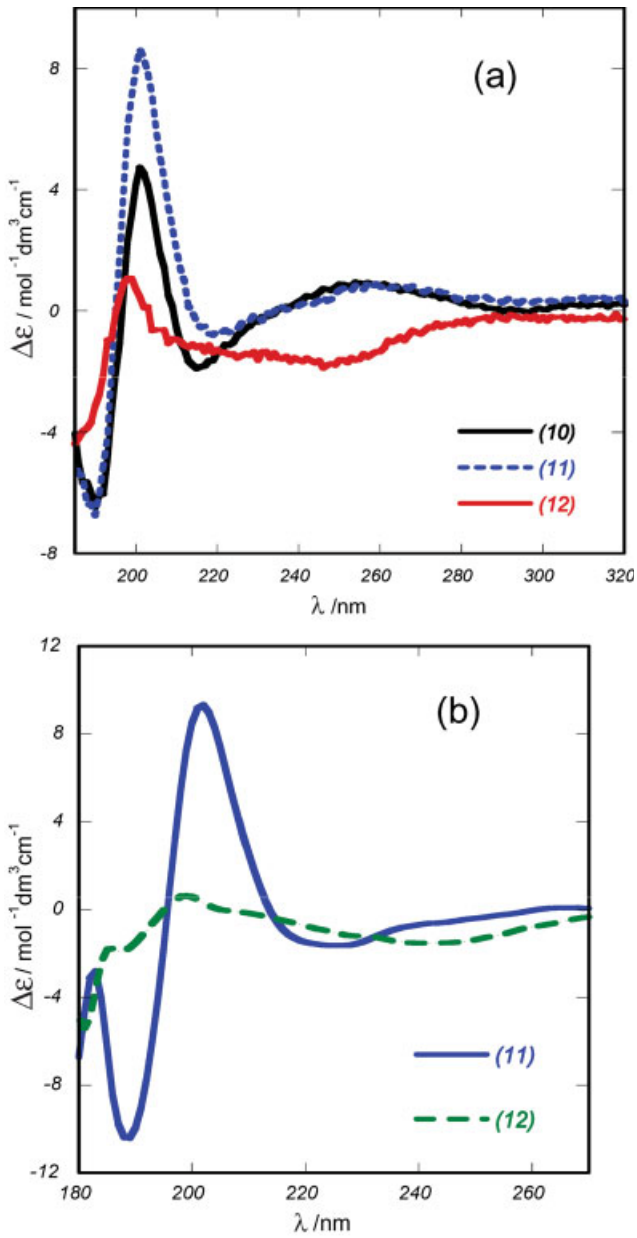

Fig. 2. (**a**) CD spectra of (A) amaranzole A (**10**), (B) compound **11**, and compound **12** (3:7 CH_3CN/H_2O, T = 23°C). (**b**) CD spectra of compound **11** and **12** (CH_3CN, T = 23°C). [Color figure can be viewed in the online issue, which is available at www.interscience.wiley.com.]

10 could not be assigned by standard methods, however, the CD spectrum of **10** (MeOH, 22°C) showed rich information that allowed configurational assignment by comparison with suitable model compounds **11** and **12**.

Compound **11** was prepared in several steps from (*R*)-(–)-2-amino-1-butanol.[7] The CD spectra of **10** and **11** were originally reported in MeOH, however, the low-wavelength CEs are less obscured in 3:7 CH_3CN/H_2O as reported here (Fig. 2a). Compound **11** displayed a weak positive CE at ~256 nm (<0.2), a negative CE at 218 nm ($\Delta\varepsilon$ –0.9) and stronger positive effect (λ 201 nm, $\Delta\varepsilon$ +8.4) followed by a strong negative CE (189 nm, $\Delta\varepsilon$ –6.4). Almost identical CEs were seen in amaranzole A (**10**), except the intensity of the CE at λ 201 nm was decreased ($\Delta\varepsilon$ +4.5); therefore we may assign a (24*R*)-configuration to **10**. The weak band at 256 nm was assigned to a weakly perturbed phenol chromophore, however the pH-dependent UV spectra suggested this chromophore was, at best, poorly conjugated to the imidazole group. Vicinal substitution of the imidazole ring by the *N*-1-alkenyl group and C4-*para*-hydroxyphenyl group gives rise to nonbonded interactions that force the two rings out of planarity; a phenomenon that is supported by molecular mechanics calculations which reveal that the imidazole and benzene rings **11** are skewed at an angle of ~77° (Fig. 3c).[6]

Because of the limited solubility of **10** in solvents other than MeOH, the analysis of the ECCD of allylic *N*-imidazoles were interpreted from measurements of **11** and **12**

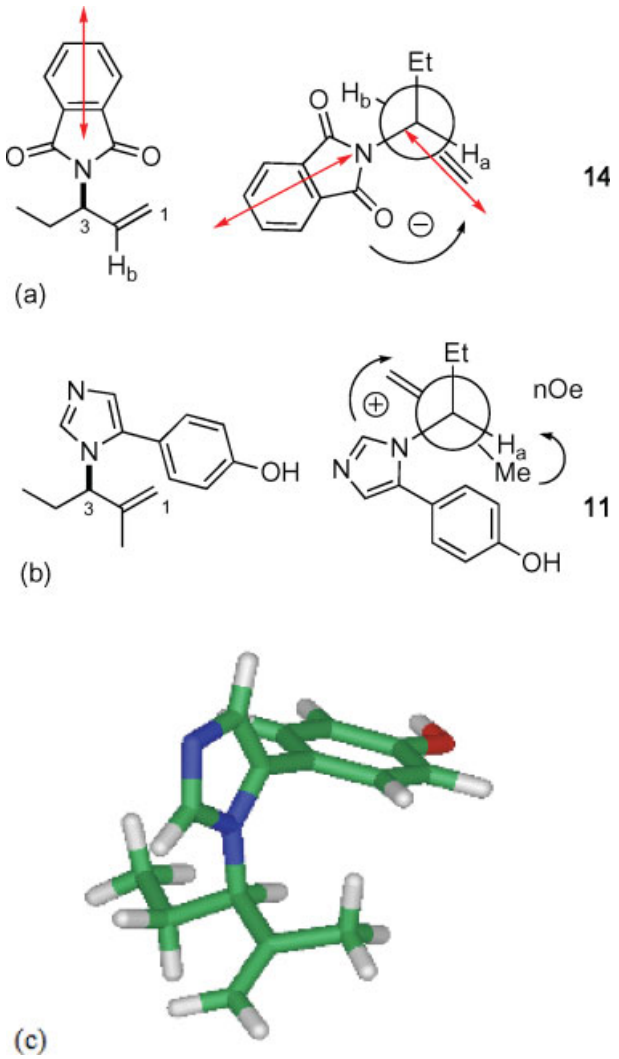

Fig. 3. Dominant conformation of (3*R*)-*N*-allylic heterocycles (**a**) (*R*)-phthalimide **14** showing directions of π-π* electronic transition dipole moments and helicity of chromophores (from Skowrońek and Gawroński[10]) (**b**) (*R*)-*N*-allyl imidazole **11** and nOe (**c**) Force field minimized conformation of **11** (MMFF94, Spartan 2004). [Color figure can be viewed in the online issue, which is available at www.interscience.wiley.com.]

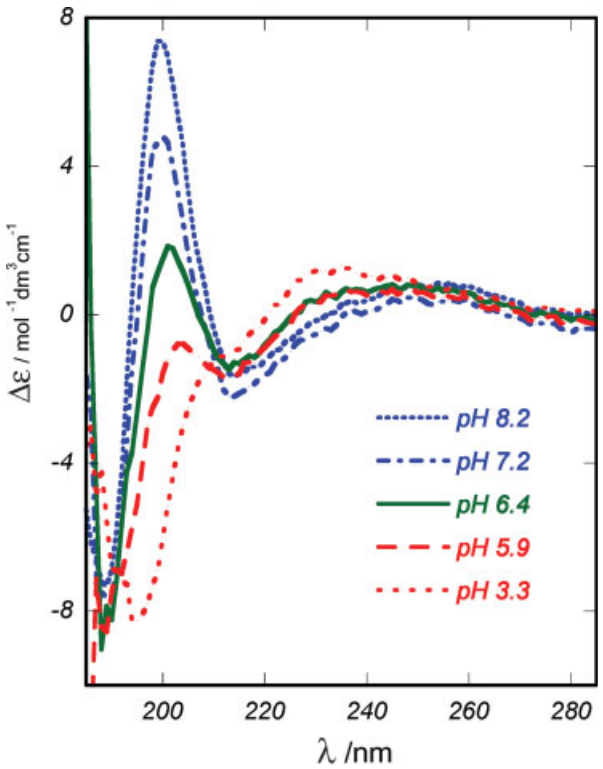

Fig. 4. pH-dependent CD spectra for compound **11** (30% CF_3CH_2OH + H_2O, 20 mM Na_2HPO_4/NaH_2PO_4), T = 23°C. [Color figure can be viewed in the online issue, which is available at www.interscience.wiley.com.]

in CH_3CN and comparisons with **10**. The electronic spectrum of the parent heterocycle, imidazole **13**, has been studied both experimentally and by quantitative MO methods.[11,12] Two short-wavelength transitions of moderate intensity are seen in neutral aqueous solutions of **13** at λ = 187 nm (ε 4200) and 207 nm (λ 4500); the former band is blue shifted at pH = 2 (λ = 178 nm).[12] Solvent and pH dependence of the CD spectrum of substituted imidazole chromophores may be expected if these transitions participate in ECCD, however, it was not clear from the outset how this would influence the CD spectrum of **10** and **11**. Despite these uncertainties, the expected directionality of the transition dipole moments in **10** and **11** based upon examination of HOMO and LUMO should roughly bisect C2 (imidazole numbering) and the mid-point of C4-C5. The 1,1-disubstituted olefin π-π* transition of **10** and **11** lies at the edge of our observation window, however its participation in ECCD is readily evident in the CD spectrum of **11** (Fig. 2b) where the strong negative short-wavelength component of the split CE is observed (λ 187 nm, Δε –11). The latter effect is absent in the CD spectrum of dihydro-derivative **12** (Compound **12** was prepared by catalytic hydrogenation of **11** (5% Pd-C, H_2, 1 atm)) where only shallow CEs remain from weak asymmetric perturbations of the imidazole and phenol chromophores (λ_{max} 200 nm, Δε < –0.2; ~250 Δε +1.5, note reversal of sign at ~250 nm, Δε –2, compared to **11**).

Analysis of the origin of the ECCD in **10** and **11** is made difficult by conformational mobility of the N1-side chain on the imidazole ring, uncertainties of the conformer populations about several rotors, including the C3—N, C2—C3, and C3—C4 bonds, and direction of the transition dipole polarization. However, early studies of allylic alcohol and amine derivatives provide some guidance. Nakanishi and coworkers demonstrated that the major conformation of benzoates esters of secondary allylic alcohols is well-defined and consistent for all members; the lowest energy conformation is that which eclipses the allylic methine H_a by the C=C bond.[13] The transition dipole moment of the benzoate chromophore is oriented roughly along the C—O bond and subtends a negative helicity in (*R*)-benzoates of allylic secondary alcohols that gives rise to a negative ECCD. In (*S*)-enantiomers, the sign of the ECCD is reversed. Skowrońek and Gawroński showed that the phthalimides derived from simple (*R*)-allylic amines (e.g. **14**) also give rise to a negative ECCD that arises from essentially the similar conformation (Fig. 3).[10] Similar trends were observed for 2-naphthamides of allylic amines.[14] In contrast, the sign of the ECCD in **10** and (+)-(*R*)-**11** is reversed; (*R*)-Allylic imidazoles **10** and **11** show a positive ECCD effect. The sign reversal implies either the transition dipole moment vector of the imidazole has changed direction with respect to the π-π* transition of the C=C double bond, or the dominant conformation of the molecules are different, or both.

The conformation of **11** was defined by nOe measurements and calculations. Irradiation of the vinyl methyl group in **11** gave rise to a significant nOe at H3, but no nOe was observed between the vinyl proton signals and H3, suggesting the major conformation is that depicted in

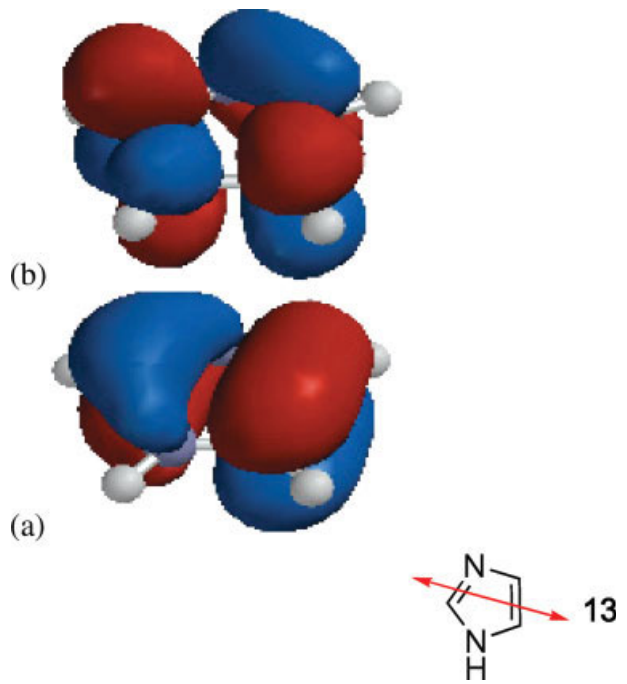

Fig. 5. Calculated frontier orbitals of imidazole (**13**) (**a**) HOMO (**b**) LUMO (PM3 level, Spartan 2004) and approximate direction of electronic transition dipole. [Color figure can be viewed in the online issue, which is available at www.interscience.wiley.com.]

Figure 3b. NOe was also observed from H3 to the ortho-protons (H1') on the phenyl ring of **11** consistent with a conformation in which the H3 methine is syn to the phenyl ring (Fig. 3b). The lowest energy conformation of **11** was also calculated using molecular mechanics (Fig. 3, MMFF94, Spartan 2004) and found to be entirely consistent with the nOe results, although, other low-lying rotamers may make minor contributions to the global conformer distribution in **2** and **11**.

To further characterize the ECCD of allylic imidazoles, we carried out pH-dependent measurements of the CD spectrum of **11** (Fig. 4). At neutral or alkaline pH, the CD spectrum of **11** (30% CF_3CH_2OH: aqueous phosphate buffer) were essentially the same, however, lowering the pH lead to a progressive diminution of the positive CE at $\lambda \sim 200$ nm until, at pH = 3.3, the sign of the long-wavelength CE was inverted ($\Delta\varepsilon$ –8). Within the limits of experimental error, it appeared that all CD spectra passed through an isobestic point at $\lambda \sim 210$ nm suggesting the pH-dependency of the CD spectrum was associated with reversible protonation of the imidazole ring. Grebow and Hooker showed that the orientation of the transition dipole moment of the neutral form of imidazole and protonated imidazole are significantly different.[12] A corresponding change in transition dipole orientation in **10** and **11** upon protonation of the imidazole nitrogen (Fig. 5) may be responsible for the significant pH-dependent CEs we observe. We cannot exclude other factors such as small changes in the Boltzman-weighted populations of conformations upon protonation of the imidazole N, although this seems unlikely, and the former explanation would seem to prevail.

CONCLUSION

In conclusion, the structure elucidation and configurational assignment of amaranzole A (**10**) has lead to the discovery of a useful ECCD in allylic imidazoles. Both components of the split CE are observable when the CD spectra were recorded in acetonitrile. From the pH dependency and solvent effects of the CD spectra of allylic imidazoles, it appears that the ECCD is fully accounted by coupling between the terminal C=C double bond and the imidazole, with negligible electronic contributions from the *p*-hydroxyphenyl group. The present study should find utility in assignment of minor congeners of amaranzole A and possible extension to other allylic azoles (e.g. 1,2-pyrazole, 1,2,4-triazole and benzimidazole).

ACKNOWLEDGMENTS

We are most grateful to J. R. Pawlik for collections of *P. amaranthus* in Key Largo, Florida.

LITERATURE CITED

1. Crabbé P. Optical rotatory dispersion and circular dichroism in organic chemistry. San Francisco: Holden-Day; 1965.
2. Lightner DA, Gurst GE. Conformational analysis and stereochemistry from circular dichroism spectroscopy. New York: Wiley-VCH; 2000.
3. Harada N, Nakanishi K. Circular dichroic spectroscopy—exciton coupling in organic stereochemistry. Mill Valley, CA: University Science Books; 1983.
4. Nakanishi K, Berova N. Exciton chirality method: principles and applications. In: Nakanishi K, Berova N, Woody RW, editors. Circular dichroism—principles and applications. New York: Wiley-VCH; 2000. p 337–382.
5. Skepper CK, MacMillan JB, Zhou GX, Masuno MN, Molinski TF. Chlorocyclopropane macrolides from the Marine Sponge *Phorbas* sp. Assignment of the configurations of Phorbasides A and B by quantitative CD. J Am Chem Soc 2007;129:4150–4151.
6. Morinaka BI, Skepper CK, Molinski TF. Ene-yne tetrahydrofurans from the Sponge *Xestospongia muta*. Exploiting a weak CD effect for assignment of configuration. Org Lett 2007;9:1975–1978.
7. Morinaka BI, Masuno MN, Pawlik JR, Molinski TF. Amaranzole A, a new *N*-imidazolyl steroid from *Phorbas amaranthus*. Org Lett 2007;9:5219–5222.
8. Blunt JW, Copp BR, Munro MHG, Northcote PT, Princep MR. Marine natural products. Nat Prod Rep 2007;24:31–86.
9. Tsukamoto S, Kato H, Hirota H, Fusetani N. Antifouling terpenes and steroids against barnacle larvae from marine sponges. Biofouling 1997;11:283–291.
10. Skowrońek P, Gawroński J. A simple circular dichroism method for the determination of the absolute configuration of allylic amines. Tetrahedron Lett 2000;41:2975–2977.
11. Horvath G, Kiss ÁI. The electronic spectra of five-membered ring heterocyclic compounds. Spectrochim Acta 1967;23:921–924.
12. Grebow PE, Hooker TM Jr. Conformation of histidine model peptides. II. Spectroscopic properties of the imidazole chromophore. Biopolymers 1975;14:871–881.
13. Gonnella NC, Nakanishi K, Martin VS, Sharpless KB. General method for determining absolute configurations of acyclic alcohols. J Am Chem Soc 1982;104:3775–3776.
14. Tanaka K, Nakanishi K, Berova N. Absolute stereochemistry of allylic alcohols, amines, and other ene moieties: a microscale cross metathesis/exciton chirality protocol. J Am Chem Soc 2003;125:10802–10803.